April 2016

Phase I Topical Report
September 1, 2015 to April 5, 2016

submitted to
U.S. Department of Energy
National Energy Technology Laboratory

Pressure Management and Plume Control Strategies through a Brine Extraction Storage Test at the Devine Test Site in Texas

Award No DE-FE0026137
in response to Funding Opportunity No DE-FOA-0001260
"Fit-for-Purpose Field Project: Developing and Validating Pressure Management and Plume Control Strategies through a Brine Extraction Storage Test (BEST)"

Principal Investigators
S. A. Hosseini, P.I. and J.-P. Nicot, co-P.I.
tel: 512 471 2360; fax: 512 471 0140; seyyed.hosseini@beg.utexas.edu

Team Members:
GE Global Research (GRC)
Geostock Sandia LLC

Bureau of Economic Geology
Jackson School of Geosciences
The University of Texas at Austin
Austin, Texas 78713-8924

April 2016

Pressure Management and Plume Control Strategies through a Brine Extraction Storage Test (BEST) at the Devine Test Site (DTS) in Texas

S. Hosseini[1], J.-P. Nicot[1], R. Darvari[1], R. Costley[1], J. Lu[1], D. Sava[1], A. Goudarzi[1], P. Mickler[1], D. Banerji[1], K. Uhlman[2], S. Walden[3], T. F. Hentz[1], H. S. Hamlin[1], R. Ganjdanesh[1], A. Sun[1], S. Hovorka[1], and B. Scanlon[1]

[1]: Bureau of Economic Geology, The University of Texas at Austin
[2]: Kristine Uhlman Consulting, Tucson, AZ
[3]: Steve Walden Consulting, Austin, TX

Bureau of Economic Geology
Jackson School of Geosciences
The University of Texas at Austin
Austin, Texas 78713-8924

Disclaimer

Abstract

This document presents the results of a study investigating the suitability of the Devine Test Site to host a field project designed to explore strategies to tackle pressure impacts at CO_2 geological storage sites. The site is located in South Texas ~50 miles southwest of San Antonio and owned by the University of Texas at Austin. Pressure buildup in the storage formation is the driving force behind many of the CO_2 storage related risks. The project's main aim and objective consists in actively extracting the formation brine while water, used as a CO_2 proxy, is injected into the target formation. In parallel, the extracted brine is used as a test-bed for brine treatment technologies with the ultimate goal of having the treated water put to beneficial use. The general potential benefits of employing brine extraction wells include increased CO_2 storage capacity, reduced stress on the sealing formation, reduced risk of brine and plume movement into unwanted formations, reduced area of review, and reduced seismic risks.

We propose to drill and operate one injection well, one brine extraction well, and one observation well. The three wells will be perforated at a depth of ~7000 ft in the Hosston Formation (Cretaceous basal sands). Numerical modeling shows that a triangular configuration with wells located at apexes of an equilateral triangle with ~150 ft sides is optimum to meet the project objectives given the geological uncertainties. Associated injection and extraction rates are 5000 and 2500 barrels per day, respectively. The geology and environment of the site is very favorable. The Hosston Formation is overlain by multiple seals made of shales and tight carbonates. In addition the location of the site in an active oil and gas province makes it very practical to deal with operational issues including waste water disposal into commercial wells if needed. Multiple sources of water can be used to maintain the injection rate for extended periods of time. In addition to recycling the extracted water, several productive aquifers are present in the vicinity and produced water from oil and gas activities can also be used. The chemical compatibility between the various sources was successfully examined.

We explored Monitoring, Verification and Accounting (MVA) plans and tools that could be deployed to demonstrate the capabilities of pressure management and plume control strategies. In addition to using conventional downhole pressure and temperature gauges to directly measure pressure differentials, we examined the use of tracers, both common (dye breakthrough time) and smart (magnetic nanoparticles illuminating the injected plume through repeat cross-well electromagnetic surveys) to track and image the injected plume, surface seismometers and downhole geophones to record small seismic events, infer pressure propagation front, and monitor the injection process in general. The option of using repeat seismic surveys to map pressure differentials through time was also investigated and deemed very feasible, if expensive.

A fraction of the extracted brine will be treated and possibly blended with Eagle Ford produced water in the feed stream to augment its salinity. Most salinity measurements (grab samples, geophysical logs) point to a salinity of ~50,000 mg/L for on-site and off-site saline waters. Blending can be complemented by a concentration pretreatment to bring the feed water TDS up to >150,000 mg/l. This report provides a design and implementation plan for the field test-bed facility to test a wide range of both pretreatment and desalination technologies.

Executive Summary

The Phase I topical report presents results of a desktop analysis to demonstrate the benefits of brine extraction strategy in alleviating pressure buildup and controlling the plume during CO_2 storage operations. In parallel, the produced brine can be beneficial if treated and used as a water source for possible off-site users. The topical report addresses topics of importance that must be considered before proceeding to the field experiments in Phase II. It discusses (1) site characterization: advantages and drawbacks of the selected site; (2) parameters of the injection and extraction doublet, which are assessed through numerical modeling; (3) monitoring and verification methods (so called MVA plans) to ensure that the project objectives are met, including numerical modeling of some of the methods to demonstrate that they will likely work at the selected site; (4) Life-cycle assessment (LCA) of the water including source, quality, transport, storage, and ultimate fate at the surface and in the subsurface; and (5) description of brine treatment technologies to be tested and that would work well and at reasonable cost for the high TDS usually encountered at depths at which CO_2 will likely be stored.

Note that, because the main objective of the project is to manage pressure and control the plume through brine extraction and also to use the extracted brine to test bed brine treatment technologies, there is no need to use CO_2. Indeed, this project will inject water and brine of various origins and also produce brine as a proxy for CO_2. This objective stems from the fact that addressing risks related to CO_2 injection plays a crucial role in determining whether industry and other end-users will adopt geological storage of CO_2 and pressure is the driving cause of many storage-related risks.

The selected site, the Devine Test Site (DTS), is located in South Texas not far from the city of San Antonio but away from population centers (closest small town of Yancey –pop. 200– at 2.5 miles). It has the benefits of being in an oil and gas province, that is, with easy physical access to the property and availability of drillers and service companies but is not so close to active and historical oil and gas fields to generate pressure interferences. In addition, the site belongs to the University of Texas and is managed by the BEG, eliminating third-party issues. The geology is favorable with the top of the target formation, the Hosston Formation, located at a depth of ~6000ft. It is a mostly fluvio-deltaic sandy ~1000 ft-thick formation of Cretaceous age directly overlying the Paleozoic basement. Although no well have reached the target formation at the site, this formation is well-known throughout the state and usually presents acceptable permeability. Shale intervals periodically interrupts the sandy succession strongly suggesting that an injection interval of suitable thickness and permeability can be found. The carbonate Sligo Formation immediately overlying the Hosston Formation forms the regional seal, reinforced by the presence of the Pearsall Shale and of another low-permeability carbonate, the Glenrose Formation. The brine hosted by the target formation and that would be produced has a relatively low TDS of ~40,000-50,000 mg/L according to examination of geophysical resistivity logs of close-by wells and sampling of wells reaching the same formation. Its water type is likely sodium-chloride with some sulfate. The stratigraphic section also shows the presence of two major fresh-water aquifers hosted by the carbonate Edwards and allied formations at ~3000 ft and the siliciclastic Carrizo-Wilcox at the surface (down to ~500 ft at the site). Both aquifers exhibits a sodium-bicarbonate water type. The interburden between them consists of mostly shaly material but also shows the presence of sands (especially in the Escondido Formation at ~1000 ft). We also performed autoclave experiments exposing Hosston Fm. rock fragments gathered from cores stored at the

BEG repository to Eagle Ford produced water and other saline waters to assess their geochemical compatibility. Observed geochemical interactions are small.

We performed numerical modeling to design the injection-extraction system. Given budget and time constraints of the Phase II, three wells (injection, location, and observation wells) located at the apexes of a equilateral triangle with ~150 ft sides were found to be a better configuration than if the wells were aligned. An injection rate of ~5000 barrel per day (bpd) and extraction rate of 2500 bpd were calculated to be the most robust design given the uncertainty in injection interval thickness and system flow properties. We also examined the option of having a passive system, that is, excess pressure in the injection interval being partly relieved by having some of resident brine flow through an open conduit connected to an overlying interval in response to the pressure gradient (Olmos in the interburden). Such a system does not meet the pressure objectives of the project unlike the active system in which the fluids are actively brought to the surface. We also modeled the various tests needed to better characterize the flow system with novel approaches such as the harmonic pulse test.

We investigated several approaches to monitor both the pressure plume and the actual injected fluid plume in addition to the conventional pressure and temperature gauges: 4D-seismic and tracers. Increased pressure modifies the compressibility of the fluid and porous medium that will in turn impact seismic wave travel time. A desktop investigation found that the approach is feasible, especially if downhole geophones are used and if the data are of excellent quality. Conventional tracer tests using dyes have used for many decades, here we proposed to use magnetic nanoparticles that can be illuminated using an electromagnetic logging tool and thus provide a 3-D image of the injected fluid plume.

The water LCA is relatively simple. Because most of the water extracted on-site cannot go through the desalination treatment test bed (only 10 gpm or ~350 bpd), most will be reinjected through the injection well. During the injection-extraction steady state period, additional water is needed because of the uneven balance between injection and production volumes, it will allow to maintain the pressure differential as designed because of pressure bleeding through the system boundaries. On-site and off-site sources are local fresh and brackish water wells taping the Carrizo-Wilcox and interburden aquifers and Eagle Ford Shale produced water, respectively.

Several treatment technologies will be examined at the site after the TDS of the feed water has been increased to the requested value of 180,000 mg/L through an initial preconcentration step or recycling of the concentrate.

The overall conclusion of this analysis is that the proposed project is highly feasible and has high chances of success at the Devine Test Site and of meeting DOE objectives.

Table of Contents

List of Figures

List of Tables

Acknowledgments

The authors would like to thank DOE NETL (Mr. William O'Dowd, Project Manager) for funding this research and the Jackson School of Geosciences at The University of Texas at Austin for providing the cost share. We are also grateful to operators and well owners who let us sample their oil and gas and water wells, in particular Basic Energy Services, Inc. thanks whom we were able to collect a large amount of brine for preliminary desalting treatment. We thank Dr. Hardage at the BEG, manager of the Devine Test Site, for his help in securing the site for this project. We are also indebted to IHS for providing free access to their Enerdeq oil and gas database.

Acronyms

APMS	Active pressure management system
BEG	Bureau of Economic Geology
BEST	Brine Extraction Storage Test
bgs	below ground surface
BHP	Bottom-hole pressure
BMP	Best management practices
BSE	Secondary electron (images)
BTEX	Benzene, toluene, xylenes, ethylbenzene
BUQW	Base of usable quality water
CZWX	Carrizo-Wilcox (aquifer)
DI water	Deionized water
DIC	Dissolved inorganic carbon
DOC	Dissolved organic carbon
DOE	Department of Energy
DTS	Devine Test Site
EAA	Edwards Aquifer Authority
EDS	Energy dispersive X-ray spectroscopy
EF	Eagle Ford
EM	Electromagnetic
EPA	Environmental Protection Agency
EQ	Environmental Questionnaire
Fm.	Formation
Fms.	Formations
GAM	Groundwater availability model
GAT	Geological atlas of Texas
GC	Gas chromatograph
GCD	Groundwater conservation district
GMA	Groundwater management area
HF	Hydraulic fracturing
ICP-MS	Inductively-coupled-plasma-mass-spectrometer
IC	Ion chromatography
LCA	Life cycle analysis
MGCD	Medina County Groundwater Conservation District
MICP	Mercury intrusion capillary pressure
MPa	Megapascal
MVA	Monitoring, Verification and Accounting

NETL	National Energy Technology Laboratory
PMP	Project management plan
PPMS	Passive pressure management system
PTA	Pressure transient analysis
PWS	Public water supply
QCSP	Queen City-Sparta (aquifer)
RRC	Railroad Commission of Texas
SE	Secondary electron (images)
SEM	Scanning electron microscopy
TCEQ	Texas Commission on Environmental Quality
TDLR	Texas Department of Licensing and Regulation
TDS	Total dissolved solids
TPH	Total petroleum hydrocarbons
TSS	Total suspended solids
TWDB	Texas Water Development Board
USGS	United States Geological Survey
USDW	Underground source of drinking water
UT	University of Texas at Austin
UWCG	Underground water conservation district
XRD	X-ray diffraction

I. Introduction

This report describes research done under a project untitled "*Pressure Management and Plume Control Strategies through a Brine Extraction Storage Test (BEST) at the Devine Test Site (DTS) in Texas.*" The project has two loosely connected objectives: (1) use brine extraction to manage formation pressure as well as plume movement for future large-scale saline CO_2 projects (however, using actual CO_2 is not a requirement for the project), and (2) investigate desalting techniques to be applied to the extracted brine that would then be put to beneficial use. For the many reasons described in this report, the Devine Test Site in South Texas is ideal to meet these high-level objectives.

There are two fundamental motivations behind this work. The astonishing recent development of oil and gas production from shale gas and other tight formations has shown the impact that massive fluid injection may have on the surface. To break open the fractures that allow fluids to flow to the surface, large amounts of water needs to be injected (Nicot and Scanlon, 2012). Some of this water comes back to the surface and must be disposed of in dedicated disposal wells. Disposal wells are not new to the oil and gas industry but in general the water being disposed of is simply produced water being returned to the subsurface. In the case of hydraulic fracturing, "new water" is added to the system, creating positive pressure differentials that can lead to induced seismicity (see recent USGS report by Petersen et al., 2016). Although currently localized in a few areas this fluid injection model can be conceptually applied to CO_2 storage as well (Zoback and Gorelick, 2012, 2015). The seismicity risk, which can doom a project, is more volatile than other well-known risks associated with CO_2 storage such as abandoned wells or leakage through faults. It follows that risk prevention or at least lowering the risk is a better approach than mitigation of a seismic event. In this context, limiting the pressure buildup in the surface is a reasonable approach. However, decreasing the commercial capacity of the storage zone is not a very attractive approach if removal of the resident fluids is feasible. Brine extraction thus appears a viable alternative especially if extracted brine can be put to beneficial use. At the same time, major water needs are emerging in many parts of the US (e.g., Konikow, 2013) and being able to treat the extracted brine at reasonable cost would be a major development in terms of water resources. Improving desalting technologies for brine represents the second motivation of this work.

This research was done in response to a Request for Proposal put out by U.S. Department of Energy National Energy Technology Laboratory (US-DOE NETL) in March 2015 (DE-FOA-0001260 "*Fit-for-Purpose Field Project: Developing and Validating Pressure Management and Plume Control Strategies through a Brine Extraction Storage Test (BEST)*"). The University of Texas Bureau of Economic Geology (UT-BEG) in collaboration with GE Global Research, an international firm recognized for its achievements in developing water treatment technologies, submitted its proposal in April 2015 and was selected for award of Phase I in early July 2015 (award No DE-FE0026137). The contract between UT and NETL became effective during summer 2015 for a period of 1 year, 9/1/2015 to 8/31/2016 (Mr. William O'Dowd, Project Manager) with 2 major deliverables: (1) proposal for the actual field experiment (Phase II) due on 5/31/2016 and (2) topical report documenting the research accomplishments. The 20% cost-share were provided by in-kind support from the Devine Test Site management (free access to the site managed by the BEG) and researcher salary support granted by the UT Jackson School of Geosciences of which BEG is one of the three components. In December 2015, NETL

requested a schedule acceleration with a project end date of 7/16/2016 and submission of the Phase II proposal no later than 4/5/2016. The acceleration came with a slight budget increase and with the addition of a 2nd subcontractor Geostock Sandia, LLC, a recognized expert in managing research sites and completing complex research wells. Phase I of the project consisted mostly in desktop analysis but also included a laboratory component.

Effective work started in September 2015 by collecting information about the geology of the site through a literature review and by building a numerical model. During the same time our main subcontractor GE Global Research collected information on the technologies applicable to saline waters projected to be available at the Devine Test Site. To complement information gathered from the literature review, the team went ahead and sampled water wells and produced water from shallow oil and gas wells in the vicinity of the Devine Test Site. We were also able to collect ~100 barrels of Eagle Ford produced water thanks to Basic Energy Services, Inc. that was shipped to GE Global Research facility in Niskayuna, NY for preliminary desalting treatment.

The project consisted of two somewhat independent components corresponding to the two objectives: a brine extraction component and a water treatment component. We discuss only the brine extraction component here. The report is organized as a topical report, that is, with relatively independent sections: site characterization (Section II), pressure management plans (Section III, complement by an appendix in Section XII), Monitoring, Verification and Accounting (MVA) plans and modeling results in Sections IV and V. These two sections are complemented by an appendix justifying drop of the passive approach to produce brine suggested in the proposal (Section XII) and a longer appendix exploring the use of 4D seismic to monitor pressure (Section XIII). The report ends with a discussion of the Life Cycle Analysis (LCA) (Section VI) and a short paragraph on screening of desalination technologies (Section VII) which is developed in a different document.

II. Site Characterization

The advantages of the site we presented in the Phase I proposal are still valid. The site offers (1) easy access and proximity to Austin, where the research team is based, allowing for daily roundtrips as needed; (2) proximity to an active oil and gas province, providing multiple opportunities to hire well drillers and other needed services, as well as access to disposal wells as needed; (3) the convenience of owning the land (owned by UT Austin); (4) location relatively far from large population centers, the closest small towns are Yancey (~200 inhabitants at 2.5 miles), Moore (650 inhabitants at 8.5 miles) and Devine (4,300 inhabitants at 14.5 miles);

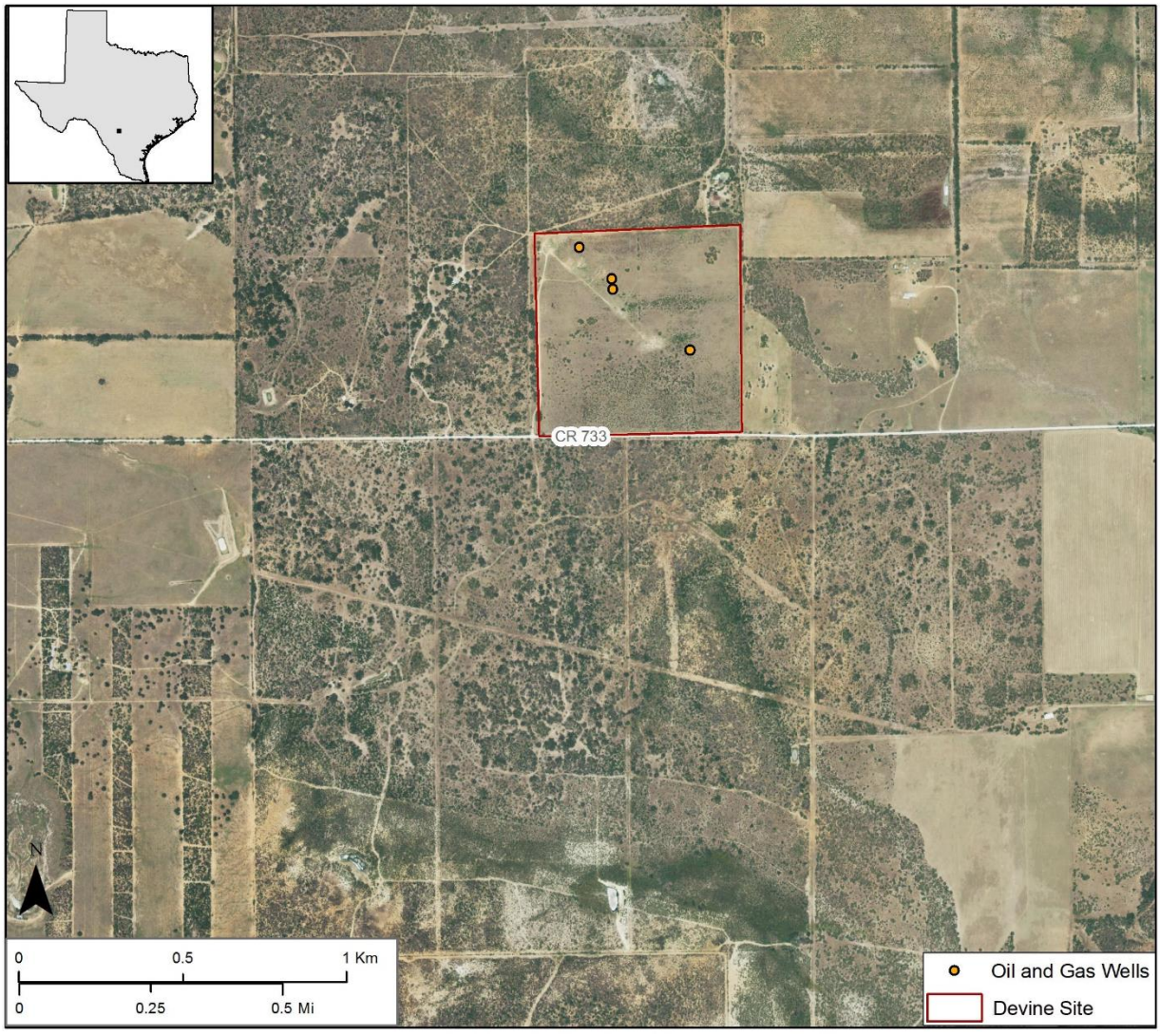

Note: DTS boundary in red, map shows the rather flat topography and the proximity of a county road (courtesy of Goggle Earth).

Figure 1. Aerial view of the proposed site, the Devine Test Site

(5) despite the proximity of an active oil province (Eagle Ford Shale) lack of activity in the immediate vicinity of the selected site, that is, likely no pressure perturbations that would obscure the proposed injection / extraction tests; (6) availability of a rich data set (well logs,

cores, cuttings, seismic surveys) because of the decade-old oil and gas activity in this area although the proposed site itself has not been directly investigated; (7) relatively shallow depth of the target formation (Trinity Group / Hosston Sands) at ~6,000 ft limiting drilling costs and allowing more intensive monitoring; (8) closed compartment sealed on top by a shale layer and a tight limestone and up dip by a non-transmissive fault but sufficiently thick (hundreds of feet) to allow use of multiple intervals for the purpose of the proposed injection/extraction experiment; and (9) saline water of ~50,000 mg/l that can be augmented by brine produced by nearby oil and gas wells and moderate permeability (according to our general knowledge of the basal sands of the Trinity Group).

II-1. Location and Geographical Features

The Devine Test Site is located near the city of Devine (population 4,350) in Medina County which is ~ 50 miles southwest of San Antonio, Texas. The site is owned by the University of Texas (UT) and has been used to test geophysical tools in several wells with maximum depths of ~3000 ft which locally corresponds to the top of the Edwards Formation. The site is in a rather flat area (Figure 1) at an elevation of ~650-680 ft and is readily accessed by a county road, which forms the southern boundary of the UT property.

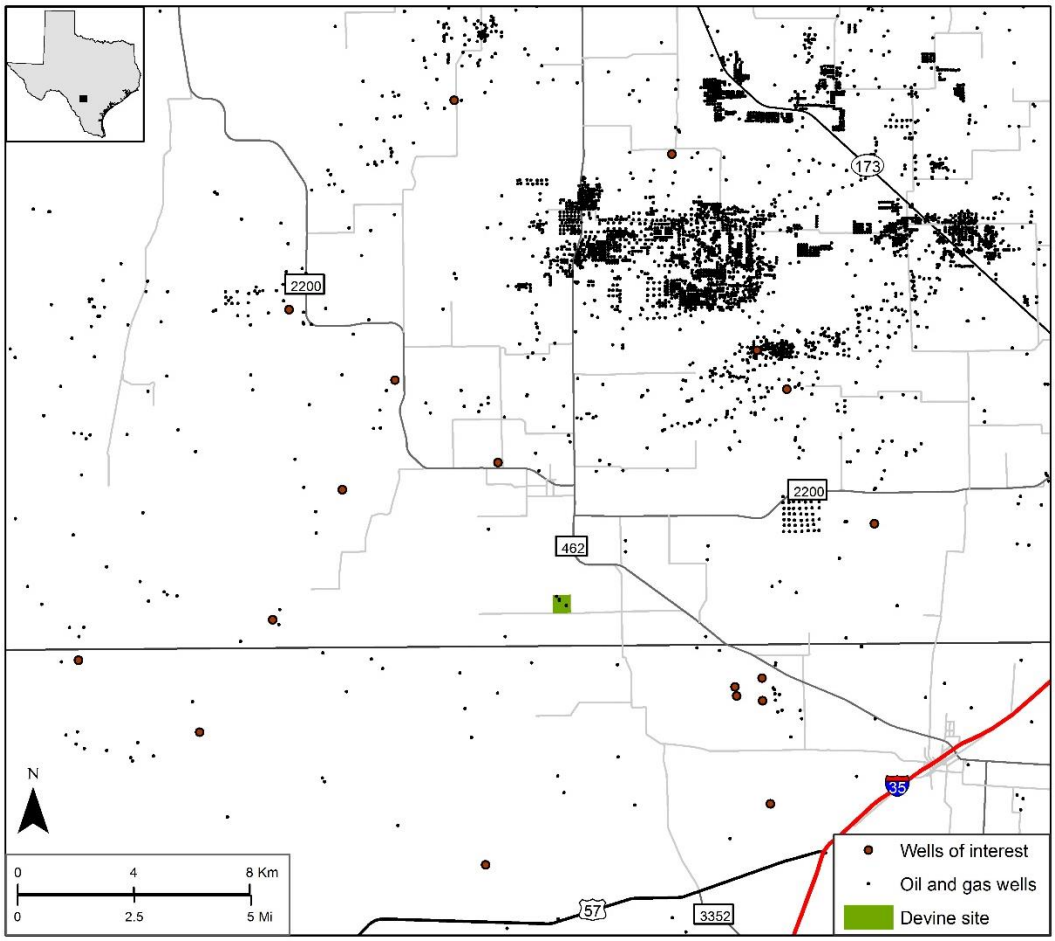

Note: "Wells of interest" are deeper wells relevant to the proposed study. The Medina-Frio county line is just south of the proposed site. Note that most of the wells shown on the map are not currently active.

Figure 2. Location of the Devine Test Site relative to major oil/gas historical production in the area.

The site is located in an active oil and gas province, a few miles north of the Eagle Ford play. The area contains oil and gas reservoirs of various ages although none is in the immediate vicinity of the proposed site (Figure 2). Zones of active oil and gas production are sufficiently distant from the site to avoid any pressure interference from injection / production by local operators.

II-2. Geology

This section describes the general geology of the area then gives a more detailed description of the site geology. An overview of the oil and gas resources is also provided as most of what is known about the site originated from oil and gas operators. There are several reports summarizing the geology and hydrogeology of the area (e.g., Nicot et al., 2010; Nicot et al., 2013 and references therein). It is also important to note that, although we did not take advantadge of the option, there is historical seismic lines available for purchase (for example, http://www.seismicexchange.com/, Figure 3) that will be useful to improve the resolution of the geological knowledge including local faults.

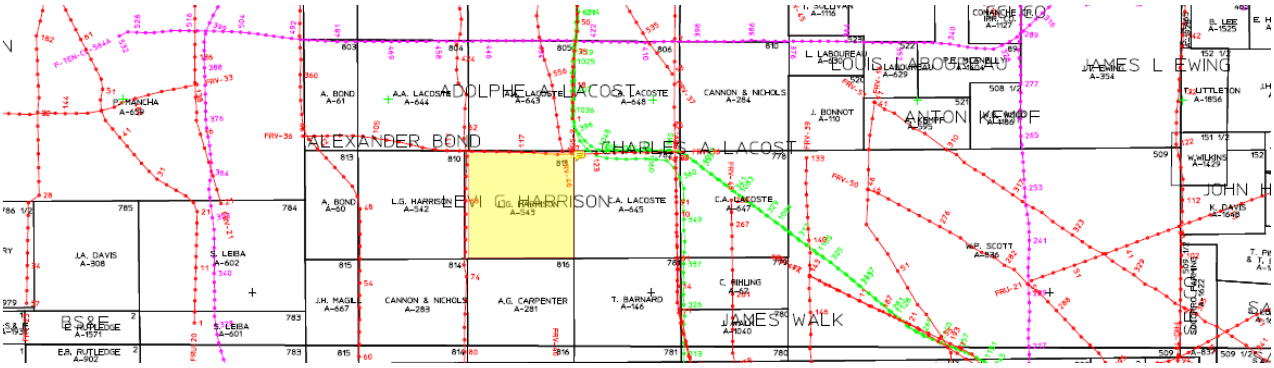

Note: Devine Test Site highlighted in yellow; Seismic line of interest highlightd in green (OSC-OTS 9 and 9A)

Figure 3. Seismic lines available for purchase

II-2-1 General Geology –Literature Review

Formations cropping out in Medina and Frio counties are mostly of Cenozoic age (Figure 4). The ***Hosston*** and ***Sligo Fms*** represent the first transgressive events on the basement and are the formations of interest to this study. The Hosston Fm. is a siliciclastic sandstone (of fluvial, deltaic, and strandline origin) transitioning upwards to and mixed with tidal sediments, including dolomite and mudstones. These formations do not crop out in the Gulf Coast side of the major structural feature slicing Texas (buried Ouachita foldbelt / Balcones Fault Zone) located in northern Medina County in the study area. The Hosston Fm. does exist and crops out in Central and West Texas on the other side of this structural feature but has never been buried as deep as it currently is in the Devine area so makes only an imperfect analog.

II-2-1.1 Stratigraphy

The proposed site is within the geologic province of the Upper Gulf Coast and is close to the Ouachita foldbelt. The Ouachita foldbelt or front is the buried remnant of a massive orogenic event of Pennsylvanian age with Paleozoic rocks consisting of intrusive material and metasediments that are collectively called “basement” in this document. The formations of interest to this study are of Cretaceous age and are the first to be deposited on top of the Paleozoic basement (Figure 5). The stratigraphic units include, starting with the oldest, the

Trinity Group (including Hosston, Sligo, Pearsall and Glenrose Fms.), the Washita-Fredericksburg Group (including Edwards, Del Rio, and Buda Fms.), the Eagle Ford Group, the Austin Group (including the Austin Chalk), and the Navarro and Taylor groups (including the San Miguel, Olmos, and Escondido Fms.). The Wilcox Group and the Carrizo sand of Eocene age complete the succession. The formations of interest for the proposed work are located between the basement and the Glenrose Fm. in the Lower and Middle Trinity Group, particularly the Hosston Sands.

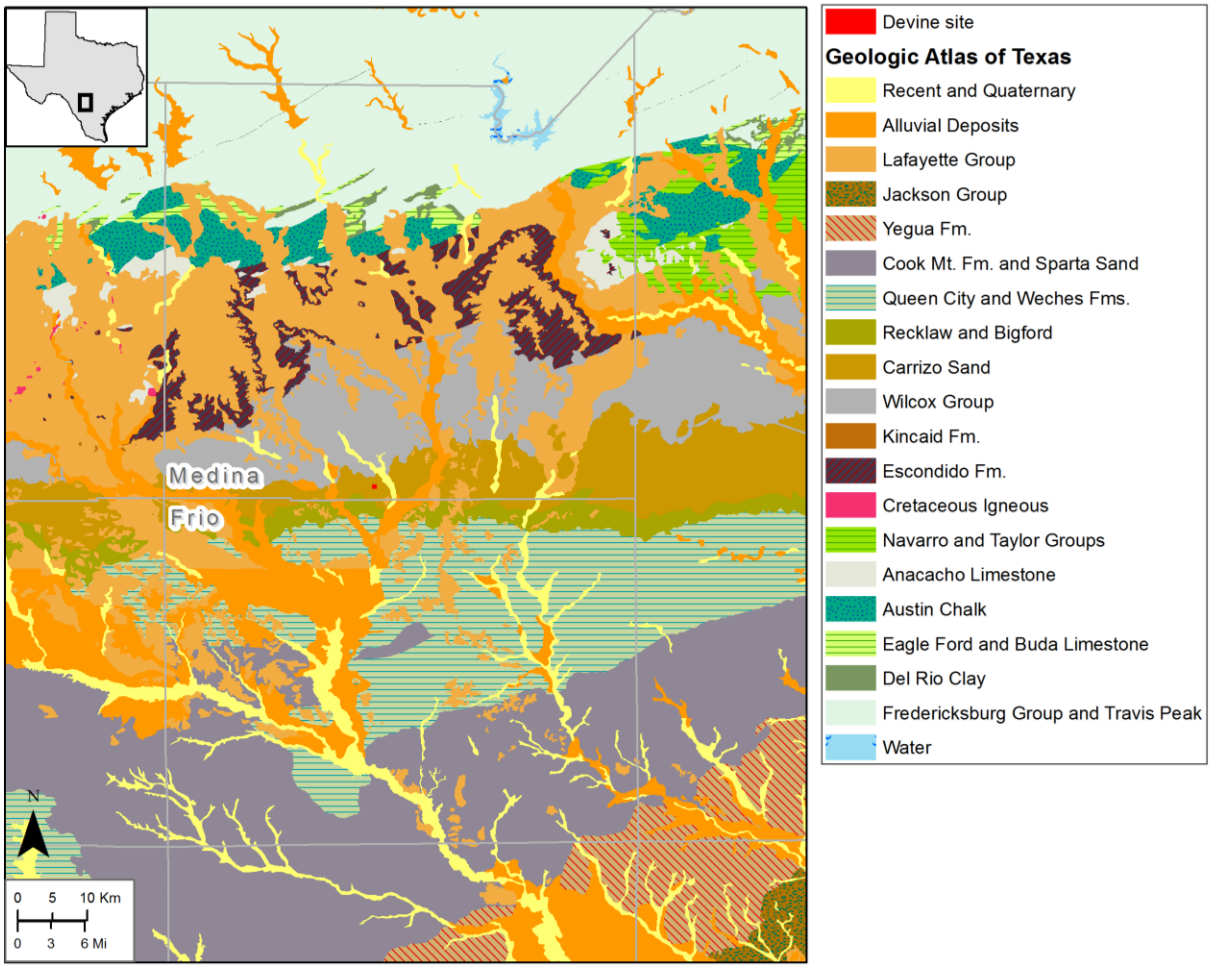

Note: the Devine Test Site is the small red dot next to the Medina-Frio county line; Source: Geologic Atlas of Texas, 1/250,000, San Antonio sheet http://www.twdb.texas.gov/groundwater/aquifer/GAT/

Figure 4. Geologic map of Medina and Frio counties

The "basement" consists of deformed and metamorphosed Paleozoic (Ouachita) sandstone, shale, and chert, locally overlain by a redbed succession, the "Blum Unit" of Permian (?) age (Ewing, 2010). Downdip from the site in Frio County, a succession of Jurassic age deposits from the oldest includes (Budd and Loucks, 1981, Fig.3): the Norphlet Fm., the Smackover Fm., the Haynesville/Buckner Fms, and the Cotton Valley Group which is overlain by the Hosston Fm. Jurassic sediments do not seem to exist at the site but only drilling and coring will provide a definitive answer. In any case, their presence will not impact the proposed study.

The ***Hosston*** and ***Sligo Fms*** (McBride et al., 1979; Bebout et al., 1981) represent the first large transgressive event on the basement (at the site) and older sediments (in general) and are the formations of interest to this study. The Hosston Fm. is a siliciclastic sandstone (of fluvial,

deltaic, and strandline origin) transitioning upwards to and mixed with tidal sediments, including dolomite and mudstones. The depositional environment of this group should result in compartmentalized sand units surrounded by lower permeability units that would serve as seals for the injection tests. The Hosston Fm. forms the base of the Trinity Aquifer that extends from Dallas to San Antonio, and has been described in outcrops and cores at many locations, and is documented as having moderate to high permeability, especially at its base. The ***Pearsall Shale*** (Loucks, 1977, 2002; Hull, 2011; Hackley, 2012; Enomoto et al., 2012) is a dolomitic and argillaceous mudstone representing a rapid transgression and comprised of three members in ascending stratigraphic order: Pine Island Shale (called Hammett Shale on the San Marcos Arch), Cow Creek Limestone, and Bexar Shale. The Pearsall Shale had been an early target of hydraulic fracturing (HF) to produce gas but efforts petered out when the nearby and younger Eagle Ford Shale was found more promising.

Next, the shallow-water carbonates of the ***Glenrose Edwards Fms.*** were deposited on a broad shelf covering most of Texas. The ***Georgetown Fm.*** was deposited in deeper water on the eroded and previously aerially exposed top of the ***Edwards Fm.*** (which gives it its karstic features and very high regional permeability). Both the Edwards and Georgetown Fms. form the Edwards Aquifer. The ***Del Rio Clay*** is a thin calcareous marine shale overlying the Georgetown Fm. The ***Buda Fm.*** is a carbonate mudstone deposited on a relatively flat depositional surface.

The ***Eagle Ford shale*** extends all the way to the Balcones Fault Zone to the north but is generally considered outside of the oil-generating window in the proposed study area. Directly overlying the Eagle Ford, the ***Austin Chalk*** is a laterally extensive open-marine fine carbonate mudstone overlain by a discontinuous carbonate bank called the Anacacho limestone or chalk. Formations from the ***Navarro*** and ***Taylor Groups*** complete the Cretaceous succession leading to the mostly clayey Midway Group. Although these formations present important sandy intervals to the south of the site, at the site they are mostly shaly.

The ***Navarro*** and ***Taylor Groups*** are considerably more developed in South Texas in the Maverick Basin next to the Mexican Border than they are at the proposed site. Since they are sandwiched between two important aquifer systems (Carizzo-Wilcox and Edwards aquifers), we describe them in more details. In the Maverick Basin, three terrigenous clastic wedges correspond to a large sediment influx resulting from erosion of the newly formed Rockies and related mountain ranges located closer to the basin: ***San Miguel, Olmos, and Escondido Fms*** (Tyler and Ambrose, 1986; Dutton et al., 1993).They contain mostly deltaic sandstones but the Olmos includes also strandplain and fluvial deposits. The San Miguel and Escondido are marine sands and shales, while the Olmos is largely non-marine and contains plant-rich shales, coal, and fluvial sediments (Scott, 2004). Deposits with significant thickness cover southern Maverick, northern Webb, Dimmit, Zavala, Frio and half of LaSalle counties. Underlying the Olmos, the San Miguel formation is very similar in terms of location of the major depocenters and overall extent (Weise, 1980, p.5). The Olmos sands contain many small oil and gas fields, some of which are tight gas and require HF to produce gas. In addition, numerous small basaltic volcanic plugs intruded these formations in South Texas. These formations transition to the Navarro (Escondido Fm.) and Taylor (San Miguel and Olmos Fms.) groups traditionally described in Central Texas. The Navarro overlies unconformably the Taylor group. The Escondido Fm. truncate the Olmos Fm. in the outcrop and shallow subsurface.

The ***Midway Group*** of Paleocene age represents the first strata of Cenozoic age and is partly composed of dense marine clays. The Midway is transitional between the fully marine deposits

of the Upper Cretaceous and the foredelta and lower delta floodplain deposits of the Lower Wilcox. The Midway Group is generally described as a thick package of marine clays. However north of the study area (10 miles), the outcrops are described as shallow marine near-shore limestones of limited thickness (40 ft) (Roy, 1984). Elsewhere (Central Texas), the Upper Midway has been described as being similar to the Lower Wilcox with sand lenses locally called Poth Sands (Hopft, 1973). The **Wilcox Group** is ~1000 ft thick at the outcrop just north of the study area. The ***Lower Wilcox*** consists of a barrier bar and lagoon-bay system with sand units up to 100 ft thick. The ***Middle Wilcox*** is composed of marine and lagoonal muds. The ***Upper Wilcox*** contains abundant lignite resources but also large sand bodies that can provide significant volumes of water. The ***Carrizo Sands*** are of fluvial origin.

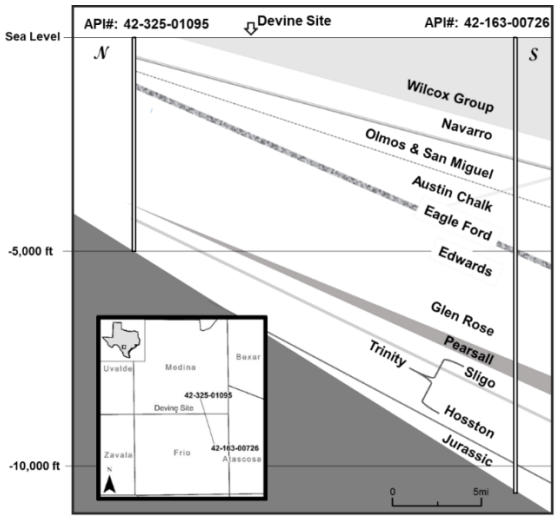

Modified from Ewing (2010, Fig.4)

Figure 5. Vertical cross section in the vicinity of the proposed site showing the various formations

Thickness of the ***Wilcox Group*** in South Texas vary progressively from ~1000 ft at the outcrop to ~4000 ft towards the shelf edge at which point it grows quickly to >8000 ft and larger (Bebout et al., 1982, Fig.8). The Wilcox is generally subdivided into lower, middle, and upper intervals. The ***Lower Wilcox*** consists in a barrier bar and lagoon-bay system (Fisher and McGowen, 1967). Sand units can be as thick as 100 ft and have an aggregated thickness between 400 and 100 ft in South Texas. Mud facies occur northwest of this bar system and forms the Lower Wilcox outcrop in South Texas. Because rocks in outcrop look (and are) different, those deposits were given a different name early on: ***Indio Fm***. The sandy bar facies transition to the southwest to muddy shelf deposits. The delta muds at the base of the Lower Wilcox transition to the marine clays of the Midway. Further north, in Central Texas the (outcrop) lagoon facies disappears to leave place to strandplain deposits and the thick so-called Rockdale delta extending further north to East Texas. The Lower Wilcox is sometimes called the Hooper Fm. in Central Texas. The ***Middle Wilcox*** of South Texas is composed of marine and lagoonal muds. The ***Upper Wilcox***, called the Calvert Fm. on Central and East Texas GAT sheets, contains abundant lignite resources indicative of a low-energy environment but also large sand bodies that can provide significant volumes of water. Nomenclature and interpretation are not always entirely settled or clear. The fluvial ***Carrizo Sands*** are well-characterized at the outcrop but its more deltaic and marine facies downdip equivalents are merged with the Upper Wilcox especially in South Texas (Bebout et al., 1982; Hamlin, 1988; Xue and Galloway, 1995; Dutton et al., 2003, p.19). Carrizo

Sands thickness increases from Central Texas to South Texas. Carrizo sands are the fluvial (continental) unit whether the marine time equivalent is included in the Upper Wilcox. The upper Wilcox subgroup consists of the South Texas Rosita delta system, the associated strand-plain and barrier-bar system, and the updip Carrizo fluvial system (Xue and Galloway, 1995) that fed the Rosita Delta. A prominent feature, the Yoakum Channel, is present mostly in Lavaca County along its boundary with De Witt County and consists in sands corresponding to an incised valley through the entire Wilcox succession.

II-2-1.2 Structural Features

The Devine Test Site is located south of an important structural feature that runs from west of San Antonio to north of Dallas through Austin and Waco: the Balcones fault zone. It separates the Gulf Coast Plains from the Edwards Plateau and is characterized by a sharp downthrow of the Gulf of Mexico side where formations currently outcropping on the Edwards Plateau (Edwards, Glenrose) are present at depths of several thousand feet. The Balcones Fault Zone consists of mainly normal faults that occur parallel to the trend of the buried Ouachita Orogenic Belt of Paleozoic age. Along these individual faults, sediments have been displaced by up to 1,500 ft, moving downward to the Gulf of Mexico.

Although the density of individual faults related to the Balcones Fault Zone decreases considerably from northern to southern Medina County, tectonic map by Ewing (1991) show some minor faults in southern Medina County (Figure 8). In addition to numerous growth faults mostly present in the lower Gulf Coast (Wilcox, Vicksburg, Frio…. fault zones), several mostly normal faults of tectonic origin exist in the upper Gulf Coast (Figure 10 and Figure 11). Faults of similar origin do not seem to be present at the proposed site but would be visible on a seismic survey (Figure 3).

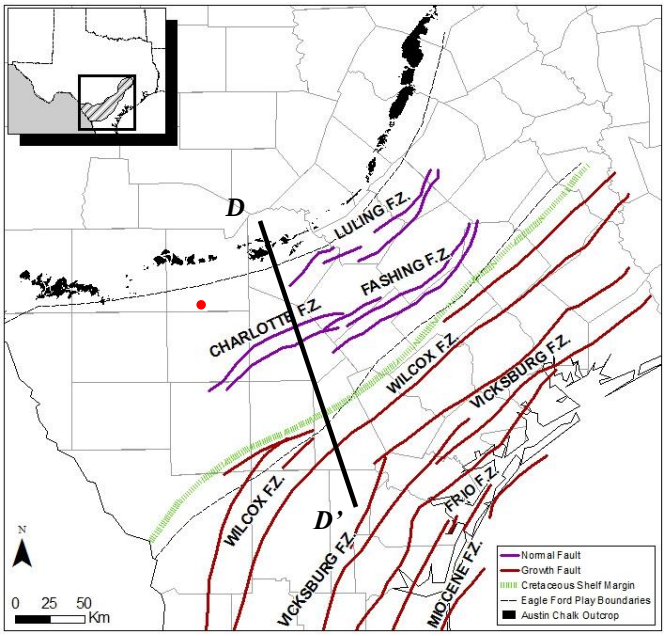

Source: Galloway et al. (1983, Plate I); Ewing (1991, Fig. 11);
Note: cross-section *DD'* of Figure 7 shown; red dot = Devine Test Site

Figure 6. Approximate location of fault zones (not necessarily all faults) in South and Central Texas

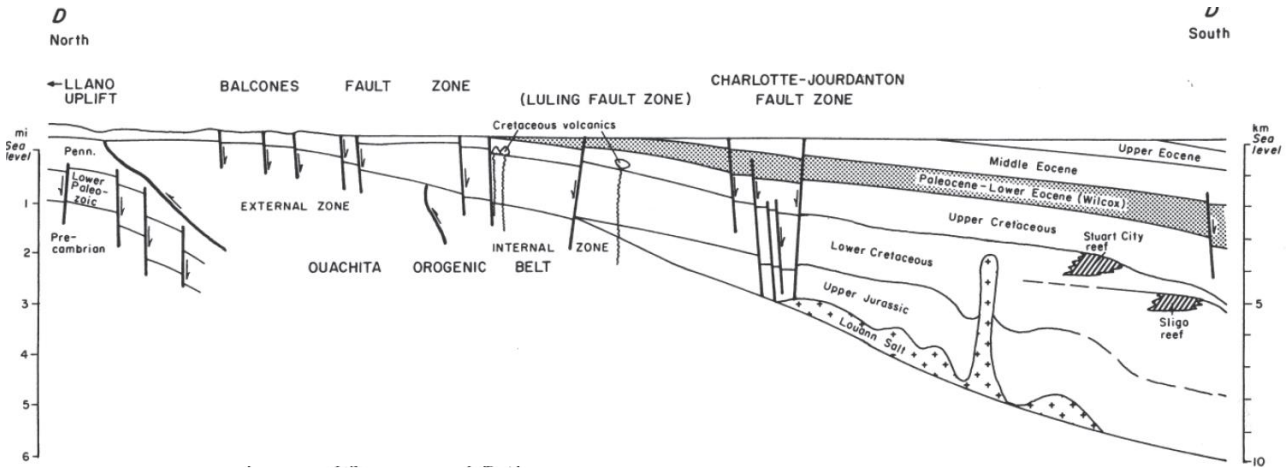

Source: Ewing (1991, Fig.12); Note: see Figure 6 for location of cross-section

Figure 7. Structural cross section of South Texas showing faults, basin margins, and diapirs

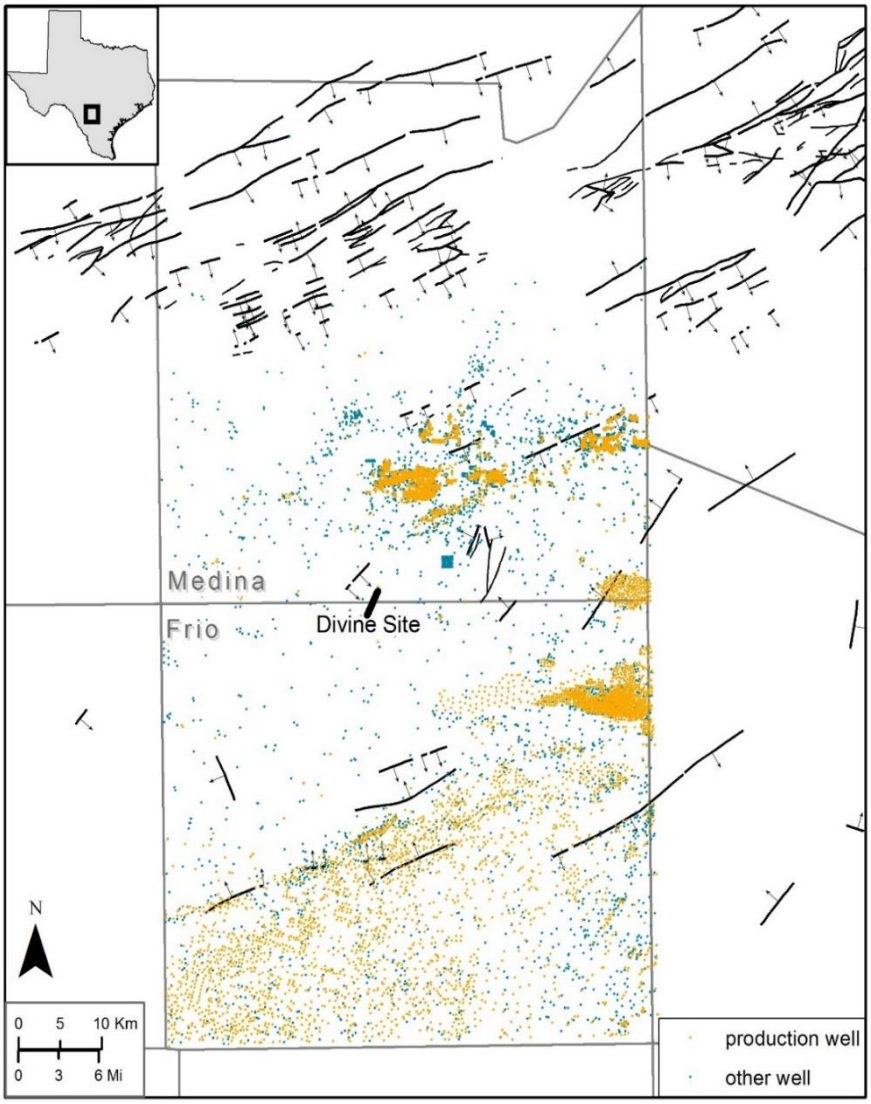

Note: Devine Test Site very close to the Medina-Frio county line

Figure 8. Mapped faults in Median and Frio counties

II-2-2 Local Stratigraphy

The detailed local stratigraphy was relatively not well known until this work because of a lack of specific studies. We focused on two sections: the Hosston Formation, host of the injection interval, and the Taylor and Navarro Groups above the large carbonate interval and a possible source of water and possibly (but unlikely) a disposal interval.

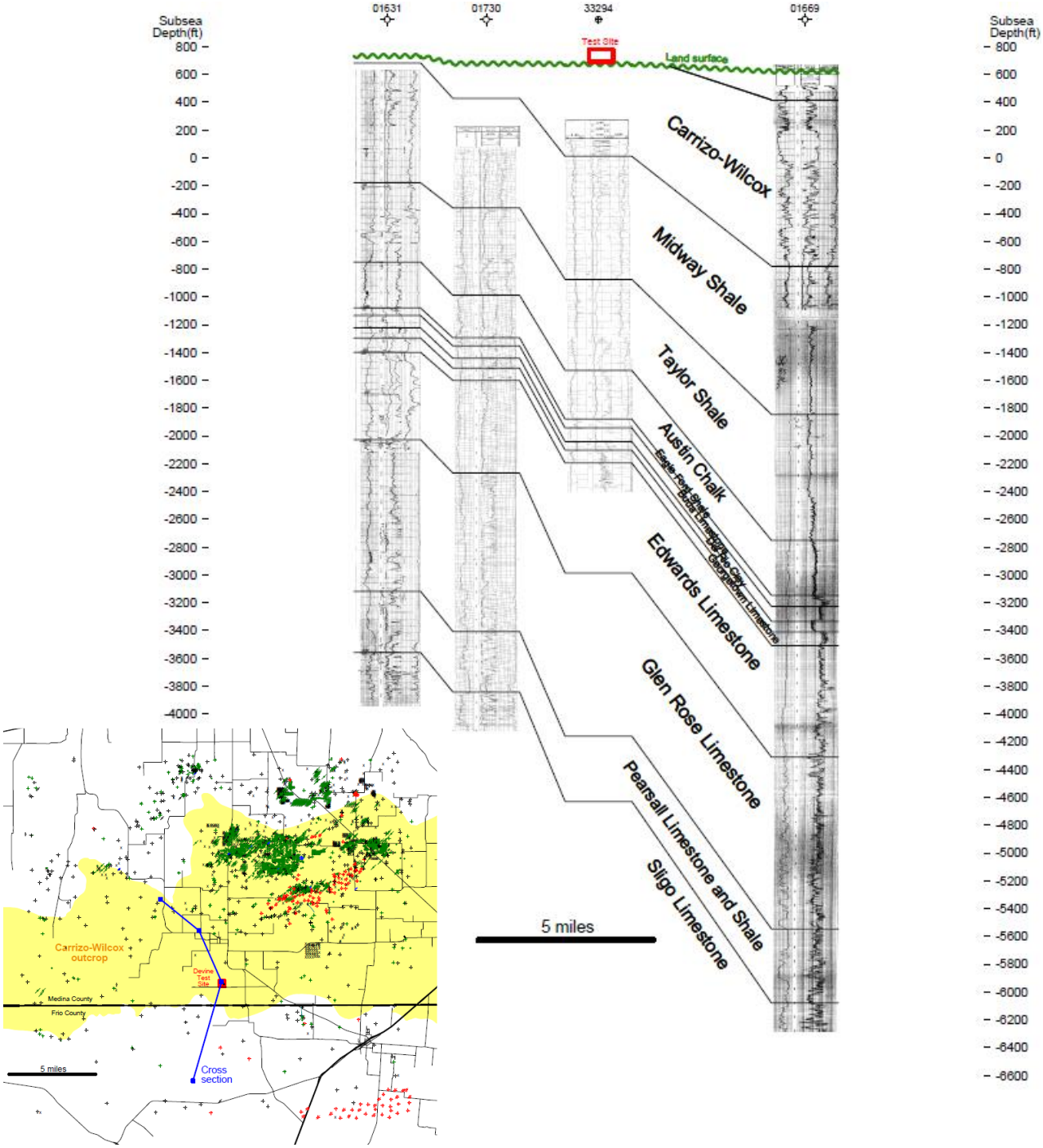

Figure 9. Preliminary interpretation of depth to formations overlying the Travis Peak/Hosston Formation

The methodology is always the same: to gather numerous (hundreds) of geophysical oil and gas (generally resistivity and spontaneous potential) and correlate them in dip- and strike-oriented cross sections. Knox et al. (2007) give a good overview of our approach.

The Devine Test Site sits on the Carrizo-Wilcox outcrop (Figure 4). Below that is a 2000-foot thick interval of shale-dominated formations down to the Austin Chalk. Below the Austin Chalk are limestone and shale formations but no sandstone to at least 6500 feet deep, which is the end of the well control in the area (Figure 9).

II-2-2.1 The Target Formation: the Hosston Formation

Depth to target formation for primary injection is ~6000 ft (preliminary work to be refined). We examined the regional and local lithostratigraphy of the Upper Jurassic and most of the Cretaceous succession in southern Medina and northern Frio counties to identify sandstone-bearing units that would be appropriate for wastewater injection at the Devine Test Site (Figure 4). Correlation of carbonate and siliciclastic units in 87 wells over the 828 mi^2 study area (Figure 10) documents that abundant sandstones of the Travis Peak Formation and thinner sandstones of

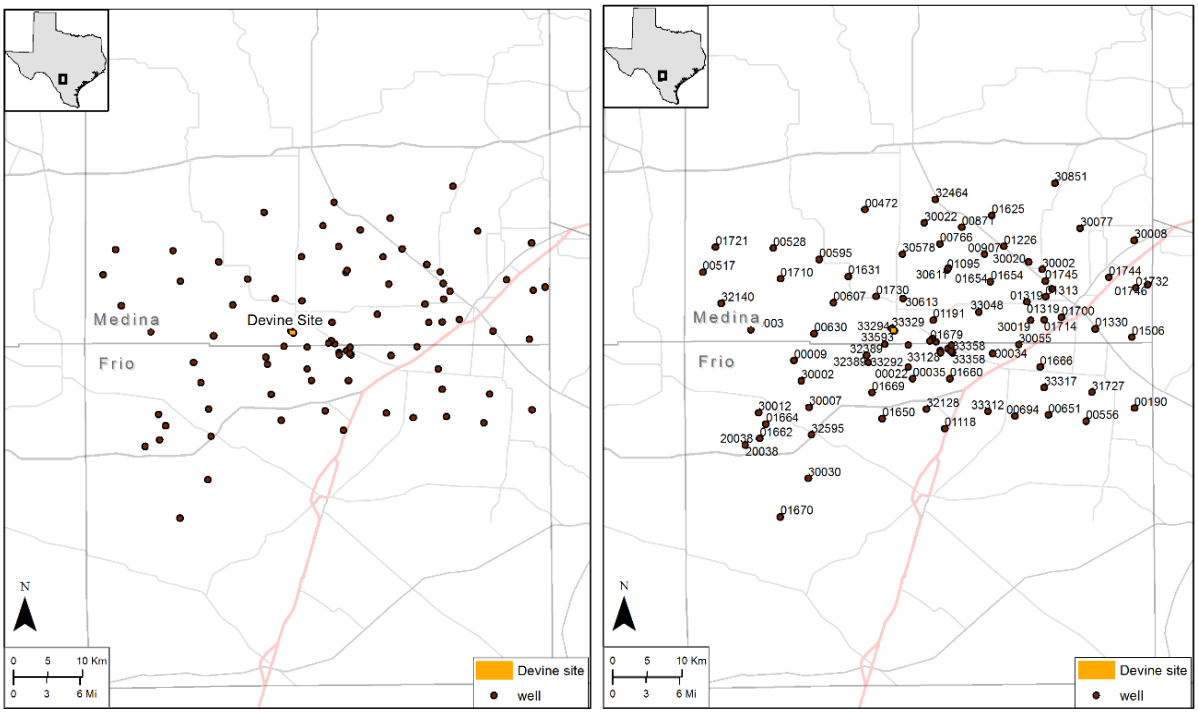

Figure 10. Map of wells correlated in the vicinity of the Devine Test Site (Hosston Formation)

the Lower Cretaceous San Miguel, Olmos, and Escondido Formations all occur within and surrounding the Devine Test Site (Figure 4). Of these units, the Travis Peak succession is the deepest and therefore probably contains formation waters with sufficiently high concentration of total dissolved solids to meet the criteria for an optimal injection target.

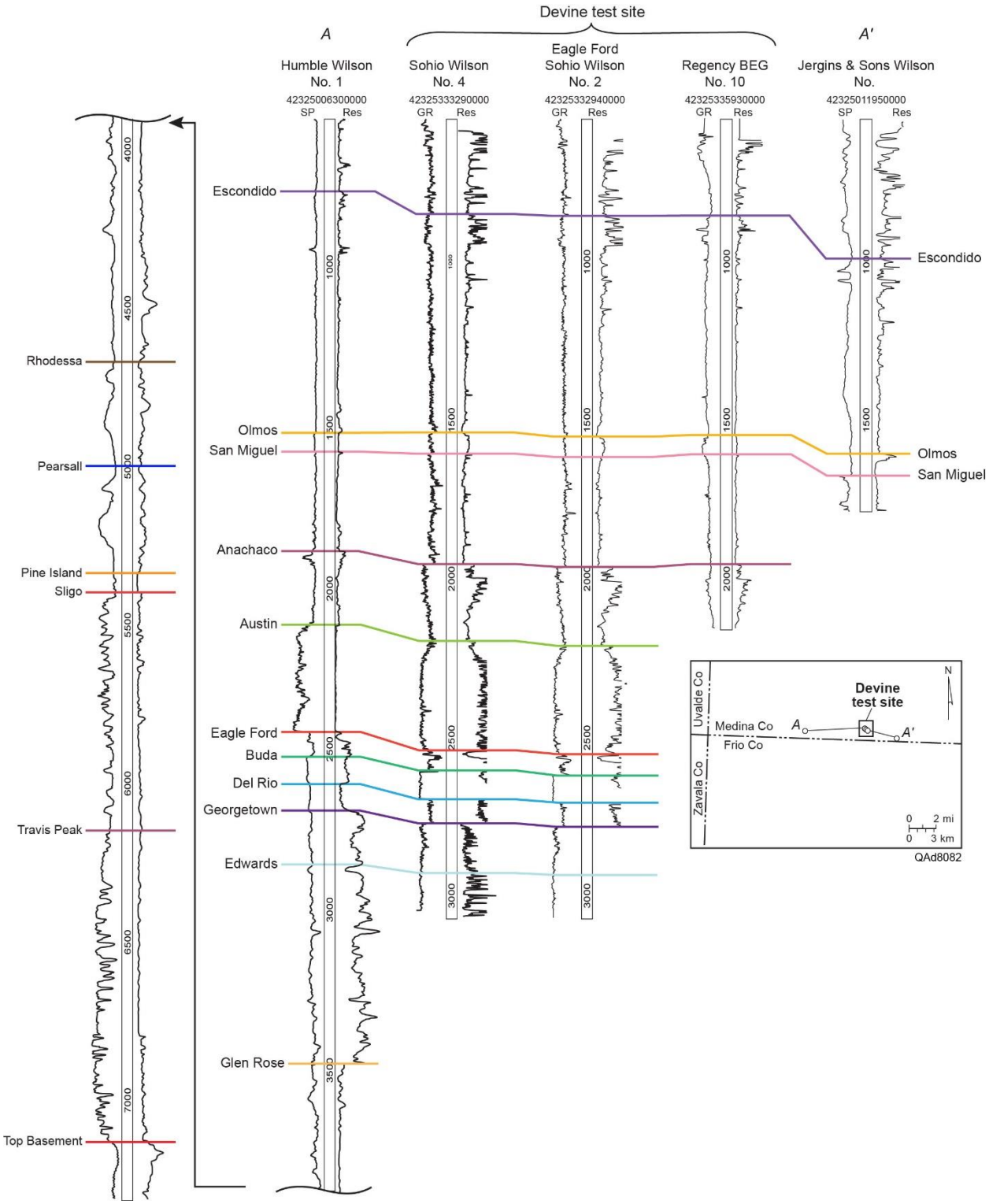

Note: Westernmost well provides an extrapolated depth for the Jurassic Travis Peak Formation of about 6,029 ft at the test site.

Figure 11. Structural west-to-east cross section showing consistency in depth of Cretaceous formations within 6 mi of the Devine Test Site.

None of the wells drilled on the Devine Test Site extend to the Travis Peak Formation. However, one nearby well, located 6.1 mi west of the site (Humble Wilson #1), that does extend to the Travis Peak section lies directly along structural strike with the wells in the Devine Test Site and can therefore be used to calculate the Travis Peak's approximate depth and thickness at the site. Correlation of the regionally extensive Georgetown, Del Rio, and Buda formations (Figure 11) from the Wilson #1 well to the wells at the Devine Test Site shows that the horizons are only about 41 ft higher in the Wilson well. Therefore, because the top of the Travis Peak succession is at about 5,988 ft in the Wilson #1 well, the extrapolated depth of the unit at the Devine Test Site is approximately 6,029 ft. Thickness of the unit in the Wilson well is about 980 ft and is probably a comparable thickness at the Devine Test Site.

II-2-2.2 Shallower Formations

We also investigated shallower formations above the carbonate section because they can a source of brackish or saline water and also possibly an on-site disposal interval. There are 3 formations/groups of interest, from the oldest to the youngest, San Miguel, Olmos and Escondido. We used a total of 176 wells to build maps (Figure 12).

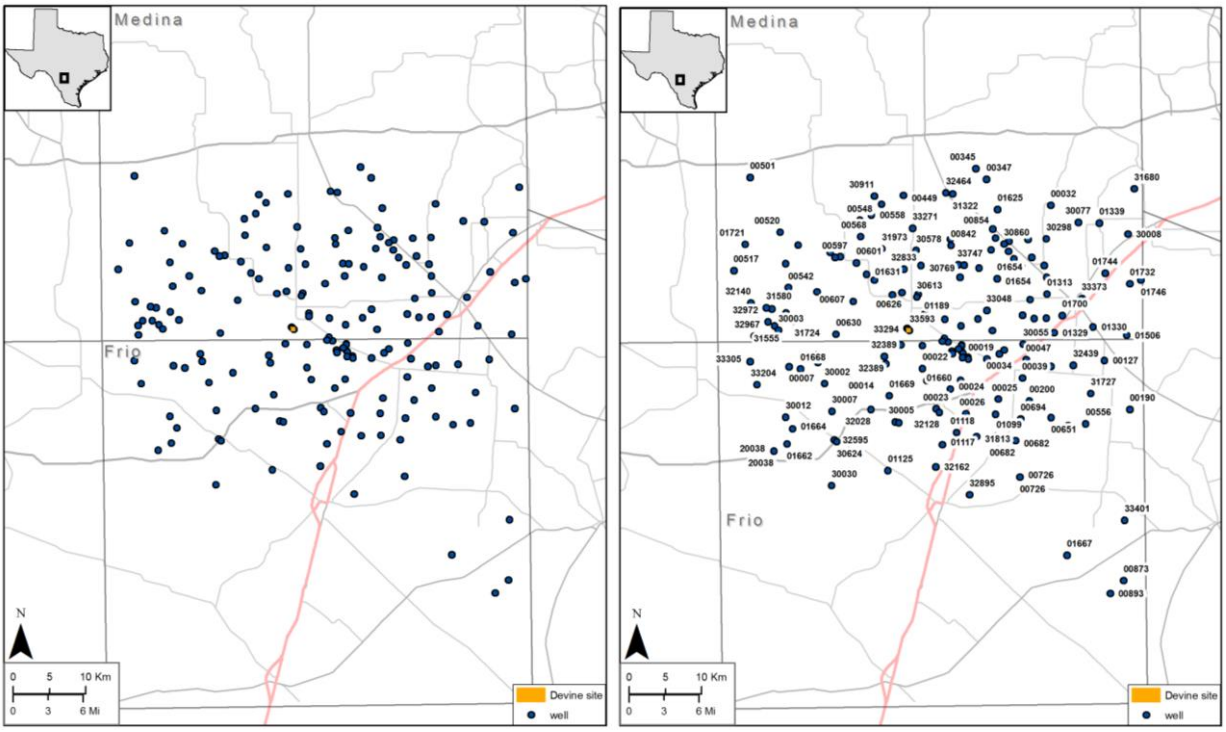

Figure 12. Map of wells correlated in the vicinity of the Devine Test Site (Taylor and Navarro groups)

Extracting the top elevation of the Escondido (Figure 13), of the Olmos (Figure 14) and of the San Miguel (Figure 15) from the maps interpolating results from the 100+ wells yields -200 ft, -500 ft, and -900 ft, respectively; obviously consistent with the well logs observed at the site. All three formations dip gently to the S-SSE at 2-5°. More interesting maps, which require subregional analysis, are the net sand maps which provide an indication about the size and extend of the sand bodies. If the Olmos interval does not seem to be promising as a water source at the site (Figure 17), the Escondido has sandy intervals that might be connected to a relatively

large sand accumulation (Figure 16). Connectivity between the various sand bodies of the Escondido and the sand layer present on site can only be determined through aquifer pump tests to be performed during Phase II. The map of Figure 16 shows variations in net sand thickness within the Escondido interval. Thickness varies from <10 to ~120 feet in the mapped area. The lobate nature of the sand-rich areas are consistent with a shoreface to wave-dominated deltaic depositional history of the system. (Pisasale, 1980; Tyler and Ambrose, 1986; Snedden, 1991). Escondido sandstones from Bexar County reported porosities of 15-30 %, and average permeabilities of 9.6-143 md (Condon and Dyman, 2003).

The map of Figure 17 shows variations in net sand thickness within the Olmos interval. Thickness varies from <10 to ~160 feet in the mapped area. The Olmos sands were deposited in a fluvio-deltaic environment. The western depocenter (not shown here) is more sand-rich than the eastern center closer to the study site shown here. While the Olmos is known to be a sand-rich interval in general, and is an oil producer in some parts of Texas, the area close to the study site shows sand thicknesses of ~10-20 feet only. The thickest parts of the Olmos are, unfortunately, relatively far from the site (>13 miles away).

Figure 18 presents a structural cross-section across the Devine Test Site focusing on the carbonate section and shallower formations. The stratigraphic cross-section of Figure 19 shows the presence of shallow sands at the top of the Escondido at the Devine Test Site.

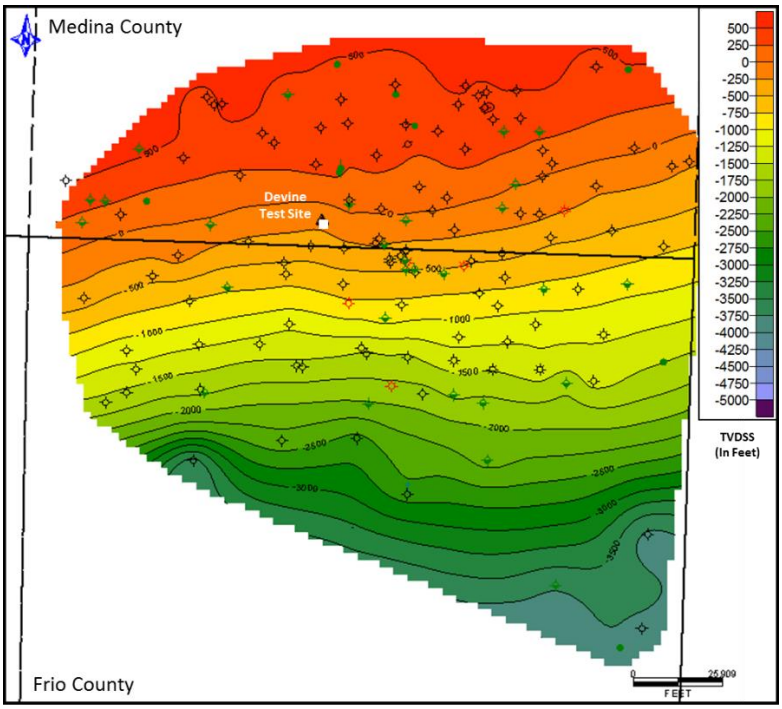

Figure 13. Structure map at the top of the Escondido

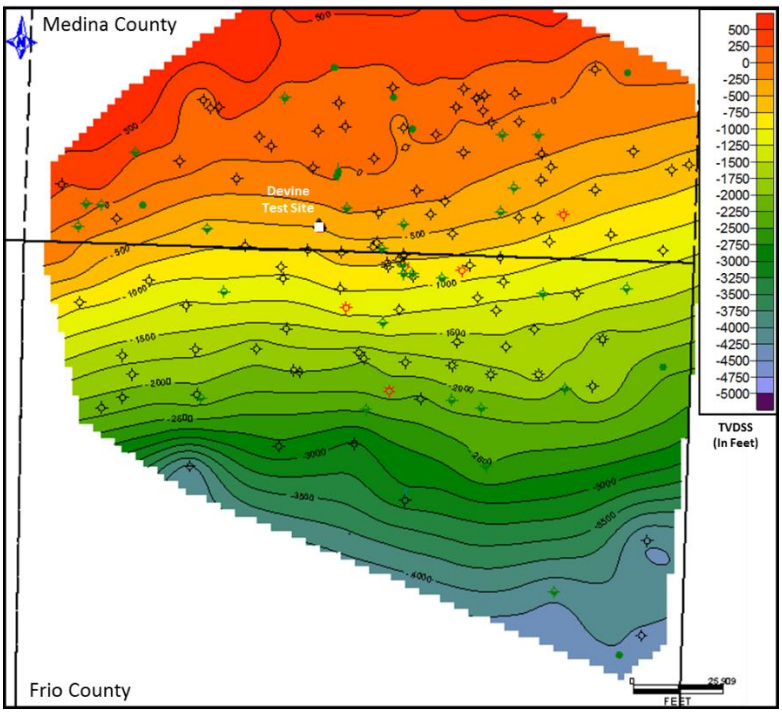

Figure 14. Structure map at the top of the Olmos

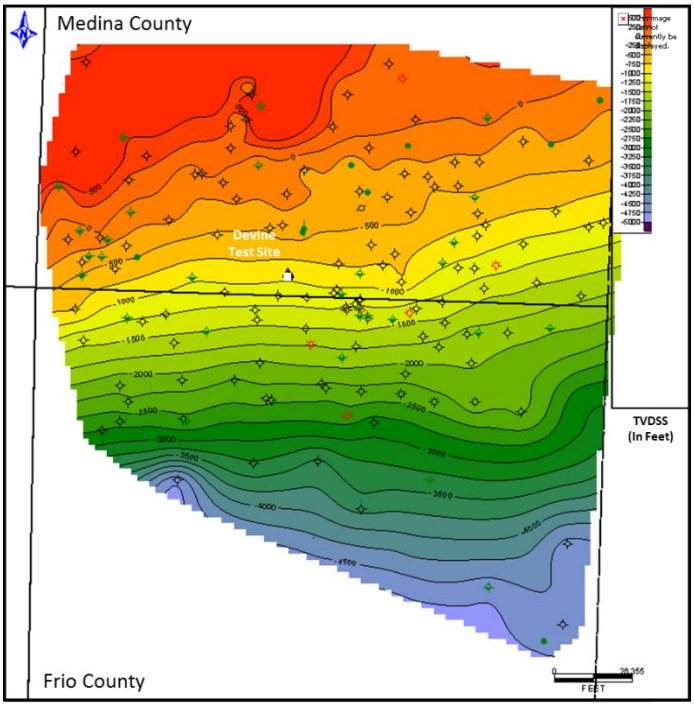

Figure 15. Structure map at the top of the San Miguel

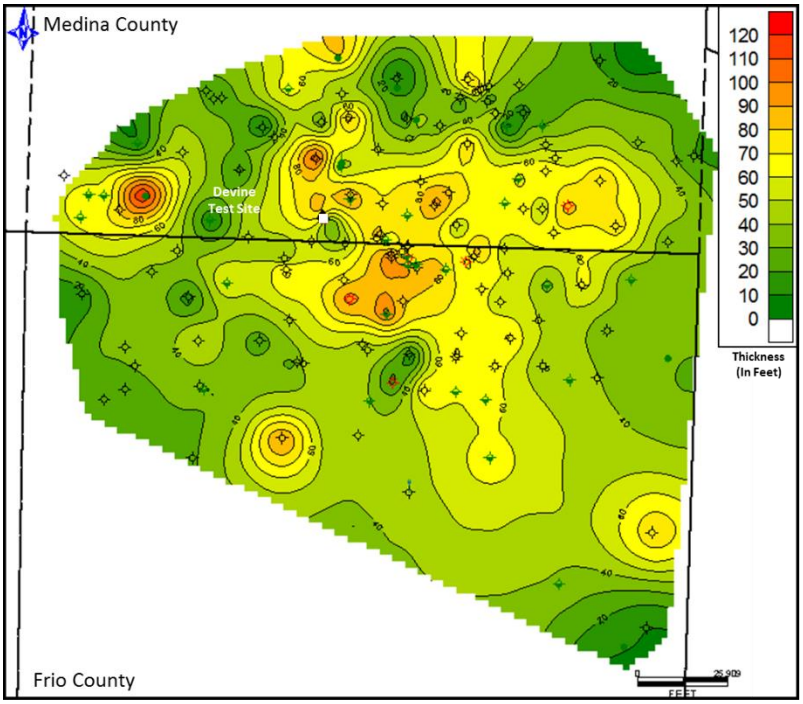

Figure 16. Net sand map of the Escondido

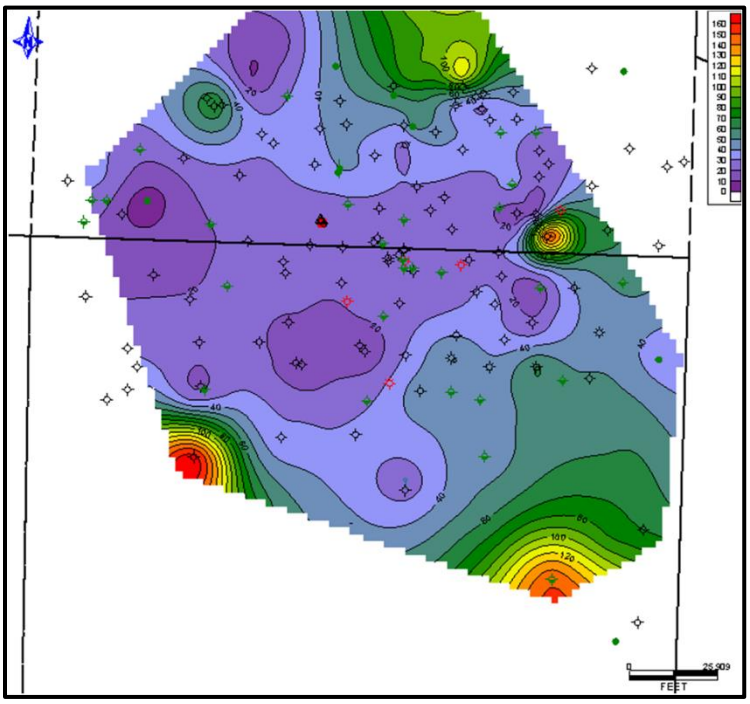

Figure 17. Net sand map of the Olmos

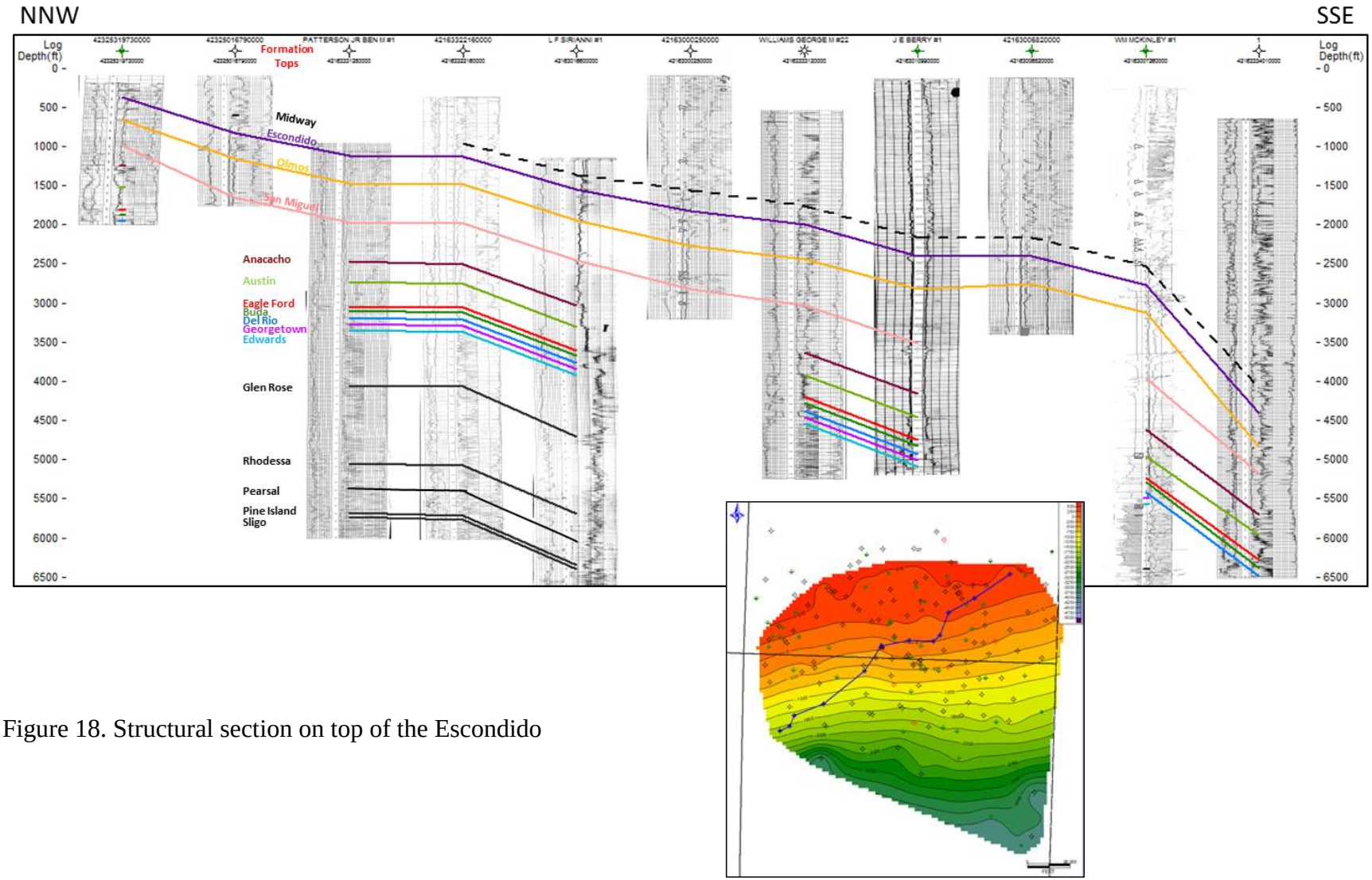

Figure 18. Structural section on top of the Escondido

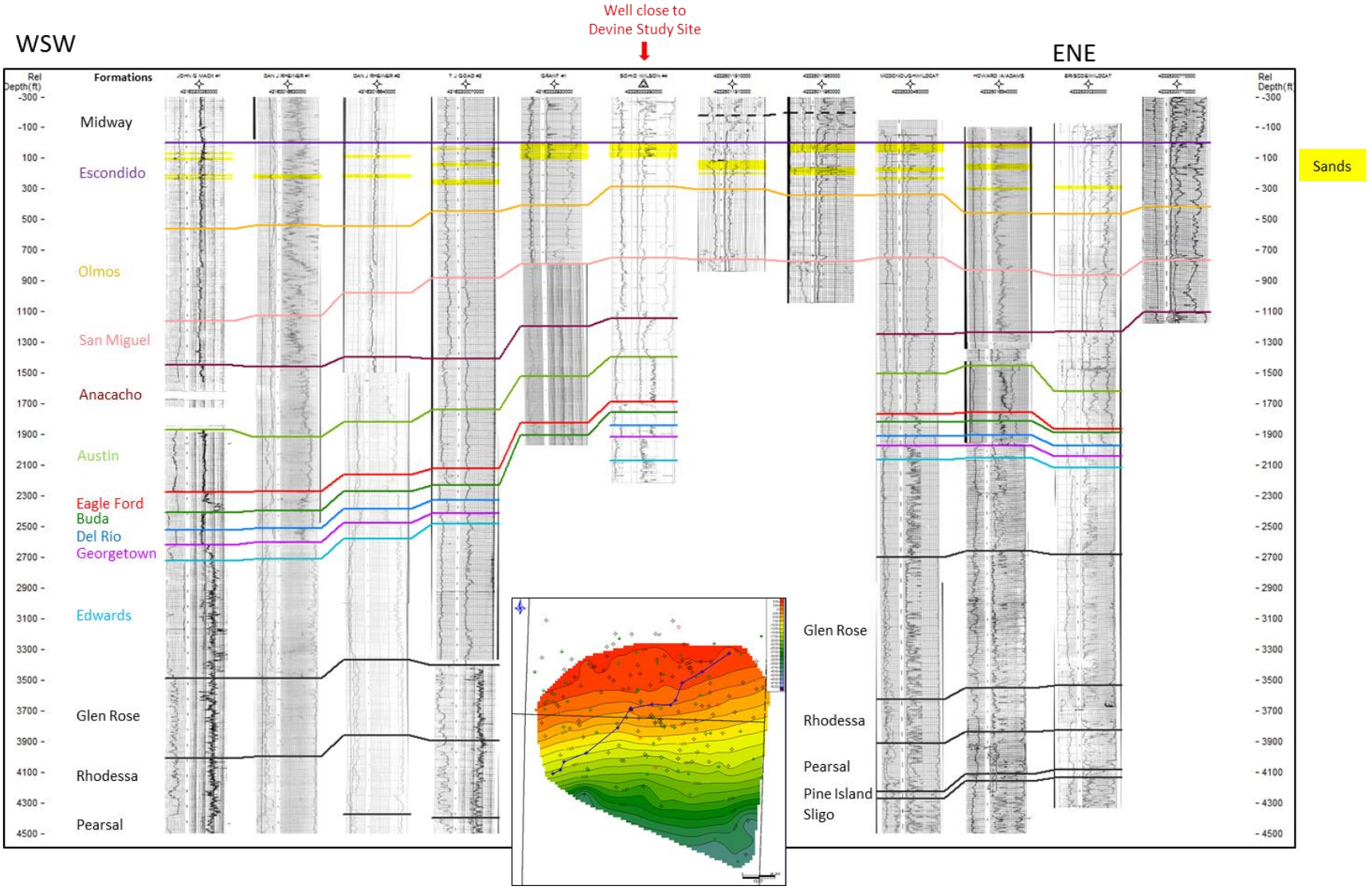

Figure 19. Stratigraphic section on top of the Escondido (flattened on top of the E.)

II-2-3 Oil and Gas and Mineral Resources

The Devine Test Site is located in a prolific oil and gas province but the site itself is away from nearby fields (Figure 20 and Figure 21). In addition to learning about the general environment of the Devine Test Site, this study of oil and gas wells was conducted to find an appropriate oil or gas well to obtain produced water to complement in volume and quality brines from the Hosston Fm. The ideal well would be an actively producing well deeper than the Edwards Fm. and South of the Balcones Fault Zone. All wells in Medina and Frio counties were downloaded from the IHS database. There are 11,758 total wells in Medina and Frio counties with only 14 of those wells in North Medina in the Balcones fault zone (Figure 8). All of those wells have been drilled and abandoned. There are 8619 production wells which are all south of the Balcones Fault zone (value excludes all injection wells). Of these 8619 wells, 2719 are actively producing. Many fields have wells in Medina and Frio counties. Figure 21 and Table 1 shows the top 10 conventional fields in Frio and Medina counties. There are also many plugged wildcat wells.

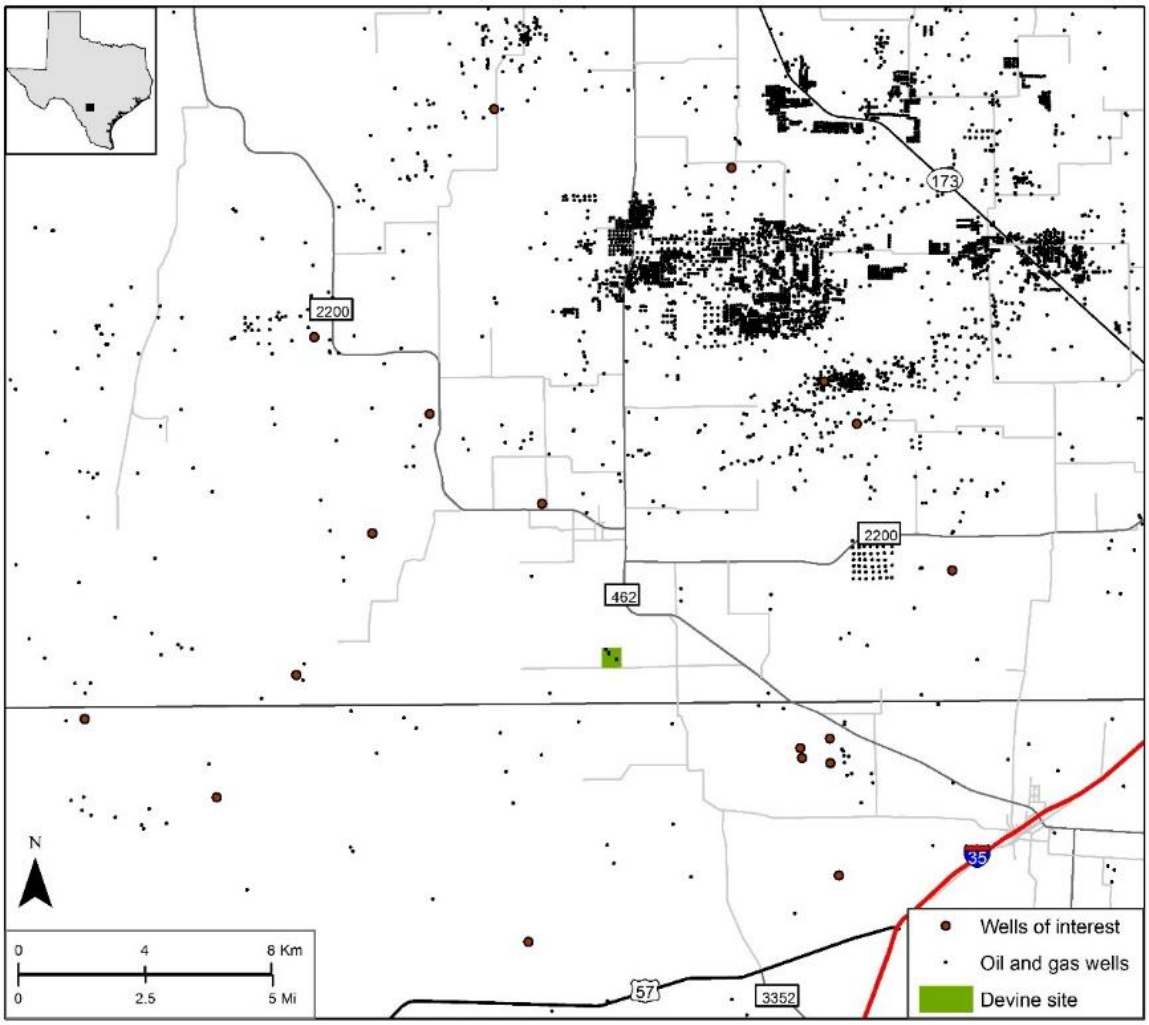

Source: IHS Enerdeq database

Note: Wells of interest" are deeper wells relevant to the proposed study. The Medina-Frio county line is just south of the proposed site. Note that most of the wells shown on the map are not currently active.

Figure 20. Location of the Divine Test Site relative to major oil/gas historical production in the area.

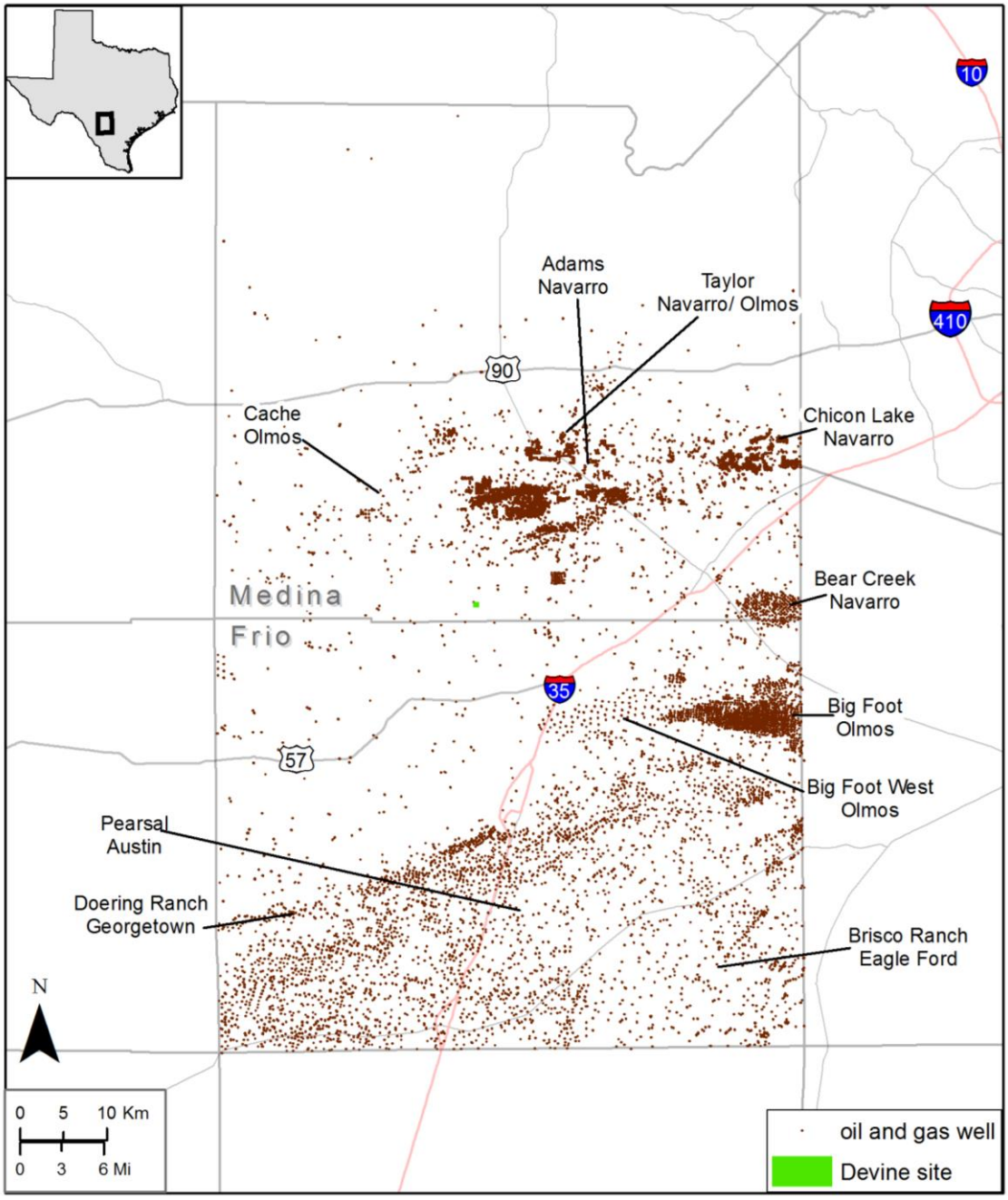

Source: IHS Enerdeq database;
Note: Field name and reservoir formation are given

Figure 21. Main oil and gas fields in the Devine Test Site area

Table 1. Top 10 fields in Medina and Frio counties

Field Name	Number of Wells	Field Name	Number of Wells
Adams	275	Chicon Lake	890
Bear Creek	275	Doering Ranch	113
Big Foot	1248	Fairfield	183
Bog Foot West	107	Pearsall	2984
Briscoe Ranch	296	Taylor-Ina	2641

Figure 22 and Table 2 show that oil is the main product in Medina and Frio counties and that there are almost 3000 active wells in the area. Figure 23 and Table 3 show the production formation: Upper Cretaceous Navarro and Olmos formations dominate followed by formations of the carbonate section (Anacacho, Austin, Georgetown, Buda) and the Eagle Ford Shale (most Eagle Ford wells are south and East of Frio County) (Figure 24 and Figure 25).

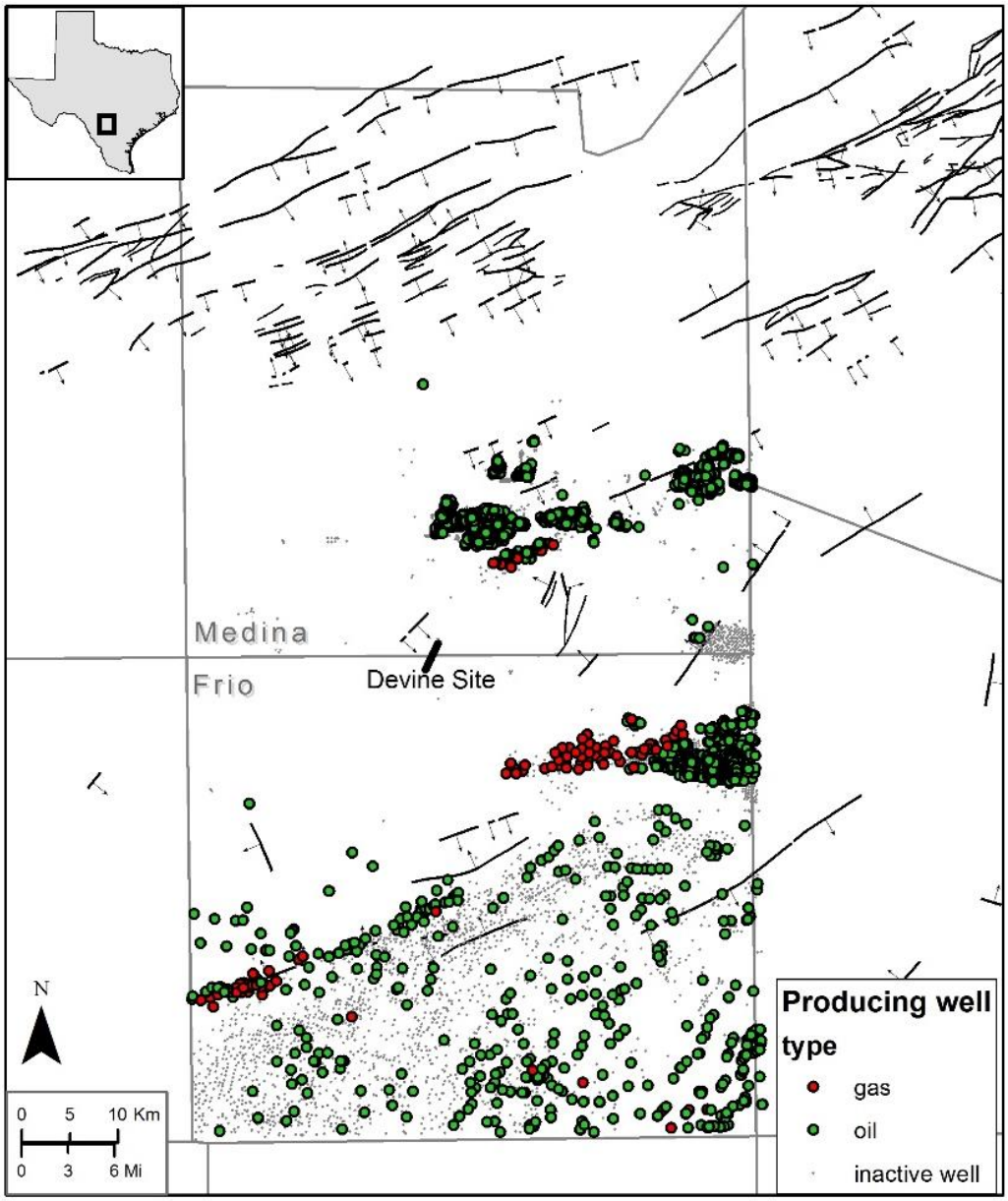

Figure 22. Oil and gas wells in Medina and Frio counties

Table 2. Oil and gas wells in Medina and Frio counties

	Active Wells	Active and Shut-in Wells
Oil	2684	8318
Gas	107	301
Injection	21	287

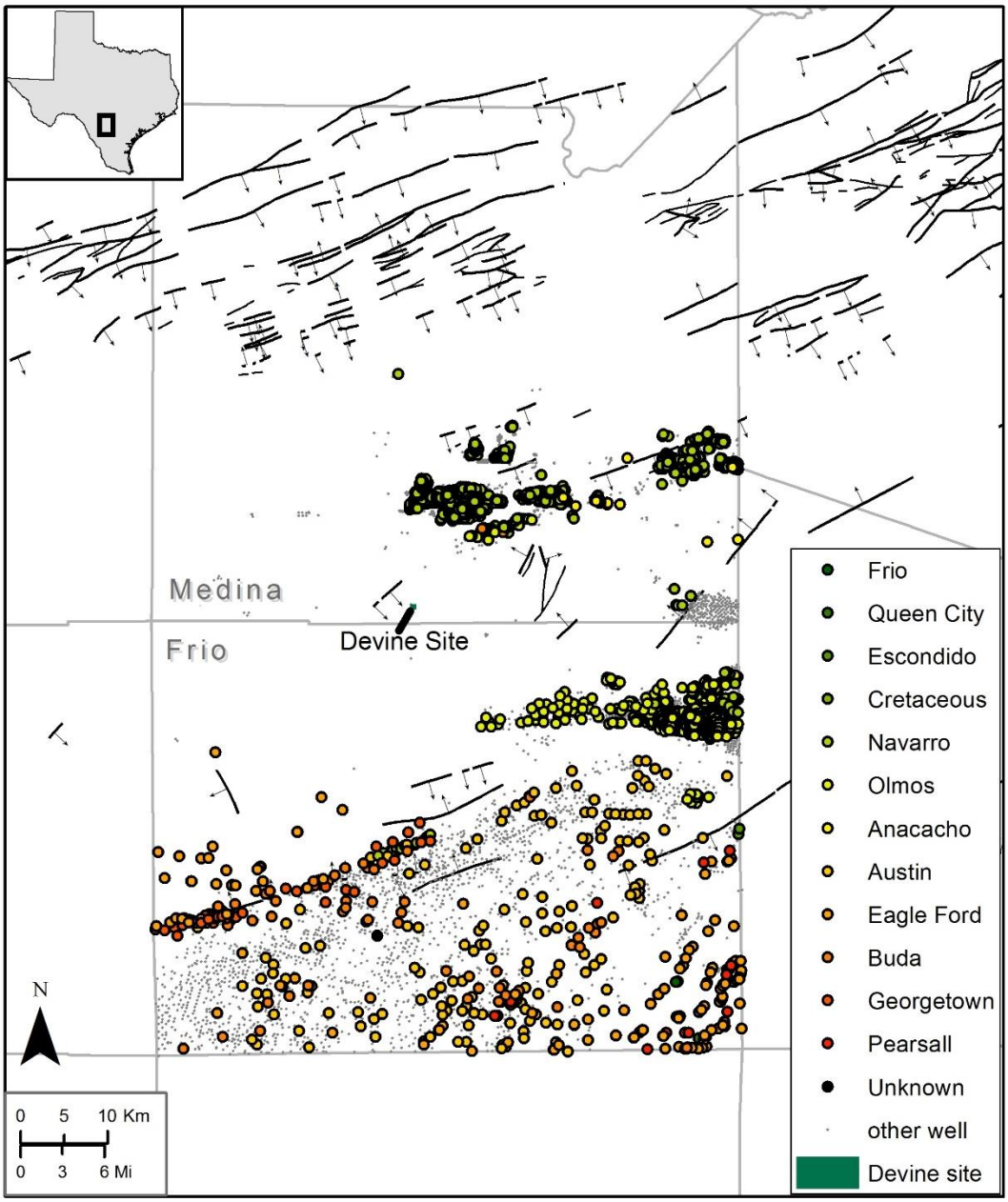

Figure 23. Producing formation for production wells

Table 3. Producing formation for production wells

Formation	Active	Inactive	Total	Formation	Active	Inactive	Total
Miocene	0	1	1	Anacacho	58	126	184
Frio	2	7	9	Austin	169	2511	2680
Queen City	1	14	15	Eagle Ford	177	17	194
Escondido	2	23	25	Buda	97	102	199
Cretaceous	2	2	4	Georgetown	40	13	53
Navarro	1733	2050	3783	Edwards	0	1	1
Olmos	489	904	1393	Pearsall	20	1	21
Taylor	0	2	2	Unknown	1	23	24
San Miguel	0	31	31	GRAND Total	2791	5828	8619

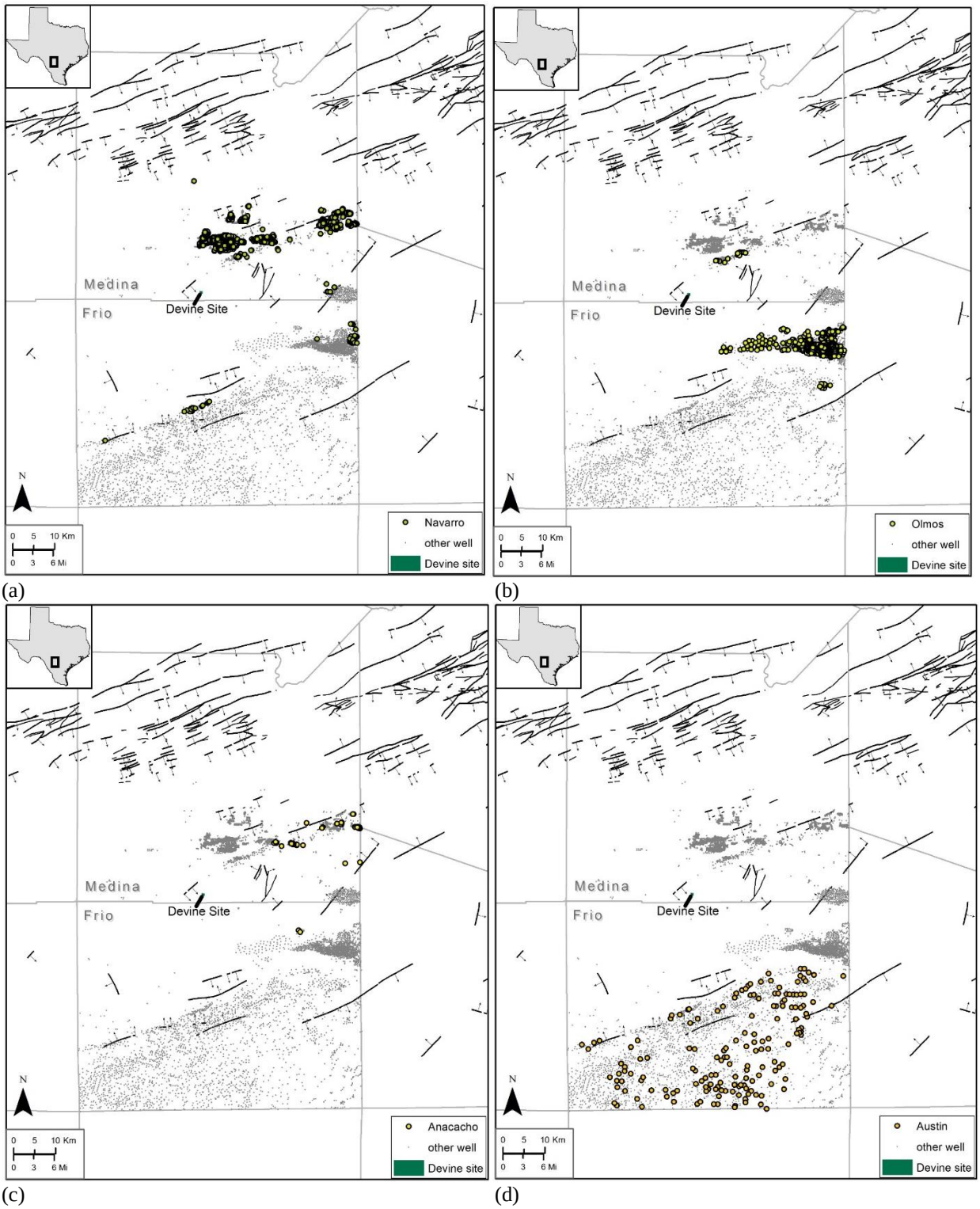

Figure 24. Map of wells producing from the Navarro (a), the Olmos (b), the Anacacho (c), and the Austin (d)

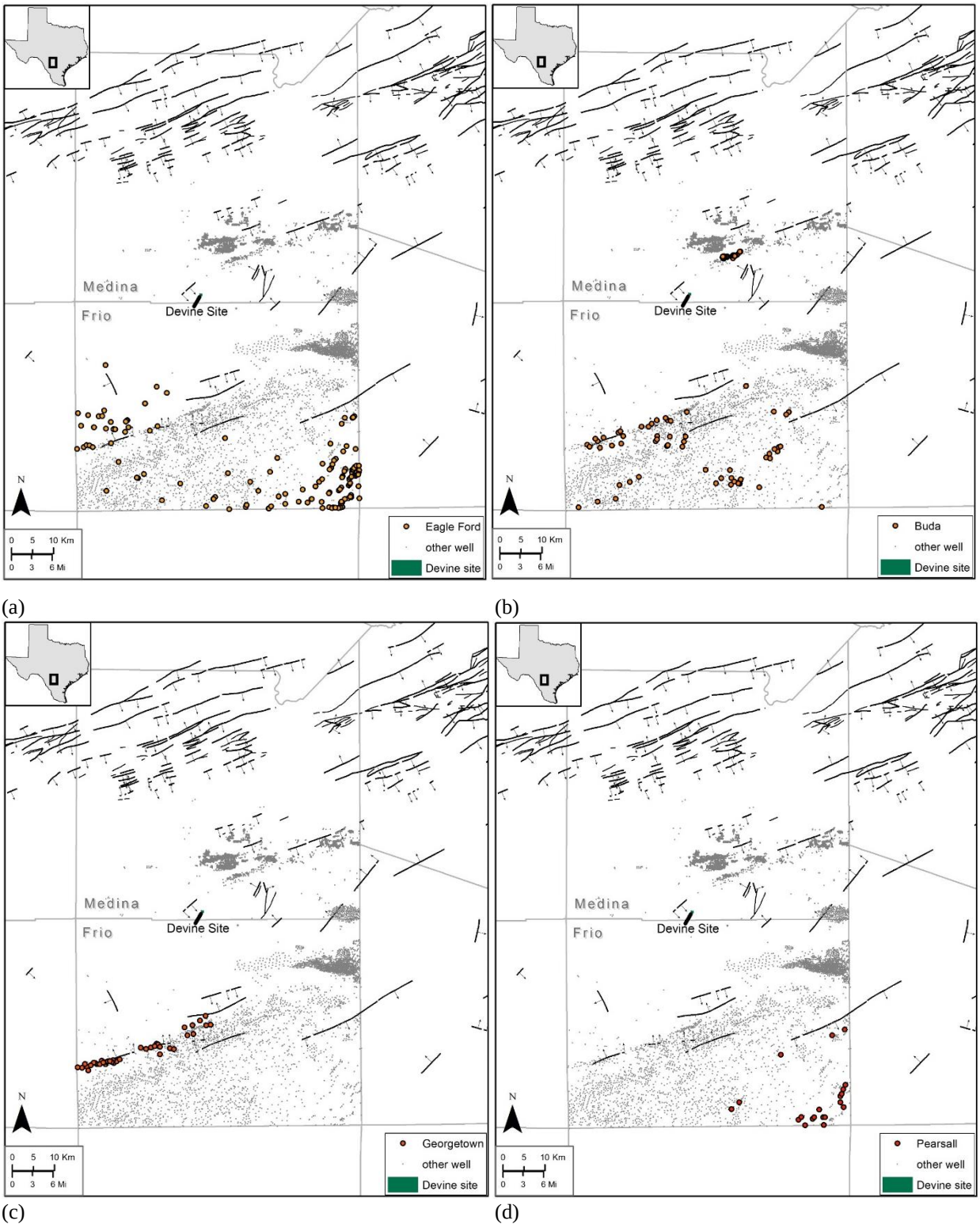

Figure 25. Map of wells producing from the Eagle Ford (a), the Buda (b), the Georgetown (c), and the Pearsall (d)

II-3. Hydrogeology

Starting almost 20 years ago, the state of Texas has embarked on a state-wide program to model all fresh-water aquifers in the state with periodic updates. The result has been that the state of Texas has well-developed groundwater programs mostly managed by the Texas Water Development Board (TWDB). TWDB and contractors have built numerical models (called groundwater availability model or GAM) covering all major and important minor aquifers across the state. Of interest to this study are the Carrizo-Wilcox, Edwards, and, to a lesser extent, the Edwards-Trinity GAMs (http://www.twdb.texas.gov/groundwater/models/gam/). TWDB has also started a strong push towards characterizing brackish water aquifer, defined as having a total dissolved solid concentration (TDS) between 1000 and 10,000 mg/L (http://www.twdb.texas.gov/innovativewater/bracs/index.asp). Aquifers are managed by county-size governmental entities called groundwater conservation districts. The study area include 2 of them, the Medina County GCD (http://medinagwcd.org/) and the Evergreen UWCD (underground water conservation district) which includes Frio County and 3 other counties (http://www.evergreenuwcd.org/). In addition, the Edwards Aquifer Authority (EAA) is a conservation district with a special status. It is federally mandated and is concerned with only one aquifer. Medina County belongs to the EAA with all or part of 7 additional counties. Because the GCD's are small compared to the size of aquifers, groundwater management areas (GMA's) were created to engage various stakeholders of individual aquifers. The area of interest is concerned with 2 GMA's: GMA 10 that includes the Edwards Aquifer and GMA 13 that includes the Carrizo-Wilcox Aquifer. All these entities produce various levels of information useful for the study.

II-3-1 General Hydrogeology

TWDB defines major aquifers as those that are important water sources for large communities or those that contain large water reserves (Ashworth and Hopkins, 1995; George et al., 2011). Minor aquifers are those that are locally important but that cannot be classified as major aquifers. Note than many aquifers are described neither as major nor minor by the TWDB. The area of interest is concerned with two major aquifers: carbonate Edwards aquifer (oldest host; deeper at ~3000 ft and limestone) and siliciclastic Carrizo-Wilcox aquifer (youngest host; shallower with large sand lenses and deposits).

For clastic aquifers, geological characteristics impacting flow properties to watch for are: strike or dip orientation of the sand packages controlling flow direction and recharge. Their general distribution such as increasing mud deposits towards the shelf with river-deposited sand packages directing flow downdip or lagoonal mudstones facies limiting recharge (as in in present-day outcrop of the Wilcox of south Texas. For carbonate aquifers, presence of a paleokarst is a strong indication of fast subsurface flow.

A summary of major aquifers in the state are presented in Ashworth and Hopkins (1995) and George et al. (2011). The Edwards aquifer is a karstic aquifer with a quick reaction time vis-à-vis external forcing. It runs from Kinney County to Hayes County though Uvalde, Median, Bexar, and Comal counties. The Edwards aquifer is the main water provider for the city and San Antonio and other towns in South Texas and is also used for irrigation in Uvalde and Medina Counties (Lindgren et al., 2004). The aquifer is strictly regulated by the Edwards Aquifer Authority (http://www.edwardsaquifer.org/). The water quality degrades quickly past the outcrop except in Medina County but, beyond the so-called "*bad water line*" representing transition from

fresh to brackish and saline waters, the Edwards Fm. itself extend all the way to the Stuart City reef. The salinity gradient across the bad water line to TDS>10,000 mg/L is relatively steep. The Edwards Fm. (aquifer and downdip areas) has a good porosity because it was karstified before the deposition of the overlying Georgetown Fm. (Senger and Kreitler, 1984, p.6).

The Carrizo-Wilcox aquifer (Deeds et al., 2003; Dutton et al., 2003; Kelley et al., 2004) is one of the most prolific aquifer in the state. It is a composite aquifer with several water-bearing intervals. The Simsboro Fm. (Middle Wilcox) of Central Texas and the Carrizo Sands of South Texas displays the high capacity and high yield. They are clastic aquifers with mostly dip-oriented sand bodies favoring deep recharge. When normal faults break up the continuity of transmissive sandstones between the outcrop and the deeper part of the aquifer (Dutton et al., 2006, p.865), the along-dip fresh water section is relatively short (as in Central Texas). Where faults die out to the southwest area of the aquifer (south Texas), the width of the aquifer increases to more than 100 km (Dutton et al., 2006).

General cross-sections extracted from LBG-Guyton (2003) illustrate the extent of the fresh water in the Trinity Aquifer (Figure 26), Edwards Aquifer (Figure 27), and Carrizo-Wilcox Aquifer (Figure 28). Note the lack of data points in the vicinity of the Devine Test Site on Figure 26 translating into the wrong extrapolation of the 3000 mg/L line that should have been drawn further to the north of the site as indicated by the added line.

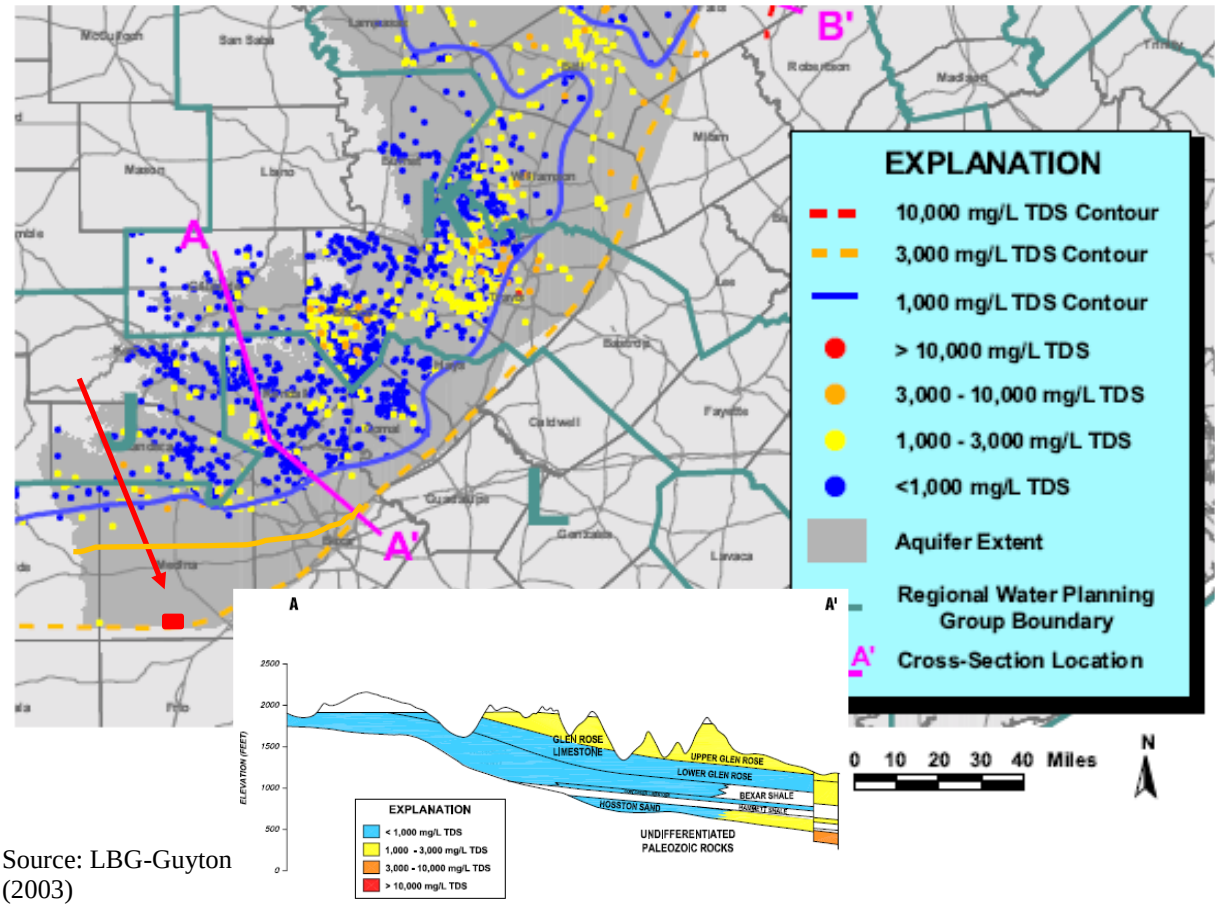

Source: LBG-Guyton (2003)

Figure 26. Wrongful interpretation of salinity of the Trinity Aquifer.

The Edwards Aquifer seems to be fresh or at least <2000 mg/L at the vertical of the Devine Test Site as suggested by Figure 27 and Figure 29 and confirmed by geophysical logs of on-site wells. The entire Carrizo-Wilcox Aquifer is fresh in the vicinity of the site (Figure 28).

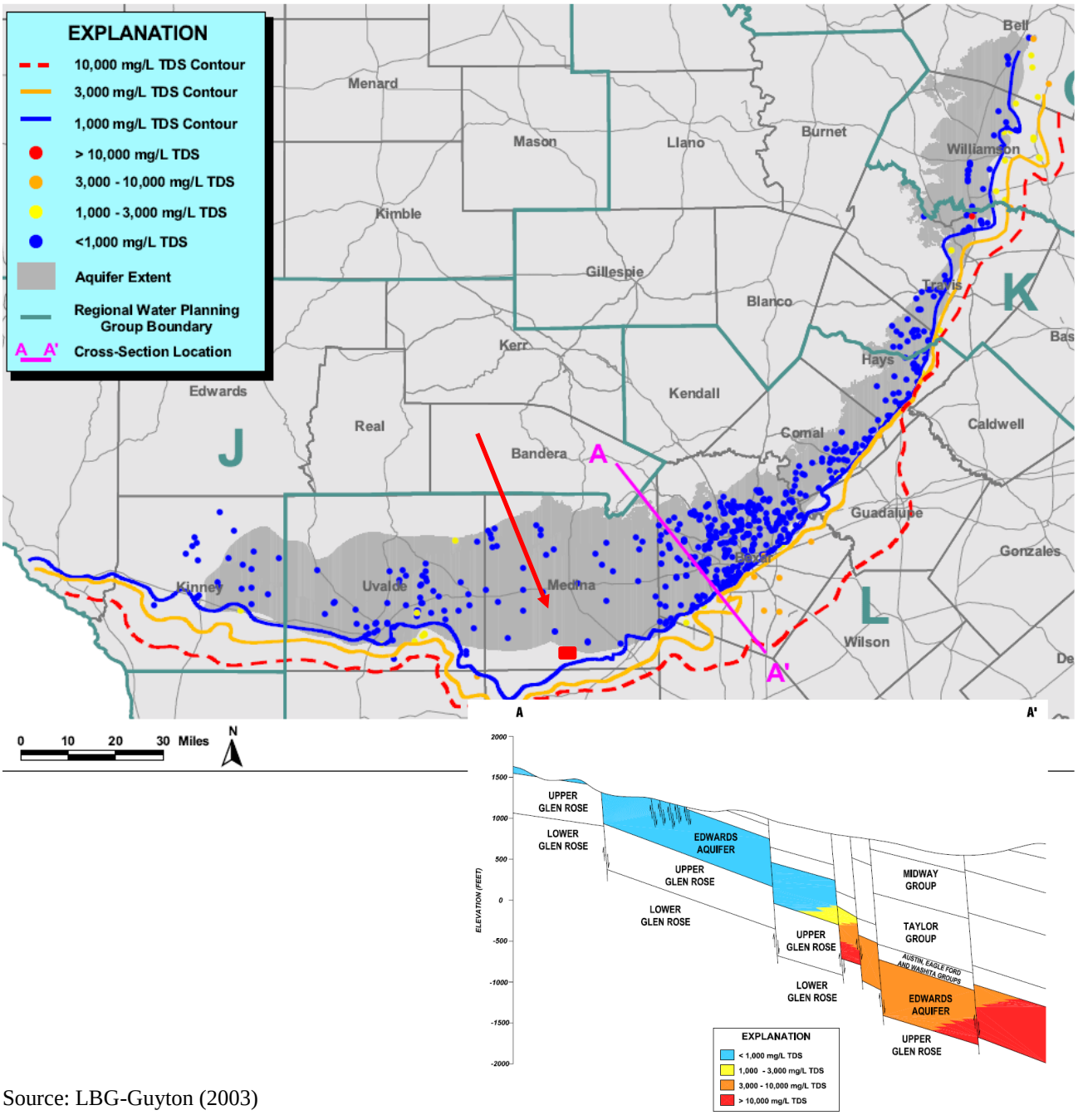

Source: LBG-Guyton (2003)

Figure 27. Edwards Aquifer extent and salinity distribution

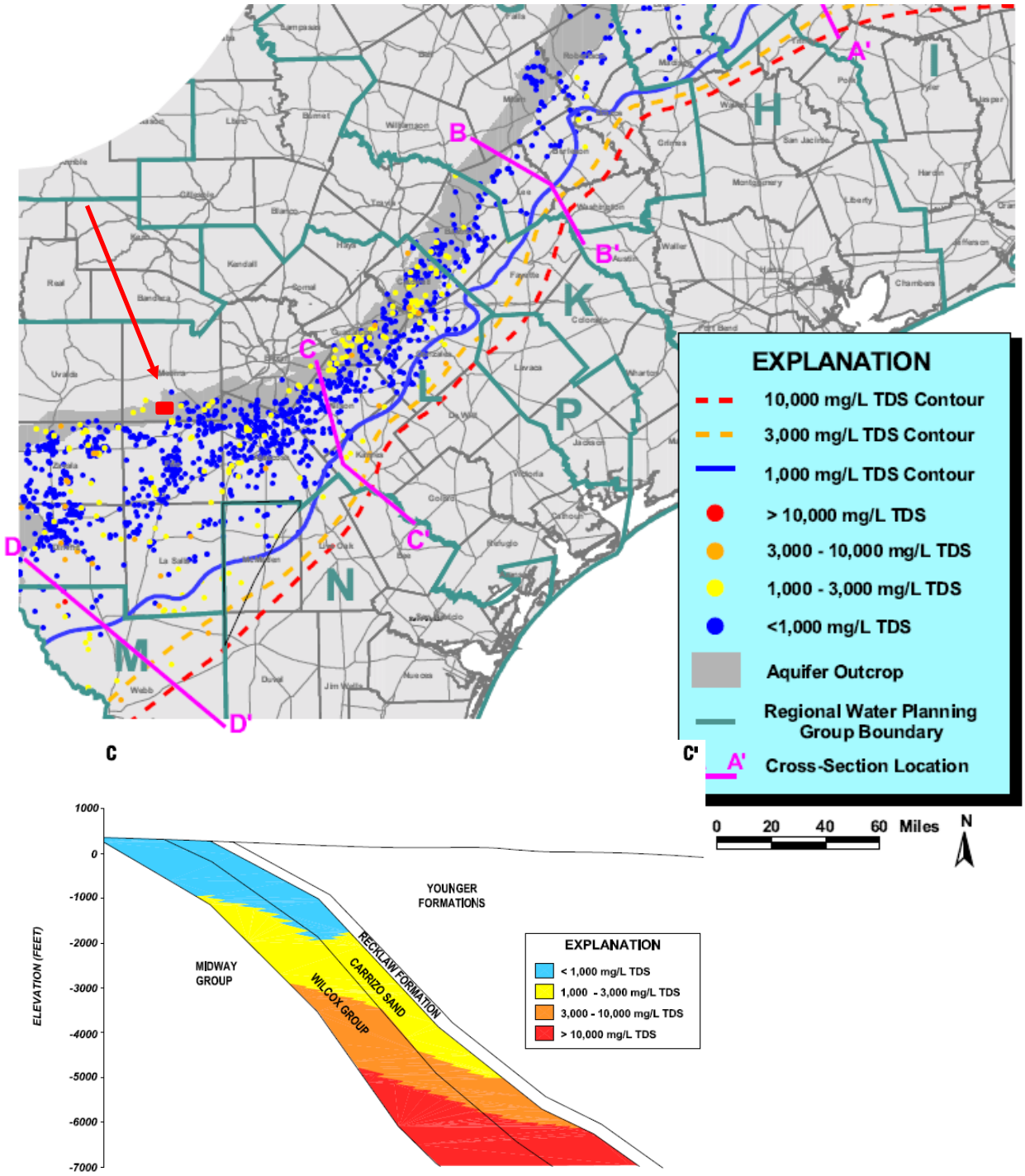

Source: LBG-Guyton (2003)

Figure 28. Carrizo-Wilcox Aquifer extent and salinity distribution

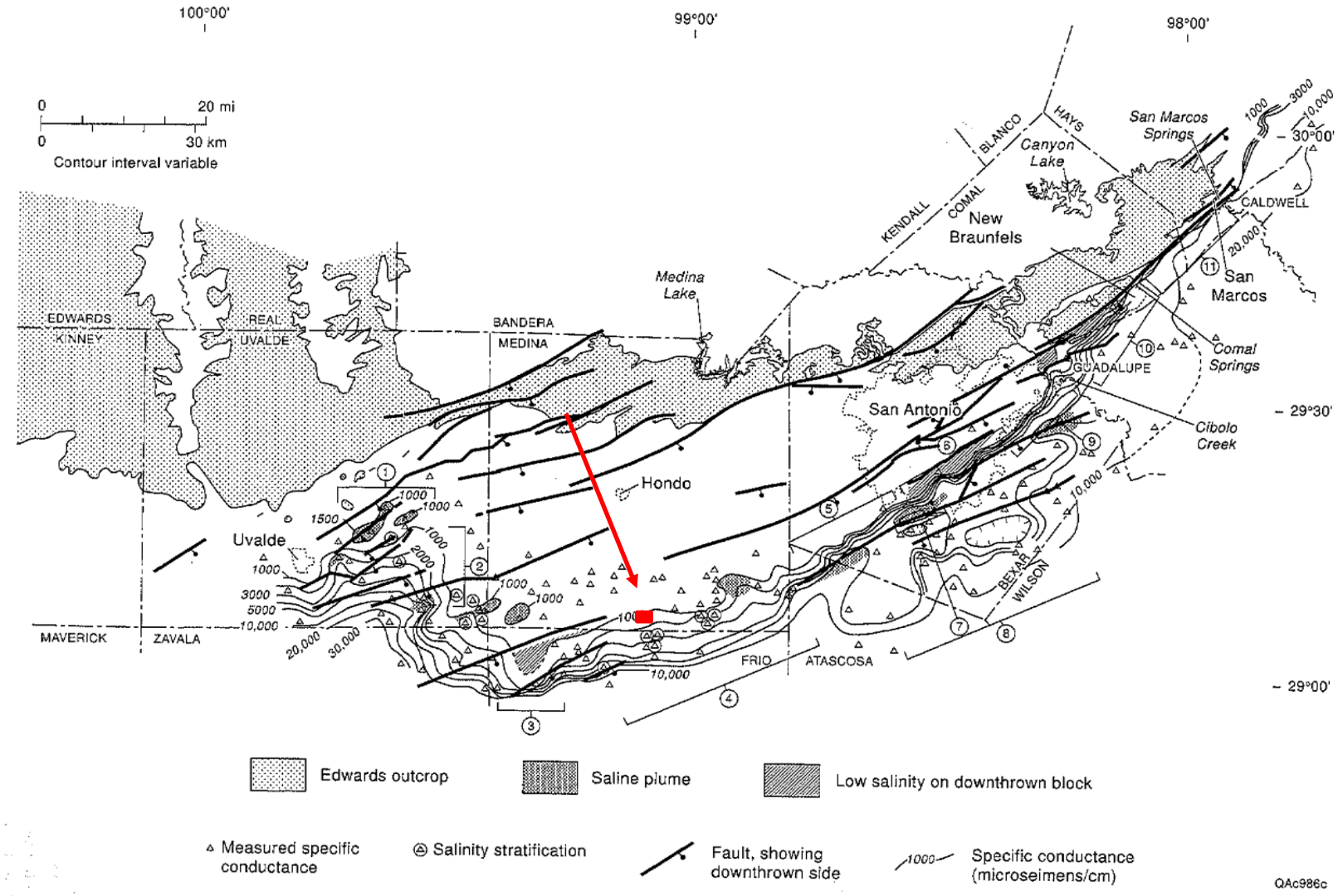

Source: Hovorka et al. (1998, Fig.4) ;

Note: Hovorka et al. (1998, p.16) notes than a rough approximation of a TDS of 1000 mg/L is a conductivity falling between 1300 and 1500 µS/cm (depending on the ionic makeup)

Figure 29. Edwards Aquifer conductivity map

II-3-2 Local Hydrostratigraphy

The local hydrostratigraphy is consistent with the regional knowledge as demonstrated by the stratigraphic studies in Section II-2-2 and summarized in a generalized hydrostratigraphic column in Figure 30: thick sandy intervals with fresh water in the Carrizo-Wilcox, slightly brackish water in the Navarro (Escondido) and maybe in the Taylor, mostly fresh water again in the Edwards Aquifer, brackish to saline in the Glenrose-Sligo interval, and saline water in the Hosston Formation. Water sources at the site or in close vicinity to the site are the Wilcox Aquifer (fresh), sand lenses from the Navarro-Taylor groups (brackish), the Edwards Aquifer (fresh to brackish), Glenrose-Sligo interval (brackish to saline), and Hosston sands (saline). If we have some general knowledge about water quality in these aquifers, we do not know much about their TDS, their ionic make-up, and their conductivity / well yield.

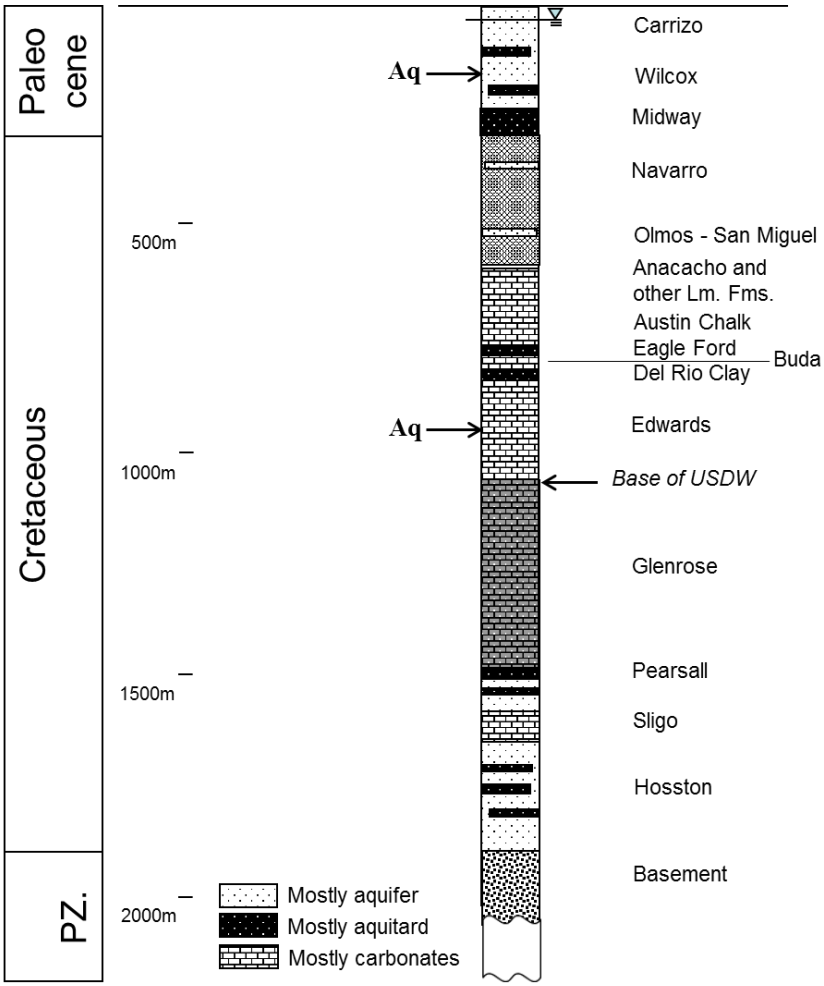

Note: USDW: Underground source of drinking water. PZ: Paleozoic

Figure 30. Generalized hydrostratigraphic column of the proposed study area.

The state of Texas collects regularly information about water levels and chemical composition of thousands of wells in producing aquifers across the state (public domain TWDB groundwater database: http://www.twdb.state.tx.us/groundwater/data/gwdbrpt.asp). It also collects technical (but not geological) information about all water wells drilled in the state (the larger TDLR driller database): http://www.twdb.texas.gov/groundwater/data/drillersdb.asp. The local GCD (Medina

County GCD) also collect information about water wells present in their jurisdiction: (http://medinagwcd.org/files/Quick%20Handbook%20MCGCD%2004%2003%202013.pdf). All the water wells on record in the vicinity of the area of interest are drilled in the Carrizo or Upper Wilcox section of the Carrizo-Wilcox Aquifer.

Source: TWDB SDR database data viewer
Note: square with red outline is the Devine Test Site

Figure 31. Locations of selected existing water wells close to the Devine Test Site.

Table 4. Characteristics of local water wells

Well	Elevation (ft)	Depth (ft)	Filter Pack (ft)	Screened Interval (ft)	Depth to Water (ft)	Yield (gpm)	Draw-down (ft)	Date Drilled
Devine	670	150	50	20	40	10	60	Feb. 19999
399934	643	420	220	80	42	75	nd	Aug. 2015
212379	675	360	100	40	160	15	22	May 2008
156641	645	220	200	40	160	18	nd	Aug. 2005
227730	645	270	100	nd	nd	10	nd	Jul. 2007
156641	630	220	120	20	100	20	nd	Feb. 2009

nd: no data; Elevation extracted from Google Earth

The Devine Test Site itself has a shallow water well and several domestic wells around the site show similar characteristics (Figure 31 and Table 4). However, it should be noted that the Devine water well seems to be a relatively poor well compared to its neighbors.

To better assess well yields in the area and their sustainability, we collected information on local domestic, irrigation, and life stock wells. The TWDB-sanctioned TDLR database captures well yield (Q) (Figure 32) and associated drawdown (s), typically after 1 hour of pumping. The ratio of these 2 parameters (Q/s) is called specific capacity and is indicative of the quality of the tapped aquifer. Applying Theis transient flow equation (iteratively), local transmissivity of the aquifer can be inferred (Figure 33). Knowing the length of the screened interval(s), conductivity can then be deduced.

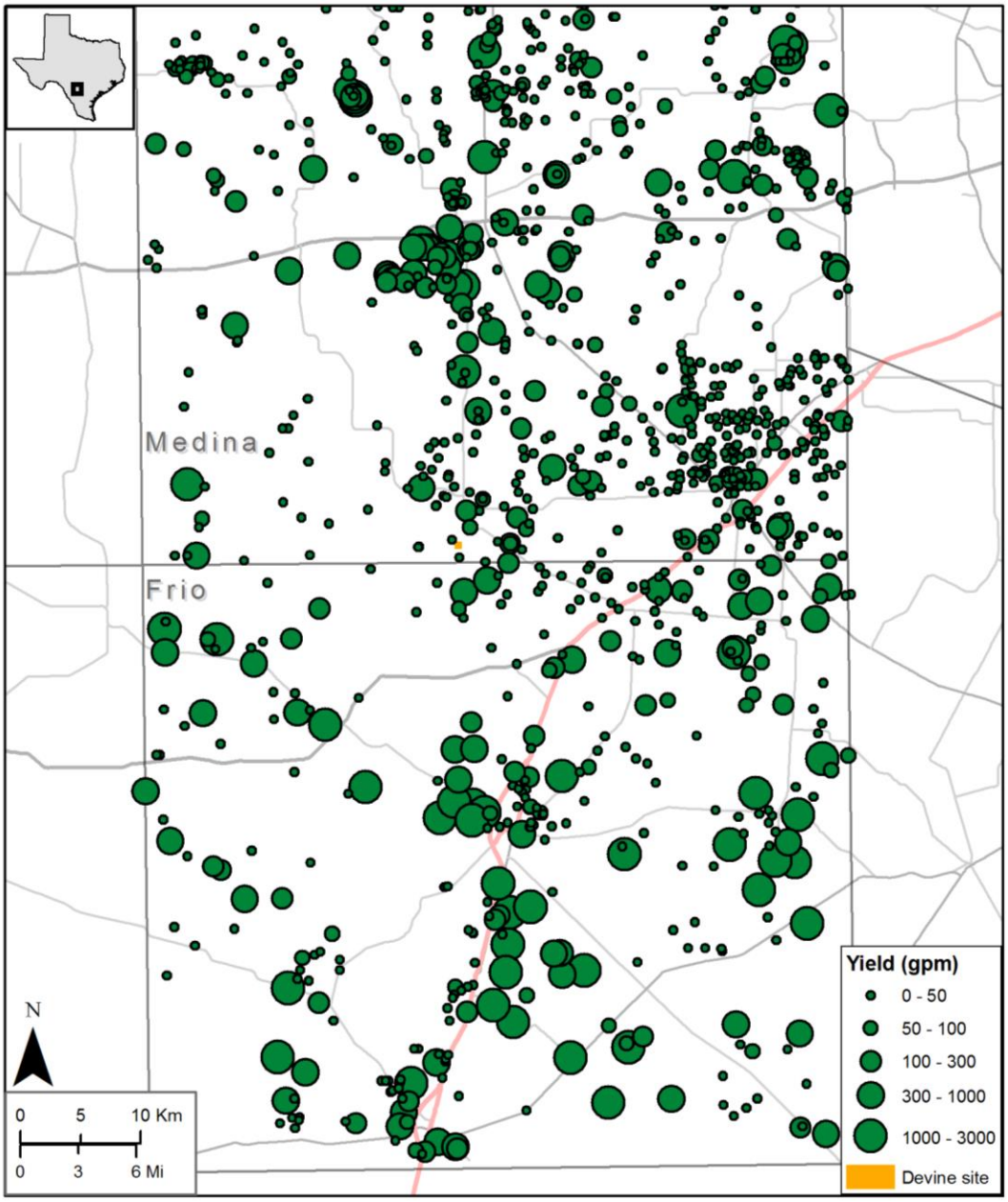

Figure 32. Water well yield in Medina and Frio counties

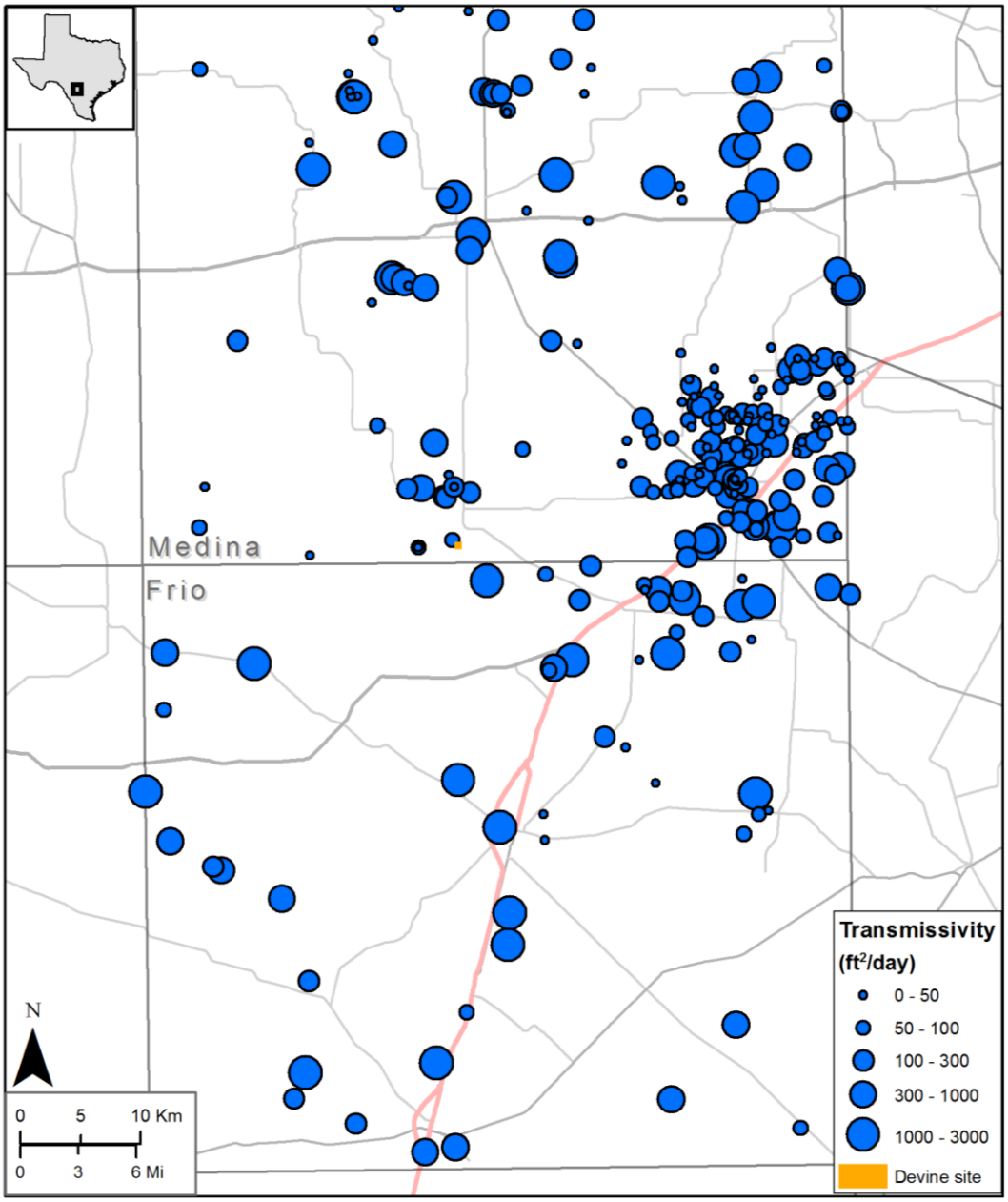

Figure 33. Water well computed transmissivity in Medina and Frio counties

Most water wells from the TDLR driller database do not state which formation they draw water from (although most "TWDB wells" do). We then estimated the water producing formation by matching the screen interval(s) depth (well owners' information) with regional groundwater model (GAM) structural information.

Section X (Appendix A: Fresh Water Well Yields) present histograms of the same dataset. Well yields less than 50 gpm are very common and the most likely yield for a typical domestic (that is, affordable) well drill in any formation. Section X also includes spatial distributions of the yield for each formation.

II-3-3 Chemical Composition of Aquifer Water

In order to perform water compatibility studies needed because of the blending between water of different sources (see LCA, Section VI), we need a good knowledge of their ionic makeup and TDS. In this section we summarize what we know about their TDS and composition. Our knowledge comes from four sources we detail below: (1) literature review of reports describing local aquifer water quality, (2) regional databases with groundwater quality of actual samples but not sampled by us (TWDB and USGS databases), (3) examination of geophysical logs, and (4) grabbing of actual samples.

II-3-3.1 Introduction and Methods

Fresh and brackish water aquifers can be characterized by two main parameters to which a third one can be added. The most important parameter is TDS / salinity. By definition a fresh water aquifer cannot have a TDS >1000 mg/L. The second important parameter is ionic make up. Major cations are Ca, Mg, and Na. Major anions are chloride, sulfate and bicarbonate. Water types are classified according to the various proportions of these dissolved constituents, typically by plotting them on the so-called Piper plot. Redox conditions form the third parameter. They control amounts of minor constituents such as H_2S and Fe and trace elements such as As or B. A fourth parameter, pH, is also important but most natural waters fall into a relatively narrow range (pH of 6-8). Several salinity thresholds have practical and regulatory significance. A total dissolved solids (TDS) <500 mg/L is preferred for human consumption but the legal limit for fresh water is 1000 mg/L. The base of usable quality water (BUQW) threshold is defined at 3000 mg/L. Texas oil and gas drillers used to set surface casing to protect groundwater resources at a depth controlled by the depth at which this threshold occurs. The threshold currently used is 10,000 mg/L in accordance with US EPA rules. Unless exempted, all groundwater sources with a TDS <10,000 mg/L is deemed an underground source of drinking water (USDW). The definition of what brackish and saline water are varies. In this document, we define as saline all waters with a TDS >35,000 mg/l (accepted average of sea water salinity) and as brackish as water between 1000 and 35,000 mg/L. A typical generalized evolution of groundwater along a flowline as TDS increases is from the Na-Ca-HCO_3 water type to the Na-Cl water type.

Literature review

The TWDB-sponsored GAM reports (Deeds et al. 2003; Kelley et al., 2004; Lindgren et al., 2004) as well as other TWDB reports (Holt, 1959; Alexander and White, 1966; Boghici, 2009; Kreitler et al., 2013) provide information about water quality of major aquifers (Carrizo-Wilcox and Edwards aquifers). These aquifers, important for Texas, have been studied and water levels and chemical composition documented for almost a century.

Databases

Data used in the analysis come from the public domain TWDB groundwater database (http://www.twdb.state.tx.us/groundwater/data/gwdbrpt.asp). It contains geochemical data for tens of thousands of wells across the state, many with several repeat samples over long periods of time. We used the most recent sample if several samples were taken at a given location. TDS was computed by adding concentrations of all dissolved species that were checked to be charge-balanced overall. The TWDB sampling coverage of South Texas aquifers is good but focused on fresh water. Brackish water samples are also collected but not in a systematic way. South Texas does contain significant amount of brackish water. However, unlike fresh water aquifers, there

are few publicly available studies of brackish aquifers in the state despite the strong interest displayed by both the State and municipalities to access the resource and desalinate it. The last comprehensive study of brackish resources in the state was done by LBG-Guyton (2003). Similarly saline aquifers latest comprehensive study across the state was done by Core Laboratories (1972).

Geophysical Logs

Examination of geophysical logs is a useful tool to extract information about water salinity, especially in siliciclastic rocks. The resistivity and spontaneous potential tracks are the most common and useful. Resistivity logs measure salinity of water near the well. Salinity is generally higher and resistivity lower in less permeable rocks such as clays. Complications arise because of the presence of drilling mud, and generally long- and short-range resistivity tools are used in combination. Spontaneous potential measurements detect differences in electrical potential between formation water and drilling mud. Deflection toward lower potential (to the left) suggests that salinity of the formation is lower than that of drilling mud, suggesting a sandy layer ("sand line"). On the other hand, deflection to the right (higher potential) suggests a less-well-flushed, clayey layer ("shale line"). Because the Devine Test Site is located in an oil and gas province, there are many wells with available geophysical logs to examine.

Field Sampling

We sampled produced water from a few shallow oil wells as well as a few water wells following usual sampling procedures. Major and other cations (Li, Na, NH_4, K, Mg, Ca) and anions (F, Cl, Br, NO_3, PO_4, SO_4) of water samples were then analyzed by ion chromatography (Dionex ICS-1100). Trace and other elements that could become important for the treatment test bed (B, Mg, Al, Si, P, K, Ca, Ti, V, Cr, Mn, Fe, Co, Ni, Cu, Zn, As, Se, Rb, Sr, Zr, Mo, Ag, Cd, Sn, Sb, Cs, Ba, Tl, Pb, Bi, Th, U) were analyzed on an Agilent 7500ce quadrupole inductively coupled plasma-mass-spectrometer (ICP-MS). Samples for trace metals were acidified with 2% HNO_3 immediately after collection and diluted so that the total dissolved solid content was close to 500 mg/L. All chemical analyses were performed at the University of Texas.

II-3-3.2 Results

We successively look at the fresh water aquifers (Carrizo-Wilcox and Edwards aquifers), the Upper Cretaceous unnamed shallow aquifers, and the Trinity aquifer whose base is hosted by the Hosston Fm. Here we use the term "*aquifer*" loosely by including saline water in its definition.

The literature review shows that Carrizo-Wilcox and Edwards water are fresh. Waters of both aquifers are of the calcium-bicarbonate type related to the presence of caliche for the former and to the nature of the formation for the latter. The Carrizo-Wilcox also shows the presence of minor sodium that becomes more dominant downdip because of ion exchange (Figure 34) (Boghici, 2009). South of Frio County, in La Salle County, the water type in the Carrizo-Wilcox Aquifer trends to sodium-bicarbonate. Chemical analysis of one sample we collected (Table 7, DG2) shows a calcium-sodium-bicarbonate water type.

The Edwards Aquifer in addition to being mostly of the calcium-bicarbonate water type also contains sulfate, particularly downdip. The water exhibits an increasing sodium-chloride footprint at the bad water line (Figure 29).

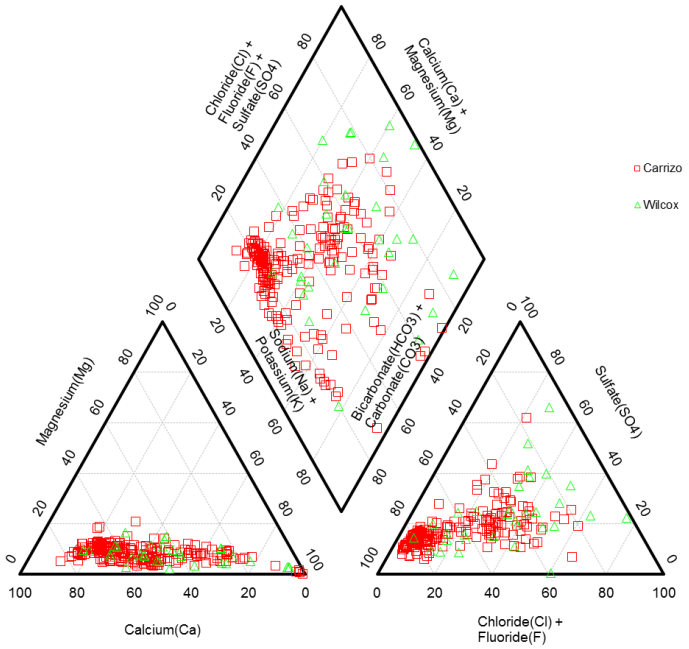

Figure 34. Piper plot of Carrizo-Wilcox wells (Frio County).

Examination of available geophysical logs indicates that water in most of the column is brackish to saline. As described above, exceptions are the shallow Carrizo and Wilcox aquifers and the Edwards Aquifer for which a transition to a TDS >1000mg/L and quick transition to >10,000 mg/L (so-called "bad water line") have been described in this area of the Medina-Frio county line. An evaluation of the geophysical logs (resistivity and spontaneous potential) in the sands of the Navarro and Taylor Groups (which form some of the formations between the Lower Wilcox and the top of the Edwards) suggests than their salinity is ~20,000 mg/L, likely because sand lenses are mostly embedded within a mudstone matrix.

We performed a desktop analysis of the 537 water wells with geochemical analyses in Medina and Frio Counties (TWDB database). Of these 537 wells, 3 wells are in the Cook Mountain Fm. (above the Sparta) and one well is in El Pico Clay (lateral equivalent to the Queen City Fm.). These wells are excluded from the rest of the processing because they tap formations recognized as aquitards. Of these 533 remaining wells, 522 wells have geochemical analyses with a charge balance error less than 10%. Table 5 shows the number of charge balanced wells in each formation.

Table 5. Distribution across formations of geochemical samples from the TWDB database

Formation	Number of Wells	Charge-balanced samples	Depth range (ft)
Leona	25	24	12-62
Queen City-Sparta	46	44	40-1285
Carrizo	219	219	70-2200
Wilcox	32	32	20-400
Escondido	12	12	84-550
Austin Chalk	6	6	40-400
Edwards	148	145	210-3406
Glenrose	44	39	91-1009
Travis Peak / Hosston	1	1	4000+
TOTAL	533	522	

TDS of the TWDB wells ranges from 145 to 4500 ppm (Figure 35). There are two wells with TDS >11,000 ppm, one in the Edwards at a depth of 2164 ft and the other one in the Wilcox with depth of 44 ft (possible typos). Figure 36a shows TDS distribution in water wells regardless of the formation source. Clearly deep water wells tap only fresh water aquifers. There are 69 wells in TWDB database with TDS >1500 mg/L. They are distributed over the entire 2-county area (Figure 36b). The distribution of these wells in different formations is presented in Table 6.

Figure 35. TDS vs. depth for Medina and Frio counties TWDB aquifer samples

Table 6. TWDB water wells in Medina and Frio counties with TDS>1500 mg/L

Well#	Formation	Date Drilled	Date Sampled	depth (ft)	TDS (mg/L)	Water Type
6841802	Escondido	1935	1951	145	3250	Na-Cl-HCO3
6948609	Escondido	1937	1951	142	3519	Na-Ca-Cl-SO4
6954101	Escondido	1942	1951	210	1812	Na-Ca-Cl
6954501	Escondido	1926	1951	275	1968	Na-Cl-HCO3
6946706	Austin Chalk	1909	1930	450	1947	Na-Cl-HCO3
6946322	Austin Chalk		1951	400	1894	Na-Cl-HCO3
6825406	Glen Rose	1950	1951	495	3760	Ca-Mg-SO4
6825602	Glen Rose		1996		3038	Ca-Mg-SO4
6825603	Glen Rose		2003	535	1841	Ca-Mg-SO4
6825617	Glen Rose	2007	2011	550	2719	Ca-Mg-SO4
6825809	Glen Rose	1981	1996	725	1833	Ca-SO4
6826102	Glen Rose	1951	1951	220	2337	Ca-Mg-SO4
6826501	Glen Rose		1994		2647	Ca-Mg-SO4
6826703	Glen Rose	1980	1994	863	2643	Ca-Mg-SO4
6826810	Glen Rose	1950	1994	671	3417	Ca-Mg-SO4
6930301	Glen Rose	1940	1950	200	3075	Ca-Mg-SO4
6930401	Glen Rose	1939	1952	400	1550	Ca-Mg-SO4
6930501	Glen Rose		2003	610	1831	Ca-Mg-SO4
6931102	Glen Rose		1950	200	3750	Ca-Mg-SO4
6931401	Glen Rose	1924	1950	354	3064	Ca-Mg-SO4
6931901	Glen Rose	1950	1950	585	4217	Ca-Mg-SO4
6932103	Glen Rose	1951	1951	237	1798	Ca-Mg-SO4
6932303	Glen Rose	1990	1996	660	2351	Ca-Mg-SO4
6932501	Glen Rose		1996		3458	Ca-Mg-SO4
6938104	Glen Rose	1946	1952	1009	2973	Ca-Mg-SO4
6825903	Glen Rose	1995	1996	740	1727	Ca-Mg-SO4
6953901	Travis Peak	1933	1951	4200	2393	Na-Cl-SO4

Source: TWDB database. Note: samples from Edwards and Carrizo-Wilcox aquifer not included

Using the USGS produced water database (with the important caveat that is far from being comprehensive), we built plots giving an overview of the TDS range in the Devine Test Site larger area (including Atascosa, Bexar, Dimmit, Frio, Karnes, La Salle, Live Oaks, Mc Mullen, Medina, Uvalde, Wilson, Zavala counties). The plots suggest that TDS increases quickly with depth (Figure 37a) and away from the site (Figure 37b).

The USGS produced water database contains 4 wells in Frio County and none in Medina County with TDS >30,000 mg/L (Figure 38). Field sampling of the Escondido and Olmos Fms. (Table 7) shows a 6000-10,000 mg/L range north of the site but higher TDS at ~35,000 mg/L south of the site. Water type of these samples is sodium-chloride.

The underlying carbonates (Austin Chalk) also show TDS much higher than that of fresh water. The fresh water wedge of the Edwards Aquifer is an anomaly due to its very high permeability. The Glenrose Fm. underlying the Edwards Fm. is generally considered an aquitard and is itself underlain by the Pearsall shale limiting any exchange between the Edwards Aquifer and the Lower Trinity formations of interest to the study. Early authors (Holt, 1959) have discussed water quality of the various formations in Medina County. They mentioned that the Glenrose Fm. can be high in sulfate and that may be true for the Hosston Fm. as well. Downdip section of the carbonate interval

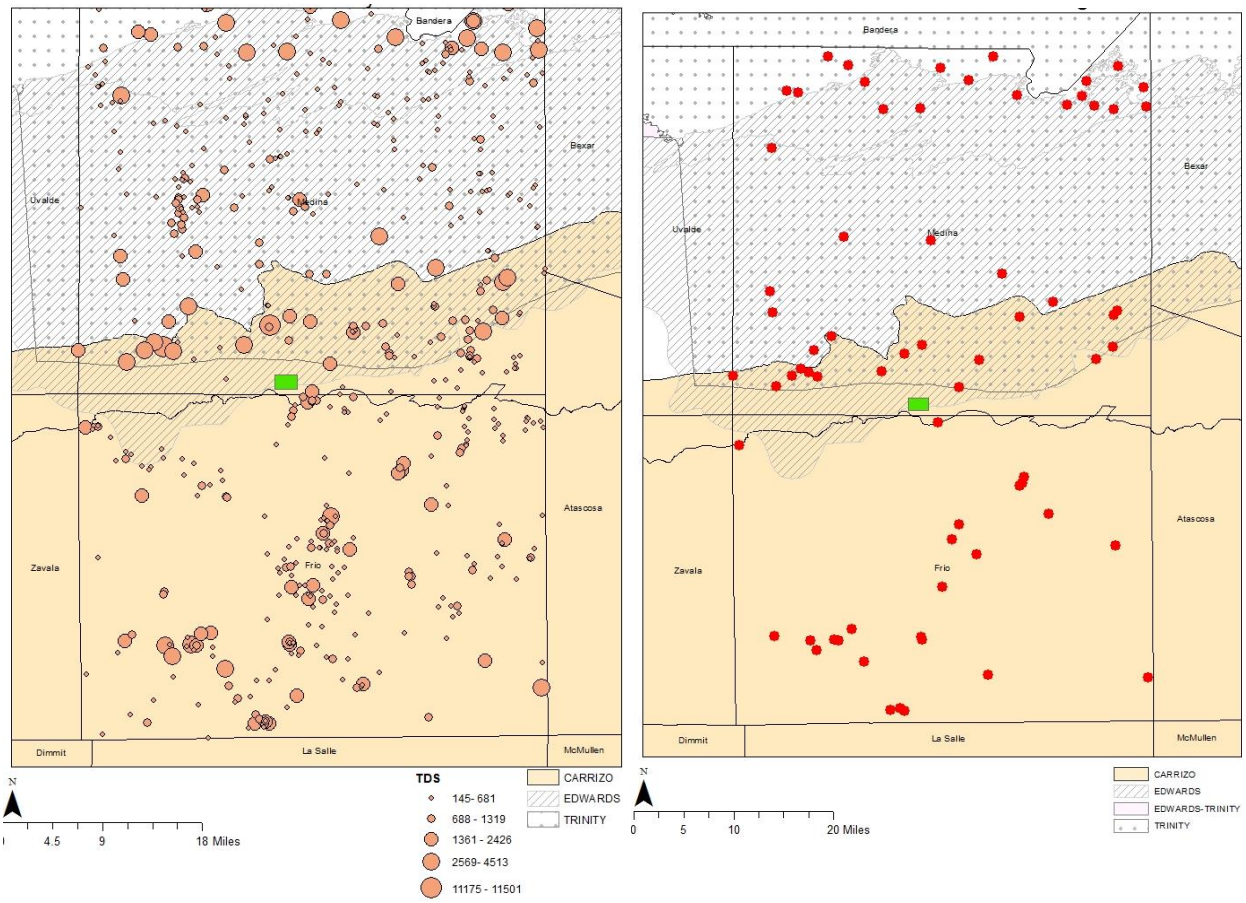

Source: TWDB database. Note: for clarity the Devine Test Site is mapped larger than it is

Figure 36. TDS of TWDB water wells in Medina and Frio counties

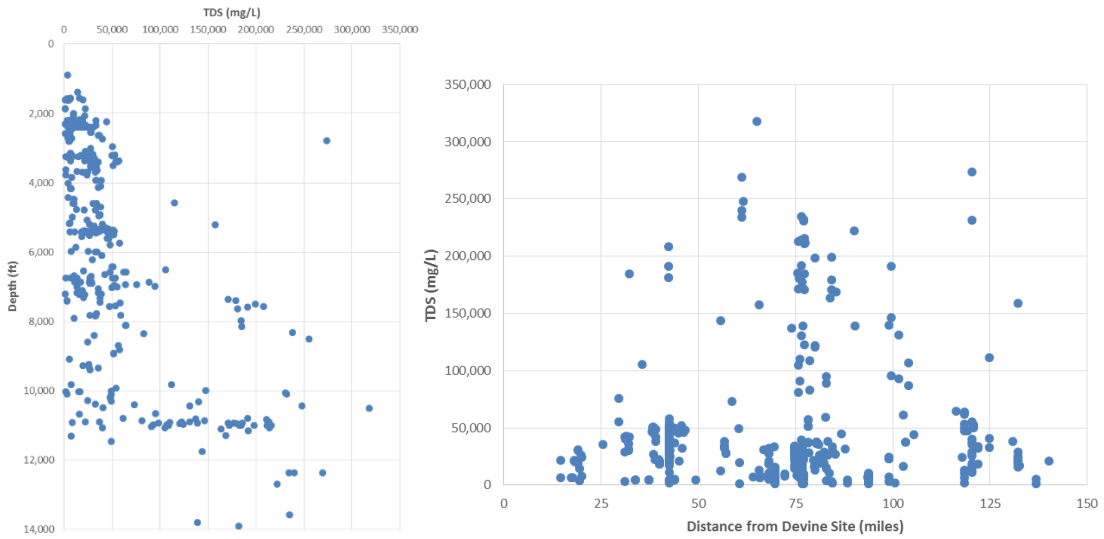

(a) (b)

Figure 37. TDS of available produced water samples (USGS) vs. depth (a) and vs. distance from the Devine Test Site (b) for selected counties

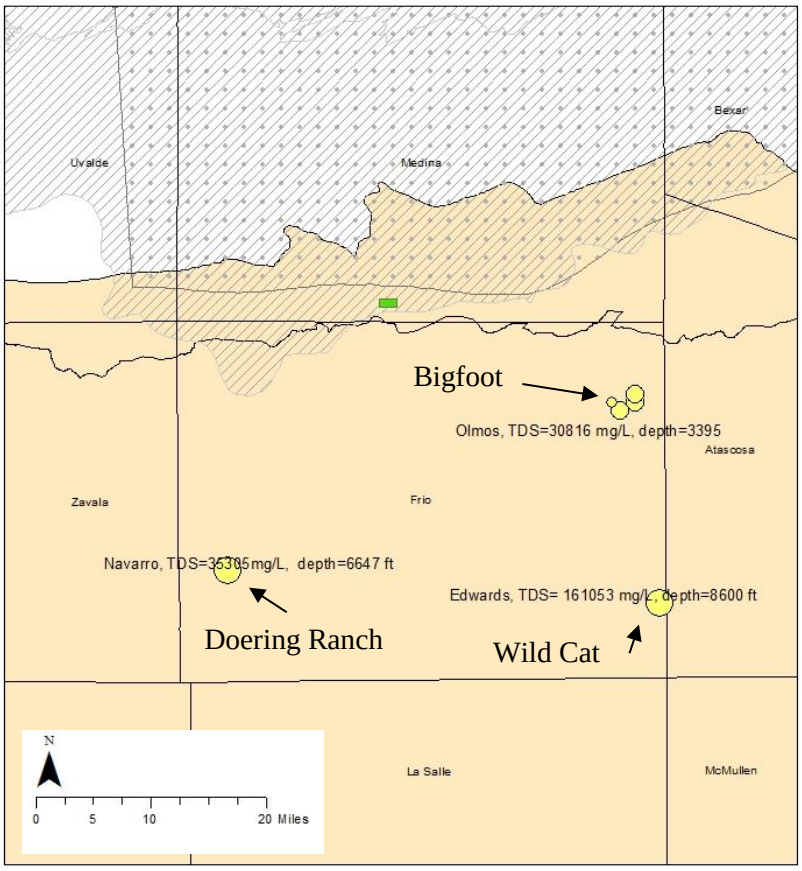

Source: USGS produced water database.

Figure 38. Samples from USGS produced water database with TDS >30,000 mg/L

Table 7. Results of sampling of Taylor and Navarro formations

ID	Na	K	Mg	Ca	Cl	Br	SO_4	HCO_3	D. (ft)	Fm. (Field)
North of the DTS										
BI1	2927	26.1	29.1	43.1	3629	12.6	0.0	929	*	Anacacho (Chicon Lake)
GH1	2108	27.9	44.5	87.0	2905	17.0	0.0	608	*	Escondido (Chicon Lake)
AL1	2251	22.7	32.7	23.5	2564	5.1	0.0	1195	*	Escondido (Chicon Lake)
AZ1	3259	18.9	7.7	12.3	3667	12.4	0.0	1622	*	Olmos (Chicon Lake)
AZ2	2977	18.4	8.1	13.4	3374	22.3	0.0	1354	*	Olmos (Chicon Lake)
AZ3	3397	20.9	10.9	33.3	4625	17.3	0.0	722	*	Olmos (Chicon Lake)
South of the DTS										
DG1	12,315	57.6	65.5	203.7	15,529	108.7	0.0	6947	3400	Olmos D (Big Foot)
CR1	12,187	54.5	58.5	322.3	16,224	92.4	3.5	5724	3100 -3200	Olmos B (Big Foot)
Water wells										
TS	266	28.8	71.5	1149	1607	4.9	1028	386	50-70	Lower Wx
DG2	45.3	3.8	2.8	61.6	66.6	0.0	30.8	189	2100	CZWX

Note: location of fields are shown on Figure 21. *: sampled from produced water tanks, range of depths unknown

We estimated formation water salinity in the Cretaceous Travis Peak Formation in the vicinity of the Devine Test Site, using electric logs from nearby oil and gas wells. Electric log resistivity curves can be used to determine formation water salinity. We used a modified version of the Archie equation to determine formation water resistivity from observed electric log resistivity values and to convert formation water resistivity to TDS (Hamlin and de la Rocha, 2015). Observed resistivity values, which can be taken directly from the logs shown on the cross section, range from 2 to 5 ohm-meters. Converting these resistivities to TDS yields 25,000 to 60,000 mg/L. The lowest observed log resistivity (2 ohm-meters) is questionable because that electric log is from an old 1940's well, and the calculated high TDS (60,000 mg/L) is greater than all other data suggest. The highest resistivity (5 ohm-meters) is rarely observed, and most Travis Peak sandstone resistivities range from 3 to 4 ohm-meters, corresponding to 30,000 to 45,000 mg/L TDS.

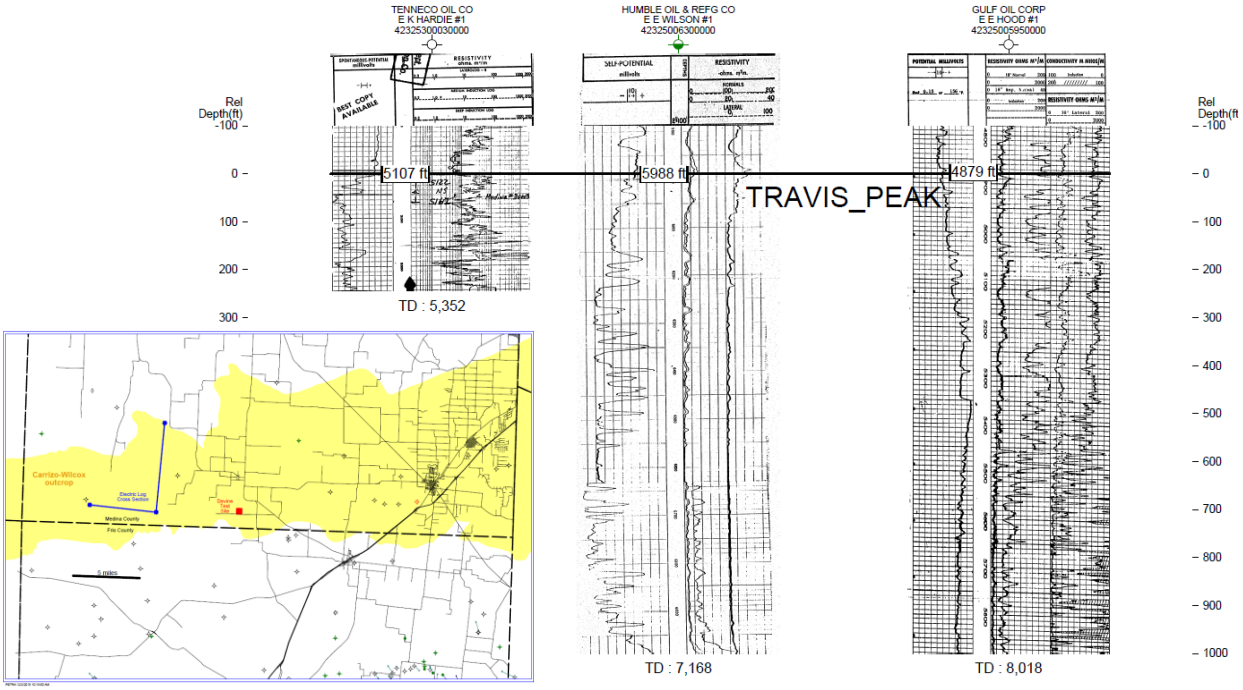

(a) (b)

Figure 39. Travis Peak well locations (a) and logs (b) used to perform the salinity evaluation

The high-SP log character of the Travis Peak / Hosston section in the Wilson #1 well at the Devine Test Site indicates that the unit is predominantly water-bearing sandstone in beds as thick as at least 40 ft, with interbedded shales as much as 20 ft thick acting as potential sealing strata (Figure 11). Moreover, the consistently low resistivity of the sandstones records that they contain solute-rich (conductive) formation water. The TDS of groundwater in Travis Peak / Hosston sandstones is estimated to be 30,000 to 45,000 mg/L. Such a salinity is consistent with a formation that does not crop out on this side of the Balcones Fault zone and thus does not receive recharge from precipitation. The logs also show that the so-called Hosston Sands are >1000ft thick but are actually composed of several sands separated by more clayey or carbonate-rich intervals providing several potential injection / production horizons. Geology of these formations offer closed compartments sealed on top by a shale layer and a tight limestone and up dip but a non-transmissive fault but still thick enough (hundreds of feet) to allow the use of multiple

intervals for the purpose of the injection / extraction experiment. We used electric logs to correlate Cretaceous stratigraphy and identify the Travis Peak Formation (Figure 39b). Although many wells in the area are too shallow to penetrate the Travis Peak Formation, three deep wells west of the Devine Test Site (Figure 39a) do penetrate at least the upper part of the Travis Peak and were used in the cross section. In this area the Travis Peak is composed of 500 to 900 feet of stacked thick sandstones interbedded with thin shales.

Because of the potential need of off-site saline water to complement the injection volume and to assist in providing suitable feedwater to the treatment facility, we sampled Eagle Ford produced water at one of the Basic Energy facilities in Frio County (Table 8). TDS is ~40,000 mg/L with Na and Cl being the dominant ions. We also sent the sample for organic content analysis: BTEX (benzene 520 ug/L; toluene 481 ug/L; ethylbenzene 101 ug/L; xylene (total) 564 ug/L) with 717 mg/L of DOC (dissolved organic carbon), including 60 mg/L of petroleum hydrocarbon (TPH, C6-C35). Results in agreement with produced water that has been in extended contact with oil.

Table 8. Chemical analysis of Eagle Ford produced water sample

Li	Na	NH_4	K	Mg	Ca	F	Cl	NO_2	Br	NO_3	PO_4	SO_4	HCO_3*
10	12,958	266	105	239	2358	64	25,006	0	131	0	0	72	488

*: only tentative, obtained through charge balance

II-3-3.1 Conclusions

The Devine Test Site area includes two fresh water aquifer systems: the Carrizo-Wilcox at the surface with active recharge and shallow downdip confined sections and the Edwards Aquifer (Edwards and allied formations) at a depth of ~3000 ft at the downdip limit of its fresh-water domain just updip of the bad water line. Both aquifers display a sodium-bicarbonate water type. The top of the target formation, the Hosston Formation, is found at ~6000 f. Geophysical logs suggest that the formation is sand-rich with shale baffles and shaly intervals limiting vertical exchanges. TDS estimates are provided by examination of geophysical logs of nearby wells reaching the formation and sampling of wells tapping the same formation. It is estimated to be ~40,000 mg/L, possibly slightly higher. Its water type is likely sodium-chloride with some sulfate. Formations in between the Wilcox and the Edwards (Escondido, Olmos) show some sandy intervals in a mostly shale matrix and are not defined as major or minor aquifer by the state. The water has a TDS in the 10,000-20,000 mg/L range and it belongs to the sodium-chloride water type. The mostly carbonate rocks between the Edwards and the Hosston have low permeability.

II-4. Petrography and Autoclave Experiments

As a first step to characterize the potential injection and brine extraction formations, a search of available and suitable cores was initiated at the Core Repository of the Bureau of Economic Geology. Cores of Hosston, Sligo, and Olmos FMs from 34 wells in Medina, Frio, Guadalupe, and Caldwell County were identified. Selected cores were described and one was selected for the autoclave experiment (Mercer #1)

II-4-1 Methods

The autoclave system, consisted of a stainless steel reactor (250 ml) connected to a high-pressure N_2 tank to pressurize the reactor. The reactors were previously used for rock-water-CO_2 experiment (Lu et al., 2012, 2014, 2016a,b). With little modification brine mixing and rock-brine reaction experiments can be conducted. Sampling ports on the reactor allowed for periodic water sampling. For each experiment, sixteen gram of Hosston core fragments is submerged in 160-mL brine, giving a brine/rock volume ratio of approximately 25. The reactor temperature was regulated by four computer-controlled heating elements and a thermocouple positioned in the reaction vessel. A magnetic stirrer was installed to homogenize the solution chemistry and remove the slower diffusion control on reactions (Figure 40). The stirring bar of the stirrer is wrapped by a PEEK sleeve with two blades to reduce contamination from steel corrosion. To remove air from the system, nitrogen is flushed through the reactor for approximately 5 min before the reactor is sealed and pressurized to the desired pressure (2800 psi; 193 bar) by adjusting the pressure regulator on the N_2 tank. Meanwhile, the reactor was heated to 80°C. Pressure and temperature conditions representative of the Hosston Fm. in at the Devine Test Site is used in the experiments. Each experiment runs for 3 weeks.

The first aqueous sample was taken as baseline through the sampling port immediately after the rock and brine were loaded to the reaction vessel. The following aqueous samples were taken with decreasing frequency during the experiments. Approximately 2 ml of fluid was purged through the sampling port to remove the old fluid that was isolated in the sampling tubing. The purged fluid was set aside and used for pH measurement. After the purge, approximately 2 ml of fluid was collected and subsampled for analyses by IC, ICP, and carbon analyzer.

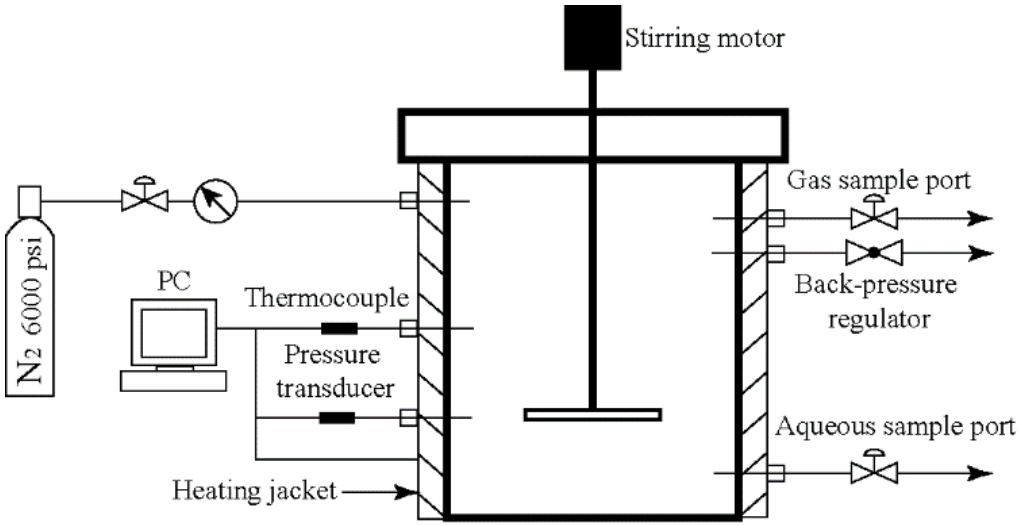

Figure 40. Schematic diagram of the autoclave system

Unreacted and reacted rock samples in the autoclave experiments will be analyzed using X-ray diffraction (XRD), mercury intrusion capillary pressure (MICP), and scanning electron microscopy (SEM) coupled with X-ray energy-dispersive spectroscopy (EDS) complemented by argon ion milling for sample preparation. SEM on ion-milled samples produces sharp images showing the topography of a microscopic surface, allowing the visual determination of mineralogy and texture. EDS gives the elemental composition of the surface of a sample and allows the creation of maps of elements of interest, for example, Fe or Ca distribution. Similar

sample preparation and analytical methods were used in previous studies (Lu et al., 2014, 2016a,b). For the completed experiment, SEM and aqueous chemical analyses have been conducted.

X-ray Diffraction

X-ray diffraction (XRD) mineral composition Bureau of Economic Geology has an advanced sample preparation system for bulk powders XRD analysis. The system includes a steel ball mill, a MicroNising Mill and a spray drier. The system is able to reduce rock powder size to less than 10 micron by means of wet grinding. The spray drier is used to produce randomly oriented powder samples for quantitative analysis. Department of GeoSciences of the University of Texas hosts a Bruker AXS D8 diffractometer for bulk sample quantitative analysis. Bruker's Eva software is used to identify mineral phases. Quantitative analysis is conducted using Topas 3, personal computer software based on the Rietveld method (Bish, 1994).

Scanning electron microscopy of ion-milled samples

For each experiment, a piece of unreacted shale shaped in a cuboid of approximately 10 × 8 × 5 mm in size is ion milled and examined by SEM. Unreacted samples were first polished by a triple ion beam miller (Leica EM TIC020) using an accelerating voltage of 8 kV, a current of 2.8 mA, and a milling time of 10 hr. The polished surfaces, perpendicular to the beddings, are shaped as shallow triangles of ~5 mm long and ~1 wide. Iridium is then sputtered on the ion-milled surfaces to create a conductive coating. Unreacted samples are examined by SEM with the aid of an X-ray EDS system. Secondary electron (SE) images, backscattered electron (BSE) images, and EDS elemental maps were obtained with location reference. Then, the coated surfaces were remilled using a broad ion beam miller (Leica EM TIC 3X) to remove the iridium coating. The uncoated sample is then placed in the reaction vessel with other core fragments (16 g in total) to react with the brine for 3 weeks.

After the reacted sample is retrieved from the reactor, the ion-milled sample is rinsed by DI water and dried overnight at 70°C. Iridium coating is applied again and SEM images are taken at the exact same areas as the prereaction images. By directly comparing the topography of the same areas of unreacted and reacted rock samples, we were able to identify mineral dissolution and precipitation that occurred during the reaction experiments.

Samples with iridium coating were examined on an FEI NovaNano SEM 430 using SE and BSE modes at an accelerating voltage of 10–15 kV and a working distance of 7–9.5 mm. X-ray EDS mapping was conducted using dual Bruker 30-mm^2 detectors. Mineral composition was documented by EDS maps in prereaction samples.

Fluid chemical analyses

Major cations and anions of water samples were analyzed on two Dionex ICS-1100 Ion Chromatography (IC) systems equipped with an Dionex AS-AP auto sampler. Aqueous samples from Exp. ME-A were diluted ~50 times for IC analysis. Trace elements were analyzed on an Agilent 7500ce quadrupole inductively coupled plasma mass spectrometer (ICP-MS). Samples for trace metals were diluted ~500 times with 2% HNO_3 immediately after collection. The pH was determined using an Orion 3-star pH meter and gel-filled pH/ATC Triode on ~2 mL purged water at room temperature and atmospheric pressure.

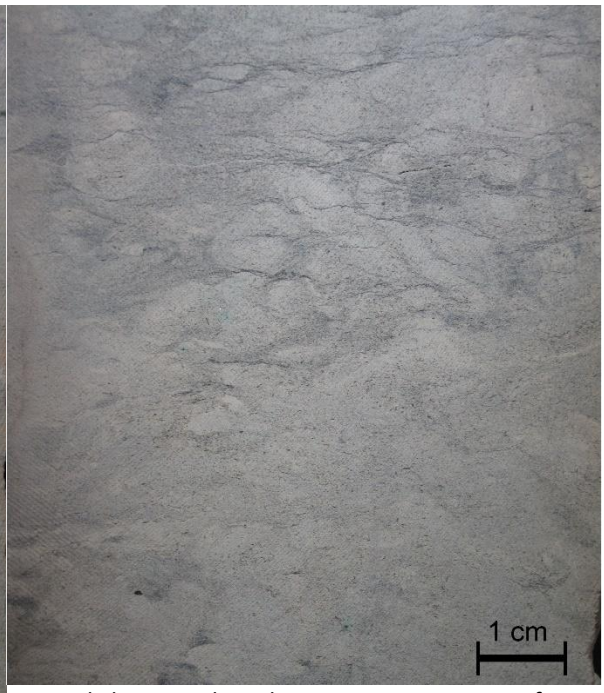

Intensely burrowed sandstone. Mercer #1, 4423 ft.

Laminated sandstone. Mercer #1, 4423 ft

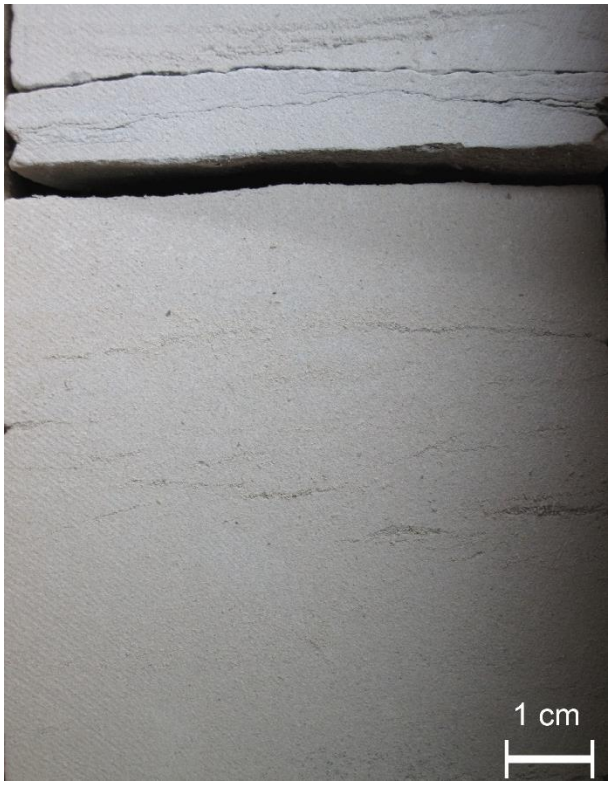

Weakly laminated sandstone. Mercer #1, 4410.7 ft.

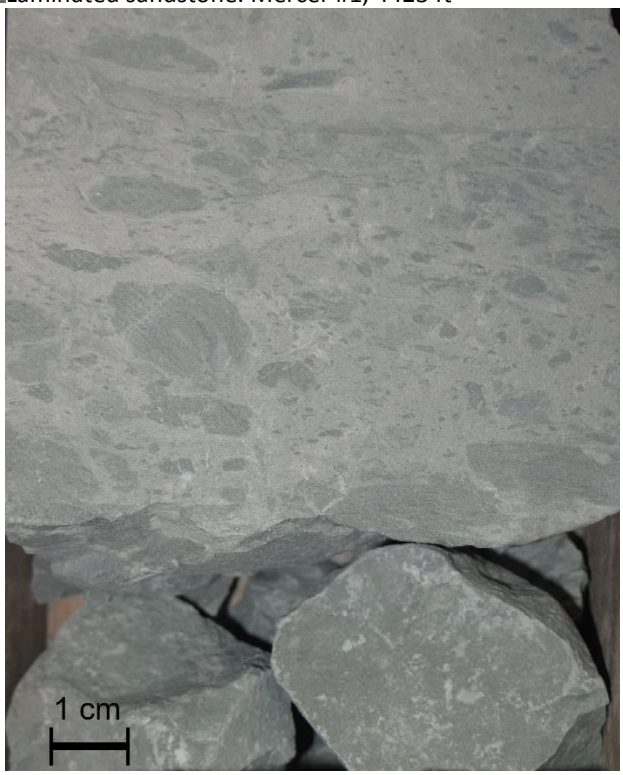

Sandstone containing abundant mud clasts. Mercer #1, 4337.7 ft

Figure 41. Photographs of major facies in Mercer #1 core, Caldwell County (Hosston Fm.)

II-4-2 Results

II-4-2.1 Core analysis

Wells in Medina and Frio County were rarely drilled to Hosston Formation and no Hosston core was found within these counties. The search area for Hosston cores was expanded to the nearby counties along the strike of the depositional setting. As a result, three Hosston cores at depth of 4000-5500 ft were found in Guadalupe and Caldwell County. One of them, Mercer #1 in Caldwell Co, was examined. It contains the top 150 ft of Hosston Formation of laminated and burrowed sandstones interbedded with mudstone (Figure 41). The core was described and three core sections were retrieved for further analyses and rock-brine reaction experiments. Additionally, thirteen core plugs have been drilled from the core for porosity and permeability measurements.

II-4-2.2 Rock-brine reaction experiments

To predict geochemical interactions caused by brine injection into the Hosston Formation, a series of autoclave experiments are being carried out under formation pressure and pressure. The main objective is to determine the impact of the geochemical reactions induced by brine injection into the Hosston formation rock. A Hosston core from Mercer #1 at 4394.7 ft was selected to react with brines. The experimental results will provide insights on the chemical interactions associated with brine injection and the potential impacts on rock properties. Besides using frequent aqueous chemical analyses to illustrate rock-water reactions, ion-milling technique is used to polish rock samples so that mineral dissolution/precipitation could be unequivocally observed by comparing the polished rock surfaces before and after the experiments using scanning electron microscopy (SEM). A total of four reaction experiments will be conducted with one completed and the second ongoing (Table 1).

Table 9. Conditions of autoclave reaction experiments

Experiment	Rock (g)	Brine (mL)	Brine composition	Pressure (psi)	Temperature (°C)	Status
ME-A	15.99	160	20,000 ppm NaCl	2800	80	Completed
ME-B	16.00	160	Eagle Ford formation water, salinity ~40,000 ppm			Ongoing
ME-C	16	160	50,000 ppm NaCl			Planned
ME-D	16	160	100,000 ppm NaCl			Planned

SEM of unreacted sample

The selected Hosston sample is a fine-grained sandstone with detrital grains primarily consisting of subangular quartz and small amounts of K-feldspar (Figure 42a-c). The authigenic components include dolomite, kaolinite, quartz overgrowth, and small amounts of anhydrite, titanium oxides, and pyrite. Dolomite occurs as euhedral and semi-euhedral cements often showing growth bands (Figure 42a-c). Kaolinite is the dominant pore-filling material and large portion of it appears to be authigenic (Figure 42a, 2c). Anhydrite is occasionally observed co-existing with pore-filling kaolinite and dolomite (Figure 42c).

The majority of the pores are remaining primary intergranular pores that are partially eliminated by cements (Figure 42). Figure 42d shows remaining interparticle pores of over 10 μm in size and intraparticle between clay platelets of microns in size. Dissolution of K-feldspar occurred during burial, producing some secondary porosity (Figure 42c).

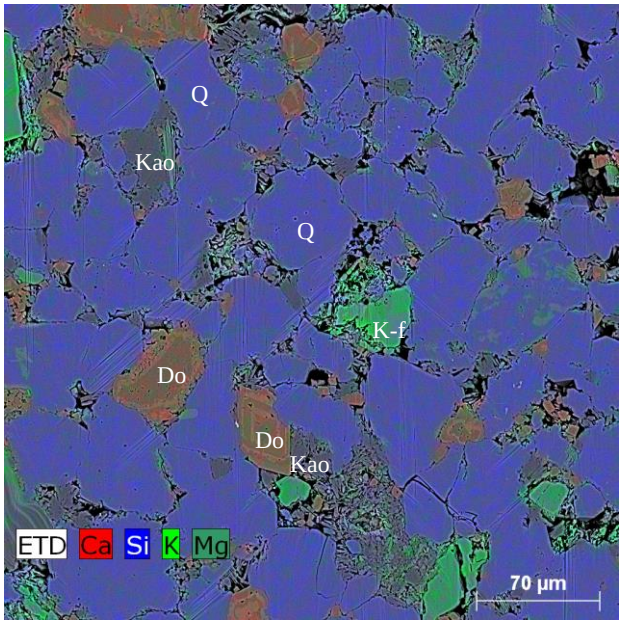

Fig. 2a. Fine-grained detrital grains of quartz (Q) and K-feldspar (K-f). Dolomite (Do) and kaolinite (Kao) largely eliminated primary pores. EDS map showing false color for elements. Unreacted sample.

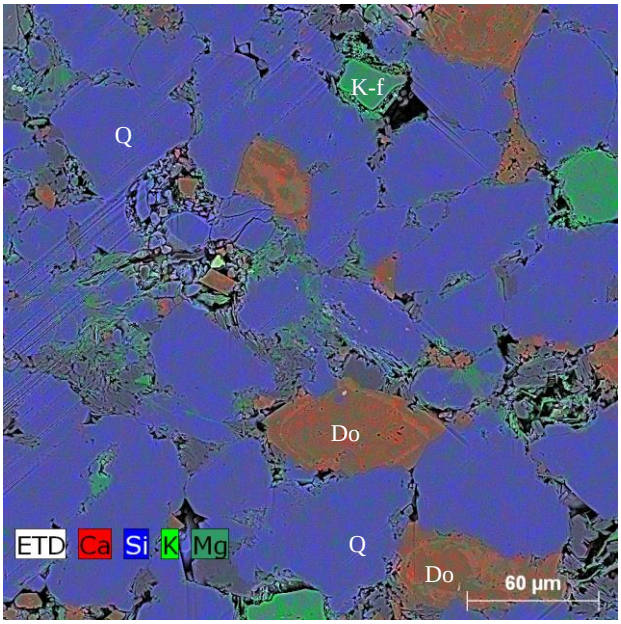

Fig. 2b. Semi-euhedral dolomite (Do) grains showing growth bands. Dark area = pore. EDS map showing false color for elements. Unreacted sample.

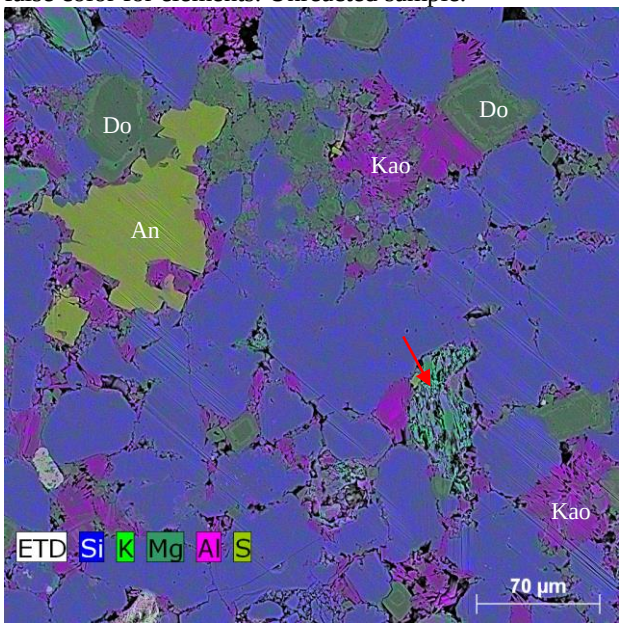

Fig. 1c. Intergranular pore space largely filled with kaolinite (Kao), dolomite (Do) and small amount of anhydrite (An). Partially dissolved K-feldspar (arrow) contains secondary pores. EDS map showing false color for elements. Unreacted sample.

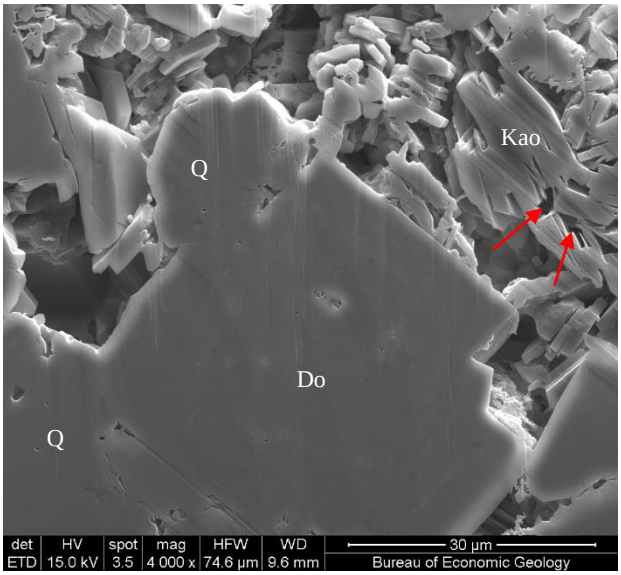

Fig. 1d. Remaining interparticle pore space surrounding authigenic minerals and micron sized intraparticle pores between clay platelets (arrows). SE image. Unreacted sample.

Figure 42. SEM of unreacted Hosston Fm. sample

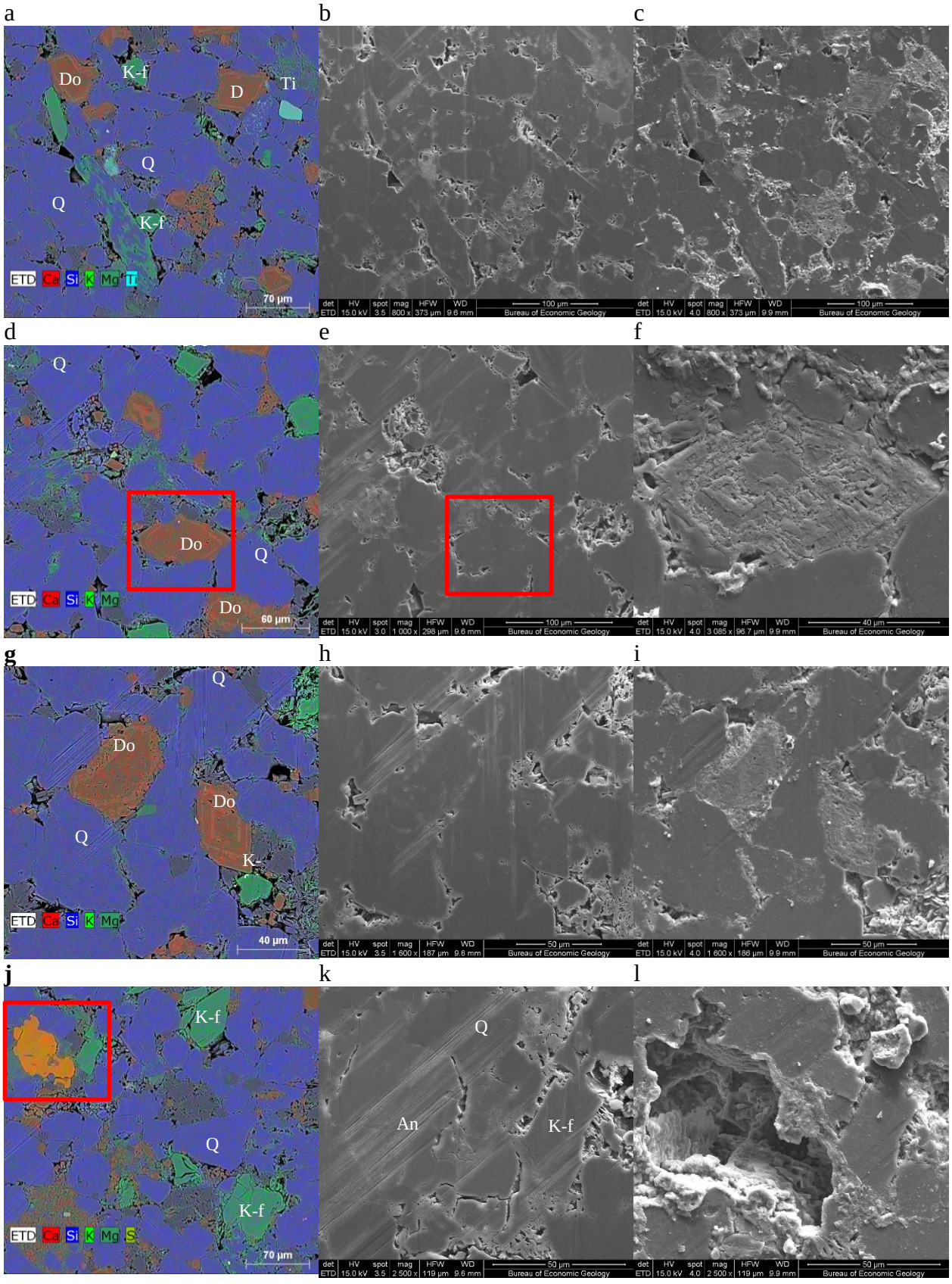
a
b
c
Do
K-f
D
Ti
Q
Q
K-f
ETD Ca Si K Mg Ti
70 µm
d
e
f
Q
Do
Q
Do
ETD Ca Si K Mg
60 µm
g
h
i
Q
Do
Do
Q
K-
ETD Ca Si K Mg
40 µm
j
k
l
K-f
Q
An
K-f
Q
K-f
ETD Ca Si K Mg S
70 µm

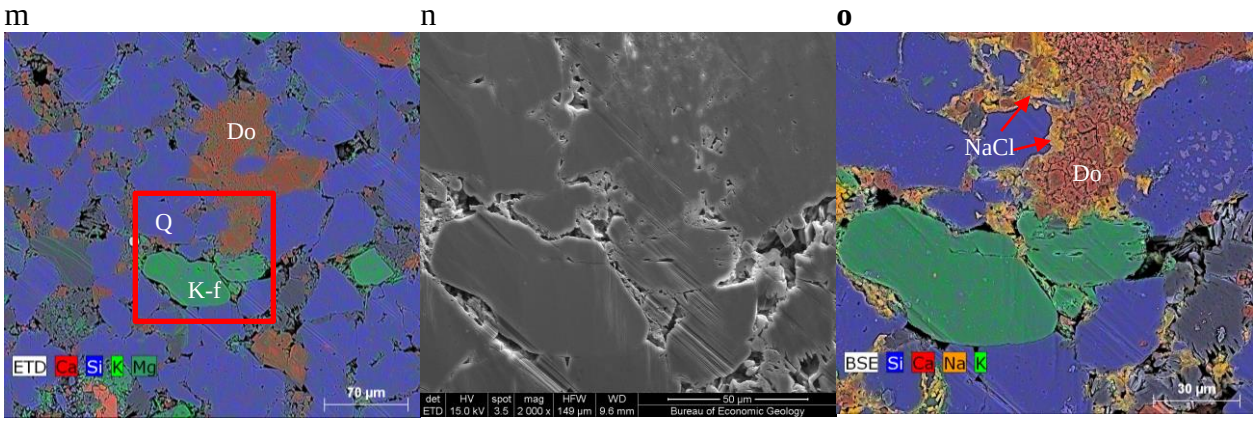

Note: Comparison of SEM images of the unreacted and reacted rock samples of Experiment ME-A. The first column contains EDS element maps of unreacted sample, second column SE images of unreacted sample, and the third column SE and EDS images of reacted sample. Red squares = area views of zoom in. Dolomite shows corroded surface while anhydrite show near total dissolution. NaCl formed on surface by drying of the remaining brine.

Figure 43. SEM of the reacted Hosston Fm. sample

SEM of reacted sample

On the reacted sample surface, SEM images were taken at the exact same areas that were imaged before the reaction experiments (Figure 43). Mineral dissolution and precipitation can be determined by comparing the images before and after reaction. The reacted surface was mildly corroded by the brine (Figure 43c). The most significant change is surface corrosion of dolomite and total dissolution of anhydrite (Figure 43l). All dolomite grains were corroded showing densely distributed grooves and holes on surface, but the major parts of the grains survived the reaction (Figure 43f,i). Micritic dolomite show up the assemblage of sub-micron crystals after reaction (Figure 43o). Little dissolution occurred to quartz and K-feldspar whose ion-milled surfaces remained intact (Figure 43f,o). Anhydrite grains were completely dissolved forming large moldic pores (Figure 43l). Trace amount of clays may have precipitated as submicron sized particles are observed on otherwise smooth detrital grains (Figure 44). However, their small size prevented from effective chemical analysis. The large pieces of the particles added to the mineral surface (several micron in size) in Figure 44 show chemical composition of clays by EDS analysis. Note that small rock fragments can be mobilized by stirring and physically transported to the observation area, therefore caution needs to be taken to determine whether these particles were newly precipitated during the experiment.

Salt crystals are observed on the reacted surface and they precipitated mostly along grain boundaries (Figure 44o). The majority of the newly formed salt is sodium chlorite. These salts were formed by evaporating remaining brine in the pores. The reacted sample was rinsed by and soaked in DI water for 5 mins, but apparently, some reaction brine remained in the pores.

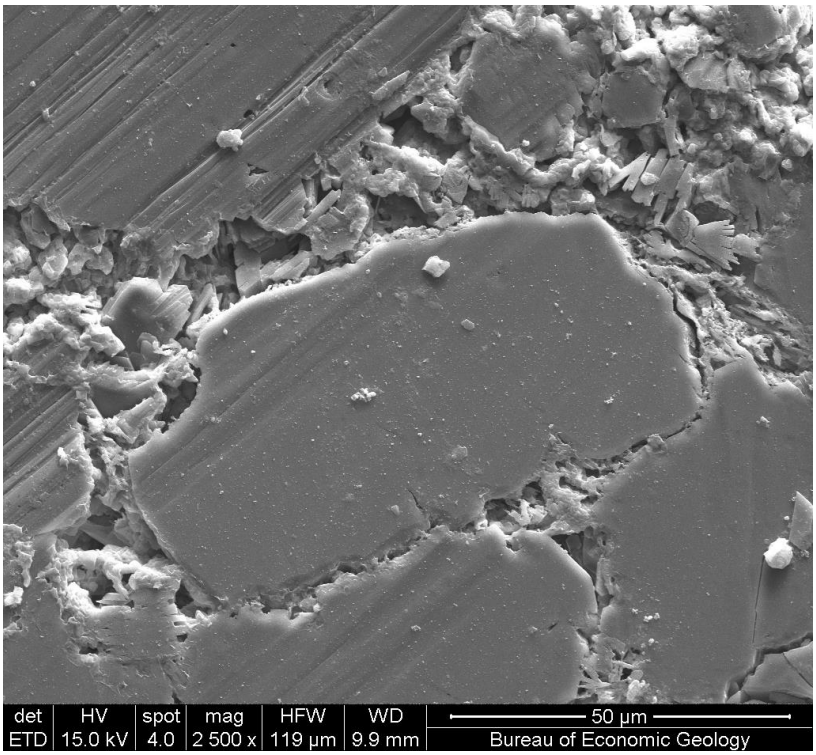

Figure 44. SE image of reacted rock samples of Experiment ME-A showing submicron particles formed on mineral surfaces during experiment.

II-4-2.3 Aqueous Geochemistry

In total, 16 aqueous samples were taken and analyzed for experiment ME-A. The chemical evolution of the reaction brine, shown in Figure 45, display modest changes. The changes in aqueous chemistry are generally in agreement with SEM observations. In the reaction solution, releases of Ca, SO_4, Si, Mg, K and Sr are the most significant changes. Ca and SO_4 concentrations showed the largest increases to 277 ppm and 575 ppm, followed by Si, Mg, K, Sr, and Mn. Other ions show smaller or negligible changes. The trend of SO_4 concentration with time is similar to that of Ca, with their final concentrations reaching 6.0 and 6.9 mmol/L, respectively. When plotted against each other, molar concentrations of Ca and SO_4 show a linear correlation close to 1:1 line (with slightly higher Ca concentration), indicating that the major source of these ion is calcium sulfate (Figure 46). Dissolution of anhydrite is observed at the reaction surface by SEM which showing large moldic pores formed from total dissolution of anhydrite (Figure 43l). All analytical results and plots are given in Appendix B: Results of Autoclave Experiments (Section XI).

Dolomite dissolution, as surface corrosion observed by SEM, supplied Mg and Ca in the solution. Final Mg concentration in the reaction brine is ~0.5 mmol/L. A similar amount of Ca should be released from dolomite dissolution, an additional source of Ca, but it only amounts to 1/14 of the amount sourced from anhydrite. Sr, Mn and Ba are also usually associated with carbonates, in this case, dolomite.

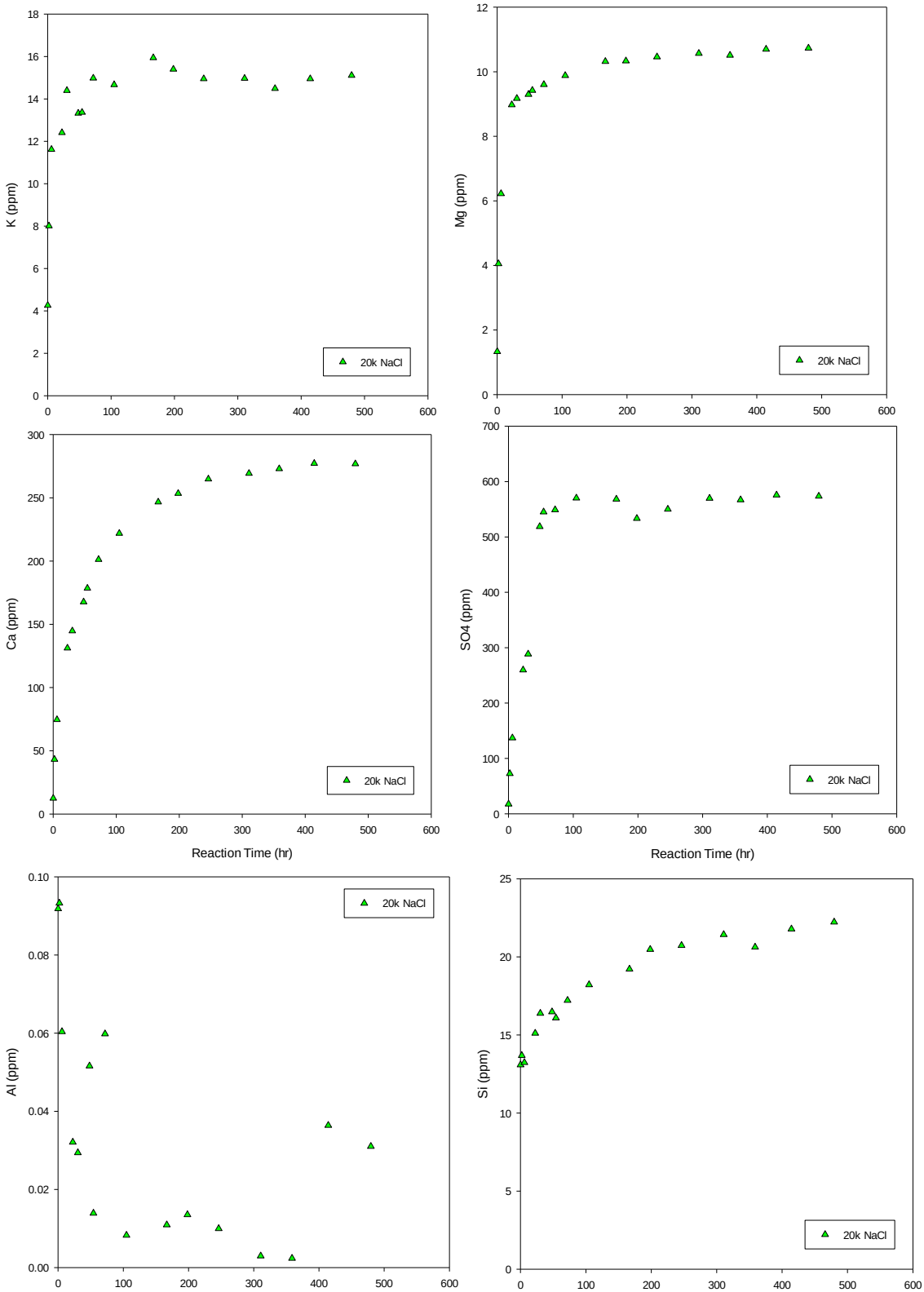

Figure 45. Changes of concentration with time of the components showing largest increase in experiment ME-A. (continued)

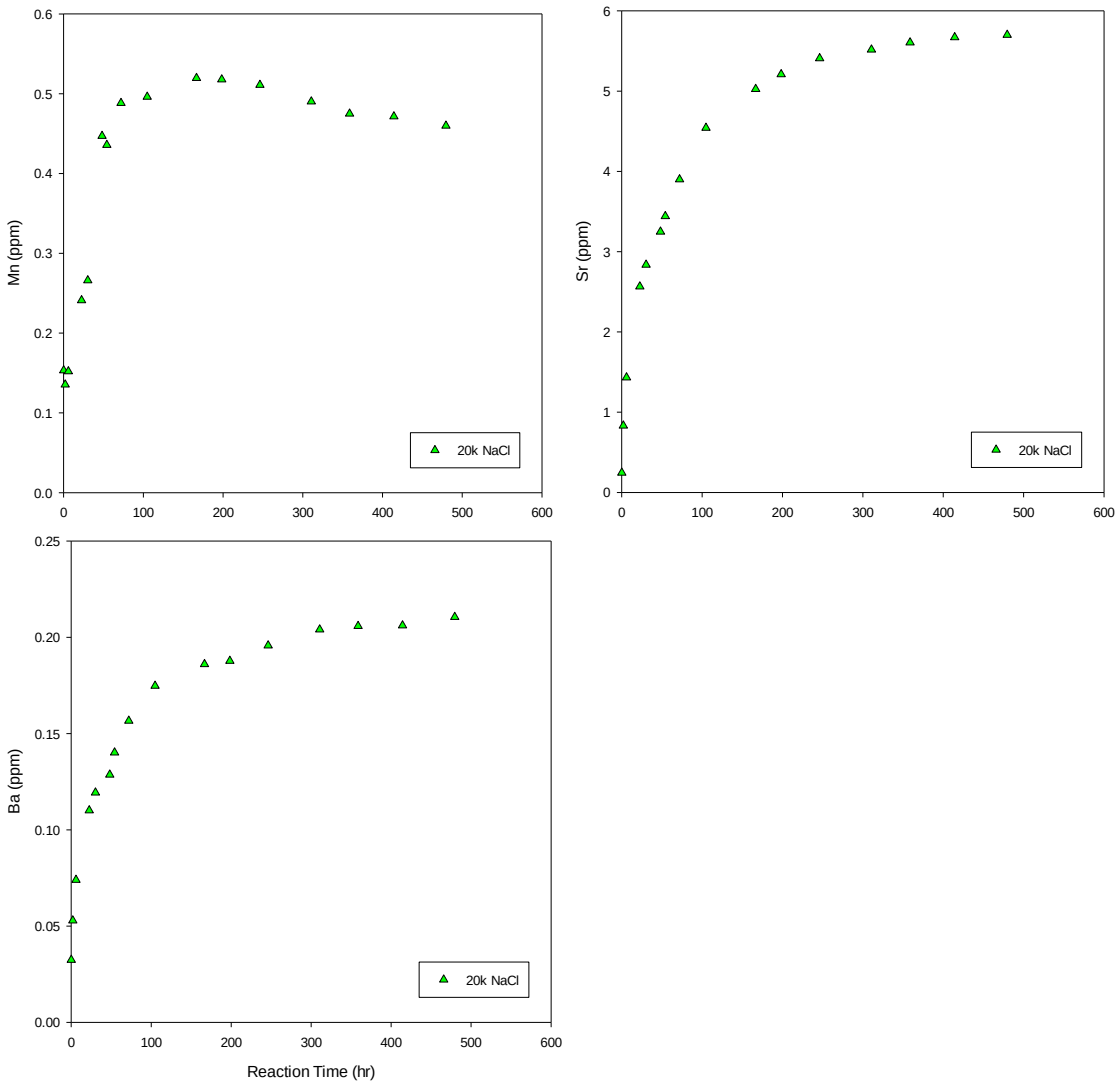

Note: Sulfate was analyzed by IC. All others analyzed by ICP-MS.

Figure 45. Changes of concentration with time of the components showing largest increase in experiment ME-A.

Dissolution of K-feldspar releases K and Si to the reaction solution. Though little evidence of K-feldspar dissolution was observed by SEM, K and Si show increasing concentrations to 15 ppm and 22 ppm in the brine, indicating a small of K-feldspar was dissolved.

There are two possible dissolution reactions of K-feldspar:

$$3KAlSi_3O_8 + 2CO_2 + 2H_2O \rightarrow KAl_2(AlSi_3O_{10})(OH)_2 \text{ (illite)} + 6SiO_2 + 2K^+ + 2HCO_3^- \quad (1)$$

$$2KAlSi_3O_8 + 2CO_2 + 3H_2O \rightarrow Al_2Si_2O_5(OH)_4 + 4SiO_2 + 2K^+ + 2HCO_3^- \quad (2)$$

These reactions produce different Si/K ratios: 3 if illite forms, and 2 if kaolinite forms. There is a relatively poor correlation between Si and K with time, but the final solution shows a Si/K ratio of near 2:1, indicating that Reaction 2 was the dominant reaction pathway (Figure 46).

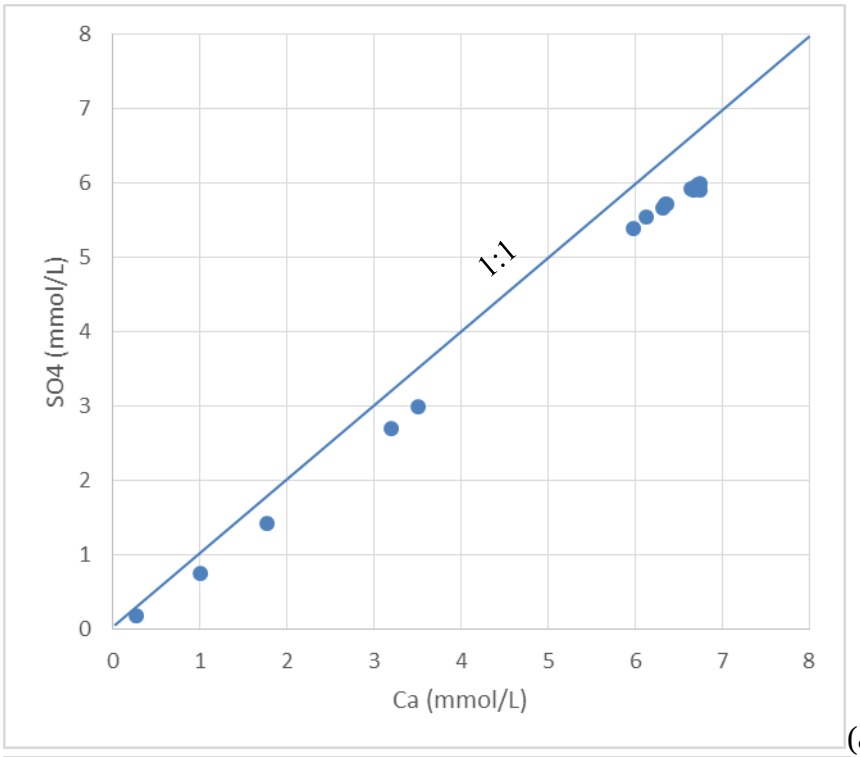

(a)

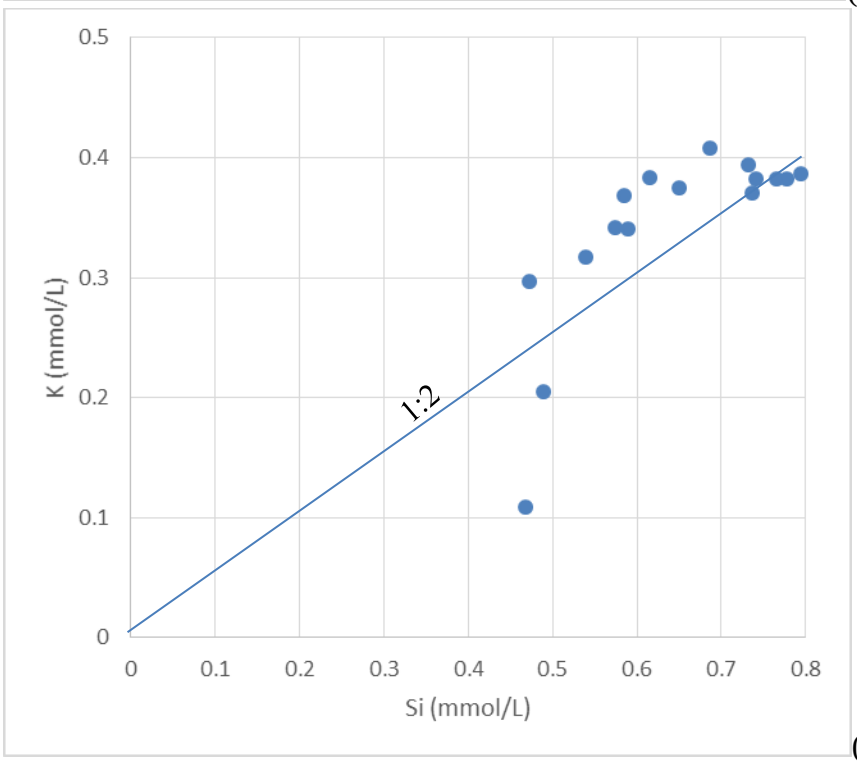

(b)

Note: Ca and SO_4 showing a near 1:1 correlation with slightly higher Ca concentrations. K and Si shows a relatively poor correlation with the final ration of 1:2.

Figure 46. Plots of Ca vs SO_4 and K vs. Si mole concentrations in the reaction brine.

III. Pressure Management Plans

III-1. Introduction

A critical issue for saline CO_2 storage projects is build-up of pressure caused by CO_2 injection. Within the context of CO_2 geological storage, excessive pressure buildup is undesirable because it creates a set of problems but that pressure management through brine extraction could solve (Figure 47).

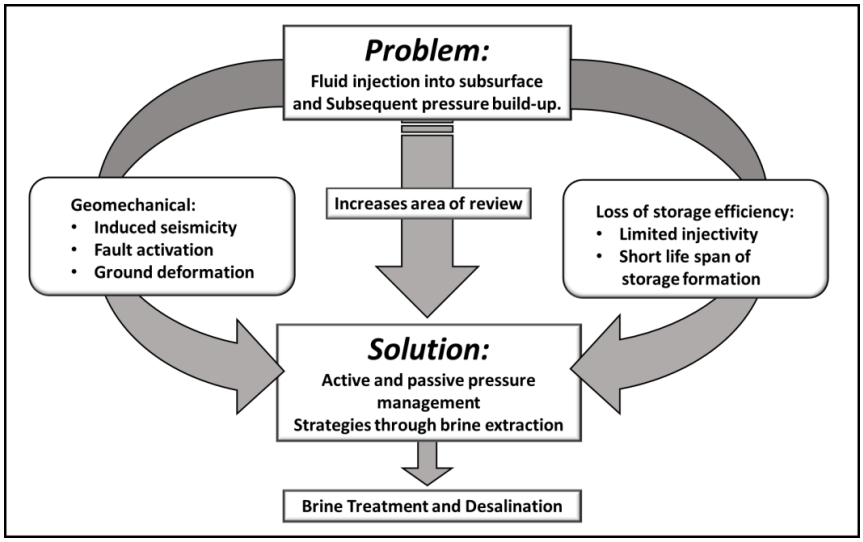

Note: Extracted brine through this process can be fed into brine treatment and desalination units for water recovery.

Figure 47. Pressure management through brine extraction can solve many of the problems associated with injection of CO_2 for geological storage.

Pressure management and plume control through brine extraction has been a topic of several studies in recent years (Flett et al., 2008; Bandilla et al., 2012; Buscheck et al., 2011, 2014; Liu et al., 2015). However, most of these studies are based on modeling analyses with minimal field tests to assess or demonstrate specific issues related to brine extraction technologies. The Gorgon project in Barrow Island off the western coast of Australia is one of the few studies with a field component, including eight injection wells and four extraction wells; however, it has not been initiated and is not expected to begin until 2016 (Flett et al., 2008; MIT 2011).

On the modeling side, brine extraction in the majority of cases has been shown to increase the storage capacity by up to several hundred percent depending on geology and structure of the storage formation. For example, numerical modeling of theoretical scenarios at the Ketzin pilot site in Germany, Zama F pool site in Canada, Gorgon site in Australia, and Teapot Dome site in the U.S. shows that storage capacity could be increased by 4 to 1300% and that the ratio of the increased CO_2 storage capacity to water extraction varies from 13:1 to 1:0.4. In all scenarios, water extraction reduced the maximum reservoir pressures by ~10-20% during injection (Liu et al., 2015). Our own previous modeling studies on brine extraction showed that CO_2 injection combined with brine extraction increased storage capacity by about 100% when reservoir pressure is appropriately managed (Hosseini and Nicot, 2012).

In addition to storage capacity, other parameters can affect the performance of the brine extraction strategies, such as reservoir size, well pattern, injection rate, reservoir heterogeneity, anisotropy ratio, and permeability sequence (Yang et al., 2014). Uncertainty in formation parameters, especially heterogeneity, is important to consider when trying to minimize the number of required extraction wells (Dempsey et al., 2015). This shows that prior formation characterization is an important step for designing and planning the appropriate brine extraction and pressure management and plume control strategies.

Previous studies have also compared Active CO_2 Reservoir Management (ACRM) with Passive CO_2 Reservoir Management (PCRM) using modeling analyses. These studies show that if the net extracted volume of brine is equal to the injected CO_2 volume, pressure buildup is minimized, greatly reducing the Area of Review, risk of seal degradation, fault activation, and induced seismicity (Buscheck et al., 2011).

The brine extraction strategy can be used to inject large amounts of CO_2 in a storage formation with no excessive increase in reservoir pressure. This strategy relies on the strategic placement of brine production wells to create negative pressure gradients. For example in one study, a multi-stage, square-ring well configuration is envisaged, in which brine production wells are repurposed for CO_2 injection upon CO_2 breakthrough, and the next concentric ring of production wells is installed at a greater distance. Numerical simulations show that long-term mass production of brine is almost two times the volume of CO_2 sequestered (Dempsey et al., 2014).

Extraction wells can also be used as injection wells after CO_2 breakthrough in the well. Dual-mode wells are initially used to extract formation brine and subsequently used to inject CO_2. The relationship between pressure drawdown during pre-injection brine extraction and pressure buildup during CO_2 injection directly informs reservoir managers about CO_2 storage capacity (Buscheck et al., 2014).

Brine extraction can be optimized (extraction volume and location of extraction) to meet local (not global) performance criteria (i.e., the goal is to limit pressure increases primarily where environmental impact is a concern). Results of another modeling study suggest that strategic well placement and optimization of extraction may allow a significant reduction in the brine extraction volumes (Birkholzer et al., 2012). Also similar methods can be used to estimate optimal rates and locations for CO_2 injection and brine extraction wells while simultaneously satisfying multiple pressure buildup constraints to avoid fault activation and caprock fracturing (Cihan et al., 2014).

Pressure differential is defined as the difference between initial pressure at a point in the subsurface (before injection) and pressure at the same point after injection starts. For monitoring of pressure differentials in the formation some studies have used a time-lapse seismic approach to monitor and map pressure and saturation fronts (Osdal et al., 2006; Tura and Lumley, 2000) but this approach has some limitations which need to be quantified for any specific site and formation (Landrø et al., 2001). The cost of collecting 4D seismic surveys has proven to be prohibitive for this pilot project. Another challenge in using 4D seismic data in monitoring pressure is that typically it is difficult to discriminate between pressure and fluid saturation changes (Landrø, 2000) but for this proposed study, because we are dealing with single phase flow (water of various salinities), distinguishing between pressure and fluid saturation changes is not a problem.

This cursory literature review suggests that brine extraction is a promising technique to alleviate pressure buildup but also reveals the large gap in field demonstration studies on pressure management and plume control studies that should be filled with this proposed study.

III-2. Proposed Pressure Management Plans

Our proposed active pressure management and plume control strategies and monitoring methods (tracers, pressure transient analyses, and microseismic surveys) are based on current commercial and emerging capabilities of the industry. We are not proposing to design or develop new instrumentation or tools and all the proposed tools and methodologies are well established or have already been used in in a field environment; therefore, industry should have no apprehensions about applying these methodologies at a commercial scale. Our main monitoring and measuring tools includes pressure and temperature gauges and application of pressure transient analysis (PTA) on collected data, application of common (dye) and smart (magnetic nanoparticles) to monitoring the plume steering capabilities of the brine extraction strategy. Our initial modeling studies demonstrate the possibility of using perforations in multiple zones to accommodate passive pressure management and plume control strategies. Passive pressure management strategies (in which extracted brine will be directly directed to other zones without being produced to surface) are less effective compared to active management strategies.

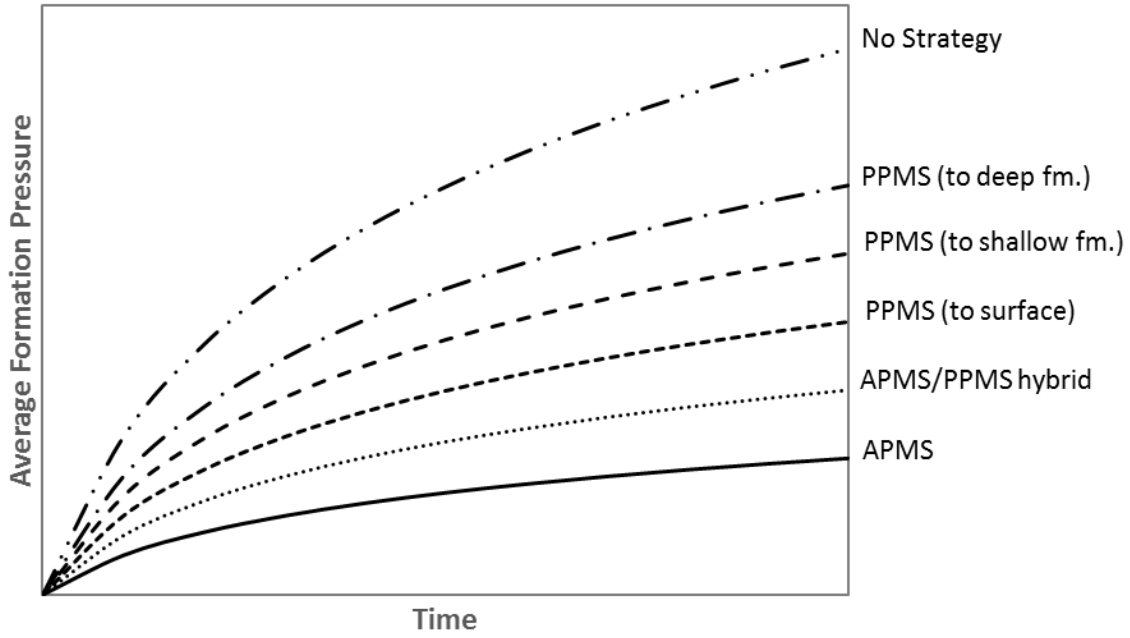

Note: Only active pressure management strategy will be deployed in Phase II as it is the most effective method to control the pressure plume differentials.

Figure 48. Envisioned effectiveness of active and passive (multiple scenarios) pressure management strategies in controlling pressure in the storage zone.

For passive scenarios as pressure in the storage formation increases, brine will flow into the extraction well and surface facility (passive control to surface). If the extraction well is choked at the surface and the well is perforated in another formation (disposal formation could be deeper or shallower than the storage formation), then excess brine will passively flow to that zone. Hybrid scenarios that combine active and passive strategies are also possible. Figure 48 illustrates the

effectiveness of different pressure management strategies in controlling the average reservoir pressure over time. Extra costs and risks associated with deploying passive pressure management strategies led us to remove this option, which we proposed in Phase I, from the Phase II implementation plan. In Phase II studies and operations, we will focus and operate only the active pressure management strategy.

In this project we are proposing to inject brine and extract brine, that is, fluids maybe of various salinities and ionic makeup but miscible in any proportion. It follows that all the fundamental engineering principles, such as Theis solution for pressure diffusion analysis and superposition theory for analysis of multi-well injection/extraction, will be applicable with minimal assumptions required. It is also notable that no relative permeability or capillary pressure issues in this single-phase flow test will confuse the results. This will significantly increase our confidence in interpretation of the pressure data. Based on well-established theory of fluid flow in porous media, injection of fluids into a formation will increase the pressure around the injection well while extraction of fluids will decrease the pressure in a quantitatively predictive fashion. Depending on volumes injected and extracted, distances between injection and extraction points and statistical and structural properties of the formation, optimal strategies can be developed to extract volumes of brine at specific locations around the injection sites to manage the pressure buildup in the formation. Figure 49 shows a schematic of our design with multiple wells assigned as injector, extractor and observation wells. Figure 50 shows technical construction details of the planned wells.

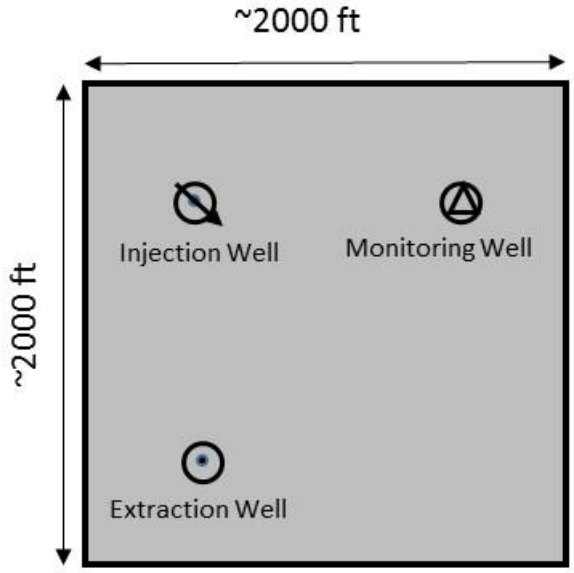

Note: As an example, considering the above design, comparing the pressure response in an observation well would help understanding how an extraction well placed between the injection and observation wells could help in managing the pressure in the observation well. Location and number of wells are generalized and distances are not to scale.

Figure 49. Schematic of the pressure management and plume control strategy plans.

For this project we are proposing to drill three wells (one injection, one extraction and one observation) to depth of 7000 ft at the DTS to the Hosston Formation. We are proposing to drill these wells on the apexes of an equilateral triangle with ~50-m sides. Based on our modeling studies, this setup would provide the best possible scenario to evaluate the brine extraction

capability in managing the pressure at a location of interest (in this case our observation well). In this project the observation well is assumed to be the risk point where we are trying to control the pressure. By comparing the pressure data in a monitoring location with and without brine extraction we will evaluate the capability of this system in pressure management. In addition, by using multiple tracers we will evaluate the performance of the system in steering the plume away from the observation well. We will test this system with varying the volume of extracted fluid and analyze the diffusion of pressure harmonics into the formation. We will use the same set of data to refine our characterization and modeling studies and to assess the level of heterogeneity in the formation (Serrano, 1996; Leven and Dietrich, 2006). Our trainable setup would maximize our capability to understand the effect of heterogeneity by having measurement point in two different direction from injection well (vs. having a linear system for three wells which will have a higher chance in failure to control the pressure differentials as well as completely missing the tracer flow direction within the time frame of this study).

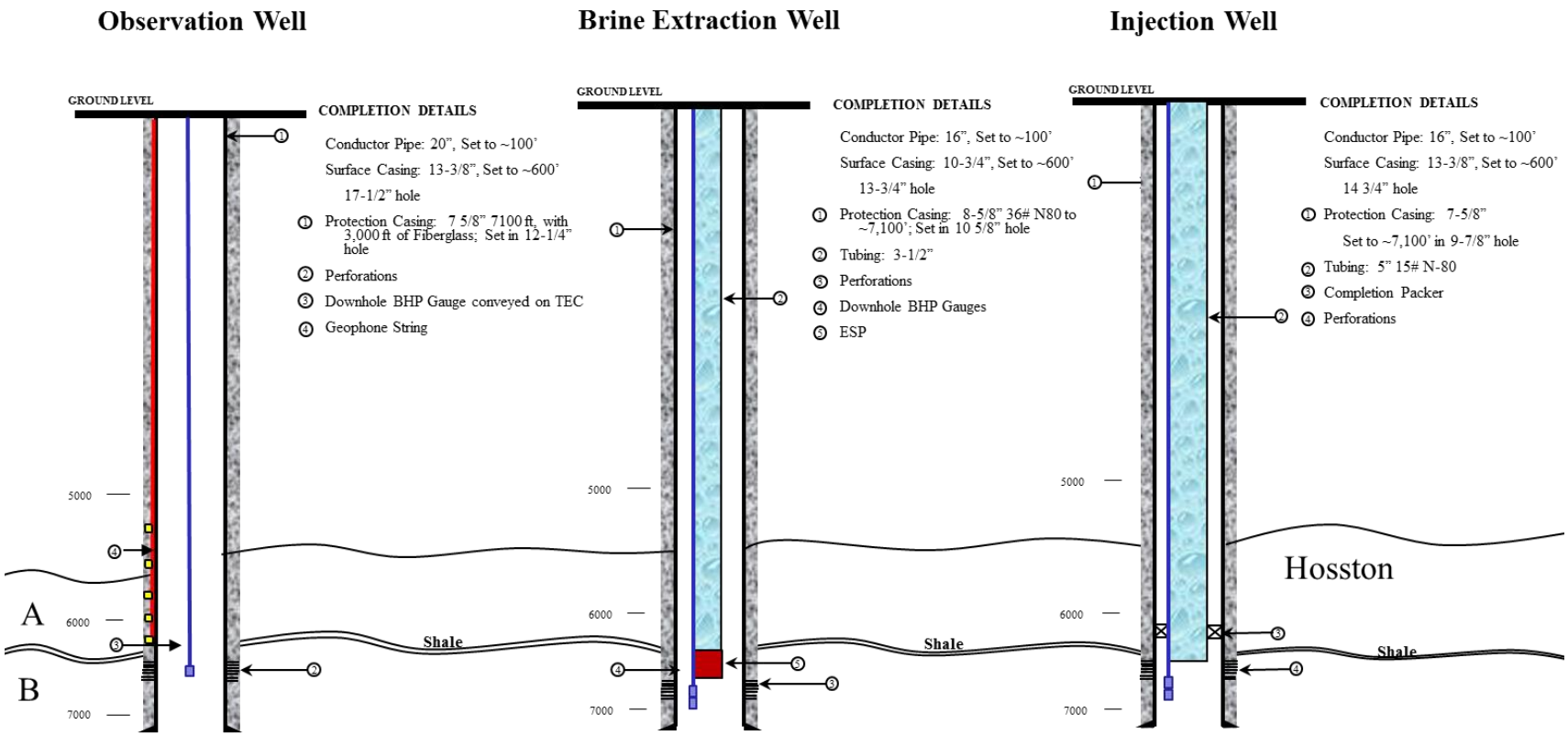

Design by GEOSTOCK SANDIA

Figure 50. Design of injection, extraction, and observation wells

IV. Monitoring, Verification and Accounting Plans

The main objective of the project is to manage the pressure and control the plume through brine extraction and also to use the extracted brine test bed brine treatment technologies. This objective stems from the fact that addressing risks related to CO_2 injection will play a crucial role in determining whether industry and other end-users will adopt geological storage of CO_2. Pressure buildup and its potential geological risks of destabilizing confining systems, plugged and abandoned wells, and local and regional faults represents a very important acceptance feature. In addition, industry and other end-users are interested in knowing whether they can optimize the value of the pore space they have acquired, i.e., store more CO_2 while still using the same surface facility. Liability in the area that they are injecting is also critical to the industry. This area (Area of Review or AoR) could be much larger if pressure buildup is not controlled than what the industry would be willing to be accountable for. Monitoring, Verification and Accounting (MVA) plans proposed in this study are designed to demonstrate capabilities and limits of pressure management through brine extraction in alleviating most of these concerns.

All the elements discussed below will be analyzed under two scenarios, with and without brine extraction, to quantify the value added of brine extraction in pressure management and plume control in the subsurface. MVA plans will be tied closely to our modeling efforts (because collected data needs to be modeled and analyzed) and the modeling section of this report presents more details on our studies regarding this topic. Our MVA plans consists of following items:

- SCADA system

  SCADA system will be in place to record all data and provide a centralized system to record and monitor the collected field data including the flowrates, bottom hole pressure and temperature for all three wells. BEG and Geostock Sandia teams have used a similar system to collect data at the SECARB Cranfield deep storage project. Pressure and temperature gauges and flow meters will be connected to the system which will be accessible through the internet.

- Installation of flow meters

  Flow meters will be installed at key points in the system to provide necessary information on the volumes of fluids produced and injected and volumes transferred to the desalination unit. This data will be central for accounting of the volumes and will feed to LCA analysis of the brine too.

- Installation of bottom hole pressure and temperature gauges

  All three wells will be equipped with commercial pressure and temperature gauges and will be connected to the SCADA system for continuous monitoring. Data collected from these pressure gauges will be central to the monitoring program and evaluation of the pressure plume in two different direction (observation and production wells will not be aligned but drilled to maximize 2D coverage). Data collected from these gauges will be used to verify and refine the modeling studies.

- • Installation of 6 surface seismometers in addition to 5-level downhole geophone array

  Six three-component near-surface seismometers will be installed and operated throughout the project operating period. These instruments will detect any seismic energy at the

ground surface, addressing public concerns about subsurface injection and detectability thresholds. In addition, a five-level downhole geophone array will be installed near the injection interval in the observation well. Data collected using the surface and subsurface arrays will be analyzed along with the collected down hole pressure data from the three wells (injection, observation and extraction wells) to understand the capabilities and limits of this system to detect the pressure perturbations (Meckel et al., 2013). It is anticipated that the subsurface array will provide data for tracking the extent and temporal evolution of the pressure plume (triggering front; Shapiro and Dinske, 2009), maximum event magnitude probabilities (Shapiro et al., 2007), as well as in-situ transport properties (seismicity-based reservoir characterization; Shapiro, 2000). Standard geophysical well log suites will be used to determine the geomechanical properties and stress state of the rocks at the target formation, allowing for an integrated study of the interrelationship between pore pressure variability and observed microseismic events during the periods of pressure variation in formation.

- Common and smart magnetic nanoparticle tracers

  Tracers have been used extensively to monitor fluid movement in geological formations (Hyndman et al., 1994). We will integrate all the static data obtained from formation characterization, along with pressure transient analysis (PTA) results and tracer results to update our predictive models based on routine history matching practices (Hosseini et al., 2013; Rubin et al., 1992). Electromagnetics (EM) provide the ability to track injected fluids in reservoirs (magnetic nanoparticle tracer).

  We plan to use both common (dyes) tracers and magnetic nanoparticles to track and image the plume within the injection formation. Magnetic nanoparticles can be imaged using electromagnetic cross well logging between the observation well (fiber glass casing) and production well. Thanks to the nanoparticles, there can be large differences in electromagnetic properties between injected and resident fluids. Engineering injectants with stable suspensions of magnetic nanoparticles to generate contrast in electrical conductivity will be injected during the operation period. Interwell plume images resulting from inversion of EM logs and breakthrough times collected from tracer tests with extraction and without extraction will help to understand the capability of brine extraction scenario to manipulate and control the pressure as well as the plume of injected fluid itself.

- Modeling studies

  As part of our verification efforts we will use modeling studies on various items mentioned above including modeling microseismic events, forward and inverse modeling for tracer analysis, forward and history matching modeling for fluid flow analysis and geomechanical modeling to understand the interaction between increase/decrease of pore pressure and any recorded micro seismic event in the site. One objective of the proposed study is to show how modeling tools perform in predicting the pressure plume differentials and find, explain, and address the possible gaps. Application of pressure harmonics specifically will be helpful to verify both numerical and analytical modeling methods applications in predicting the extent of the pressure diffusion in the formation.

V. Modeling Results

In this section, we discuss modeling studies related to Phase I and to Phase II future field work: (1) modeling of water injection and extraction and pressure evolution; (2) modeling of tracer studies to help in the mapping of the injected plume (contrast in TDS and ionic makeup); (3) modeling of fluid pressure and impact on seismic waves from an active source (not implemented in Phase II); and (4) modeling of harmonic pulse test that would be performed at the site to collect bulk fluid properties.

V-1. Model Description and Pressure Management Scenarios

The objective of this modeling study is to use brine extraction wells to manage formation pressures as well as plume movement for future saline CO_2 projects. The simulation study was performed using the CMG-STARS simulator and the model include three wells (injection, extraction, observation). We are proposing to test active brine extraction wells (i.e. pumps at the surface, active pressure management system, APMS). We have shown previously that passive pressure management strategies are not as effective as active pressure management strategies (see Appendix C: Preliminary Results of Brine Extraction Modeling, Section XII for details). In APMS, brine is actively extracted using pumps at the surface. The potential benefits of employing brine extraction wells include increased storage capacity, reduced stress on the sealing formation, and reduced risk of brine and CO_2 plume movement into unwanted formations. Evaluation of these benefits through predictive modeling studies and field scale projects should demonstrate the reliability of permanent geological storage of CO_2 to industry and other end-users. In this section we analyze pressure management strategies for different scenarios.

A Cartesian model was set up to simulate different pressure management scenarios with constant rate brine injection and constant rate extraction for different homogeneous and heterogeneous cases. The Devine Test Site area is represented by coarse gridblocks in a 400×400 m^2 domain. The size of gridblocks was uniform 2×2 m in the horizontal directions. The model includes three main formations with the Hosston Fm. as the lowermost one. It is 10 m thickness and subdivided into 5 layers each of 2-m thick (layers 3-7). The Hosston Fm. is a siliciclastic rock containing a ~50,000 mg/L brine as suggested by early readings of geophysical logs. Three wells (injection, extraction, and observation) are completed in the Hosston Fm. at a depth of 6500 ft and the distance between wells is ~45 m. The other overlying formations are each modeled with one layer. To capture the heterogeneity of the injection formation different heterogeneous permeability distributions were used beside the homogeneous case (Figure 51). Table 10 reproduces the input data including model properties used for the simulations. Two different configurations of linear and triangular well pattern designs as shown in Figure 52 were used. The main metrics to compare scenarios are bottom hole pressures (BHP) and the tracer breakthrough time at the observation and extraction wells.

Several simulations were performed for each homogeneous and heterogeneous cases to study the impact of injection design and reservoir properties. The extraction scenarios are summarized as follows: (1) Base Case (No Extraction): Brine was injected at constant rate of 5000 bbl/day for 90 days and the extraction well was shut in; and (2) Active Extraction from the Hosston Fm. (Constant Rate Production): Brine was injected at constant rate of 5000 bbl/day for 90 days and the extraction well was produced at a constant rate of 2500 bbl/day.

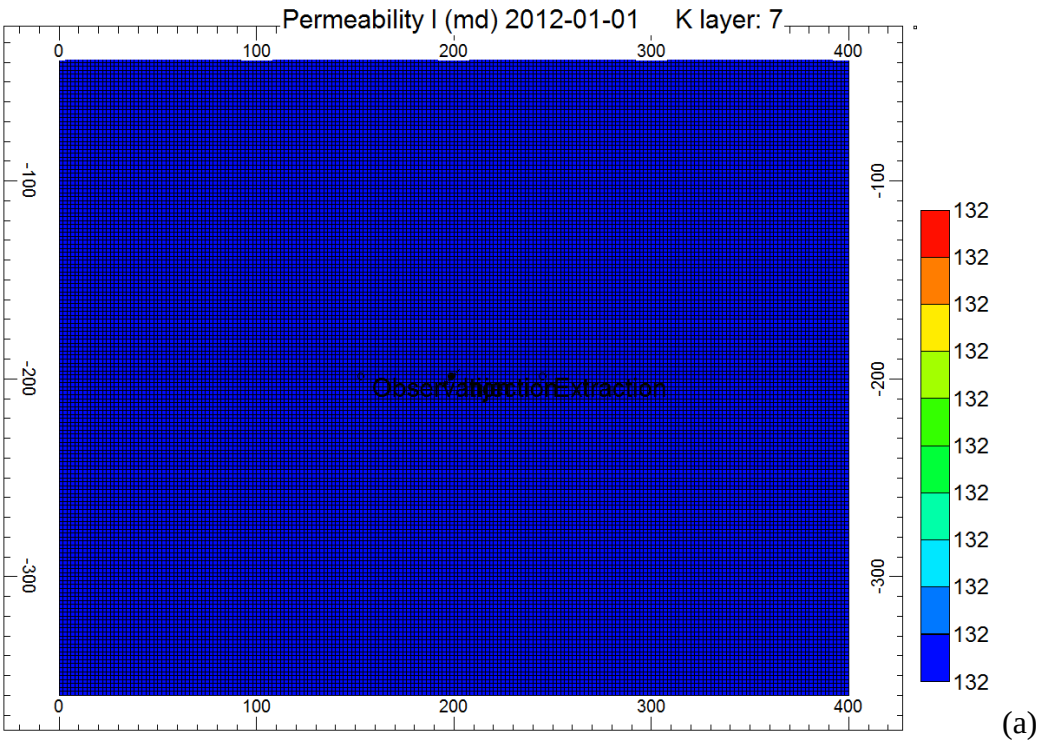
Permeability I (md) 2012-01-01 K layer: 7
0
100
200
300
400
-100
-200
-300
Observation
Injection
Extraction
132
132
132
132
132
132
132
132
132
132

(a)

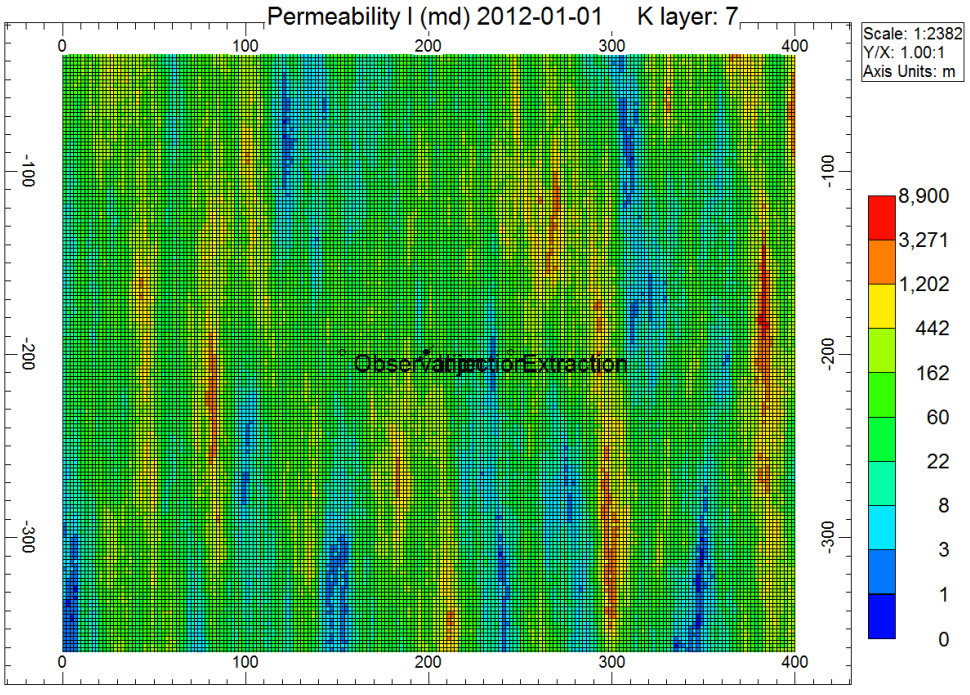
Permeability I (md) 2012-01-01 K layer: 7
Scale: 1:2382
Y/X: 1.00:1
Axis Units: m
0
100
200
300
400
-100
-200
-300
Observation
Injection
Extraction
8,900
3,271
1,202
442
162
60
22
8
3
1
0

(b)

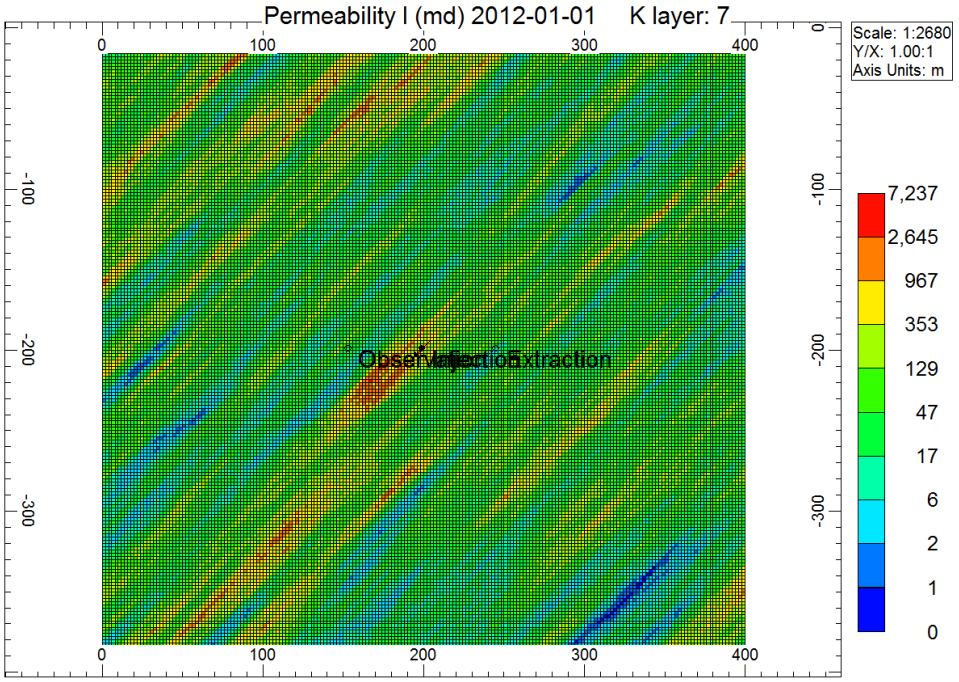

Figure 51. Permeability distribution for homogeneous case 1 (a), heterogeneous case 2 (b), case 3 (c), and case 4 (d).

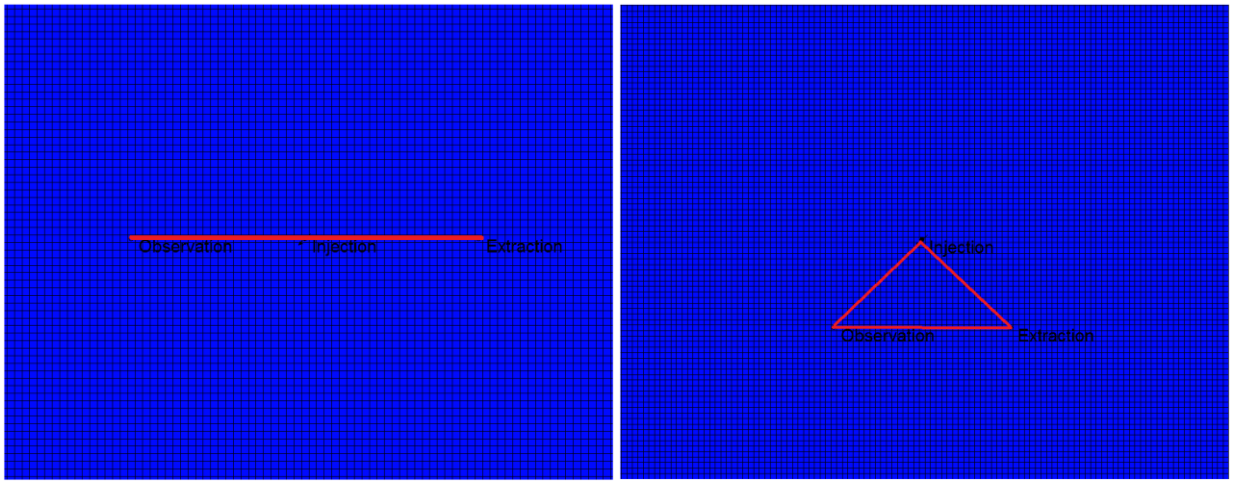

Figure 52. Two different linear and triangular configurations for injection, extraction, and observation wells.

Table 10. Base case data used for different pressure management strategies.

Model	3-Dimensional Cartesian
No. Of Coarse and Fine Grids	200×200×7
Δx , Δy , Δz	6.5, 6.5, 6.5 ft
Average Porosity and Average Permeability	0.25, 132 md
Depth of Injection	6500 ft
Thickness of Injection Layer (Hosston)	33 ft (10 m)
Water saturation	100 %
K_v/K_h	1
Injection Rate (constant rate)	5000 bbl/day
Production Rate (constant rate)	2500 bbl/day
Well configuration (3 wells)	1 injection, 1 extraction, 1 observation
Well distance	45 m
Formation salinity	50,000 ppm
Initial reservoir pressure	3400 psi
Average reservoir temperature	65 ^{0}C (150 ^{0}F)
Waterflood:	**Days injected:**
Tracer conc. : 1 %wt	90 Days

V-2. Results

Comparison of bottom hole pressure between homogeneous and different heterogeneous cases for No-Extraction scenario

Figure 53 and Figure 54 show the BHP comparison at the observation well and injection well for different linear and triangular well configurations in heterogeneous Case-2 when there is no extraction. The results demonstrate that BHP at the observation well increases more for the triangular configuration than for the linear pattern. There was around 1000 psi increase in injection well pressure for Case-2.

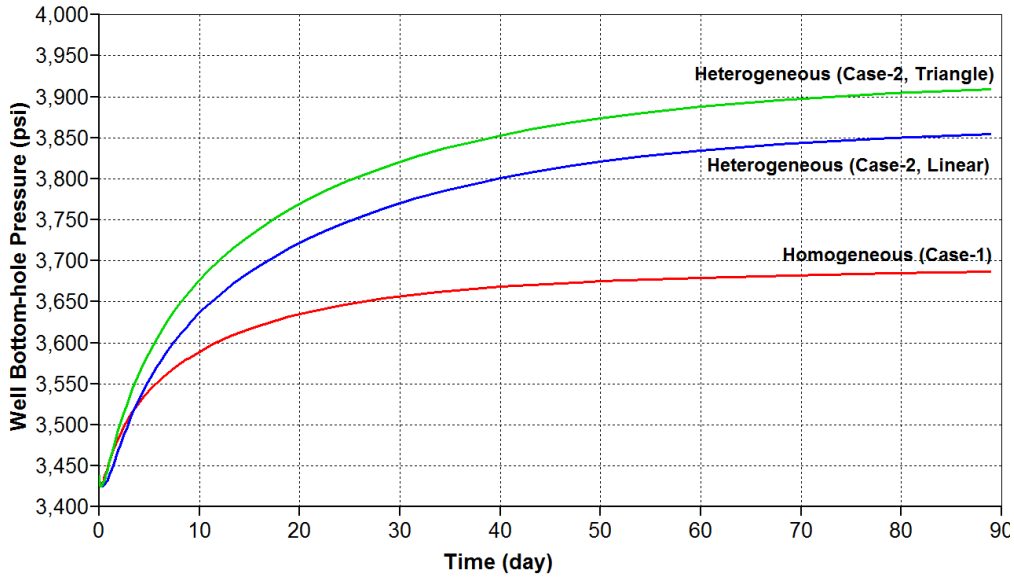

Figure 53. Comparison of bottom hole pressure at the observation well between homogeneous and heterogeneous Case-2 (No Extraction Scenario).

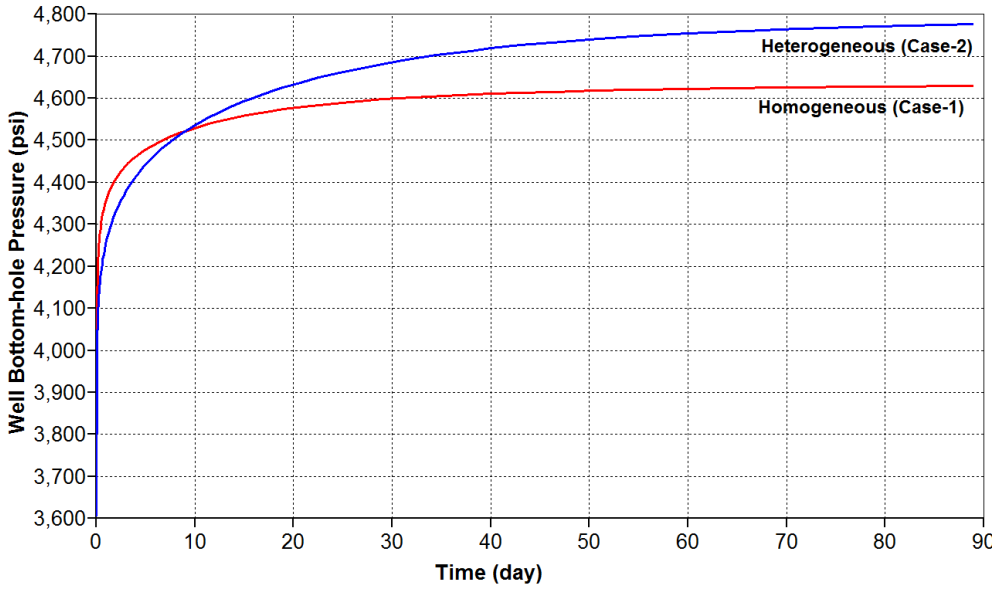

Figure 54. Comparison of bottom hole pressure at the injection well between homogeneous and heterogeneous Case-2 (No Extraction Scenario).

Similarly, results for Case 3 (Figure 55 and Figure 56) which includes heterogeneity shows an increase of ~500 psi in the observation well BHP for the no-extraction scenario in the triangular configuration. Figure 57 and Figure 58 show the BHP comparison at the observation well and injection well for the linear and triangular configurations in the heterogeneous Case 4 for which there was a ~400 psi increase in the observation well BHP. However, injection well pressure showed very large increase of ~4000 psi in BHP.

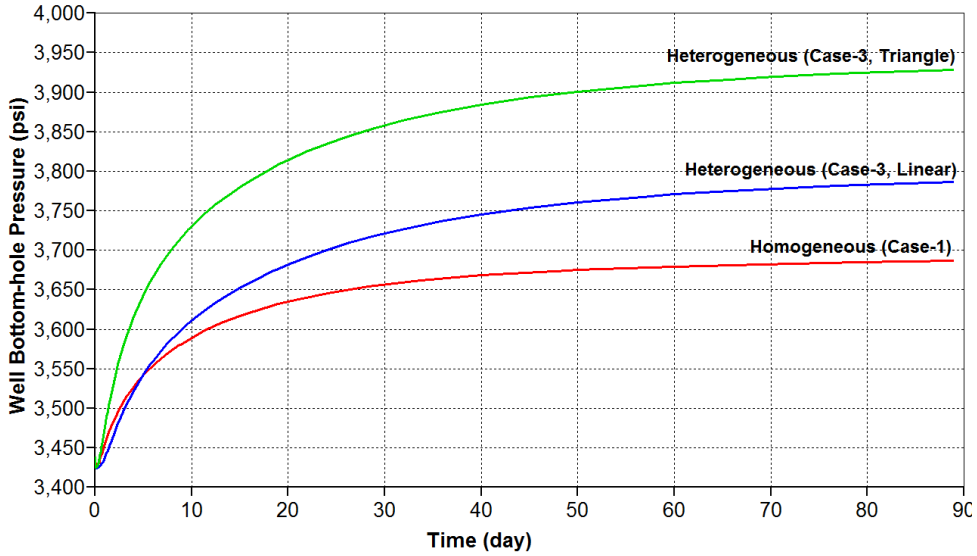

Figure 55. Comparison of bottom hole pressure at the observation well between homogeneous and heterogeneous Case-3 (No Extraction Scenario).

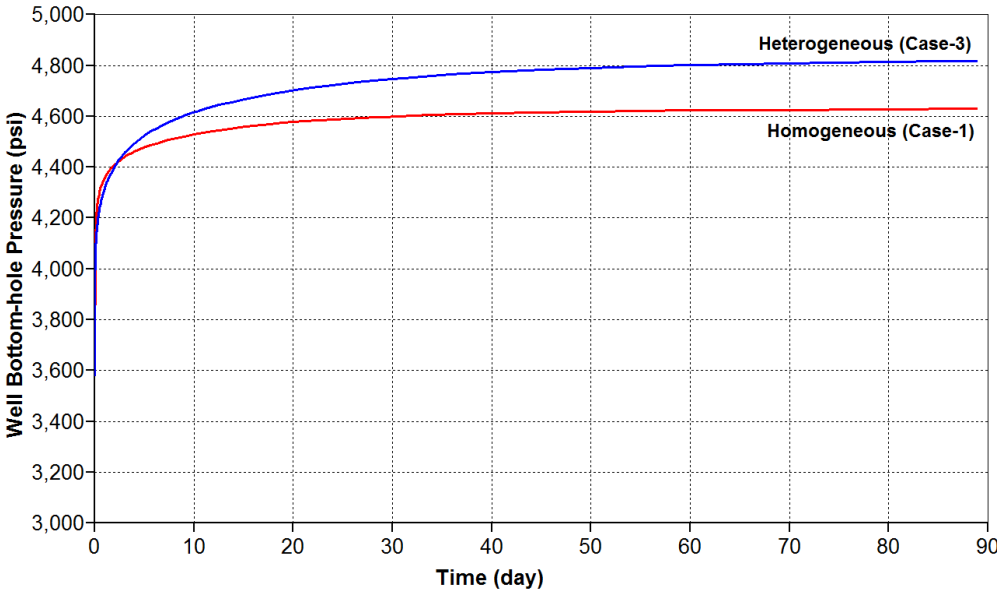

Figure 56. Comparison of bottom hole pressure at the injection well between homogeneous and heterogeneous Case-3 (No Extraction Scenario).

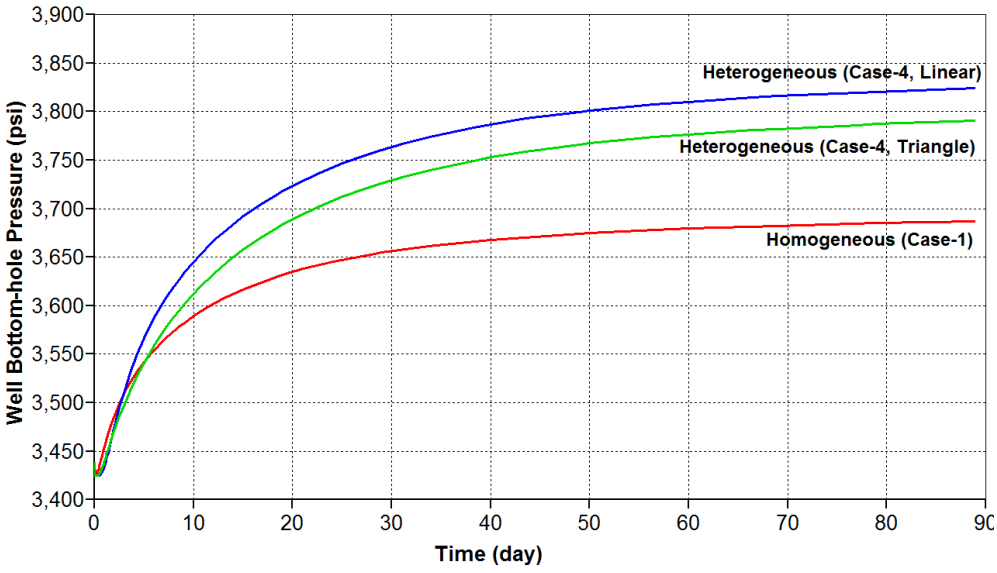

Figure 57. Comparison of bottom hole pressure at the observation well between homogeneous and heterogeneous Case-4 (No Extraction Scenario).

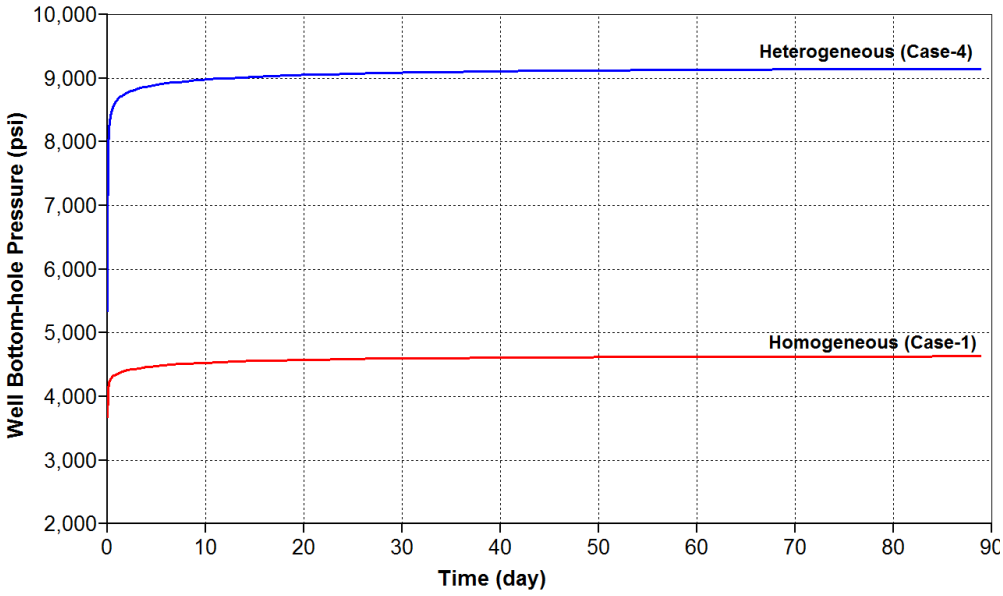

Figure 58. Comparison of bottom hole pressure at the injection well between homogeneous and heterogeneous Case-4 (No Extraction Scenario).

Comparison of bottom hole pressure between homogeneous and different heterogeneous cases for Active-Extraction scenario

Figure 59 and Figure 60 show the BHP comparison at the observation well and injection well for different linear and triangular well configurations in the homogeneous Case-1 in the active extraction scenario. The results demonstrate that BHP control at the observation well is considerably more favorable for the triangular configuration rather than the linear pattern.

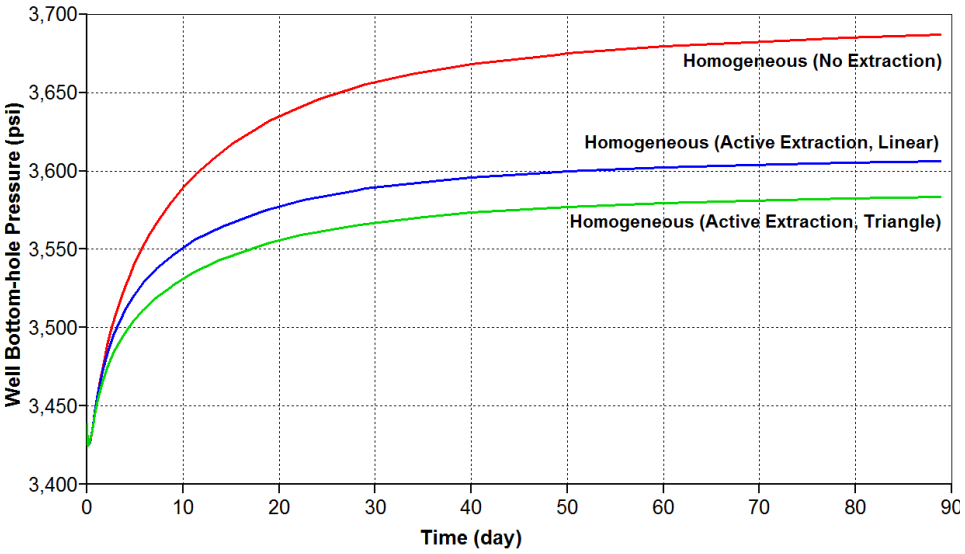

Figure 59. Comparison of bottom hole pressure at the observation well for active scenario in homogeneous Case-1 (linear and triangular configuration).

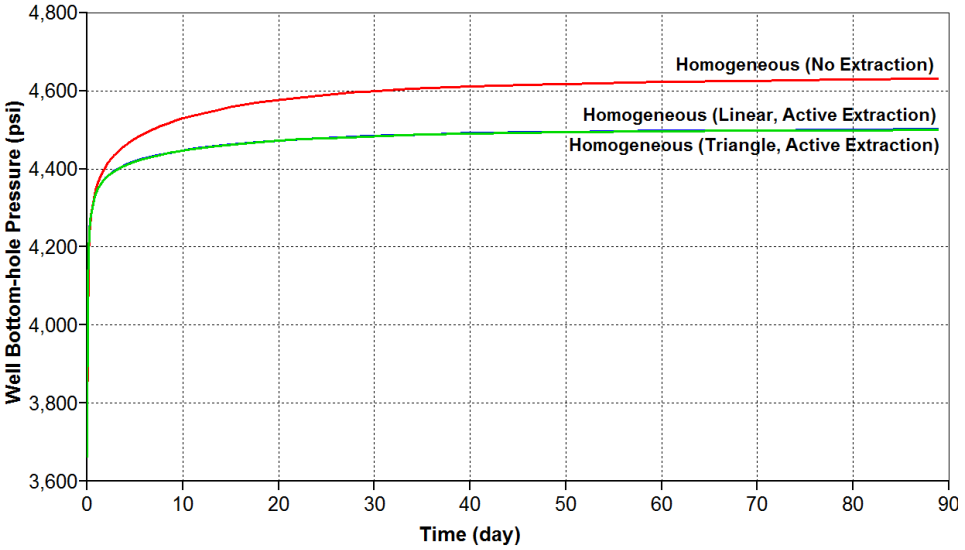

Figure 60. Comparison of bottom hole pressure at the injection well for active scenario in homogeneous Case-1 (linear and triangular configuration).

Figure 61 and Figure 62 show the comparison of BHP in observation and injection wells for active vs. no extraction scenarios when the well configuration is linear. Similarly, Figure 63 and Figure 64 show the comparison of BHP in observation and injection wells for active vs. no extraction scenario when the well configuration is triangular. The results demonstrate that control of BHP with active extraction scenario is better when using a triangular configuration compared to a linear configuration.

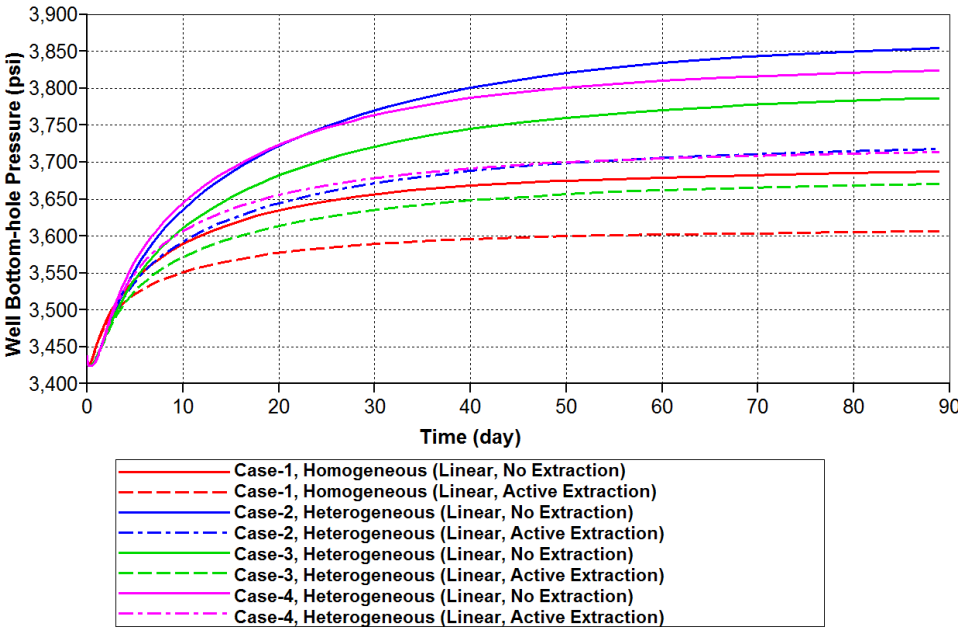

Figure 61. Comparison of bottom hole pressure at the observation well for active scenario in different heterogeneous cases (linear configuration).

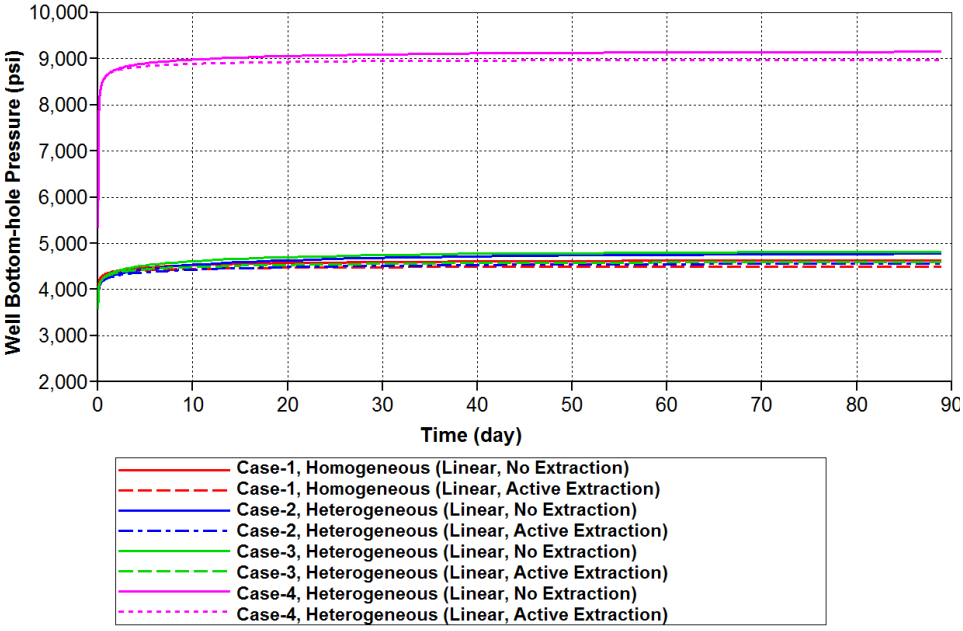

Figure 62. Comparison of bottom hole pressure at the injection well for active scenario in different heterogeneous cases (linear configuration).

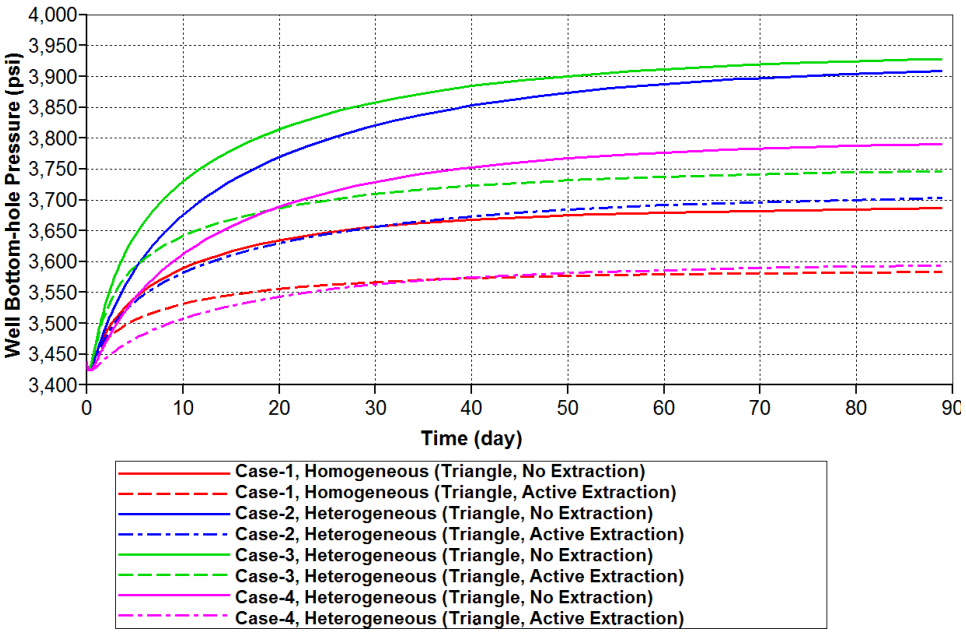

Figure 63. Comparison of bottom hole pressure at the observation well for active scenario in different heterogeneous cases (triangular configuration).

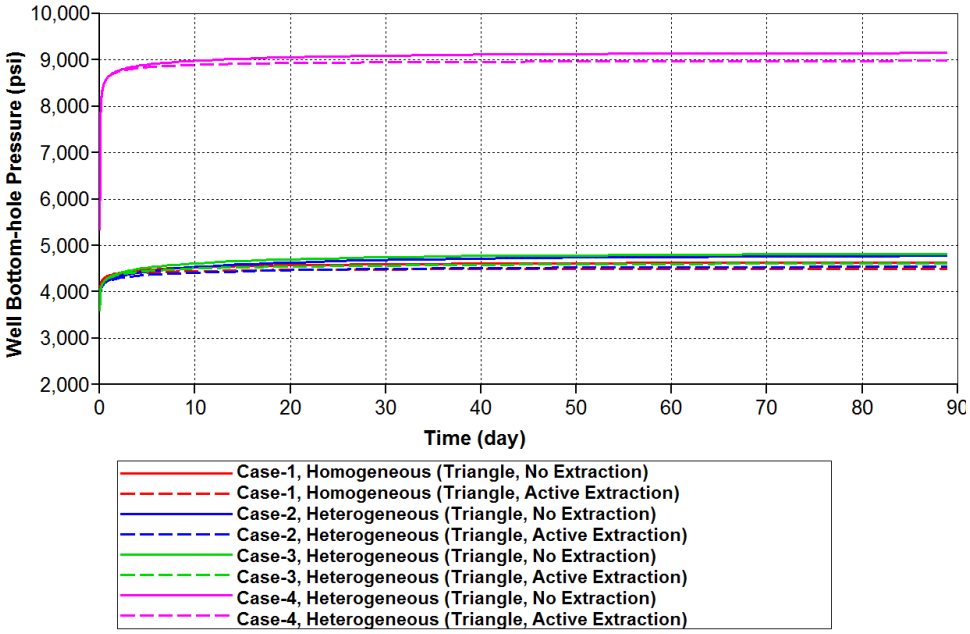

Figure 64. Comparison of bottom hole pressure at the injection well for active scenario in different heterogeneous cases (triangular configuration).

V-3. Modeling Related to Tracer Studies

Using tracers help in determining where the bulk of the injected water went and how the spatial distribution of the injected volume matches the pressure distribution. We plan to use conservative dyes but also magnetic nanoparticles, the latter will allow us to map the plume in addition to recording only the breakthrough times for the chemical dyes. Figure 65 shows the tracer concentration in the observation well for an active scenario when the well configuration is linear. Figure 66 shows the tracer concentration in observation well for active scenario when the well configuration is triangular. It illustrates that for the triangular configuration, tracer will break through in the observation well earlier than in the linear configuration. However, heterogeneity will play a crucial role in the breakthrough time for different well configurations. Figure 67 shows the tracer concentration map after 90 days in the linear active extraction scenario with different heterogeneous permeability distributions. Figure 68 maps the tracer concentration after 90 days for the triangular active extraction scenario with different heterogeneous permeability distributions. The concentration maps also illustrate that tracer breakthrough at the observation well for the triangular configuration occurs considerably earlier than for the linear configuration.

It is helpful to visualize cross sectional tracer concentrations along line AB (Figure 69) for both linear and triangular configurations. Figure 70 shows the cross sectional tracer concentrations (along cross section AB) after 90 days for the linear active extraction scenario with different heterogeneous permeability distributions. Figure 71 shows the cross sectional tracer concentrations (along cross section AB) after 90 days for the triangular active extraction scenario with different heterogeneous permeability distributions.

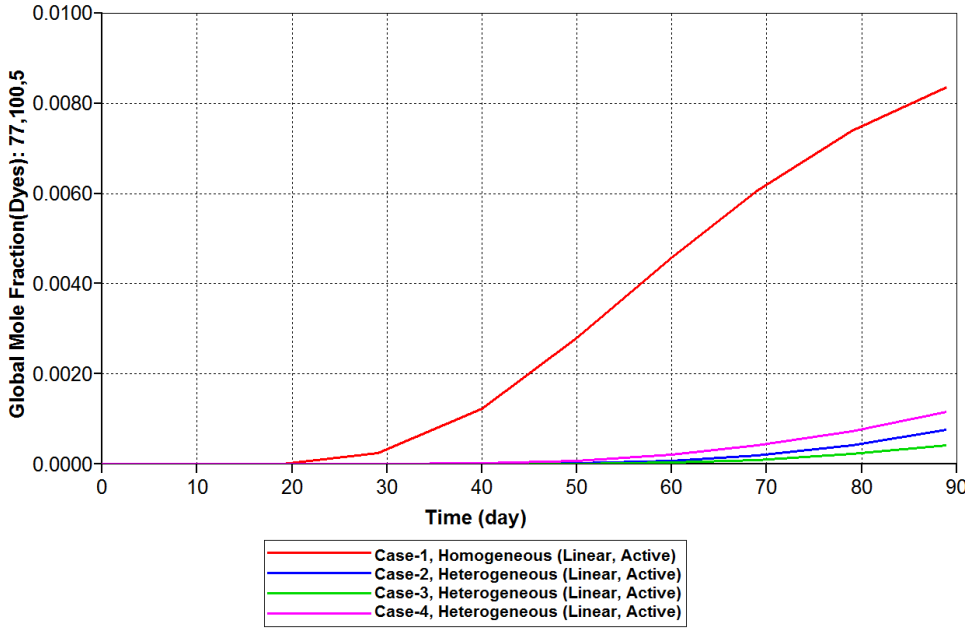

Figure 65. Comparison of tracer concentration breakthrough at the observation well for active scenario in different heterogeneous cases (Linear Configuration).

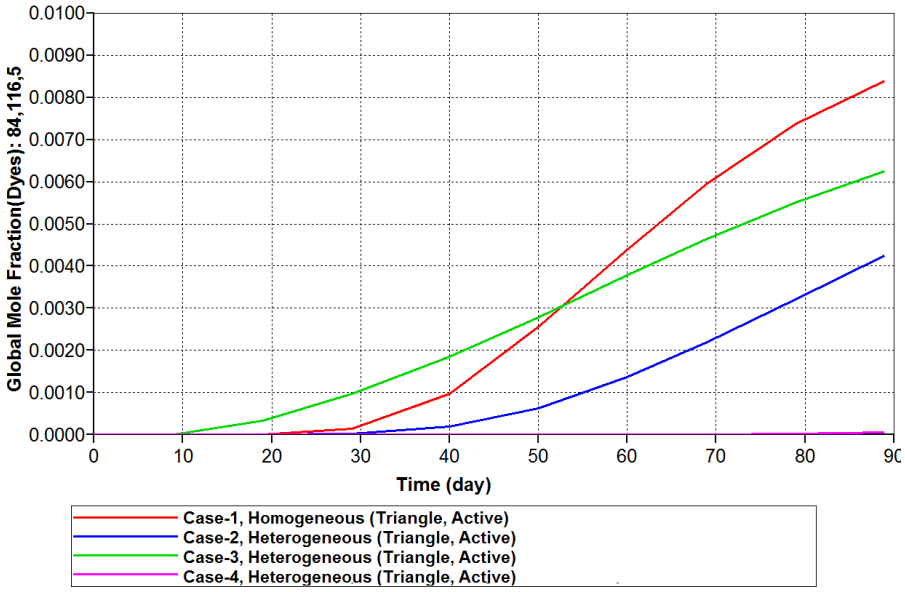

Figure 66. Comparison of tracer concentration breakthrough at the observation well for active scenario in different heterogeneous cases (triangular configuration).

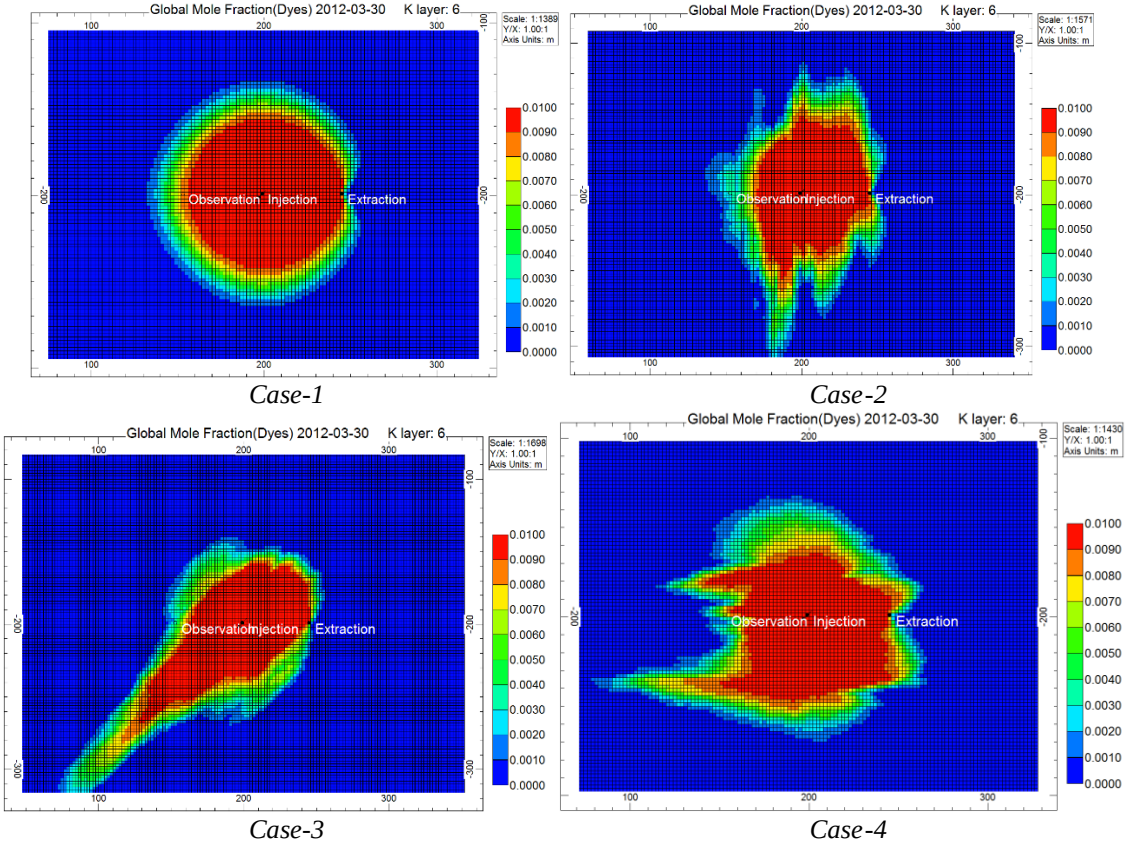

Figure 67. Comparison of tracer concentration profile at the 90 days for active scenario in different cases (linear configuration).

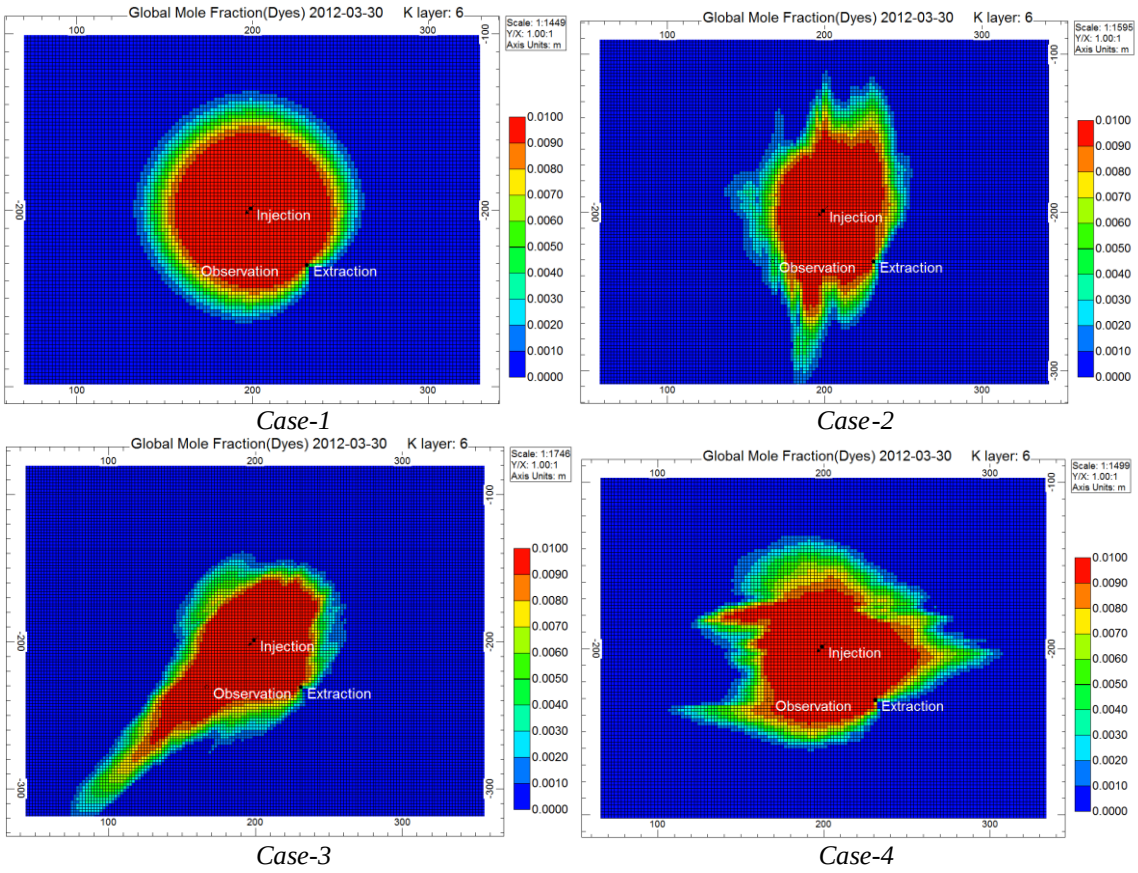

Figure 68. Comparison of tracer concentration profile at the 90 days for active scenario in different cases (triangular configuration).

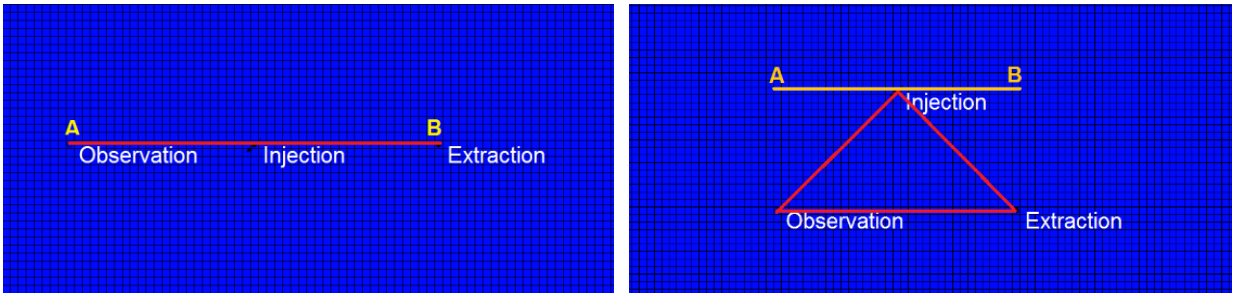

Figure 69. Illustration of cross sectional tracer concentration profile at the 90 days for active scenario in different cases for (a) linear and (b) triangular configurations.

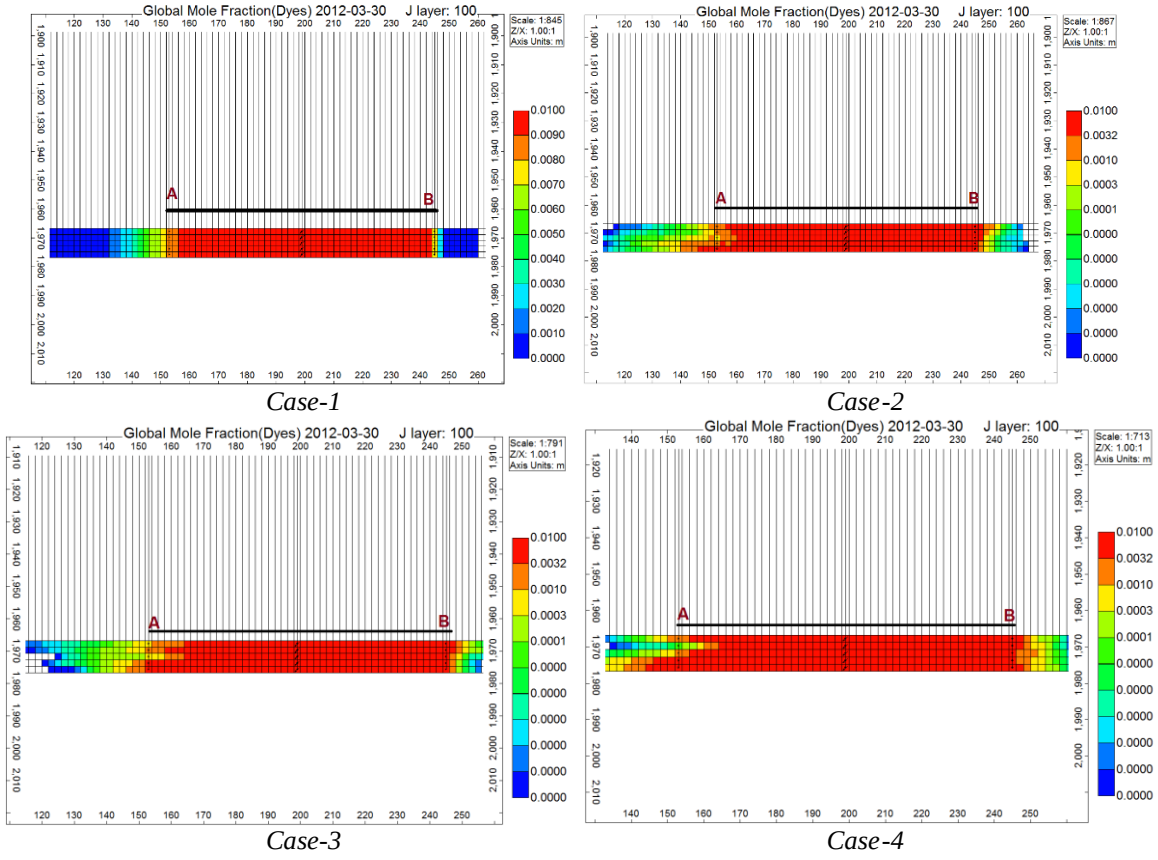

Figure 70. Comparison of cross sectional tracer concentration (AB) profile at the 90 days for active scenario in different cases (linear configuration).

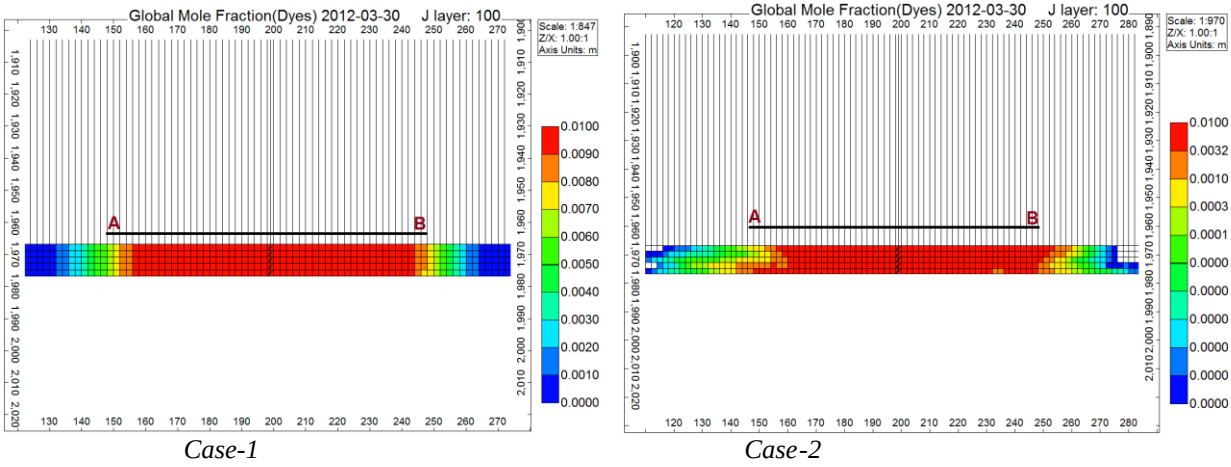

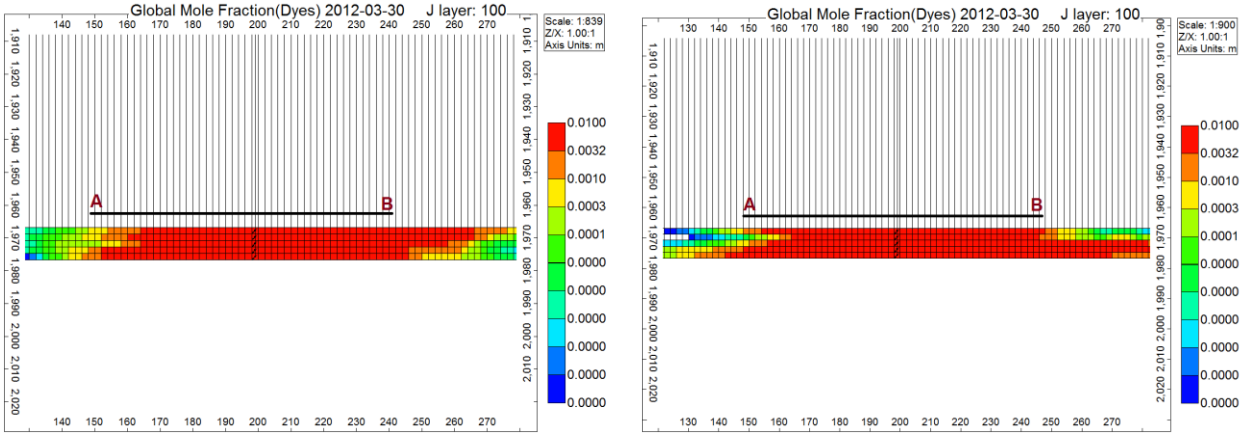

Case-3 *Case-4*

Figure 71. Comparison of cross sectional tracer concentration (AB) profile at the 90 days for active scenario in different cases (triangular configuration).

Modeling related to effectiveness of magnetic nanoparticles

We also plan to use a more sophisticated tracer: magnetic nanoparticles injected with the water (along with more conventional tracers) and imaged with EM technology (Rahmadi et al., 2015). It will allow to map a 3D view of the injected water plume. UT-BEG is in the midst of a field experiment to prove the validity of the concept (Spring 2016). Coincidentally, the experiment is

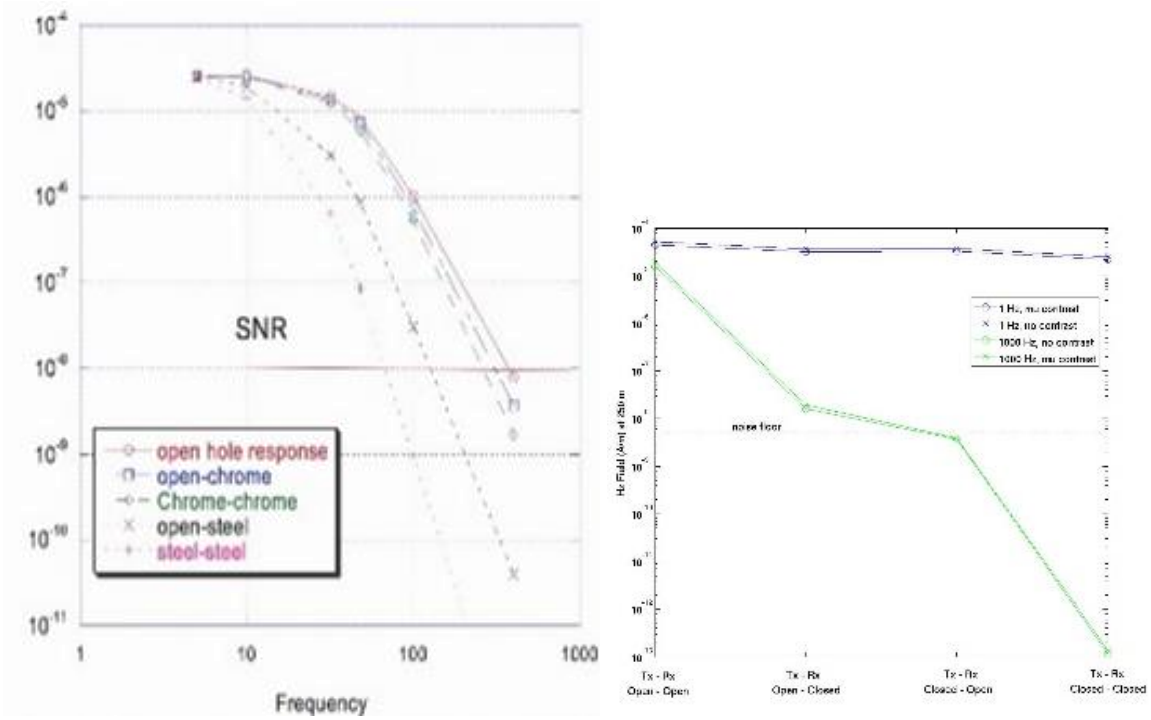

Note: Left panel shows field measurements from a deployed EM tool in various casing configurations as a function of frequency. Right panel shows magnetic contrast in open and steel well parings for two different frequencies. Both studies indicate that low frequency presents very little attenuation through casing.

Figure 72. Electromagnetic attenuation in casing studies.

being performed at the Devine Test Site (although shallower than the formation targeted in this study). If using magnetic nanoparticles as a tracer allows us to map the injected water plume, the injection has to be carefully planned. One of the challenges with borehole EM sensing is that the steel casing attenuates much of the signals (Figure 72a.).

This presents a challenge because the detection of electrical conductivity contrast performs best at higher frequencies. The excitement of magnetic water floods is that low frequency detection is possible, allowing for imaging through the casing (Figure 72b). Additionally, when compared to a conductive flood, magnetic waterfloods allow for earlier detection of departure of injected fluids due to different detection physics (Figure 73).

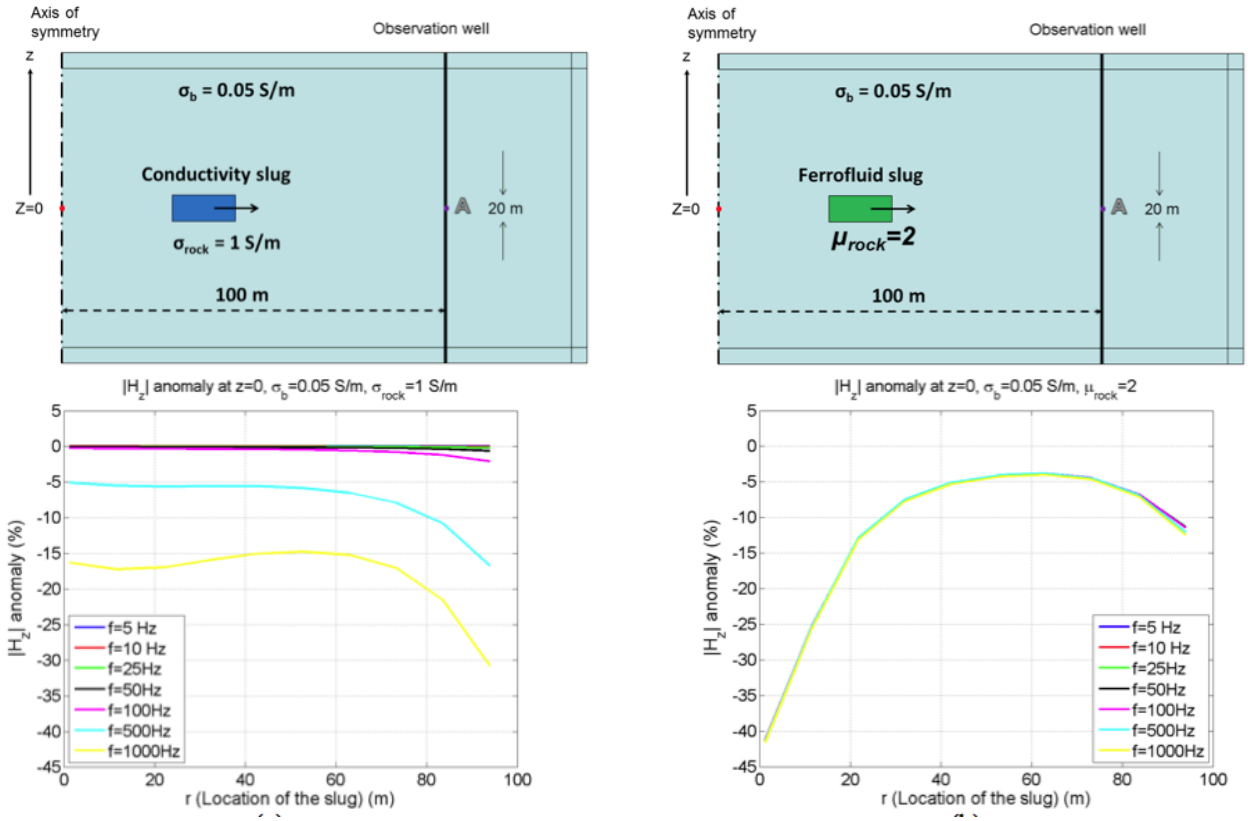

Note: the top plot shows a schematic for an injection of a slug of either conductive (left) or magnetic (right) fluid into a reservoir. As the slug propagates into the reservoir the detection signals are presented for conductive (bottom left) and magnetic (bottom right). Magnetic slugs present opportunity for early, low frequency detection.

Figure 73. Numerical study: conductive brine vs. magnetic particles.

V-4. Modeling of Relationship Between Formation Pore Pressure and Seismic Properties

Among all the monitoring methods for CO_2 sequestration and associated pore pressure changes due to injection, seismic surveys could provide the volumetric coverage needed to understand the 3D subsurface fluid and pore pressure front movement. However, seismic data are only indirectly related to pore pressure and CO_2 saturation. Therefore, we need to build quantitative links between the measured seismic properties of the sequestering formation and the CO_2 saturation and pore pressure. These quantitative links are given by rock physics theories for elastic properties of porous media. This study focuses on the pore pressure effects on the P- and

S-wave seismic velocities. The injected fluid is assumed to be a brine and similar to the formation water in the sequestering formation. The geologic formation under study is represented by the Hosston sandstone from the Devine Test Site. There are no well-log data that penetrate Hosston Formation at the study site. Therefore, there is a large uncertainty associated with the porosity, clay content and elastic properties of the formation. Our analysis focuses on the impact of each of these parameters on the velocity-pressure relation, with the goal of quantifying how much the pore pressure should be increased through injection to be able to monitor the pore pressure front movement using compressional (P) and shear-wave (S) seismic velocities. The first part of the study focuses on the analysis of laboratory data on compressional and shear-wave velocities as a function of pressure, for different sandstone samples. In the absence of such direct measurements on samples from Hosston Fm., this experimental data set is invaluable to help predicting the elastic behavior of the Hosston Fm. due to changes in pore pressure. The second part of the study presents a theoretical rock physics model that relates P and S-wave velocities to pressure changes through an analytical model. However, this model needs to be calibrated with actual measurements in order to have any predictive power.

We consider two different scenarios for the Hosston Fm.: Model 1 (optimistic), with a larger volumetric fraction of the compliant pores, and Model 2, (more plausible, based on the analysis of Han (1986)'s data), with a lower volumetric fraction of the compressible pores. Both models have the same total porosity of 16%.

Model 1: optimistic scenario

We computed the relative decrease in P and S-wave velocities with increasing pore pressure, starting from the hydrostatic state of 18 MPa. Figure 74 and Figure 75 show how the modeling results compare with Han (1986)'s laboratory measurements on P and S-wave velocities. These modeling results for the relative decrease of P and S-wave velocity with increasing pore pressure indicate an optimistic scenario, for which the required pore pressure needed to produce a detectable seismic response (5% change) is at the lower range of the values derived from laboratory measurements on the 48 sandstone samples.

Model 2: more plausible scenario

The second model has a lower volumetric fraction of the pressure-dependent pores, equal to 0.00067. We again compute the relative decrease in P and S-wave velocities with increasing pore pressure, starting from the same hydrostatic state of 18 MPa. Figure 76 and Figure 77 show how the theoretical results for both Model 1 and Model 2 compare with Han's laboratory measurements on P and S-wave velocities. As discussed, Model 1 represents an optimistic scenario, because the required pore pressure needed to produce a detectable seismic response (5% change) is 25 MPa, and is at the lower range of the values derived from laboratory measurements on the 48 sandstone samples. However, for Model 2, the required increase in pore pressure from the hydrostatic state is up to 30.5 MPa, closer to the average of 31 MPa derived from the Han data set first row in Table 2 from previous section). Based on the comparison between modeling results and lab analysis, we conclude that Model 2 is more likely.

For convenience, we included Table 11 summarizing the results of seismic analysis section. Complete results of this analysis is provided in Appendix D: Rock-Physics Study for Velocities-Pore Pressure Relation (Section XIII).

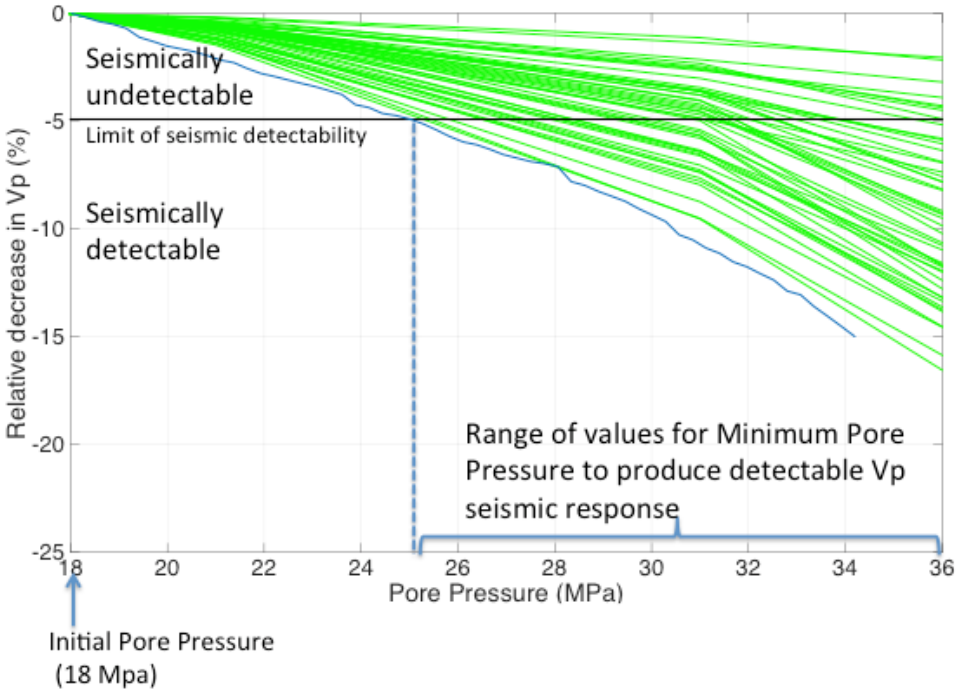

Note: Superimposed is the 5% limit of seismic detectability for relative change in P-wave velocity and the range of minimum pore pressure values that produce a detectable seismic response.

Figure 74. Relative decrease in P-wave velocity (percentage) as a function of Pore Pressure for laboratory data (green curves) and the modeling results for the optimistic scenario (blue curve).

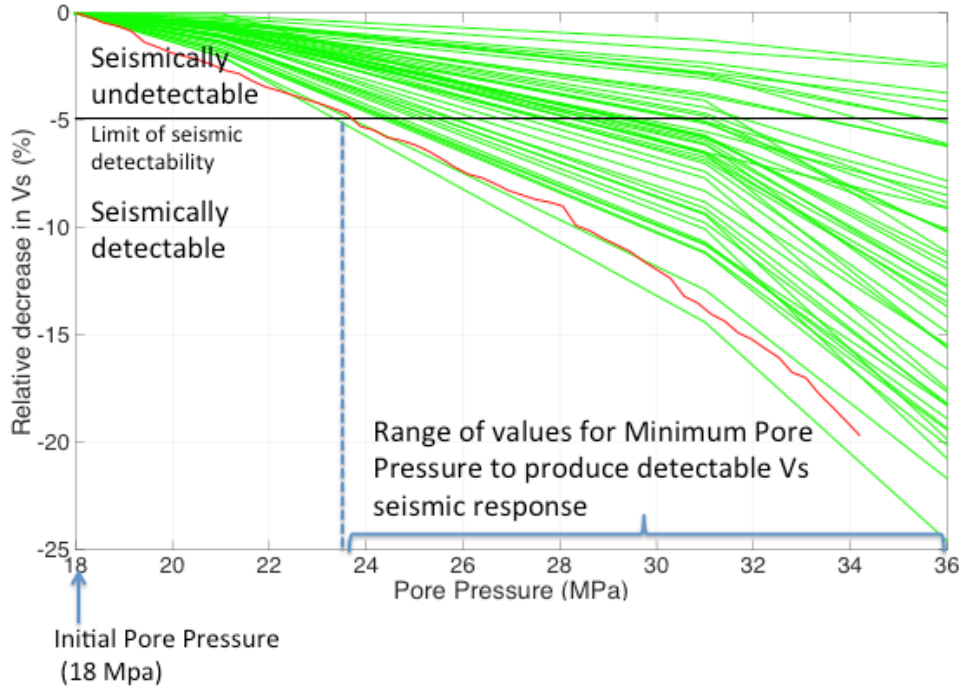

Note: Superimposed is the 5% limit of seismic detectability for relative change in S-wave velocity and the range of minimum pore pressure values that produce a detectable seismic response.

Figure 75. Relative decrease in S-wave velocity (percentage) as a function of Pore Pressure for laboratory data (green curves) and the modeling results for the optimistic scenario (red curve).

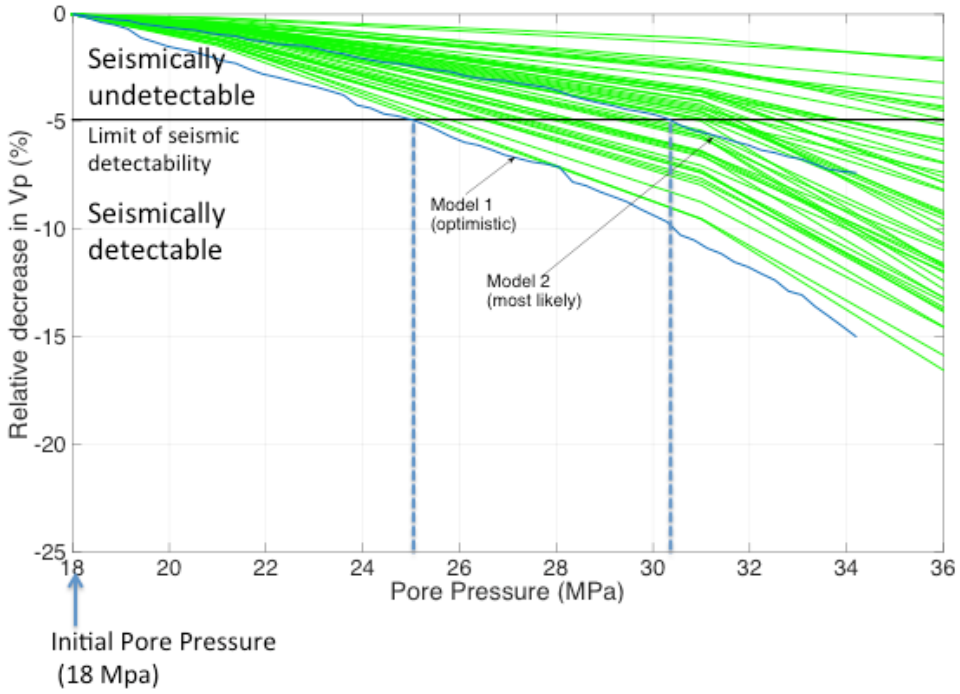

Note: Superimposed is the 5% limit of seismic detectability for relative change in P-wave velocity and the range of minimum pore pressure values that produce a detectable seismic response.

Figure 76. Relative decrease in P-wave velocity (percentage) as a function of Pore Pressure for laboratory data (green curves) and the theoretical Model 1 and Model 2 (blue curves)

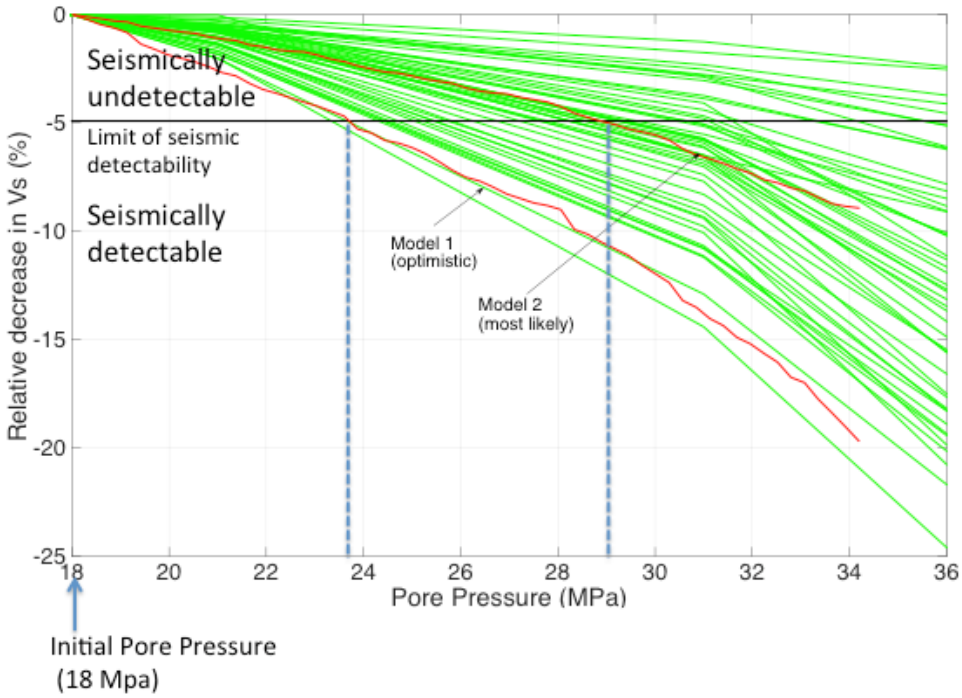

Note: Superimposed is the 5% limit of seismic detectability for relative change in S-wave velocity and the range of minimum pore pressure values that produce a detectable seismic response.

Figure 77. Relative decrease in S-wave velocity (percentage) as a function of Pore Pressure for laboratory data (green curves) and the theoretical Model 1 and Model 2 (red curves)

Table 11. Expected minimum pressure values and the minimum increase from hydrostatic pore pressure to produce a detectable seismic response in P and S-wave velocity (3% and 5% change).

Depth 5000ft (15 MPa hydrostatic Pp)	Minimum expected pore pressure (MPa)	Minimum expected increase from hydrostatic Pp (MPa)
5% change in Vp	25.0 MPa (std. 2.0 MPa)	10.0 MPa
3% change in Vp	23.0 MPa (std. 2.5 MPa)	8.0 MPa
5% change in Vs	24.0 MPa (std. 2.5 MPa)	9.0 MPa
3% change in Vs	21.5 MPa (std. 2.7 MPa)	6.5 MPa
Depth 6000ft (18 MPa hydrostatic Pp)		
5% change in Vp	31.0 MPa (std. 2.7 MPa)	13.0 MPa
3% change in Vp	28.0 MPa (std. 3.0 MPa)	10.0 MPa
5% change in Vs	29.0 MPa (std. 3.0 MPa)	11.0 MPa
3% change in Vs	26.0 MPa (std. 2.7 MPa)	8.0 MPa

Note: The assumed depths are 5000 ft with an initial hydrostatic pore pressure of 15 MPa presented at the top of the table and 6000 ft with an initial hydrostatic pore pressure of 18 MPa presented at the lower part of the table.

V-5. Harmonic Pulse Test Design

Pressure pulse testing by creating harmonics in pressure (by intermittent production and shut-in periods) can create pressure signals that can be analyzed for diffusive properties of the formation in addition to the statistic properties of formation (e.g. porosity, permeability, etc) (Sun et al., 2014, 2015, 2016) (Figure 78). This approach has already been tested at another BEG test site.

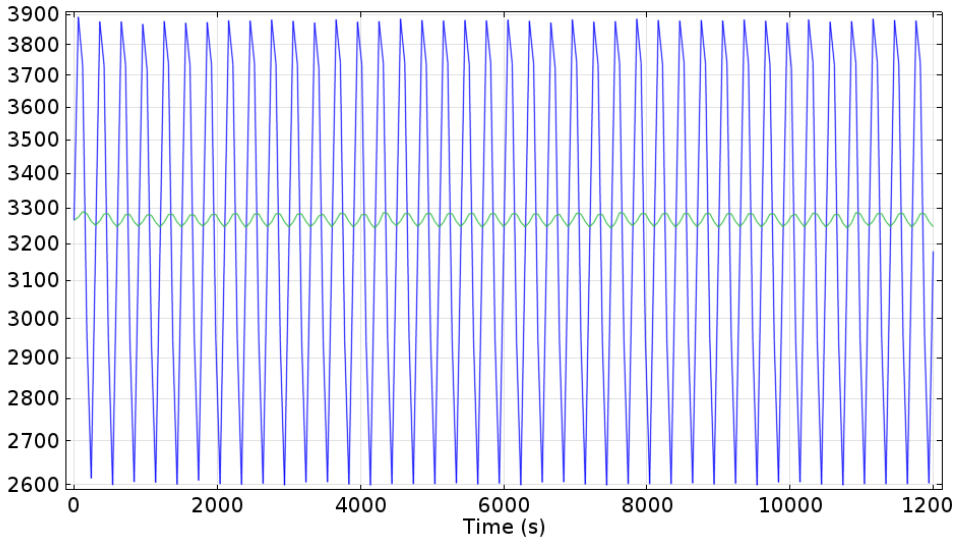

Figure 78. Plot of BHP (psi) of injector (blue) and observation (green) wells

We set up a model to simulate at the Devine Test Site the pressure pulses both in time and frequency domain to understand the pressure plume diffusion in the formation. Figure 79 shows the model with injection well at center and boundaries at 50 m (where observation and extraction wells will be drilled). Our analysis based on the input parameters used throughout the study and

provided in Table 10 shows that with current deigned injection and extraction rates we should be able to create pressure differential big enough for the analysis purposes.

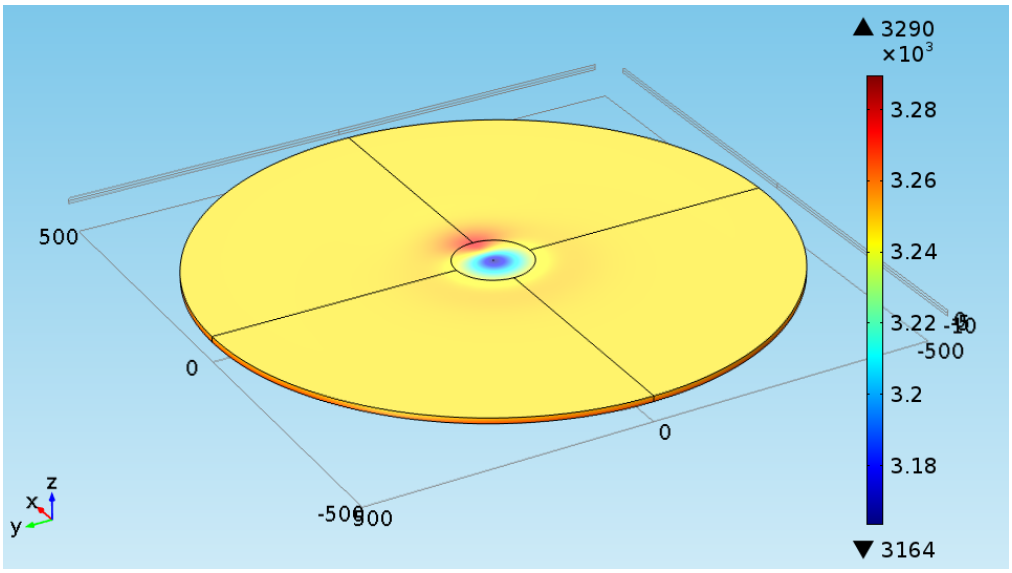

Figure 79. Simple 2D model for pressure transient analysis in DTS.

V-6. Overall Conclusions

- We have performed numerical simulations for different brine extraction scenarios using CMG-STARS to optimize pressure control well configuration design and rates.
- Robustness of the design is ensured by testing different well configurations (line and triangle), well spacing, and several heterogeneous permeability distributions to explore the impact of brine extraction on pressure control.
- Active extraction using the triangular configuration better meets project objectives compared to the linear configuration.
- Passive extraction is not as effective as active extraction and it comes with higher investment (double perforated wells are needed) but for sites where brine treatment cannot be done or can to be done at a small scale only, passive extraction could be the favored option in order to reduce the large volumes of brine brought up to surface using active extraction.
- The sensitivity simulations indicated that main brine extraction design variables are initial reservoir pressure (that is, depth), permeability, layer thickness, porosity, injection rate, and rock compressibility.
- Conventional and novel pressure transient analysis can be successfully deployed at DTS.
- Common (dye) and smart (magnetic nanoparticles) can be deployed at DTS to image and trace the plume in subsurface.
- Application of magnetic nanoparticles at DTS is possible and the injection fluid plume shape can be imaged.
- Increase in target formation pressure to tease out pressure differemtials is computed to be ~1000 psi.

VI. Water Life Cycle Analysis

VI-1. Life Cycle Analysis

A preliminary life cycle analysis (LCA) is presented in this section. For example, we did not perform LCA simulations because it is not clear until a well is drilled how much water will be needed to increase the formation pressure to the chosen levels. The LCA presented here assumes a relatively high formation permeability with open boundaries, conservative assumptions in terms of water use. We also neglected water use and fate of the well drilling period; such water needs are small compared to the injection period of the project (2 years intermittently). In addition, we did not attempt an all-encompassing cradle to grave type of assessment that would include all equipment and supplies as well as energy used but rather focus on the geological system. In any case, the overall cycle is fairly simple (Figure 80a): locally-sourced fresh water complemented by externally sourced Eagle Ford produced water is injected at a depth of 6,000-7,000 ft to build pressure in a carefully chosen sandy interval within the Hosston Formation. Once the pressure in the injection interval has reached a threshold determined by modeling, a production well is allowed to extract native formation water from the injection interval. We assume the steady state production rate to be only half of the injection rate to account for fluid loss through the boundaries of the system. A fraction of the water withdrawn through the production well is then sent to the GE treatment facility while most of the water, along with the concentrate output from treatment pilot, is send back to the injection well. As the recycling of the water produced from the injection interval increases, the amount externally sourced from the Eagle Ford decreases. However, a small fraction of the Eagle Ford produced water may always be needed to meet the salinity requirements of the treatment facility. The feed water to the G.E. treatment facility will then consist of formation water from the injection interval mixed with Eagle Ford produced water. The facility output will consist in fresh water and concentrate streams that will be blended before being send to the injection well and reinjected into the injection interval. In addition, the option of sending some of the produced water and maybe some of the treatment facility cleaning waste that cannot be reinjected to a nearby commercial disposal well is always available.

Fresh water to brackish will be supplied from several potentially available sources (Figure 80b): (1) from on-site wells tapping the Carrizo-Wilcox aquifer, this water is definitely fresh; (2) possibly from the Olmos Formation that seems to contain sandy intervals locally, TDS might be in the 5000 to 10,000 mg/L range; (3) from on-site wells tapping the Edwards Aquifer with the caveat listed in Section VI-2 "*Permitting Issues*", TDS is in the 10,000 to 15,000 mg/L range; and (4) purchased from local well owners or on the water market, which is well-developed because of the proximity of the Eagle Ford play and of the operators' need for hydraulic fracturing water, this water will be fresh too. In all cases, the origin of the water is likely to be groundwater. Given the local well yields and the cost of hauling water we estimate that the fresh and brackish water sources will cover about 1000 bpd (~30 gpm). Storage tanks will buffer water before it is injected.

To complement the previous water sources, we plan to tap Eagle Ford flowback and produced water. Although the drilling activity in the Eagle Ford play has considerably decreased, many previously drilled wells are still active and producing, including formation water. In addition, conventional fields also send produced water to commercial disposal wells. Contacts with waste

water disposal companies show this source is viable (it was already used to provide actual saline water from the site to the treatment subcontractor –GE– during phase 1). We estimate that the TDS of this water source to be in the 50,000 to 70,000 mg/L range. Good coordination with the supplier may increase the TDS available. This source will be used on a as-needed basis to ensure a controlled injection rate.

As injection proceeds and pressure increases in the injection interval, formation water will be produced at a rate approximately half that of the injection. Examination of geophysical logs have suggested that the TDS of the formation water is around 40,000 to 50,000 mg/L. The water produced on site will be either reinjected into the injection well depending on the injection needs, send off to a nearby commercial disposal well, possibly disposed of through on-site injection, or send to the GE treatment facility. Commercial disposal wells in Frio County (south of the Devine Test Site) typically injects in the Olmos Formation or deeper. Remember that both dip and thickness of the formation increase downdip towards the coasts. The area boasts tens of disposal wells (IHS data). The option of injecting on site in an interval of the Hosston (that is, below the USDW) different from that chosen for injection is also technically possible although remote from an operational standpoint as it would require drilling an additional injection well dedicated to water disposal.

Formation water produced from the extraction well is then blended with the externally-sourced produced water from the Eagle Ford and stored in a buffer storage tank. This feed stream (10 gpm, maybe 20 gpm –700 bpd) is then treated in the GE facility where the product water (fresh) is combined with the concentrate to be reinjected into the injection well. Some water loss is expected in this step as the TDS of the feed water needs to be raised to a TDS >150,000 mg/L in addition to backwash and other cleaning and washing events. The likely fate of these waters with a high total suspended solids (TSS) is disposal into a commercial disposal well as these facilities are generally equipped to deal with solids.

Considering the system as the Devine Test Site from the surface to the top of the geological basement (Figure 81 and Figure 82), overall the project adds water to the system because its goal is to increase the pressure, goal that can be attained only by injecting additional water. Some externally-sourced fresh-water and Eagle Ford produced water are added to the system and a lesser amount is disposed of into commercial disposal well. Ultimately the additional volumes of water injected into the chosen injection interval will tend to migrate laterally off-site as the extra-pressure dissipates. Similarly any fresh water withdrawn from on-site aquifers will tend to be replenished by lateral flow. A minor amount of water will be lost by evaporation from surface equipment and actions. Within the system itself, there is a vertical transfer of water from the surface to the injection interval and a transfer of salt in the other direction. Losses from the system include water disposed of into commercial well and, a minor component, water lost to atmosphere or run off during the injection/extraction and treatment operations.

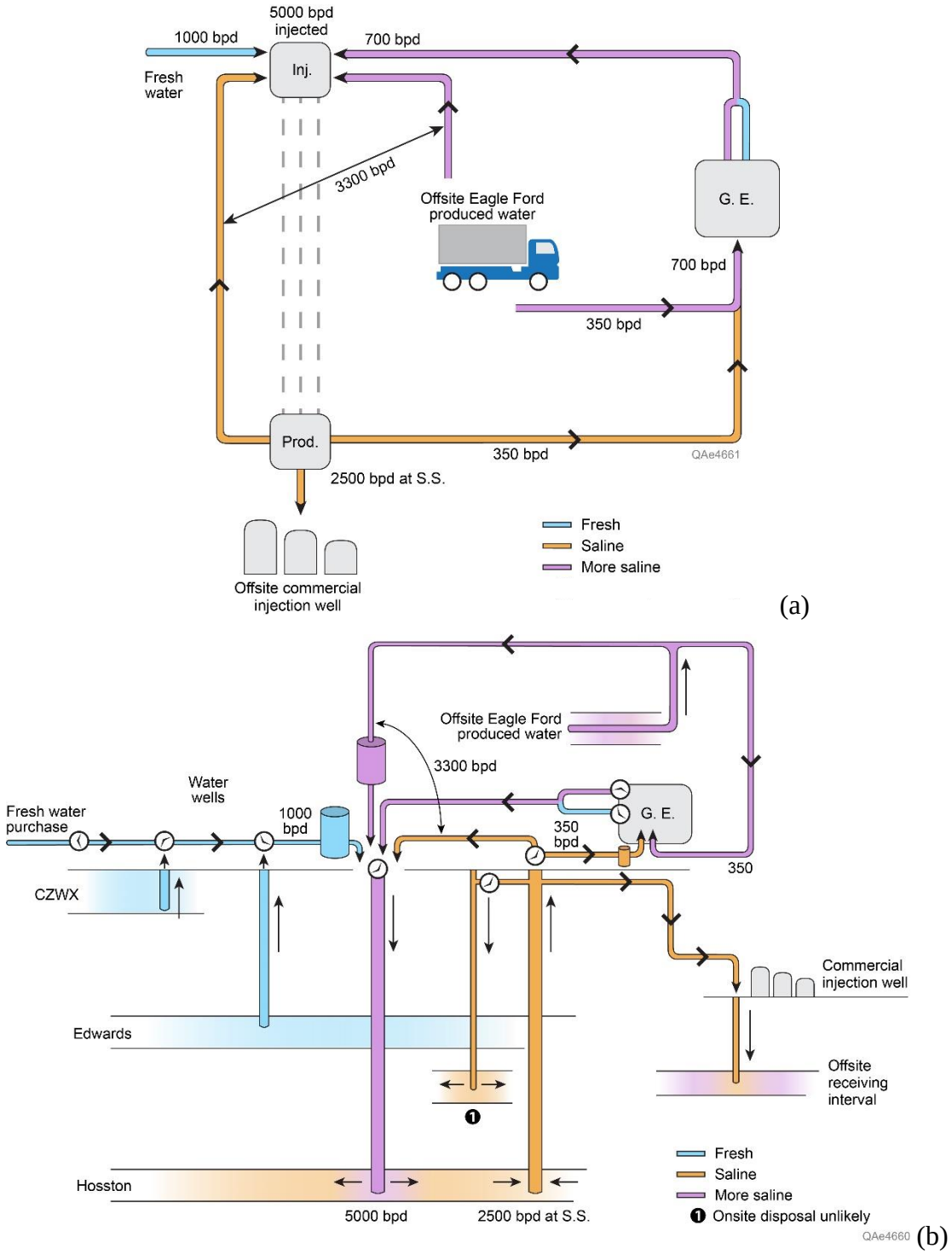

Note: rates shown (in bpd, barrels per day) are preliminary, actual rates will be determined after field tests of wells to be drilled.

Figure 80. Life cycle analysis diagrams. (a) overview; (b) detailed cross-section.

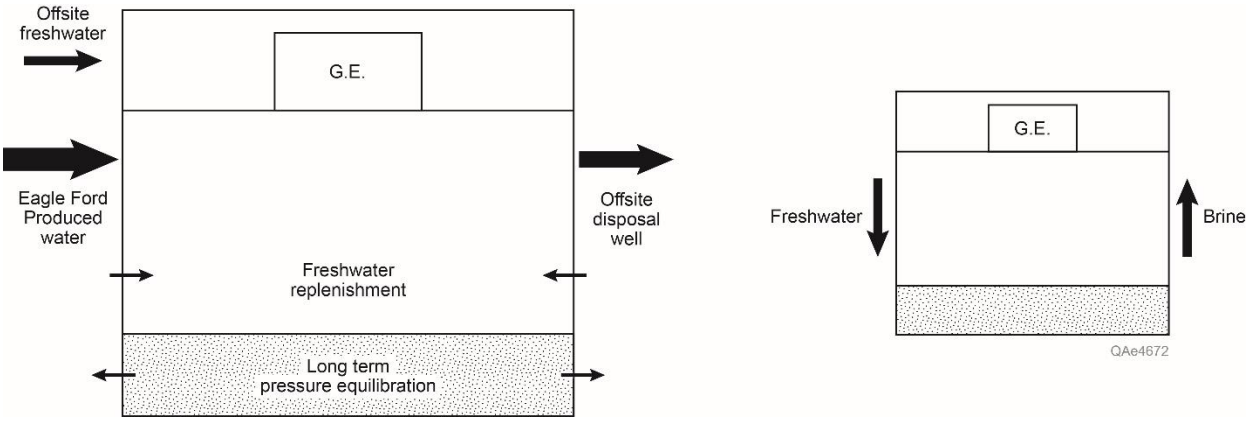

Figure 81. Overall water balance of the project at the Devine Test Site

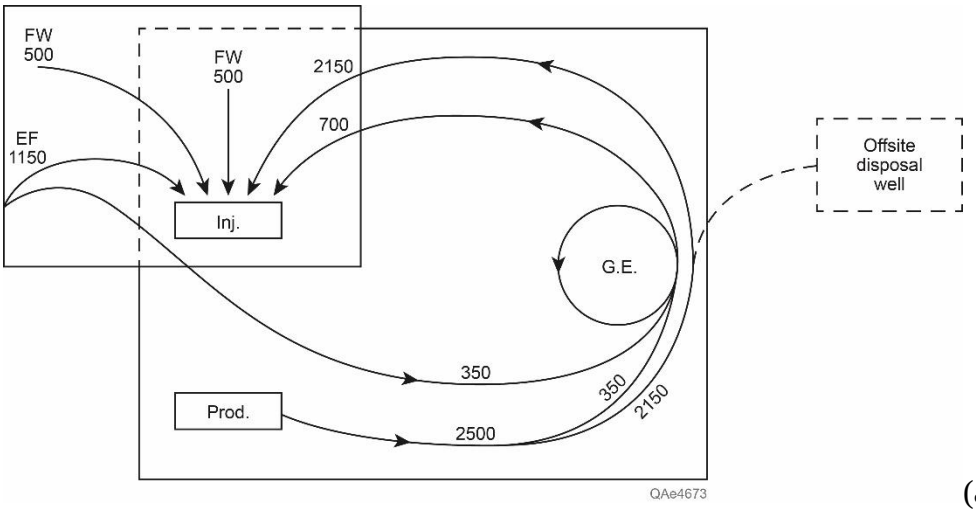

(a)

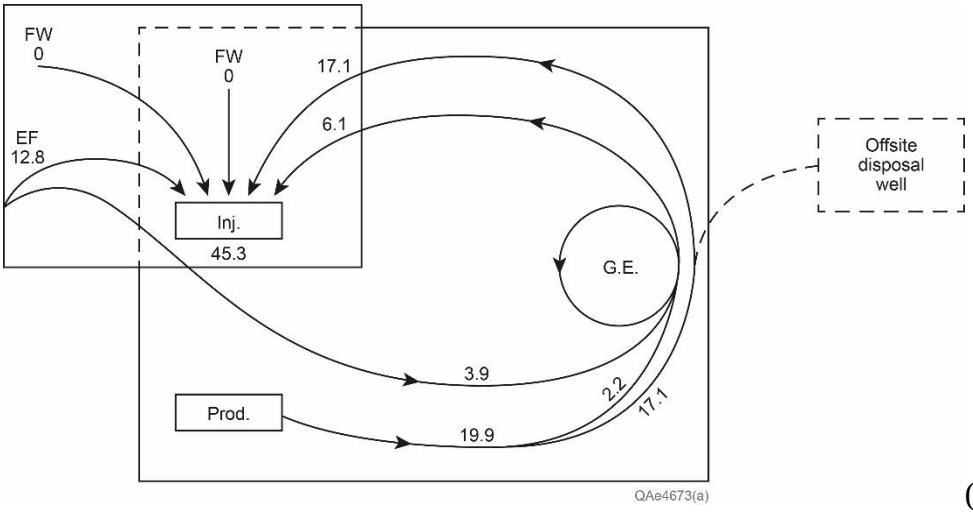

(b)

Figure 82. Flow chart showing fluxes between the various components of the system for water in barrel per day (a) and salt in ton per day (b).

VI-2. Permitting Issues

In support of the viability of the LCA, we summarize here results of the permitting inquiries with a compilation of regulatory permits or authorizations needed for Phase 2. The following items described steps for all proposed "actions taking place on the site". Each item on the "action" list was researched to determine the appropriate agency and type of permit or authorization required by that agency. The following is listing of the field "actions": (1) Disturbing the site, (2) Installing the injection well, (3) Deep penetrations through the Edwards aquifer, (4) Constructing deep brine extraction and deep monitor wells and a shallow water production well for injection flow, (5) Transporting "produced water" from area oil and gas sources (most likely Eagle Ford produced water) for high TDS brine addition to site's extracted brine, and (6) Above-ground brine treatment technology experiments. The permits/authorizations narrative was developed through a combination of communications with agencies' staff, past experiences with the agencies and online research of each agency's relevant regulations and guidance documents.

(1) DOE NETL, NEPA Process - prior to the site being disturbed with project activity a detailed and complete "Environmental Questionnaire (EQ)" will be submitted to DOE-NETL. Preliminary EQ preparation work on this site indicates that the site is likely to receive a "finding of no significant impact" which would allow a "categorical exclusion" to be granted by DOE-NETL.
Duration- we expect the EQ will be completed and submitted to DOE-NETL within 60-90 days of the inception of Phase 2. DOE-NETL's "record of decision" could potentially be issued within 90 days of the receipt of the EQ submittal.

(2) TCEQ Injection well Underground Injection Control (UIC) permits - Texas Commission on Environmental Quality UIC staff will likely "authorize" by letter (no permit required) the injection well as Class V Experimental well. The TCEQ staff will perform a thorough technical review to determine confirm the well's design and site's "area of review" analysis shows the project, as described in the submittal, is protective of USDWs.
Duration- Based on our prior experiences with TCEQ authorizations of Class V Experimental UIC wells we expect TCEQ's "plan review" to be complete and authorization issued 6-8 weeks after submittal of the application and supporting design documents.

(3a) Edwards Aquifer Authority (EAA) - This regional agency focuses on protecting the quality of the Edwards aquifer and adjudicates extraction permits from the Edwards aquifer. The Edwards aquifer is approximately 3000 ft bgs on this site. Accordingly, the deep injection well(s), monitor wells, which pass through the Edwards formation will require a "drilling through the Edwards" (Crossing) permit. EAA's Crossing permit application is straight-forward and designed to insure that this aquifer is isolated and protected by casing and grout from other water sources above and below the Edwards formation.
Duration- the EAA Crossing permits are typically issued 7-10 days after submitting an application.

(3b) Edwards Aquifer Authority (EAA) – obtaining a permit for on-site withdrawing of water from the Edwards Aquifer will require purchasing unused water rights from another entity as the amount of water that can be removed from the aquifer is capped and fully allocated. Early discussions with the agency suggest that such a purchase should be readily feasible.
Duration- unclear but enough water can be extracted from other on-site aquifers or purchased on the water market to satisfy project water needs.

(4a) Medina County Groundwater Conservation District (MGCD) - This local agency oversees the issuance of water well permits for all county aquifers except the Edwards (which is permitted by EAA). Thus, the deep brine extraction well into the Trinity-Hosston formation and the shallow water well for the injection source (likely to be into the Carrizo or Wilcox formations) will need a water well "operating permit".
Duration- MCGCD typically issues an operating permit approximately 6 weeks after receipt of the application.

(4b) Texas Department of Licensing and Regulation (TDLR) - the project's water wells (deep and shallow) and the monitor wells must be constructed by a TDLR licensed water well driller. TDLR requires licensed drillers to follow many "best practices" as stated in the TDLR regulations. One pertinent regulation requires drillers to assure that the construction of water wells and monitor wells do not allow sustained migration or mixing of any encountered "injurious water" into good-quality formation waters. Accordingly, we will utilize experienced, licensed water well drillers. No drilling permit is required from TDLR but drillers are required to file "water well completion reports" with TDLR within 30 days of well completions.

(5) Railroad Commission of Texas (RRC) - The RRC regulates oil & gas activities in Texas. We propose to transport high TDS "produced water" brines to the project site for water treatment technology experiments. Thus this project will interface with RRC oversight. Typically the RRC regulated "waste haulers" must have a special RRC permit to transport produced water to a non-RRC regulated location. Fortunately, the RRC rules allow the transport of waste (produced water) to sites authorized by other state or federal agencies. In this case, a TCEQ authorized injection well will be the final storage of all treated and residual streams from the water treatment experiments. Thus the RRC's only regulatory requirement will require the produced water hauler to file a copy of the produced water transport manifest with the appropriate RRC District office within 30 days of delivery. No permits are required.

(6) Brine treatment technology experiments will use water from the brine extraction well (expected to be 50,000 mg/l TDS) and regional "produced water" brines for the water source to test the capabilities of several robust treatment technologies. Given that the treatment outputs will flow to the authorized injection well and all treatment units, water storage and piping will be water-tight and above ground, no permits are required by any agency.

In summary, we are confident permits and authorizations for the proposed site will be swiftly obtained by our experienced team working in close collaboration with the above noted agencies.

VII. Brine Treatment Technology Screening

See separate confidential appendix whose abstract follows:

Deep saline formations constitute a vast resource for carbon sequestration as supercritical CO2. However, many formations will require water to be extracted to avoid over-pressurization and to direct the CO_2 plume. Cost-effective, scalable desalination technologies will be needed to manage extracted water from these formations, particularly high-salinity extracted water. This report focuses on desalination of extracted water that contains 180 gm/L total dissolved solids (TDS) and uses the cost of desalination as the key metric for process evaluation. A cost analysis of three commercial brine concentration and crystallization options showed that the appropriate base case is a falling film evaporator with mechanical vapor recompression (FF-MVR) to form a brine concentrate (without salt crystallization) for re-injection. A water lifecycle analysis was conducted for this base case. Techno-economic modeling for five alternate desalination technologies enabled cost-benefit comparisons against this base case. These technologies include forward osmosis (FO), membrane distillation (MD), humidification-dehumidification (HDH), clathrates, and turbo-expander-based freeze technology. This techno-economic analysis shows that if waste heat (~120°C) is available at no cost, HDH is the lowest cost option, whereas if heat costs $6/MMBTU and electricity costs $0.10/KWH, then both clathrates and FO are the lowest cost options. A research gap analysis for these candidate desalination technologies is included. This report provides a design and implementation plan for a field test-bed facility to test a wide range of both pretreatment and desalination technologies.

VIII. Synthesis and Conclusions

This topical report presents findings of tasks proposed for Phase I (Table 12). Overall, no major surprise occurred in the course of collecting information and preparing documents required for Phase II renewal application. All elements gathered confirm that the Devine Test Site is adequate to perform Phase II field experiment. The risk the most likely to slow down or even delay the implementation of the project (low likelihood, high impact seismic risk due to overpressure of basal sands) has been tackled head on by associating our MVA plan with the research group at the BEG working specifically on this topic (TexNet / CISR).

Table 12. Phase I tasks and corresponding topical report section

Task	Title	Section
1 Project Management and Planning		N/A
2 Pressure Management Strategies		
2.1	Pressure management strategies analysis	Sections III and XII
2.2	Monitoring methods and plans	Sections IV, V-3, V-4, and V-5
2.3	Lab scale high P-T brine mixing and numerical modeling	Section II-4
2.4	Cost analysis and justification for implementation of each strategy into Phase II	See Phase II submission
3 Site Characterization		
3.1	Regional and local geology and hydrogeology	Sections II-2 and II-3
3.2	Well log analysis, seismic analysis, and building of a static model	Sections II-2 and II-3, V-4 and XIII, and V-1
3.3	Target formation salinity analysis using well logs and limited field sampling	Sections II-3-3
3.4	Petrographic analysis of cores and cuttings	Sections II-4-1 and II-4-2.1
4 Operation and Field Support		Section VI-2
5 Water LCA and Brine Technologies Assessment		
5.1	LCA	Section VI
5.2	Brine handling and disposal plans	See GRC report
5.3	Define Extracted Water Pretreatment and Desalination System	See GRC report
5.4	Validate Extracted Water Recovery System at Lab/Pre-pilot Scale	See GRC report
5.5	Define Field Pilot	See GRC report
5.6	Research Gap Analysis	See GRC report

IX. References

Alexander, Jr., W. H. and D. E. White, 1966, Ground-Water Resources of Atascosa and Frio Counties, Texas, Texas Water Development Board Report #32, 200p.

Ashworth, J.B. and J. Hopkins, 1995, Aquifers of Texas, Texas Water Development Board report #345.

Bandilla, K. W., Court, B., Elliot, T. R., & Celia, M. A. (2012). Comparison of brine production scenarios for geologic carbon sequestration operations. Carbon Management Technology Conference. 7-9 February, Orlando, Florida, USA.

Bebout, D.G., D.A. Budd, and R.A. Schatzinger, 1981, Depositional and diagenetic history of the Sligo and Hosston Formations (Lower Cretaceous) in South Texas, The University of Texas at Austin Bureau of Economic Geology Report of Investigations #109, 70p.

Bebout, D.G., B.R. Weise, A.R. Gregory, and M.B. Edwards, 1982. Wilcox Sandstone reservoirs in the deep subsurface along the Texas Gulf Coast; their potential for production of geopressured geothermal energy: The University of Texas at Austin, Bureau of Economic Geology Report of Investigations No. 117, 125 p.

Birkholzer, J. T., Cihan, A., & Zhou, Q. (2012). Impact-driven pressure management via targeted brine extraction—Conceptual studies of CO_2 storage in saline formations. International Journal of Greenhouse Gas Control, 7, 168-180.

Bish, DL. 1994. Quantitative XRD analysis of soils, p.267-295 *in*: eds. JE Amonette & L Zelazny, Quantitative methods in soil mineralogy. S.S.S.A. Misc. Publ. Madison, WI.

Boghici, R., 2009, Water Quality in the Carrizo-Wilcox Aquifer 1990–2006, Texas Water Development Board Report 372, 33p.

Budd, D. A. and R. G. Loucks, 1982, Smackover and Lower Buckner Formations South Texas: Depositional Systems on a Jurassic Carbonate Ramp, The University of Texas at Austin Bureau of Economic Geology Report of Investigations #112, 38p.

Buscheck, T. A., Sun, Y., Hao, Y., Wolery, T. J., Bourcier, W., Tompson, A. F., Aines, R. D. (2011). Combining brine extraction, desalination, and residual-brine reinjection with CO2 storage in saline formations: Implications for pressure management, capacity, and risk mitigation. Energy Procedia, 4, pp. 4283-4290.

Buscheck, T. A., White, J. A., Chen, M., Sun, Y., Hao, Y., Aines, R. D., Bielicki, J. M. (2014). Pre-Injection brine production for managing pressure in compartmentalized CO2 storage reservoirs. Energy Procedia, 63, pp. 5333 – 5340.

Cihan, A., Birkholzer, J., & Bianchi, M. (2014). Targeted pressure management during CO2 sequestration: Optimization of well placement and brine extraction. Energy Procedia, 63, pp. 5325 – 5332.

Condon, S.M., and T.S. Dyman, 2003, "2003 Geologic Assessment of Undiscovered Conventional Oil and Gas Resources in the Upper Cretaceous Navarro and Taylor Groups, Western Gulf Province, Texas" In Petroleum Systems and Geologic Assessment of Undiscovered Oil and Gas, Navarro and Taylor Groups, Western Gulf Province, Texas, US:

Geological Survey Digital Data Series 69–H. http://pubs.usgs.gov/dds/dds-069/dds-069-h/REPORTS/69_H_CH_2.pdf.

Core Laboratories Inc.,1972, A survey of the subsurface saline water of Texas. Texas Water Development Board Report 157.

Deeds, E., V. Kelley, D. Fryar, T. Jones, A. J. Whallon, and K. E. Dean, 2003, Groundwater Availability Model for the Southern Carrizo-Wilcox Aquifer: Intera, Austin, TX, final report prepared for the Texas Water Development Board, variously paginated

Dempsey, D., Kelkar, S., & Pawar, R. (2014). Passive injection: A strategy for mitigating reservoir pressurization, induced seismicity and brine migration in geologic CO_2 storage. International Journal of Greenhouse Gas Control, 28, 96-113.

Dempsey, D., O'Malley, D., & Pawar, R. (2015). Reducing uncertainty associated with CO_2 injection and brine production in heterogeneous formations. International Journal of Greenhouse Gas Control, 37, 24-37.

Dutton, A. R., Harden, R., Nicot, J.-P., and O'Rourke, D., 2003, Groundwater availability model for the central part of the Carrizo-Wilcox aquifer in Texas: The University of Texas at Austin, Bureau of Economic Geology, final technical report prepared for Texas Water Development Board, under contract no. 2001-483-378, 295 p. + apps.

Dutton, A. R., Nicot, J.-P., and Kier, K. S., 2006, Hydrologic convergence of hydropressured and geopressured zones, Central Texas, Gulf of Mexico Basin, USA: Hydrogeology Journal, v. 14, p. 859–867.

Dutton, S. P., S. J. Clift, D. S. Hamilton, H. S. Hamlin, T. F. Hentz, W. E. Howard, M. S. Akhter, and S. E. Laubach, 1993, Major low-permeability sandstone gas reservoirs in the continental United States, The University of Texas at Austin Bureau of Economic Geology Report of Investigations No. 211, 221p.

Enomoto, C. B., K. R. Scott, B. Valentine, P. C. Hackley, K. Dennen, and C. Lohr, 2012, Preliminary evaluation of the shale gas prospectivity of the Lower Cretaceous Pearsall Formation in the onshore Gulf Coast region, United States: Gulf Coast Association of Geological Societies Transactions, v. 62, p. 93–115.

Ewing, T. E., 1991, The tectonic framework of Texas: The University of Texas at Austin. Bureau of Economic Geology, 36 p.

Ewing, T. E., 2010, Pre-Pearsall geology and exploration plays in South Texas: Gulf Coast Association of Geological Societies Transactions, v. 60, p. 241-260.

Flett, M., Beacher, G., Brantjes, J., Burt, A., Dauth, C., Koelmeyer, F., Tankersley, T. (2008). Gorgon project—subsurface evaluation of carbon dioxide disposal under Barrow Island. SPE Asia Pacific Oil and Gas Conference, SPE 116372. October 20-22, Perth, Australia.

Galloway, W. E., Ewing, T. E., Garrett C. M., Jr., Tyler N., and Bebout, D. G., 1983, Atlas of Major Texas Oil Reservoirs: The University of Texas at Austin, Bureau of Economic Geology, 139 p.

George, P.G., R.E. Mace, and R. Petrossian, 2011, Aquifers of Texas, Texas Water Development Board report #380, 172p.

Hackley, P. C., 2012, Geological and geochemical characterization of the Lower Cretaceous Pearsall Formation, Maverick Basin, south Texas: A future shale gas resource?, AAPG Bull., 96(8), p.1449–1482.

Hamlin, H. S., and de la Rocha, L., 2015, Using electric logs to estimate groundwater salinity and map brackish groundwater resources in the Carrizo-Wilcox Aquifer in South Texas: GCAGS Journal, v. 4, p. 109-131.

Hamlin, H. S., 1988, Depositional and Ground-Water Flow Systems of the Carrizo-Upper Wilcox, South Texas, The University of Texas at Austin Bureau of Economic Geology Report of Investigations #175, 61p.

Han, D. H., 1986, Effects of porosity and clay content on acoustic properties of sandstones and unconsolidated sediments, Ph. D. dissertation, Stanford University.

Holt, C.L.R. Jr., 1959, Geology and Ground-Water Resources of Medina County Texas, USGS Water-Supply Paper 1422, 213p.

Hopf, R.W., 1973, Delta Environments in the Upper Midway Formation of Wilson County, Texas: South Texas Geological Society Bulletin, 13(5), p.9-26.

Hosseini, S. A. and Nicot, J. P. (2012). Scoping analysis of brine extraction/re-injection for enhanced CO2 storage. Greenhouse Gases: Science and Technology, 2(3), 172-184.

Hosseini, S. A., Lashgari, H., Choi, J.-W., Nicot, J. -P., Lu, J., and Hovorka, S. D., 2013, Static and dynamic reservoir modeling for geological CO_2 sequestration at Cranfield, Mississippi, U.S.A.: International Journal of Greenhouse Gas Control, v. 18, p. 449-462.

Hovorka, S. D., R. E. Mace, and E. W. Collins, 1998, Permeability Structure of the Edwards Aquifer, South Texas—Implications for aquifer management, The University of Texas at Austin Bureau of Economic Geology Report of Investigations #250, 55p.

Hull, D.C., 2011, Stratigraphic Architecture, Depositional Systems, and Reservoir Characteristics of the Pearsall Shale-Gas System, Lower Cretaceous, South Texas, M.S. Thesis, The University of Texas at Austin, 192p.

Hyndman, D. W., Harris, J. M., & Gorelick, S. M. (1994). Coupled seismic and tracer test inversion for aquifer property characterization. Water Resources Research, 30(7), 1965–1977.

Kelley, V. A., Deeds, N. E., Fryar, D. G., and Nicot, J.-P., 2004, Groundwater availability model for the Queen City and Sparta aquifers: final report prepared for the Texas Water Development Board: INTERA, Inc., Austin, Texas, final report prepared for the Texas Water Development Board, variously paginated

Konikow L., 2013, Groundwater depletion in the United States (1900–2008), US Geological Survey Scientific Investigation Report 2013–5079, 63p.

Knox, P. R., V. A. Kelley, A. Vreugdenhil, N. Deeds, and S. Seni, 2007, Structure of the Yegua-Jackson aquifer of the Texas Gulf Coast Plain: Intera, Inc., Austin, Texas, report prepared for the Texas Water Development Board, variously paginated.

Kreitler, C., R. Bassett, J. Beach, L. Symank, D. O'Rourke, A. Papafotiou, J. Ewing, and V. Kelley, 2013, Evaluation of Hydrochemical and Isotopic Data in Groundwater Management

Areas 11,12, and 13, contract report prepared by LBG-Guyton, Austin, Texas for the Texas Water Development Board, July 2013, 454p.

Landrø, M. (2000). Discrimination between pressure and fluid saturation changes from time-lapse seismic data. Geophysics, 66(3), 836–844.

Landrø, M., Digranes, P., & Strønen, L. K. (2001). Mapping reservoir pressure and saturation changes using seismic methods - possibilities and limitations. First Break, 19(12), 671–684.

LBG-Guyton & Associates, 2003, Brackish groundwater manual for Texas Regional Water Planning Groups: Report prepared for the Texas Water Development Board, Austin, Texas, 188p.

Leven, C., & Dietrich, P. (2006). What information can we get from pumping tests?-comparing pumping test configurations using sensitivity coefficients. Journal of Hydrology, 319(1-4), 199-215.

Lindgren, R.J., A.R. Dutton, S.D. Hovorka, S.R.H. Worthington, and Scott Painter, 2004, Conceptualization and Simulation of the Edwards Aquifer, San Antonio Region, Texas, U.S. Geological Survey Scientific Investigations Report 2004–5277, 143p. + plates

Liu, G., Gorecki, C. D., Saini, D., Bremer, J. M., Klapperich, R. J., & Braunberger, J. R. (2015). Storage capacity enhancement and reservoir management using water extraction: Four site case studies. International Journal of Greenhouse Gas Control, 35, 82-95.

Loucks, R.G., 1977, Porosity development and distribution in shoal-water carbonate complexes – Subsurface Pearsall Formation (Lower Cretaceous), South Texas, *in* Cretaceous Carbonates of Texas and Mexico: Applications to Subsurface Exploration D. G. Bebout and R. G. Loucks Editors, The University of Texas at Austin Bureau of Economic Geology Report of Investigations #89, 322 p.

Loucks, R. G., 2002, Controls on Reservoir Quality in Platform-Interior Limestones Around the Gulf of Mexico: Example from the Lower Cretaceous Pearsall Formation in South Texas, Gulf Coast Association of Geological Societies Transactions (GCAGS), 52, p.659-672.

Lu, J., Kharaka, Y. K., Thordsen, J. J., Horita, J., Karamalidis, A., Griffith, C., Hakala, J. A., Ambats, G., Cole, D. R., Phelps, T. J., Manning, M. A., Cook, P. J., and Hovorka, S. D., 2012, CO_2-rock-brine interactions in Lower Tuscaloosa Formation at Cranfield CO_2 sequestration site, Mississippi, U.S.A.: Chemical Geology, v. 291, p. 269-277.

Lu, J., Mickler, P., Nicot, J.-P., Yang, C., and Romanak, K. D., 2014, Geochemical impact of oxygen on siliciclastic carbon storage reservoirs: International Journal of Greenhouse Gas Control, v. 21, p. 214-231, http://doi.org/10.1016/j.ijggc.2013.12.017

Lu, J., Mickler, P., Nicot, J.-P., Yang, C., and Darvari, R., 2016a, Geochemical impact of O_2 impurity in CO_2 stream on carbonate carbon-storage reservoirs: International Journal of Greenhouse Gas Control, v. 47, p. 159-175, http://doi.org/10.1016/j.ijggc.2016.01.039.

Lu, J., Nicot, J.-P., Mickler, P., Ribeiro, L. H., and Darvari, R., 2016b, Alteration of Bakken reservoir rock during CO_2-based fracturing--An autoclave reaction experiment: Journal of Unconventional Oil and Gas Resources, v. 14, p. 72-85.

McBride, M. W., C.M. Woodruff, Jr., Lisa E. Craig, 1979, Facies Distribution within the Hosston Formation Central Texas -- Implications to Low Temperature Geothermal Waters, Gulf Coast Association of Geological Societies Transactions, Vol.29, p.172-178

Meckel, T.A., M. Zeidouni, S.D. Hovorka, and S.A. Hosseini, 2013, Assessing sensitivity to well leakage from three years of continuous reservoir pressure monitoring during CO2 injection at Cranfield, MS, USA, International Journal of Greenhouse Gas Control, 18: 439-448.

MIT. (2011). Gorgon fact sheet: Carbon dioxide capture and storage project. Retrieved April 2015, from http://sequestration.mit.edu/tools/projects/gorgon.html

Nicot, J.-P., Scanlon, B. R., Yang, C., and Gates, J., 2010, Geological and geographical attributes of the South Texas Uranium Province: The University of Texas at Austin, Bureau of Economic Geology, contract report prepared for the Texas Commission on Environmental Quality, 156 p.

Nicot, J. -P., and Scanlon, B. R., 2012, Water use for shale-gas production in Texas, U.S.: Environmental Science and Technology, v. 46, p. 3580-3586.

Nicot, J. -P., Costley, R., and Huang, Y., 2013, Geographical, geological, and hydrogeological attributes of formations in the footprint of the Eagle Ford Shale: The University of Texas at Austin, Bureau of Economic Geology, contract report prepared for the Houston Advanced Research Center (HARC) Phase III, 200 p.

Osdal, B., Husby, O., Aronsen, H.A., Chen, N., Alsos, T., 2006, Mapping the fluid front and pressure build up using 4D data on Norne field. The Leading Edge, 25(9), 1134-1141.

Petersen, M. D., C. S. Mueller, M. P. Moschetti, S. M. Hoover, A. L. Llenos, W. L. Ellsworth, A. J. Michael, J. L. Rubinstein, A. F. McGarr, and K. S. Rukstales, 2016, One-Year Seismic Hazard Forecast for the Central and Eastern United States from Induced and Natural Earthquakes, US Geological Survey Open-File Report 2016-1035, 52p., doi:10.3133/ofr20161035.

Pisasale, E. T., 1980, Surface and subsurface depositional systems in the Escondido Formation, Rio Grande Embayment, South Texas: The University of Texas at Austin, Master's thesis, 172 p.

Rahmani, A. R., S. L. Bryant, C. Huf, M. Ahmadian, W. Zhang, and Q. H. Liu, 2015, Characterizing reservoir heterogeneities using magnetic nanoparticles: SPE Reservoir Simulation Symposium, Society of Petroleum Engineers 173195-MS.

Roy, E. C. Jr., 1984, Stratigraphy and Sedimentology of the Kincaid Formation, Midway Group (Paleocene), Upper Rio Grande Embayment, Texas: Gulf Coast Association of Geological Societies Transactions, 34, p.211-216

Rubin, Y., Mavko, G., & Mavko, J. (1992). Mapping permeability in heterogeneous aquifers using hydrologic and seismic data. Water Resources Research, 28(17), 1809–1816.

Scott, R. J., 2004, The Maverick Basin: New Technology - New Success, Gulf Coast Association of Geological Societies Transactions (GCAGS), 54, p.603-620.

Senger, R. K. and C. W. Kreitler, 1984, Hydrogeology of the Edwards Aquifer, Austin Area, Central Texas, The University of Texas at Austin Bureau of Economic Geology Report of Investigations #141, 35p.

Serrano, S. E. (1996). The Theis solution in heterogeneous aquifers. Ground Water, 35, 463-467.

Shapiro, S.A., 2000, An inversion for fluid transport properties of three-dimensionally heterogeneous rocks using induced microseismicity, Geophysical Journal International, 143: 931-936.

Shapiro, S.A., C. Dinske, and J. Kummerow, 2007, Probability of a given-magnitude earthquake induced by a fluid injection, Geophysical Research Letters, 34: L22314.

Shapiro, S.A., and C. Dinske, 2009, Fluid-induced seismicity: Pressure diffusion and hydraulic fracturing, Geophysical Prospecting, 57: 301-310.

Snedden, J.W., 1991, Origin and sequence stratigraphic significance of large dwelling traces in the Escondido Formation (Cretaceous, Texas, USA): Palaios, v. 6, no. 6, p. 541–552.

Sun, A. Y., Lu, J., Freifeld, B., Hovorka, S., Islam, A., 2016. Using pulse testing for leakage detection in carbon storage reservoirs: A field demonstration. International Journal of Greenhouse Gas Control, 46, 215-227.

Sun, A. Y., Lu, J., and Hovorka, S., 2015. A harmonic pulse testing method for leakage detection in deep subsurface storage formations. Water Resources Research, 51(6), 4263-4281.

Sun, A.Y., Kianinejad, A., Lu, J., Hovorka, S., 2014. A frequency-domain diagnosis tool for early leakage detection at geologic carbon sequestration sites. Energy Proc. 63, 4051–4061.

Tura, A., & Lumley, D. (2000). Estimating pressure and saturation changes from time-lapse AVO data. Offshore Technology Conference, OTC12130.

Tyler, N. and W.A. Ambrose, 1986, Depositional systems and oil and gas plays in the Cretaceous Olmos Formation, South Texas, The University of Texas at Austin Bureau of Economic Geology Report of Investigations #152, 42p.

Weise, B.R., 1980, Wave-dominated delta systems of the Upper Cretaceous San Miguel Formation, Maverick Basin, South Texas, The University of Texas at Austin Bureau of Economic Geology Report of Investigations #107, 39p.

Xue, L., and Galloway, W. E., 1995, High-resolution depositional framework of the Paleocene middle Wilcox strata, Texas coastal plain: American Association of Petroleum Geologists Bulletin, v. 79, no. 2, p. 205–230.

Yang, F., Bai, B., Dunn-Norman, S., Nygaard, R., & Eckert, A. (2014). Factors affecting CO2 storage capacity and efficiency with water withdrawal in shallow saline aquifers. Environmental Earth Sciences, 71, 267-275.

Zoback, M. D., and S. M. Gorelick, 2012, Earthquake triggering and large-scale geologic storage of carbon dioxide, Proceedings of the National Academies of Science, 109(26), p.10164–10168, doi: 10.1073/pnas.1202473109.

Zoback, M. D., and S. M. Gorelick, 2015, To prevent earthquake triggering, pressure changes due to CO_2 injection need to be limited, Proceedings of the National Academies of Science, 112(33), p.E4510, doi/10.1073/pnas.1508533112.

X. Appendix A: Fresh Water Well Yields

In order to assess typical water well yields in the general area of the Devine Test site (Medina and Frio counties), we collected TDLR data and created histograms of their distributions for each formation (Figure 83, Figure 84, Figure 85, and Figure 86). Two side by side histograms are displayed for each formation. The left panel has the full range, from 0 gpm to 2000 gpm, except Edwards (Figure 86b) and below Wilcox and undefined Edwards (Figure 86c) whose maximum x-axis value is 4000 gpm. The right panel focuses on the typically more frequent values with a 0-100 gpm range.

Well yields less than 50 gpm are very common and the most likely yield for a typical domestic (that is, affordable) well drill in any formation. We also mapped wells for which we have information about the producing formation (Figure 87a). There are 1246 wells shown in the map out of 2320 wells in the TDLR database in Medina and Frio counties. Figure 87, Figure 88, and Figure 89 displays fresh water well yield per formation starting with the youngest in Southern Frio County (Sparta, Figure 87b) and ending with the oldest in Medina County (Edwards, Figure 89b). Clearly the formations with wells with large yields are the Carrizo and related Upper Wilcox (Figure 88b,c) whereas the more clayey Middle and Lower Wilcox (Figure 88d and Figure 89a) with lower net sand, more spatially restricted sand lenses, and more brackish water display only a few large wells. Middle and Lower Wilcox as well as Queen City (Figure 87d) are penetrated only in the outcrop, consistent with the relatively poor quality of the host formation and water quality. The Edwards (Figure 89c) also displays large wells in its downdip version.

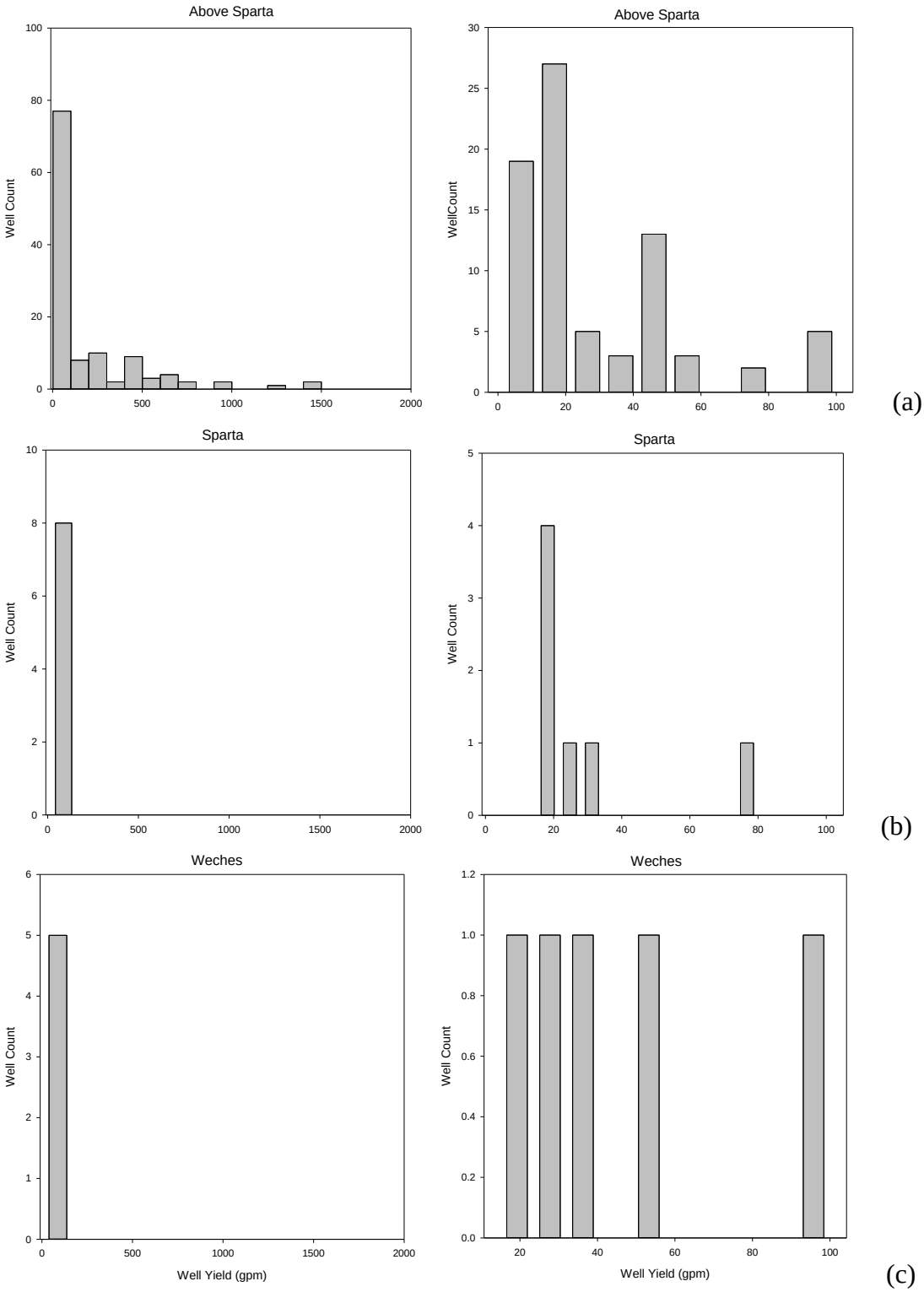

Figure 83. Histogram of well yield in Weches (c), Sparta (b) and younger layers (a)

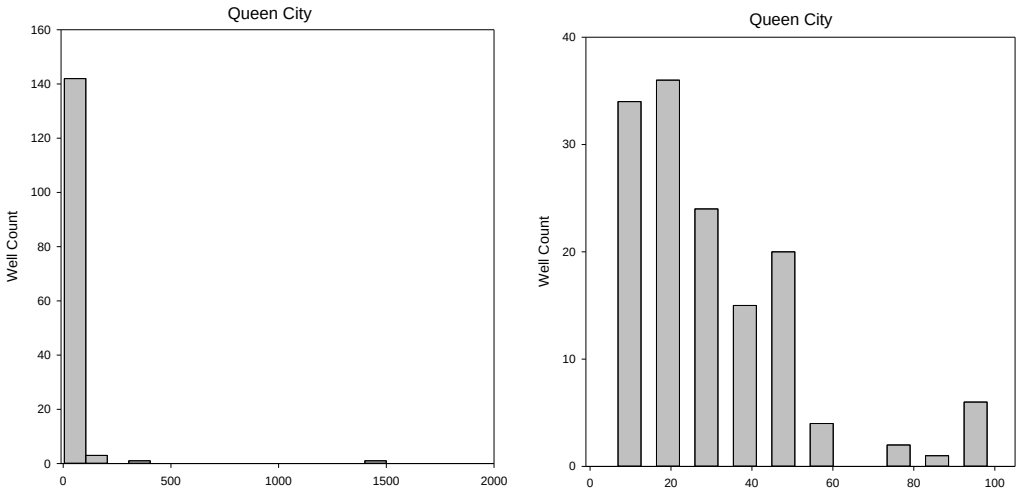

(a)

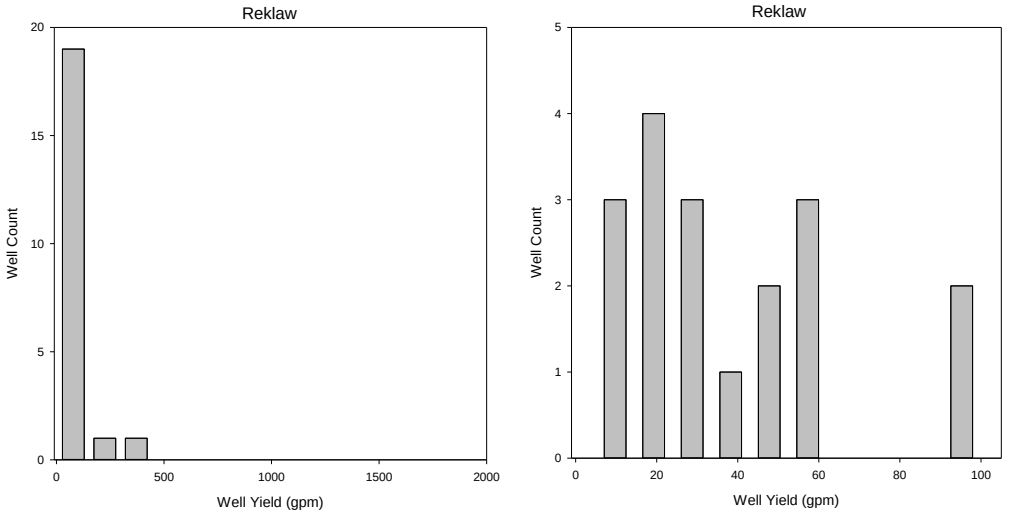

(b)

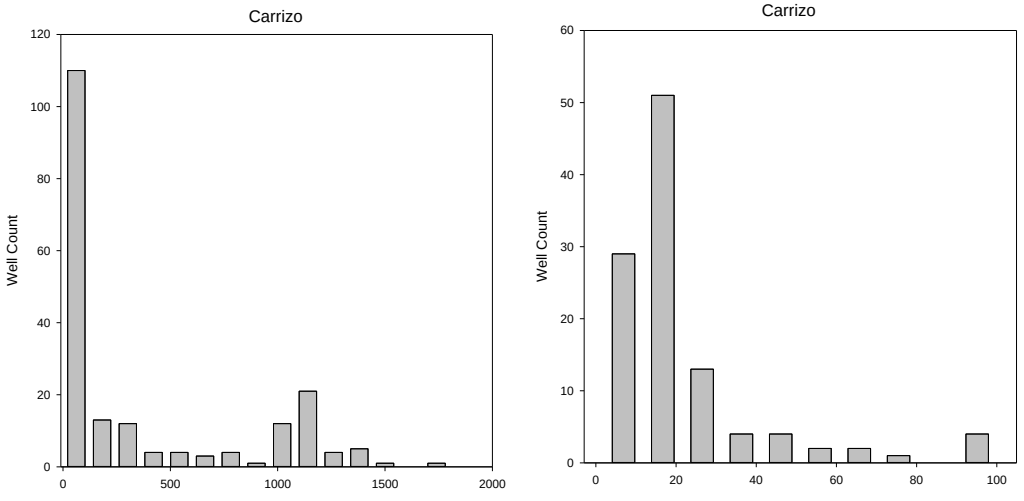

(c)

Figure 84. Histogram of well yield in Queen City (a), Reklaw (b) and Carrizo (c)

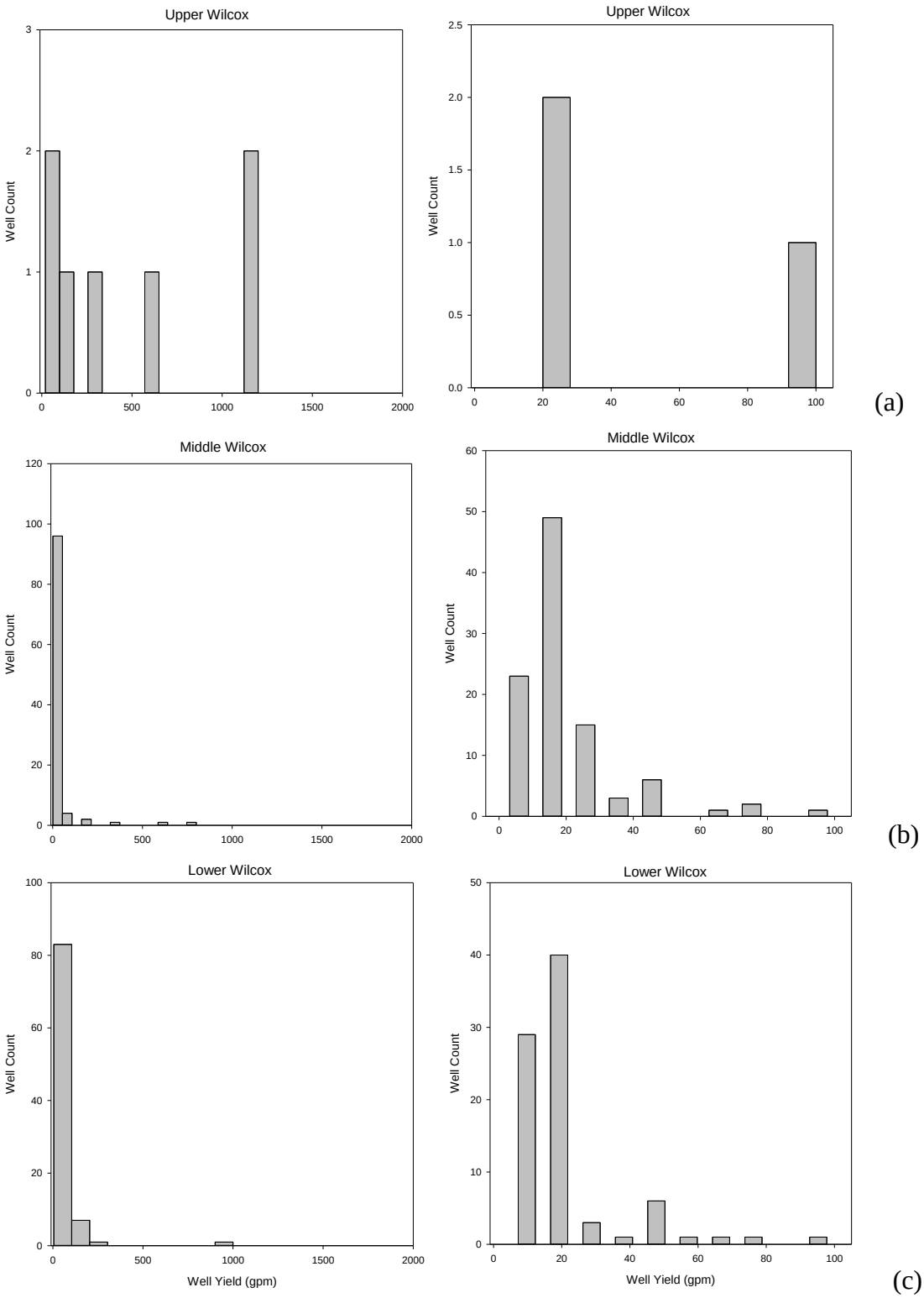

Figure 85. Histogram of well yield in Upper (a), Middle (b) and Lower Wilcox (c)

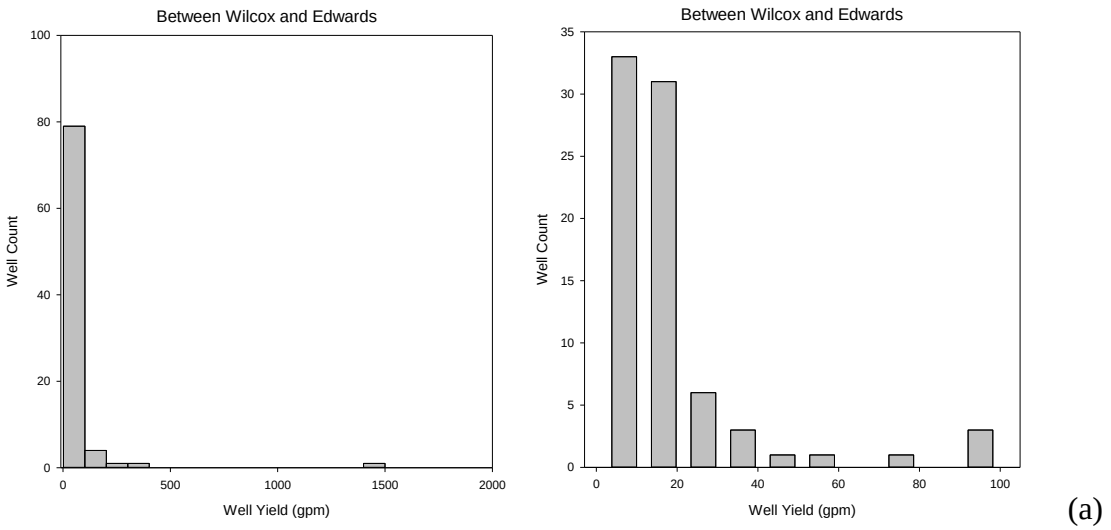

(a)

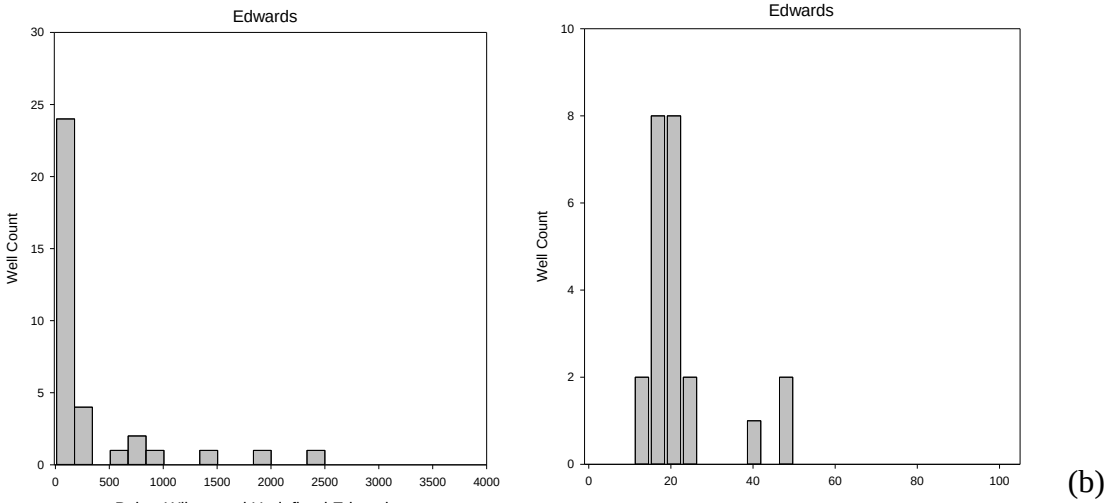

(b)

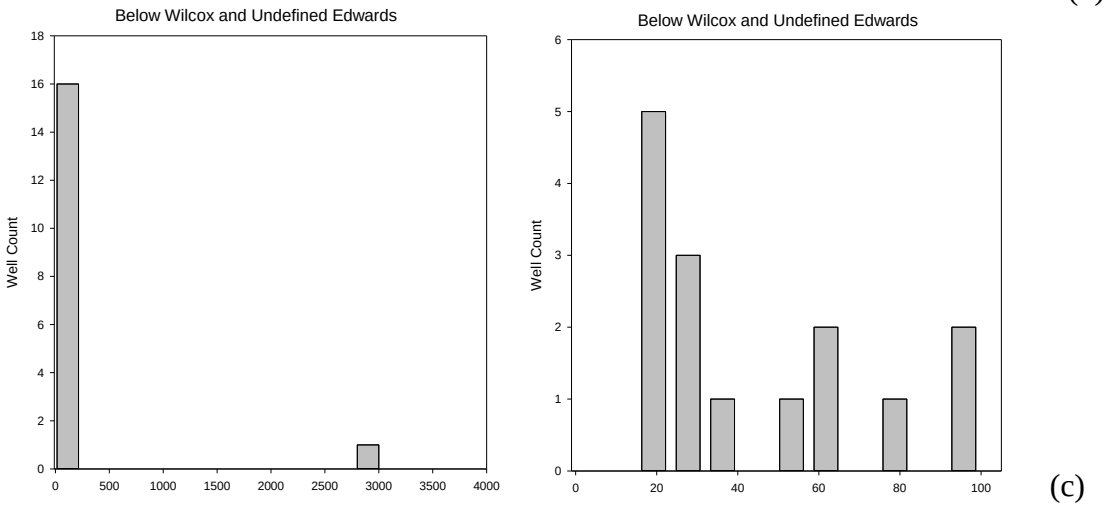

(c)

Figure 86. Histogram of well yield in formations between Wilcox and Edwards (a), Edwards (b) and older layers (c)

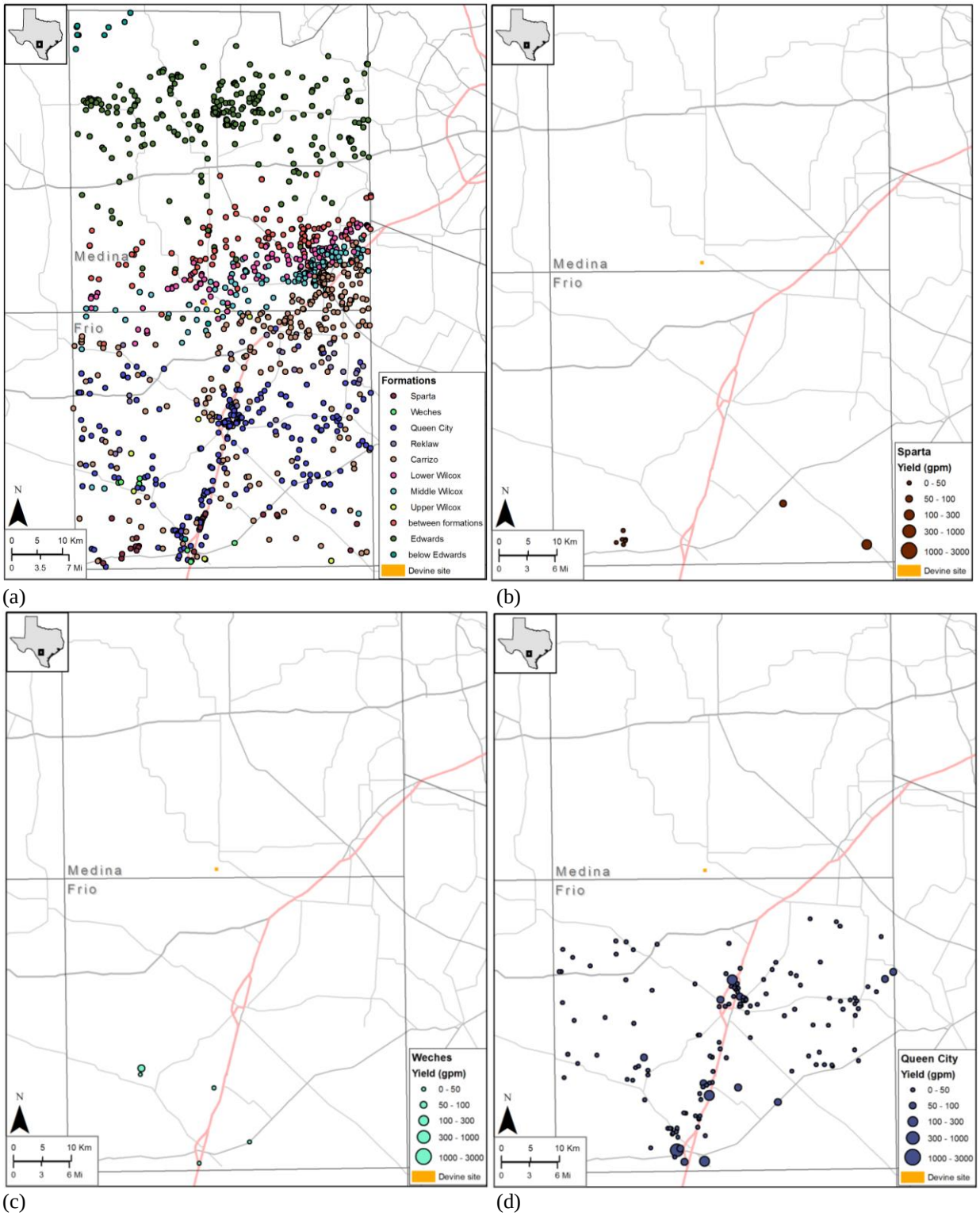

Figure 87. Spatial distribution in well yields: all formations (a), Sparta (b), Weches (c), and Queen City (d).

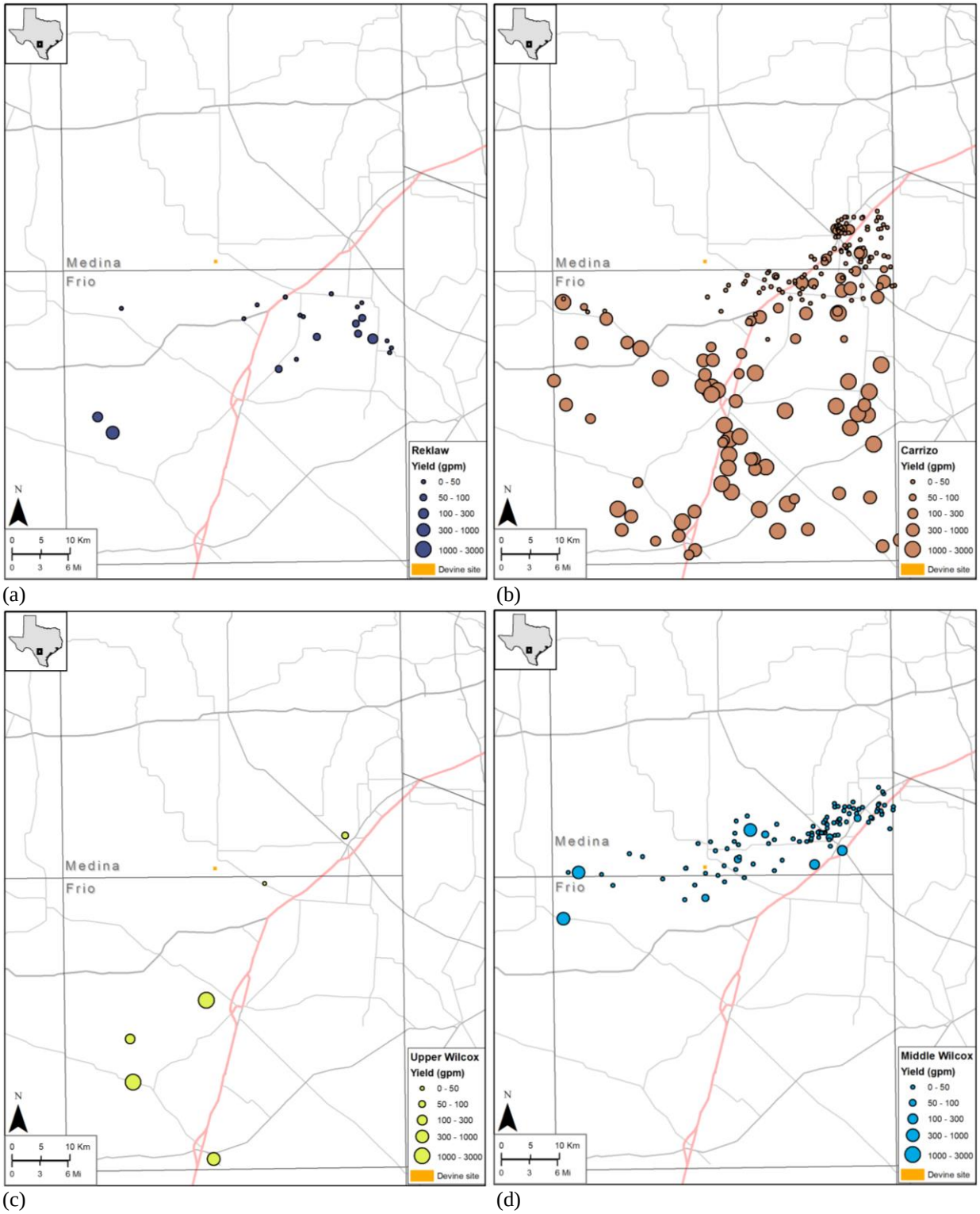

Figure 88. Spatial distribution in well yields: Reklaw (a), Carrizo (b), Upper Wilcox (c), and Middle Wilcox (d).

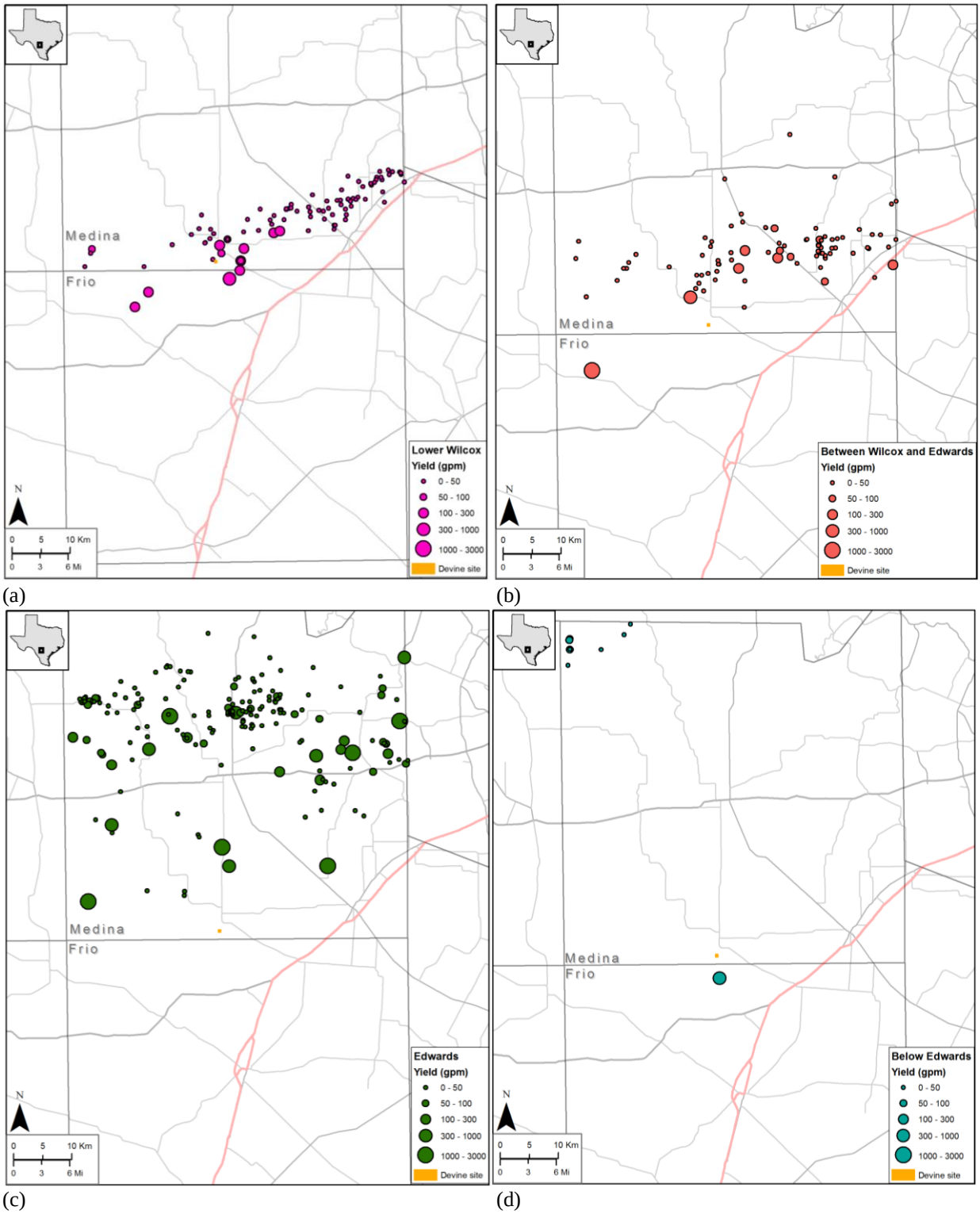

Figure 89. Spatial distribution in well yields: Lower Wilcox (a), between Edwards and Wilcox (b), Edwards (c) and below Edwards (d).

XI. Appendix B: Results of Autoclave Experiments

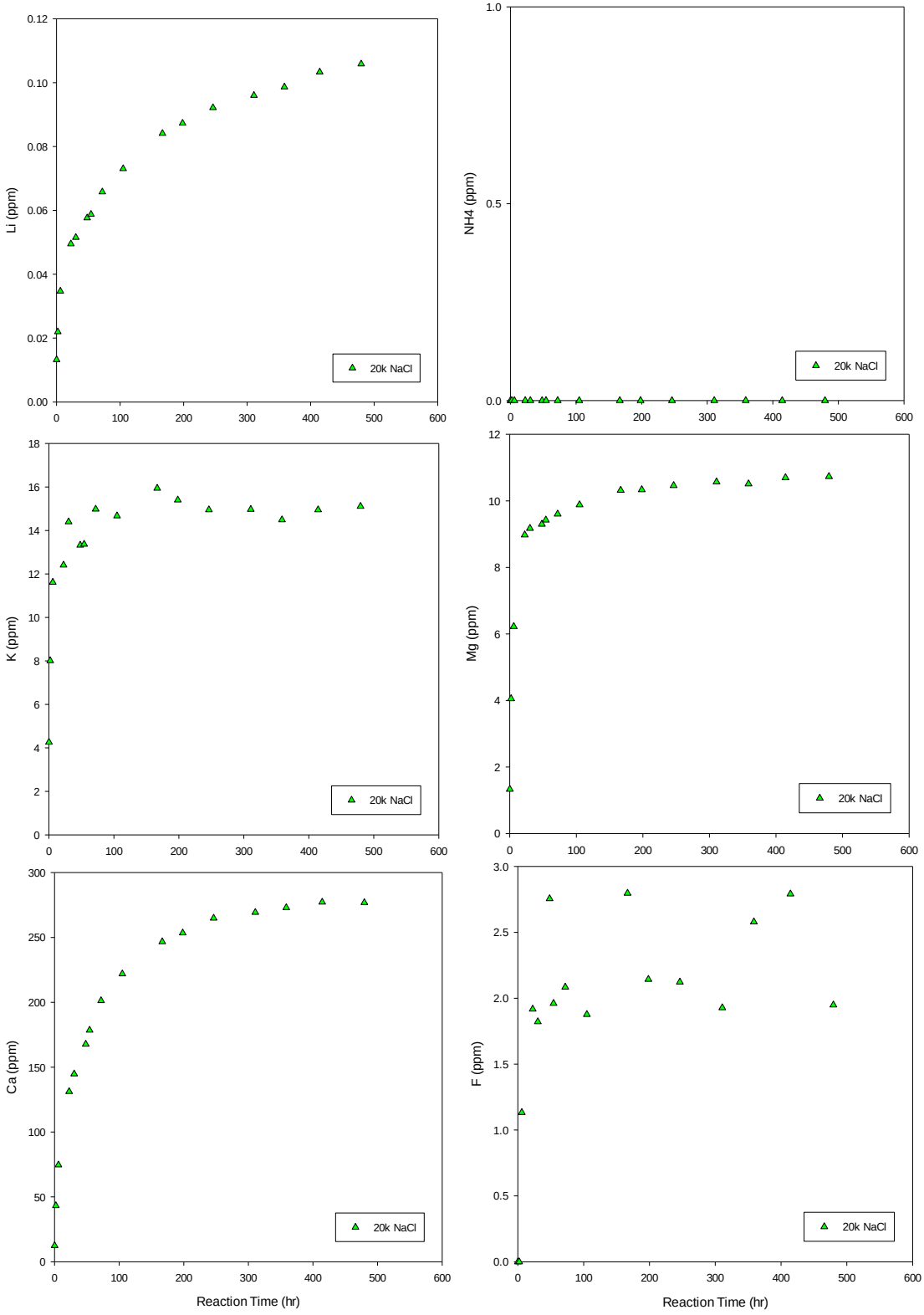

Figure 90. Analytical results of autoclave experiments: Li, NH_4, K, Mg, Ca, F

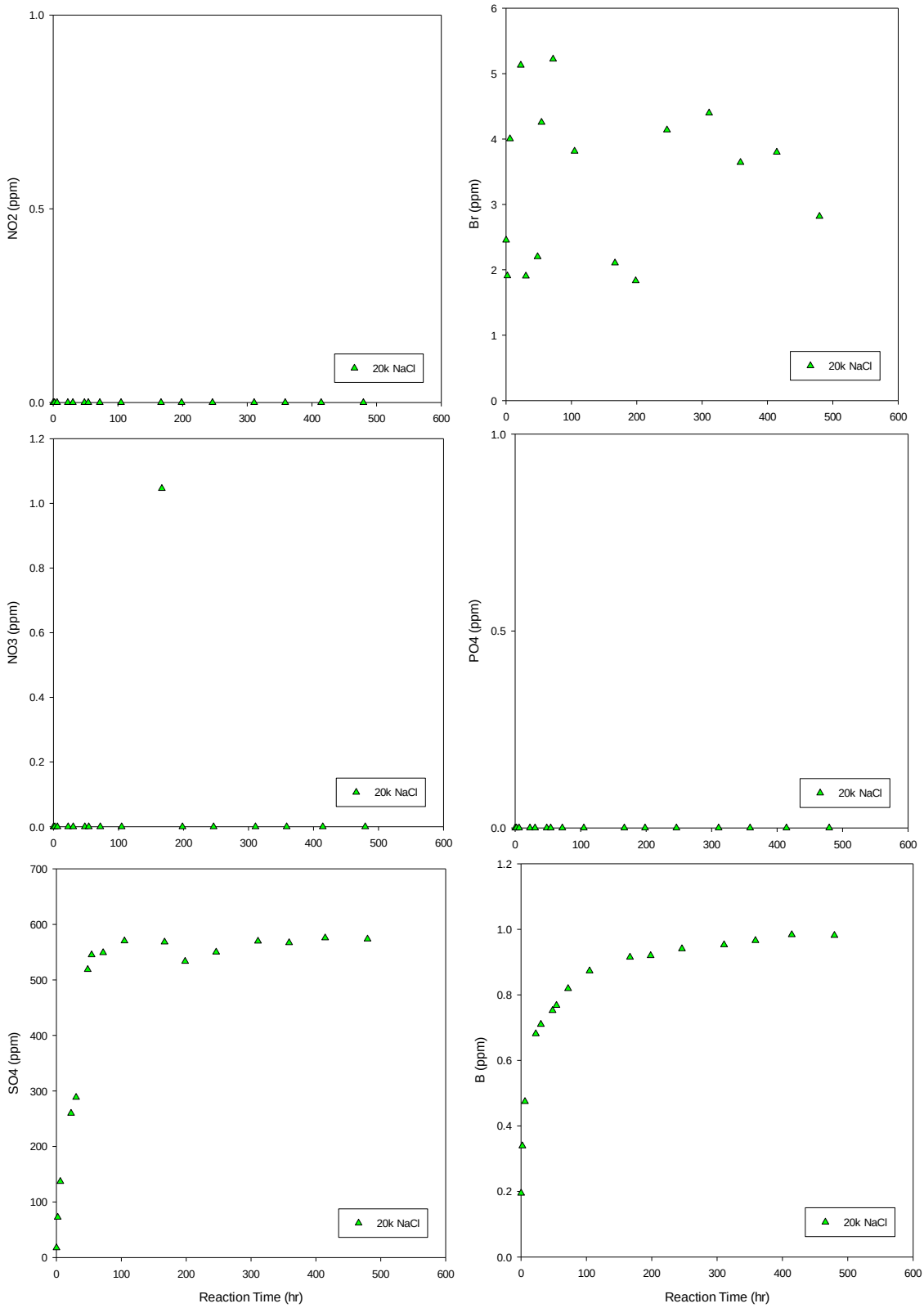

Figure 91. Analytical results of autoclave experiments: NO_2, Br, NO_3, PO_4, SO_4, B

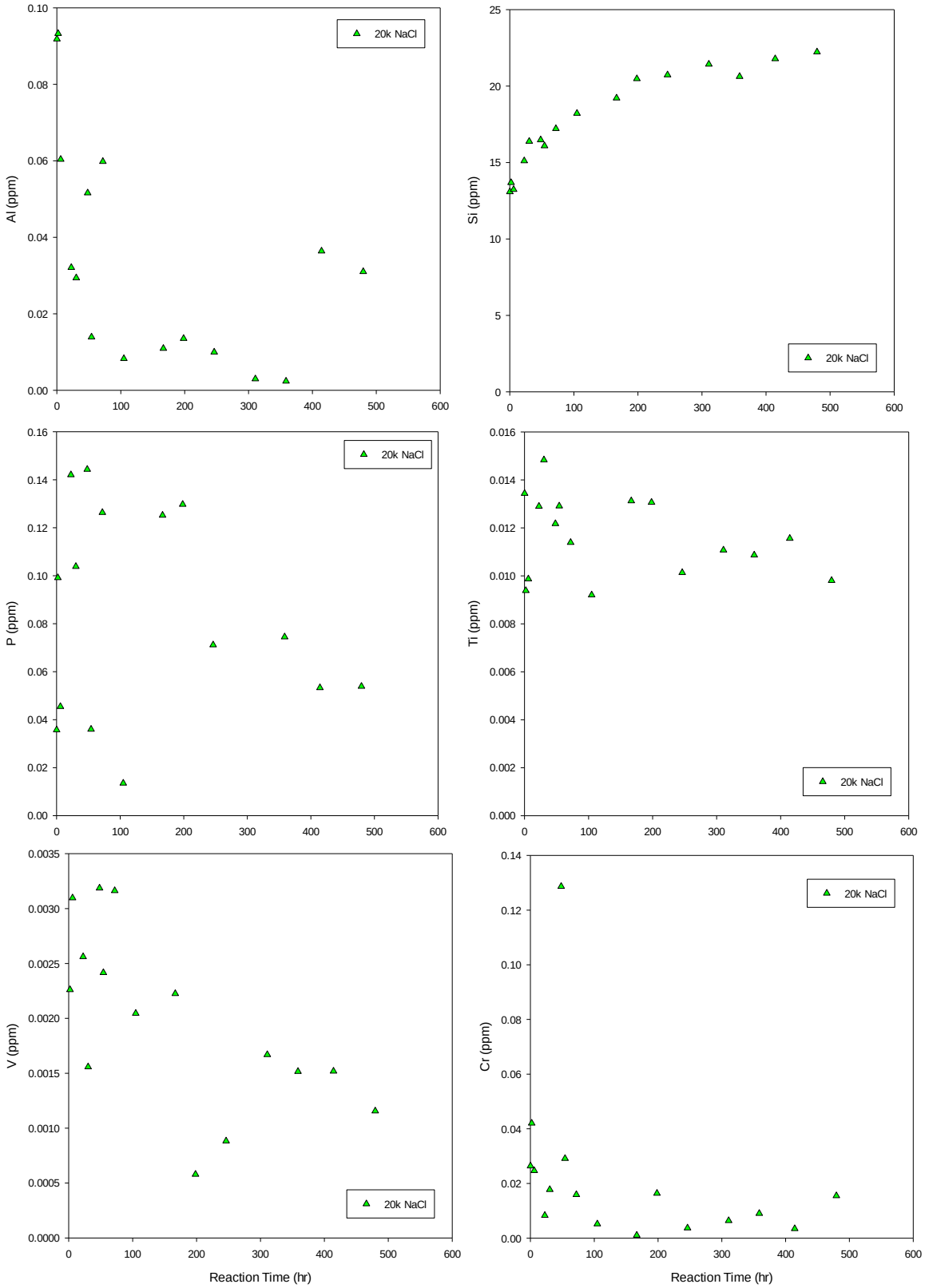

Figure 92. Analytical results of autoclave experiments: Al, Si, P, Ti, V, Cr

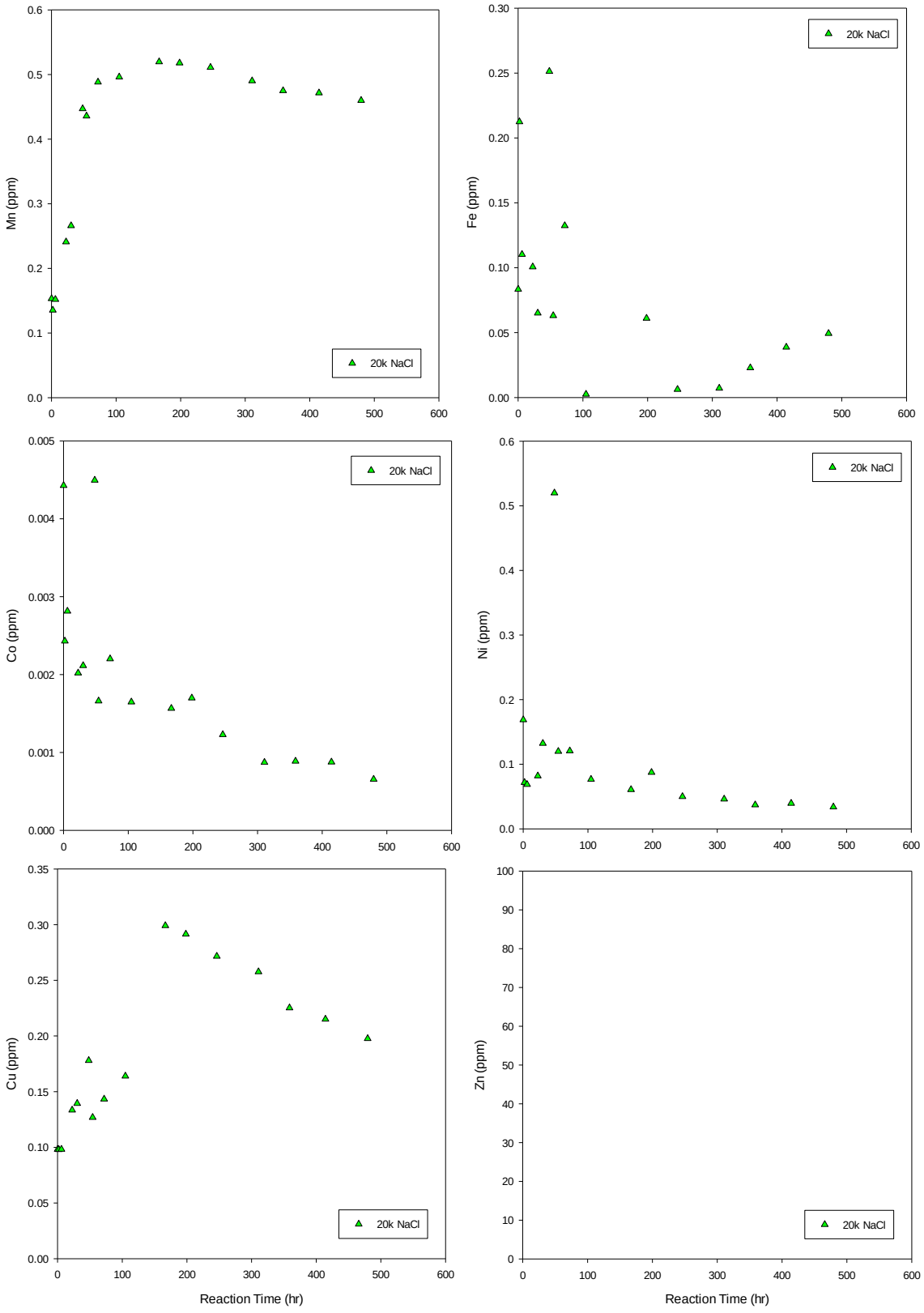

Figure 93. Analytical results of autoclave experiments: Mn, Fe, Co, Ni. Cu, Zn

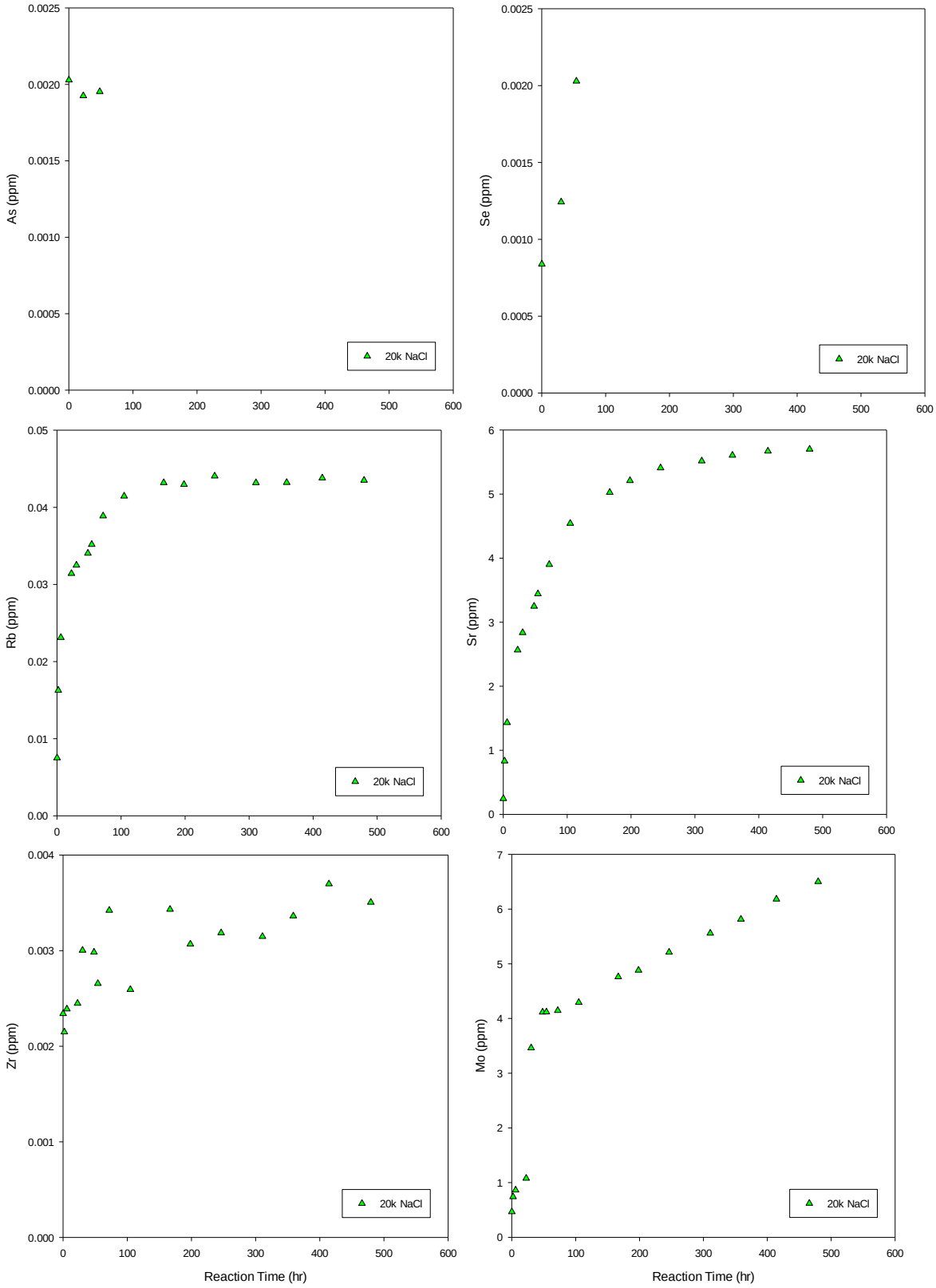

Figure 94. Analytical results of autoclave experiments: As, Se, Rb, Sr, Zr, Mo

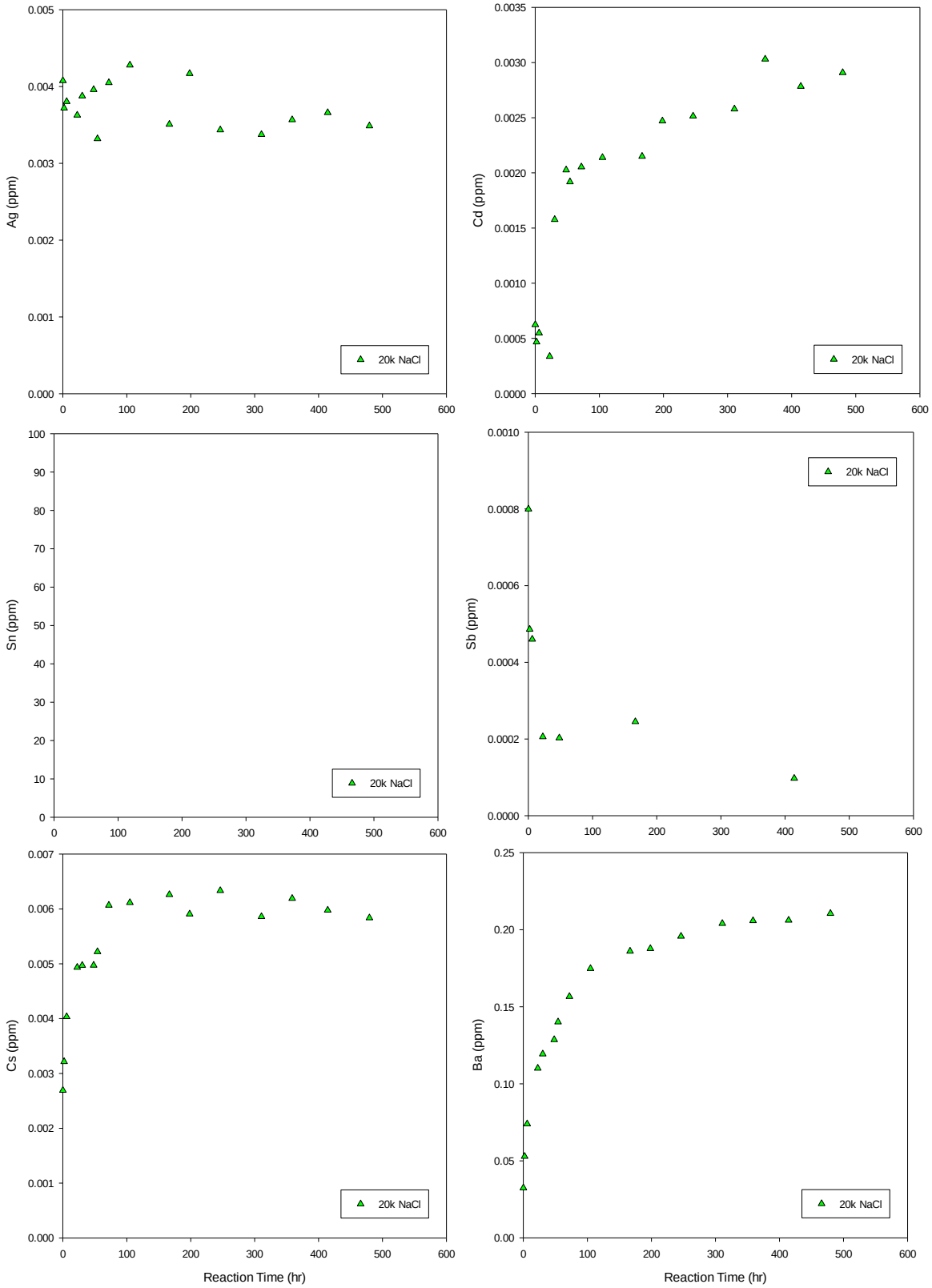

Figure 95. Analytical results of autoclave experiments: Ag, Cd, Sn, Sb, Cs, Ba

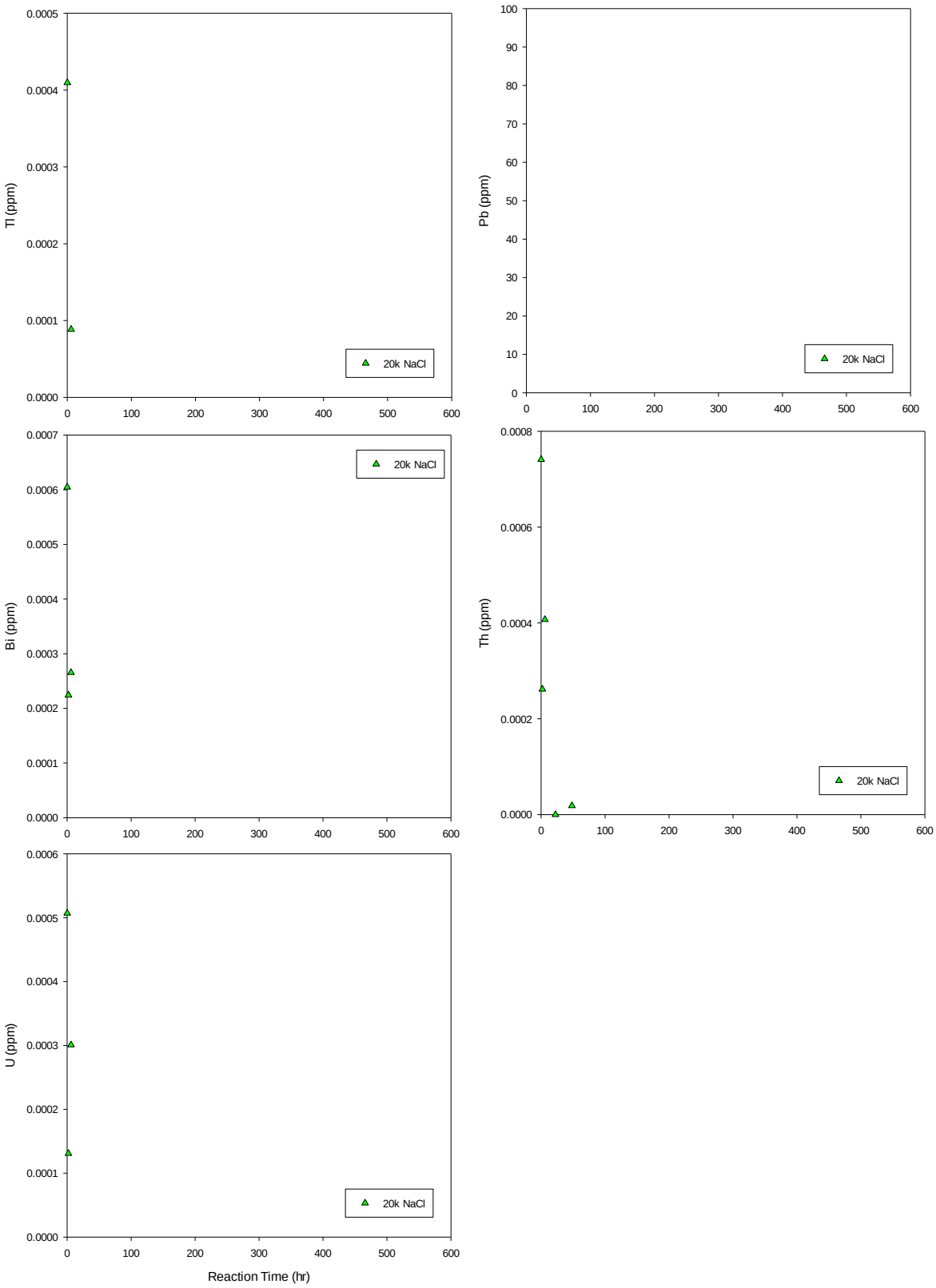

Figure 96. Analytical results of autoclave experiments: Tl, Pb, Bi, Th, U

Table 13. Analytical results of autoclave experiments.

IC results:

20k NaCl, 80C, 280 bar

Sample ID	Li	Na	NH4	K	Mg	Ca	F	Cl	NO2	Br	NO3	PO4	SO4	HCO3
ME-A1	0.00	7480.51	0.00	4.56	0.00	10.91	0.00	8236.42	0.00	2.45	0.00	0.00	17.54	5694.97
ME-A2	0.00	7492.41	0.00	8.43	1.21	40.09	0.00	8252.61	0.00	1.91	0.00	0.00	72.53	5730.21
ME-A3	0.00	7539.87	0.00	10.69	2.01	70.98	1.13	8316.56	0.00	4.00	0.00	0.00	136.93	5760.72
ME-A4	0.04	7728.39	0.00	13.08	4.00	127.76	1.92	8430.08	0.00	5.13	0.00	0.00	259.83	6092.76
ME-A5	0.05	7634.91	0.00	13.45	4.59	140.51	1.82	8458.61	0.00	1.90	0.00	0.00	288.45	5804.34
ME-A6	0.05	8026.74	0.00	15.23	5.54	239.10	2.76	8747.14	0.00	2.20	0.00	0.00	518.80	6359.59
ME-A7	0.06	8198.14	0.00	15.88	6.25	252.88	1.96	8877.32	0.00	4.26	0.00	0.00	545.18	6604.49
ME-A8	0.07	8002.76	0.00	15.84	5.64	254.32	2.08	8705.74	0.00	5.22	0.00	0.00	549.12	6376.33
ME-A9	0.10	8150.64	0.00	15.33	7.02	266.37	1.88	8852.99	0.00	3.81	0.00	0.00	570.25	6533.10
ME-A10	0.07	8101.72	0.00	16.05	6.58	266.87	2.80	8760.61	0.00	2.10	1.05	0.00	568.34	6562.46
ME-A11	0.12	7979.48	0.00	15.37	5.63	245.40	2.14	8670.13	0.00	1.83	0.00	0.00	533.48	6370.15
ME-A12	0.10	7960.30	0.00	15.61	5.50	254.20	2.12	8746.91	0.00	4.14	0.00	0.00	550.06	6190.89
ME-A13	0.13	8146.42	0.00	15.44	6.48	265.80	1.93	8781.66	0.00	4.40	0.00	0.00	569.83	6640.36
ME-A14	0.12	8193.64	0.00	15.48	7.06	270.11	2.58	8773.93	0.00	3.64	0.00	0.00	567.13	6796.97
ME-A15	0.13	8126.99	0.00	15.80	6.78	269.71	2.79	8846.86	0.00	3.80	0.00	0.00	575.74	6480.73
ME-A16	0.10	8121.82	0.00	15.29	7.27	268.80	1.95	8858.69	0.00	2.82	0.00	0.00	573.67	6451.58

ICP results:

20k NaCl, 80 C, 280 bar

Sample ID	time(hr)	Li / 7 [#3]	B / 11 [#3]	Na / 23 [#3]	Mg / 26 [#3]	Al / 27 [#3]	Si / 28 [#2]	P / 31 [#3]	K / 39 [#1]	Ca / 44 [#3]	Ti / 47 [#3]	V / 51 [#1]
ME-A1	0.05	0.01	0.2	7987.9	1.3	0.09	13.1	0.04	4.3	12.4	0.01	<0.00001
ME-A2	1.98	0.02	0.3	7960.1	4.1	0.09	13.7	0.10	8.0	43.2	0.01	0.002
ME-A3	6.00	0.03	0.5	7957.9	6.2	0.06	13.2	0.05	11.6	74.6	0.01	0.003
ME-A4	22.53	0.05	0.7	8075.0	9.0	0.03	15.1	0.14	12.4	131.2	0.01	0.003
ME-A5	30.25	0.05	0.7	8081.3	9.2	0.03	16.4	0.10	14.4	144.8	0.01	0.002
ME-A6	48.17	0.06	0.8	7943.8	9.3	0.05	16.5	0.14	13.3	167.7	0.01	0.003
ME-A7	54.23	0.06	0.8	8102.3	9.4	0.01	16.1	0.04	13.4	178.4	0.01	0.002
ME-A8	71.95	0.07	0.8	8142.6	9.6	0.06	17.2	0.13	15.0	201.3	0.01	0.003
ME-A9	104.78	0.07	0.9	8263.9	9.9	0.01	18.2	0.01	14.7	221.9	0.01	0.002
ME-A10	166.65	0.08	0.9	8228.9	10.3	0.01	19.2	0.13	15.9	246.7	0.01	0.002
ME-A11	198.30	0.09	0.9	8161.5	10.3	0.01	20.5	0.13	15.4	253.5	0.01	0.001
ME-A12	246.15	0.09	0.9	8202.1	10.5	0.01	20.7	0.07	15.0	264.9	0.01	0.001
ME-A13	310.75	0.10	1.0	8192.9	10.6	0.00	21.4	<0.001	15.0	269.3	0.01	0.002
ME-A14	358.80	0.10	1.0	8121.2	10.5	0.00	20.6	0.07	14.5	273.0	0.01	0.002
ME-A15	414.25	0.10	1.0	8233.2	10.7	0.04	21.8	0.05	15.0	277.2	0.01	0.002
ME-A16	479.63	0.11	1.0	8191.6	10.7	0.03	22.2	0.05	15.1	276.8	0.01	0.001

Sample ID	Cr / 52 [#1]	Mn / 55 [#3]	Fe / 56 [#2]	Co / 59 [#3]	Ni / 60 [#3]	Cu / 63 [#3]	Zn / 66 [#3]	As / 75 [#1]	Se / 78 [#2]	Rb / 85 [#3]	Sr / 88 [#3]	Zr / 90 [#3]
ME-A1	0.03	0.2	0.083	0.004	0.2	0.1	<0.0002	0.002	0.001	0.01	0.2	0.002
ME-A2	0.04	0.1	0.213	0.002	0.1	0.1	<0.0002	<0.00005	<0.00002	0.02	0.8	0.002
ME-A3	0.02	0.2	0.110	0.003	0.1	0.1	<0.0002	<0.00005	<0.00002	0.02	1.4	0.002
ME-A4	0.01	0.2	0.101	0.002	0.1	0.1	<0.0002	0.002	<0.00002	0.03	2.6	0.002
ME-A5	0.02	0.3	0.065	0.002	0.1	0.1	<0.0002	0.000	0.001	0.03	2.8	0.003
ME-A6	0.13	0.4	0.251	0.004	0.5	0.2	<0.0002	0.002	<0.00002	0.03	3.2	0.003
ME-A7	0.03	0.4	0.063	0.002	0.1	0.1	<0.0002	<0.00005	0.002	0.04	3.4	0.003
ME-A8	0.02	0.5	0.132	0.002	0.1	0.1	<0.0002	<0.00005	<0.00002	0.04	3.9	0.003
ME-A9	0.01	0.5	0.003	0.002	0.1	0.2	<0.0002	<0.00005	<0.00002	0.04	4.5	0.003
ME-A10	0.00	0.5	<0.001	0.002	0.1	0.3	<0.0002	<0.00005	<0.00002	0.04	5.0	0.003
ME-A11	0.02	0.5	0.061	0.002	0.1	0.3	<0.0002	<0.00005	<0.00002	0.04	5.2	0.003
ME-A12	0.00	0.5	0.006	0.001	0.0	0.3	<0.0002	<0.00005	<0.00002	0.04	5.4	0.003
ME-A13	0.01	0.5	0.007	0.001	0.0	0.3	<0.0002	<0.00005	<0.00002	0.04	5.5	0.003
ME-A14	0.01	0.5	0.023	0.001	0.0	0.2	<0.0002	<0.00005	<0.00002	0.04	5.6	0.003
ME-A15	0.00	0.5	0.039	0.001	0.0	0.2	<0.0002	<0.00005	<0.00002	0.04	5.7	0.004
ME-A16	0.02	0.5	0.049	0.001	0.0	0.2	<0.0002	<0.00005	<0.00002	0.04	5.7	0.004

Sample ID	Mo / 95 [#3]	Ag / 107 [#3]	Cd / 111 [#3]	Sn / 118 [#3]	Sb / 121 [#3]	Cs / 133 [#3]	Ba / 137 [#3]	Tl / 205 [#3]	Pb / 208 [#3]	Bi / 209 [#3]	Th / 232 [#3]	U / 238 [#3]
ME-A1	0.5	0.004	0.0006	<0.00003	0.0008	0.0027	0.0	0.00041	<0.00003	0.0006	0.00074	0.00051
ME-A2	0.7	0.004	0.0005	<0.00003	0.0005	0.0032	0.1	<0.00003	<0.00003	0.0002	0.00026	0.00013
ME-A3	0.9	0.004	0.0005	<0.00003	0.0005	0.0040	0.1	0.00009	<0.00003	0.0003	0.00041	0.00030
ME-A4	1.1	0.004	0.0003	<0.00003	0.0002	0.0049	0.1	<0.00003	<0.00003	<0.00003	0.00000	<0.00002
ME-A5	3.5	0.004	0.0016	<0.00003	<0.00002	0.0050	0.1	<0.00003	<0.00003	<0.00003	<0.00002	<0.00002
ME-A6	4.1	0.004	0.0020	<0.00003	0.0002	0.0050	0.1	<0.00003	<0.00003	<0.00003	0.00002	<0.00002
ME-A7	4.1	0.003	0.0019	<0.00003	<0.00002	0.0052	0.1	<0.00003	<0.00003	<0.00003	<0.00002	<0.00002
ME-A8	4.1	0.004	0.0021	<0.00003	<0.00002	0.0061	0.2	<0.00003	<0.00003	<0.00003	<0.00002	<0.00002
ME-A9	4.3	0.004	0.0021	<0.00003	<0.00002	0.0061	0.2	<0.00003	<0.00003	<0.00003	<0.00002	<0.00002
ME-A10	4.8	0.004	0.0022	<0.00003	0.0002	0.0063	0.2	<0.00003	<0.00003	<0.00003	<0.00002	<0.00002
ME-A11	4.9	0.004	0.0025	<0.00003	<0.00002	0.0059	0.2	<0.00003	<0.00003	<0.00003	<0.00002	<0.00002
ME-A12	5.2	0.003	0.0025	<0.00003	<0.00002	0.0063	0.2	<0.00003	<0.00003	<0.00003	<0.00002	<0.00002
ME-A13	5.6	0.003	0.0026	<0.00003	<0.00002	0.0059	0.2	<0.00003	<0.00003	<0.00003	<0.00002	<0.00002
ME-A14	5.8	0.004	0.0030	<0.00003	<0.00002	0.0062	0.2	<0.00003	<0.00003	<0.00003	<0.00002	<0.00002
ME-A15	6.2	0.004	0.0028	<0.00003	0.0001	0.0060	0.2	<0.00003	<0.00003	<0.00003	<0.00002	<0.00002
ME-A16	6.5	0.003	0.0029	<0.00003	<0.00002	0.0058	0.2	<0.00003	<0.00003	<0.00003	<0.00002	<0.00002

XII. Appendix C: Preliminary Results of Brine Extraction Modeling

A critical issue for saline CO_2 storage projects is buildup of pressure caused by CO_2 injection. The magnitude of the pressure buildup depends on many factors, including the injection rate, static properties of the reservoir, nature of the in-situ and injected fluids, and the formation boundary conditions. Maximum pressure increase is localized at the injection well; however, a the pressure front diffuses into the formation, increasing the pressure regionally far from the injection well. Within the context of CO_2 geological storage, excessive pressure buildup is undesirable because it increases risks of the CO_2 plume transport accumulating into unwanted zones, reduces the storage capacity of the formation and can limit the life of a storage project.

The objective of the research is to use brine extraction wells to manage formation pressures as well as plume movement. The simulation study was performed using the CMG-STARS simulator and the model includes three wells (injection, extraction, and observation wells). We numerically tested active brine extraction wells (i.e. pumps at the surface, active pressure management system, APMS) and (passive) pressure relief wells (passive pressure management system, PPMS). In APMS, brine will be actively extracted using pumps at the surface whereas in PPMS, brine will passively move from the storage reservoir to other geological formations responding to pressure gradients without pumping. The potential benefits of employing brine extraction wells include increased storage capacity, reduced stress on the sealing formation, and reduced risk of brine and CO_2 plume movement into unwanted formations.

The proposed study site whose characteristics are used in the model is located about 50 miles southwest of San Antonio, Texas, in Medina County. Here we show that the APMS approach is more conducive of achieving research goals than the PPMS approach.

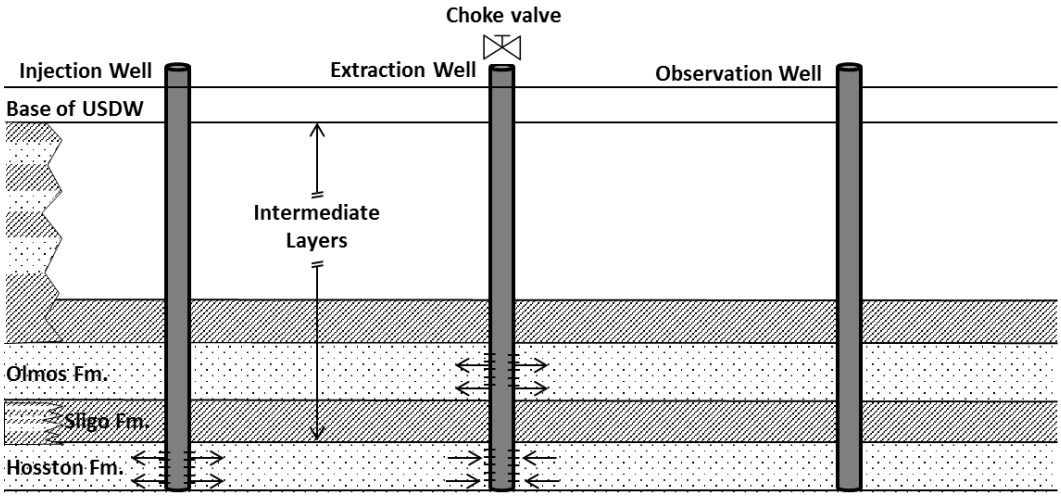

Figure 97. PPMS approach

XII-1. Model Description and Scenarios

A Cartesian model was set up to simulate different pressure management scenarios with constant rate brine injection and extraction at different strategies. The Devine Test Site area of $10\times10km^2$ is represented by coarse $100\times100m^2$ horizontal gridblocks. The central area is refined into

smaller gridblocks of 1×1×5 and includes the injection, extraction, and observation wells used for the brine extraction study (Figure 98**)**. Three wells (injection, extraction, and observation) are completed in the third layer (Olmos Fm.) and the distance between wells is about 45 m.

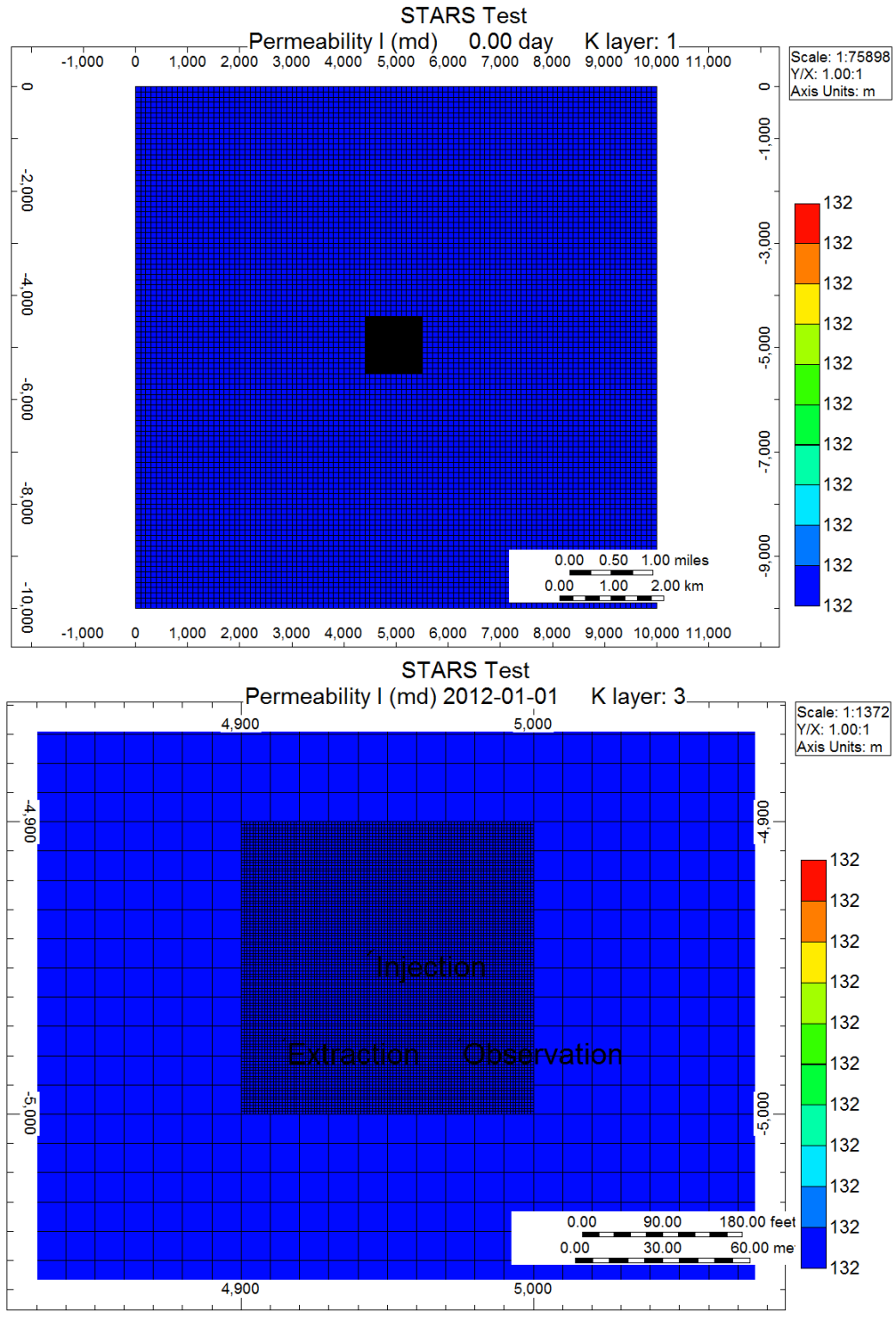

Figure 98. Simulation model of coarse and fine grids including injection, extraction, and observation wells.

Table 14 gives the input data including model properties used for simulations. The main objective is to compare bottom hole pressures (BHP) and also tracer breakthrough time at the observation well for different scenarios. The main focus is on different injection/extraction scenarios in the Olmos layer (layer 3 with a thickness of 30 m) and the Hosston layer (layer 5 with a thickness of 180 m) which are separated from each other by shale layers of zero permeability.

Several simulations were performed to study the impact of injection design and reservoir properties.

- Base Case (No Extraction): Brine was injected at constant rate for 90 days and the extraction well was shut in.
- Active Extraction from Olmos formation (Constant BHP Production): Brine was injected at constant rate for 90 days and the extraction well was producing at constant BHP.
- Active Extraction from Olmos formation (Constant Rate Production): Brine was injected at constant rate for 90 days and the extraction well was producing at constant rate.
- Passive Extraction from Olmos to Upper Layer: Brine was injected at constant rate for 90 days and the extraction well was shut in. However, by assigning a high permeability conduit between Olmos and upper layer, brine from Olmos was diverted into upper zone.

Table 14. Base case data used for different pressure management strategies

Model	3-Dimensional Cartesian
No. of Coarse and Fine Grids	100×100×5
Δx , Δy , Δz	$(100, 100, 30)_{\text{Coarse Grid}}$, $(1, 1, 30)_{\text{Fine Grid}}$ m
Porosity and permeability	0.25, 132 md
Water saturation	100 %
K_v/K_h	1
Injection Rate (constant rate)	1590 m^3/day
Well Configuration (3 Wells)	1 Injection, 1 Extraction, 1 Observation
Well Distance	45 m
Waterflood:	**Days injected:**
Tracer Conc. : 0.1 %wt	90 Days

XII-2. Results

Bottom-hole pressures

Figure 99 shows the BHP at the observation well for different scenarios. The results demonstrate that BHP at the observation well increases from 2500 psi to around 2840 psi due to brine injection (no extraction scenario) which indicates an incremental of ~340 psi at the observation well. However, by the brine extraction at constant BHP scenario, the results showed an incremental of ~223 psi at the observation well. There was only 40 psi increase in the observation well BHP using the scenario with brine extraction at constant rate. We also tested passive extraction from the Olmos to the upper layer and the results indicated that BHP at the observation well increased ~300 psi which is ~40 psi less than in the no extraction scenario. Figure 100 and Figure 101 show the BHP at the injection well and extraction well for different scenarios. The results illustrate that, considering constant injection rate in all scenarios, the BHP at the injection well will stay almost constant for a constant extraction rate while it will increase

from initial pressure of 2500 psi up to 3400 psi for other designs. Figure 102 illustrates that *tracer will break through at the observation well after 20 days in the active extraction case.*

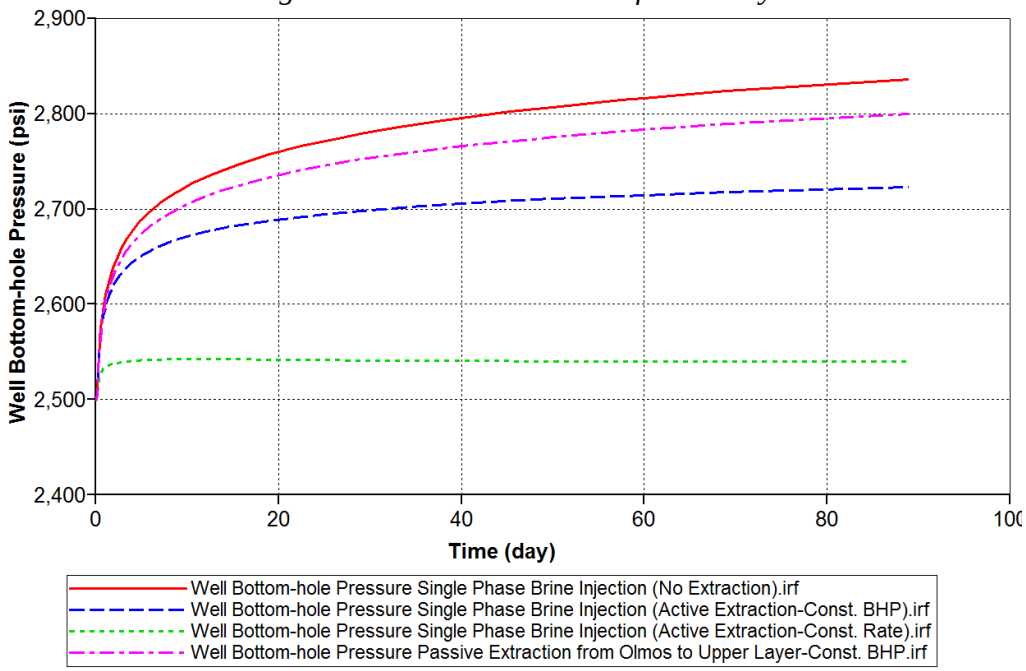

Figure 99. Comparison of bottom hole pressure at the observation well for different strategies.

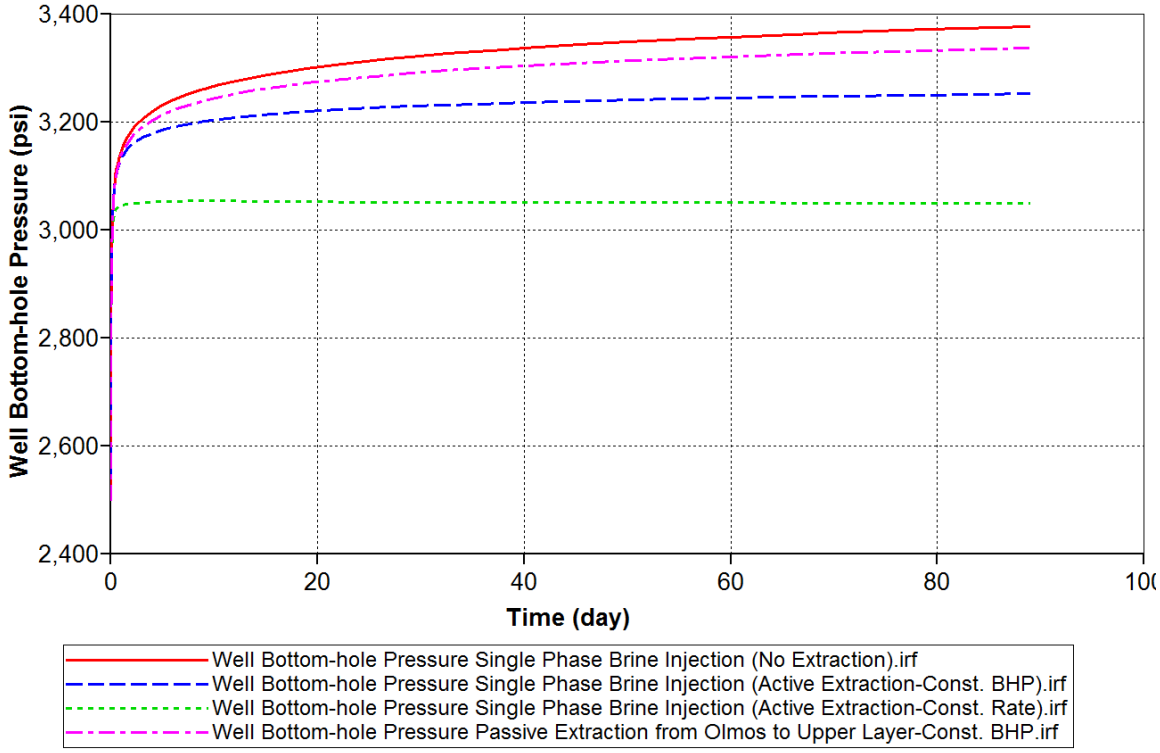

Figure 100. Comparison of bottom hole pressure at the injection well for different strategies.

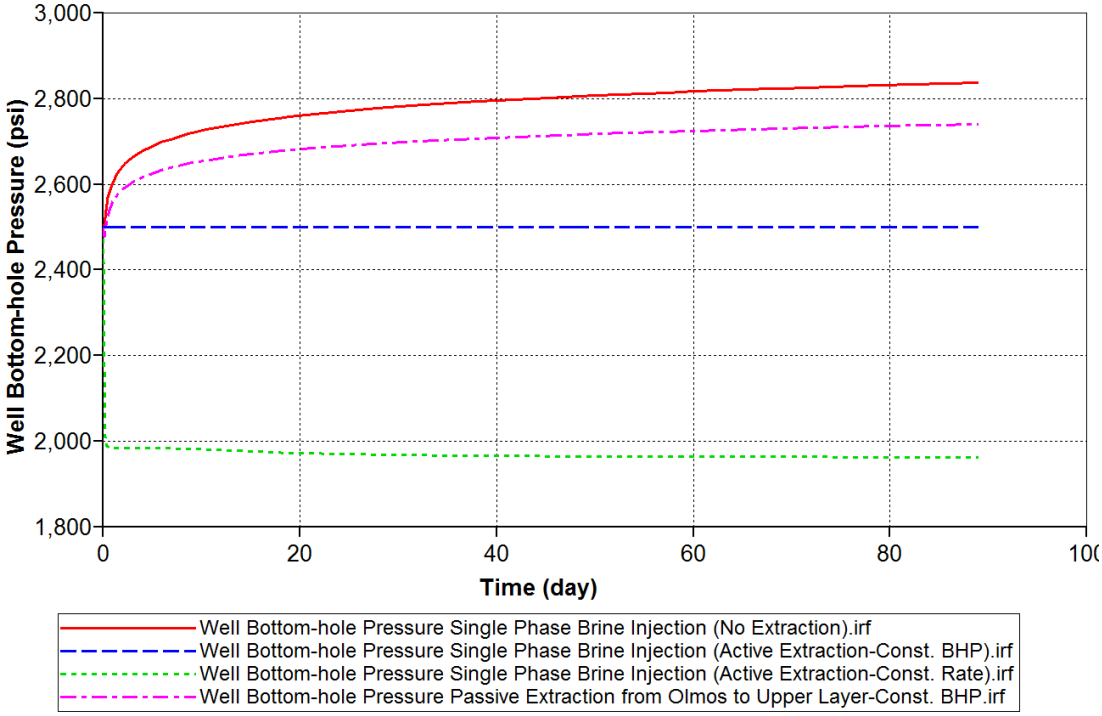

Figure 101. Comparison of bottom hole pressure at the extraction well for different strategies.

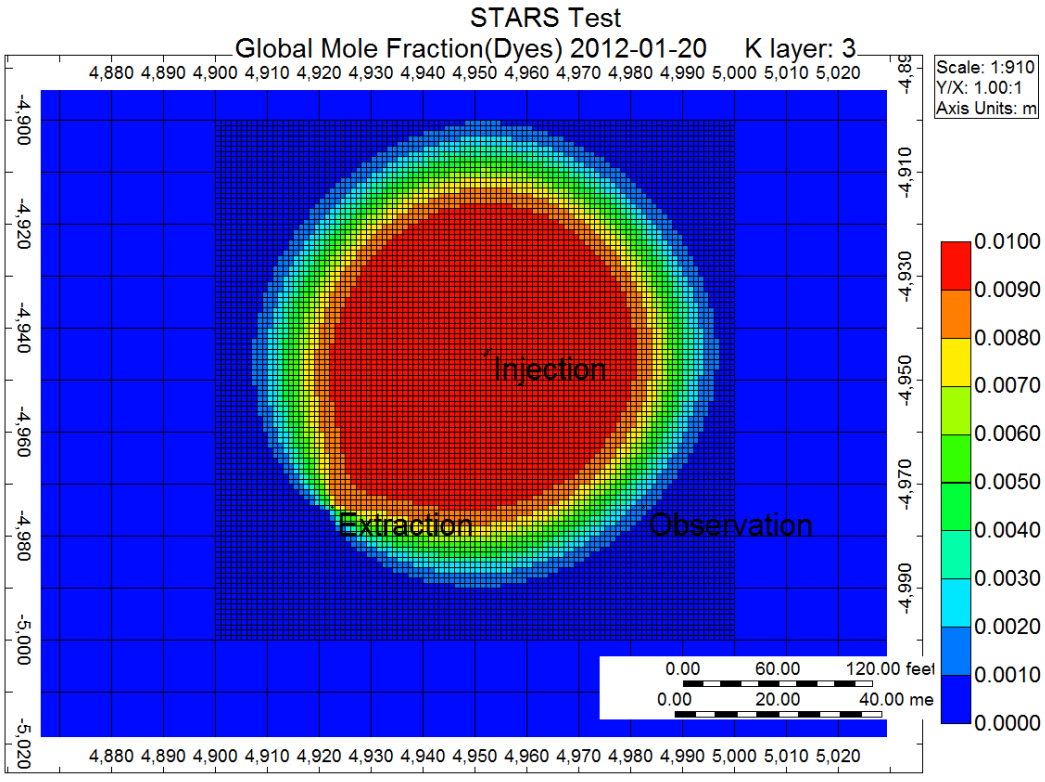

Figure 102. Tracer Concentration after 20 days for active extraction scenario.

Sensitivity Simulations

Sensitivity analysis were performed to optimize the pressure control during brine extraction. The key sensitivity parameters were layer thickness, permeability, porosity, and rock compressibility. CMG-CMOST was used to perform sensitivity simulations for active extraction from the Olmos Fm. for different parameters. Figure 103 shows the sensitivity of BHP for different parameters. The results demonstrate that higher permeability and thickness is favorable for pressure control at the observation well. Porosity and rock compressibility have negligible effect on bottom hole pressure.

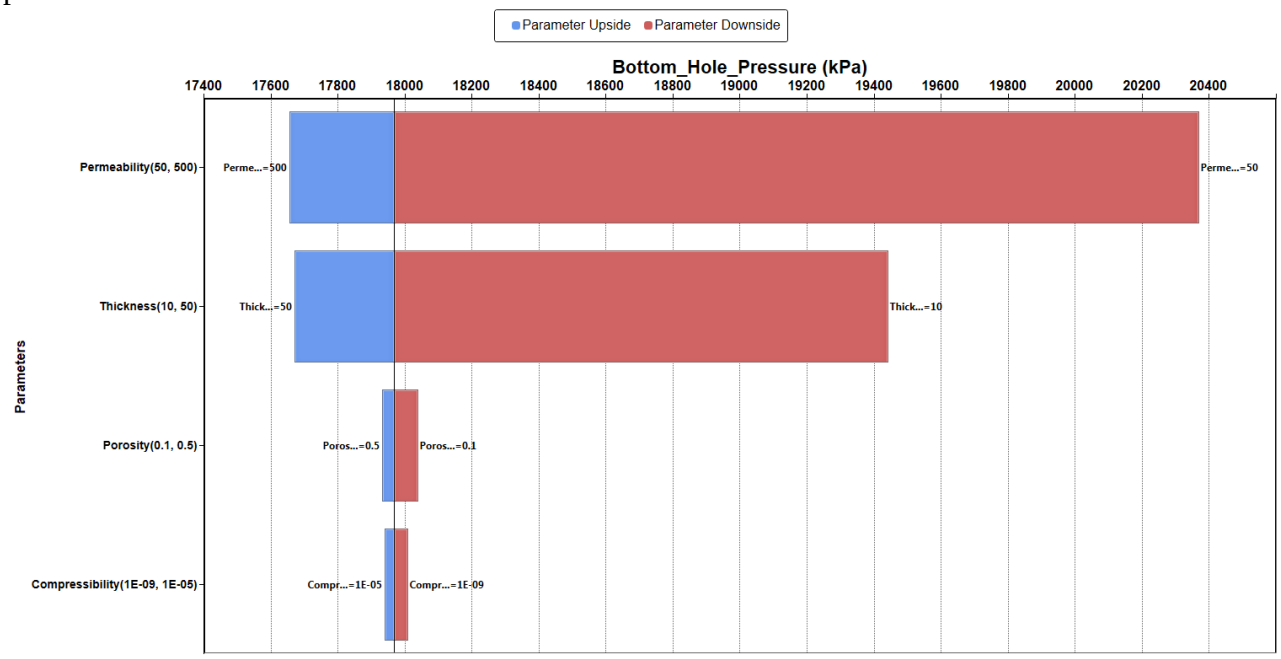

Figure 103. Sensitivity analysis of bottom hole pressure at the observation well respect to different parameters (Thickness, Permeability, Porosity, Rock Compressibility).

XII-3. Summary and Conclusions

We have performed numerical simulations for different brine extraction scenarios using CMG-STARS to optimize the best pressure control design.

The results demonstrated that brine injection leads to an increase of 340 psi in bottom hole pressure during no extraction scenario. However, we could control and lower pressure increase by either active or passive extraction.

The sensitivity simulations indicated that main brine extraction design variables are permeability, layer thickness, porosity, and the rock compressibility.

Higher permeability and reservoir thickness are favorable for lowering bottom hole pressure and better pressure control. However, lowering porosity and rock compressibility have negligible effect on pressure control.

XIII. Appendix D: Rock-Physics Study for Velocities-Pore Pressure Relation

Among the monitoring methods for CO_2 sequestration and associated pore pressure changes due to injection, seismic surveys provide the volumetric coverage needed to understand the 3D subsurface fluid and pore pressure front movement. However, seismic data are indirectly related to pore pressure and CO_2 saturation. Therefore, we need to build quantitative links between the measured seismic properties of the sequestering formation and the CO_2 saturation and pore pressure. These quantitative links are given by rock physics theories for elastic properties of porous media. This study focuses on the pore pressure effects on the P and S-wave seismic velocities. The injecting fluid is considered to be brine, the same as the host fluid of the sequestering formation. The geologic formation under study is represented by the Hosston sandstone from the Devine Test Site. There are no well-log data that penetrate Hosston Formation at the study site. Therefore, there is a large uncertainty associated with the depth of formation, porosity, clay content and elastic properties of the Hosston Formation. Our analysis focuses on the impact of each of these parameters on the velocity-pressure relation, with the goal of quantifying how much should the pore pressure be increased through injection to be able to monitor the pore pressure front movement using compressional and shear-wave seismic velocities. The first part of the study focuses on the analysis of laboratory data on compressional and shear-wave velocities as a function of pressure, for different sandstone samples. This data set is invaluable to predict the elastic behavior of Hosston formation due to changes in pore pressure, in the absence of such direct measurements on samples from this formation. The second part of the study presents a theoretical rock physics model that relates P and S-wave velocities to pressure changes through an analytical model. However, this model needs to be calibrated with actual measurements in order to have any predictive power. **Pressure Effects on Elastic Properties: Fundamental Observations**

A fundamental observation in Rock Physics is the increasing of the compressional and shear velocities with effective pressure (Nur and Simmons, 1969; Nur, 1971). Effective pressure is the difference between confining and pore pressure, therefore it is sometimes called the differential pressure. To the first order, the elastic properties of the rocks depend on this difference between confining and pore pressure, and not on the absolute levels of each. Effective pressure increases the P-wave (compressional) and S-wave (shear) velocities because of the closing of cracks, flaws and grain boundaries, which elastically stiffen the mineral frame of the rocks. As a consequence, the increasing pore pressure softens the elastic mineral frame, by opening crack-like pores, flaws and grain boundaries, with the effect of lowering the P and S-wave velocities.

The challenge is that the pressure dependence of velocities is highly variable from sample to sample, depending on the amount and the geometric shapes of compressible, crack-like pores. Therefore, the only way to know the pressure dependence of velocities for a particular rock is to measure it in the lab. The laboratory measurements should be performed on dry samples, because the fluid-related dispersion effects at high ultrasonic frequencies can partially mask the pressure effects (Mavko and Jizba, 1991).

At this first stage of the study there are no measurements of pressure dependence of velocities from Hosston sandstone. Therefore, we use a comprehensive data set by Han (1986) on 48 sandstone samples. The first section of the report presents the analysis of this data set and its

relevance and implications to Hosston sandstone. Since in nature there is a large variability in the pressure dependence of velocities even within the same formation, only a statistical analysis can give guidelines of what to expect in the field in terms of monitoring pressure fronts with seismic data.

XIII-2. Laboratory Data Analysis of Velocities versus Pressure

Han (1986) performed ultrasonic compressional and shear velocities measurements as a function of confining pressure for 48 sandstone samples. The confining pressure varied from 5 MPa up to 40 MPa in five steps: 5MPa, 10 MPa, 20 MPa, 30 MPa and 40 MPa. Pore Pressure was set at 1 MPa, such that the Effective Pressure varies from 4 MPa to 39 MPa. Han also performed measurements on brine-saturated samples. However, in this study we analyze only the data from the dry samples to avoid frequency dependent dispersion associated with ultrasonic measurements of velocities on brine-saturated samples in the lab. Fluid effects are taken into account by using theoretical modeling (Gassman, 1951) of the dry samples. Gassmann theory allows us to predict the velocities of the rocks for the saturated state assuming low frequency, as it is the case in field seismic surveys. The ultrasonic frequencies used in the laboratory are contaminated by fluid dispersion effects (Mavko and Jizba, 1991), which are not occurring at seismic frequencies.

XIII-2-1 Dry sandstone samples analysis

The sandstone samples measured by Han come from different environments and were collected from either quarry or well-log cores, ranging from tight sandstones to more poorly consolidated ones. The porosity of the samples varies between 2% and 30%. Figure 104a presents a histogram with the distribution of porosity values for the sandstone samples given as a volumetric fraction. The mean value is about 16.6%. This average value of porosity is very similar with the porosity expected for the Hosston sandstone of also 16.6% at a depth of around 6000ft (Bartberger et al., 2003 USGS Report, page 15). The standard deviation for the porosity values is 7%.

Since there are no well-log data available that penetrate the Hosston formation at Devine Test Site, the Han data set represents a valuable analogue for our sandstone formation of interest. The mean value of porosity (16.6%) of the Han's data set is similar with what is expected for the porosity of Hosston formation and the standard deviation of the Han's data set (7%), even though large, can be viewed as the uncertainty associated with the average value for the Hosston Formation.

The sandstone samples used by Han in his analysis have variable clay content. Hosston formation, also, has variable mineralogy: predominantly quartz, but including feldspar and clay minerals, such as illite and chlorite (Bartberger et al., 2003). The volume of clay in the Han data set varies from 0% to 50%. Figure 104b presents a histogram for this clay content given as a volumetric fraction. Most of the data have clay content lower than 20%. However there are samples with higher clay content that makes the analysis and comparison with the Hosston Formation even more relevant in the absence of well-log data penetrating the formation of interest at the Devine Test Site.

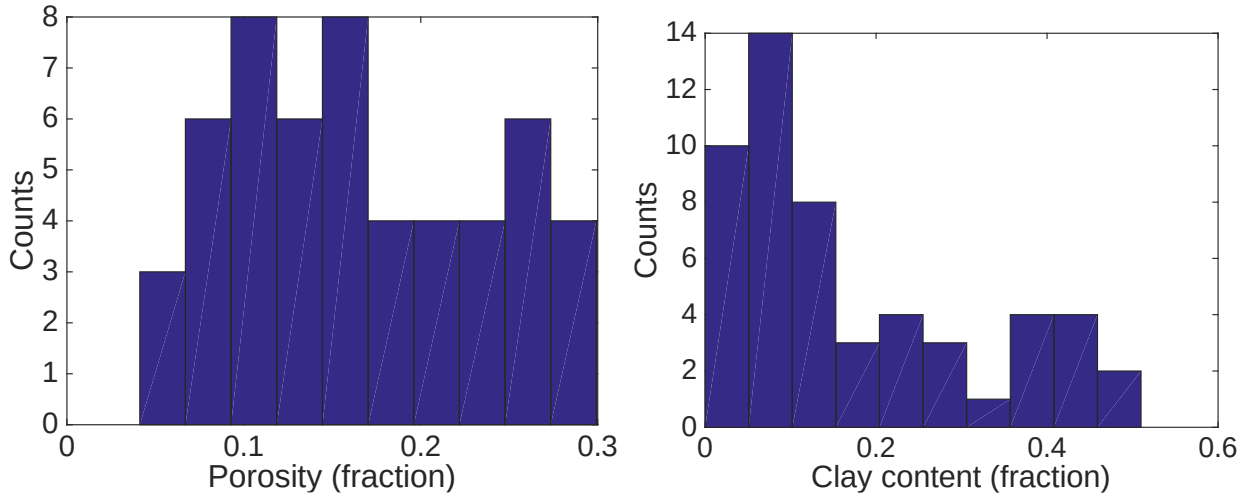

Figure 104. Histogram for the porosity (volumetric fraction) and clay content of the Han data set.

The most valuable measurements to our study performed by Han on his data set are the compressional and shear-wave velocities at variable confining pressure. Figure 105 presents the P-wave velocity and the S-wave velocity measurements respectively as a function of confining pressure for 49 dry sandstone samples. Each sample was measured at 5 MPa, 10 MPa, 20 MPa, 30 MPa and 40 MPa confining pressure. The pore pressure is kept at 1 MPa, such that the differential pressure, which is the difference between confining and pore pressure, spans a range from 4 MPa to 39 MPa.

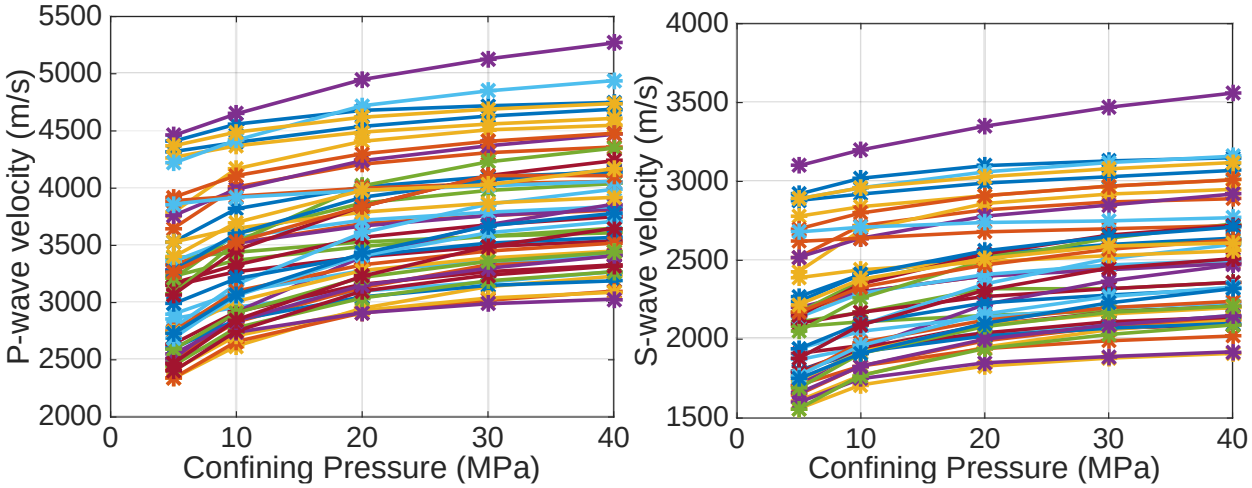

Note: Measured ultrasonic data are represented by the star symbols, which are linearly interpolated for visualizing the trends and for providing more detailed analysis.

Figure 105. P-wave and S-wave velocities as a function of confining pressure for all dry sandstone samples.

Figure 106 presents the porosity variation for each sample as a function of confining pressure. The data is linearly interpolated to help visualizing the trends and for more detailed analysis. As expected, both P and S-wave velocities increase with confining pressure, due to stiffening of the dry frame caused by closing of the flaws and crack-like pores with small aspect ratios.

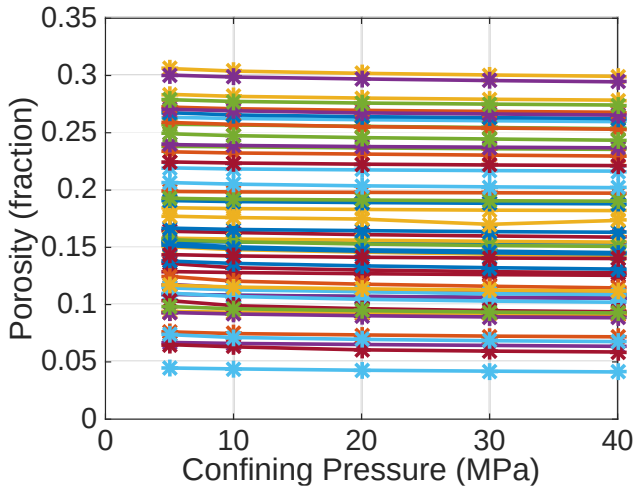

Note: Measured porosity data are represented by the star symbols, which are linearly interpolated to better visualize the trends.

Figure 106. Porosity as a function of confining pressure for all samples.

The increase in both P and S-wave velocities can be significant, as the histograms from Figure 107 and Figure 108 show, respectively. The mean increase in P-wave velocity with increasing confining pressure is 692 m/s, which represents an average increase of 18%. The mean increase in S-wave velocity is 383.75 m/s, which represents an average increase of 16%. As discussed, the increase in P and S-wave velocities is caused by closing of the small aspect ratio cracks. These cracks do not occupy a large volume and they represent a small fraction of the total porosity. The decrease in porosity with increasing confining pressure is shown in the histogram on Figure 109. The mean is less than half percent absolute decrease in porosity due to increasing confining pressure from 5 MPa to 40 MPa (mean=0.48%). The crack-like pores represent a tiny fraction of the total porosity, but they have a big impact on both compressional and shear velocities.

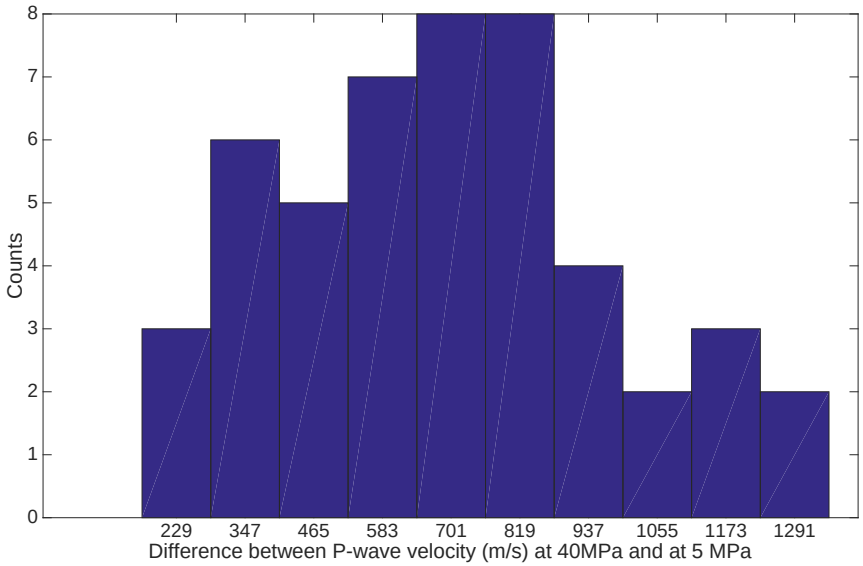

Note: Mean is 692 m/s with standard deviation of 285 m/s.

Figure 107. Histogram for P-wave velocity difference (m/s) between 40M Pa and 5 MPa confining pressure for dry samples.

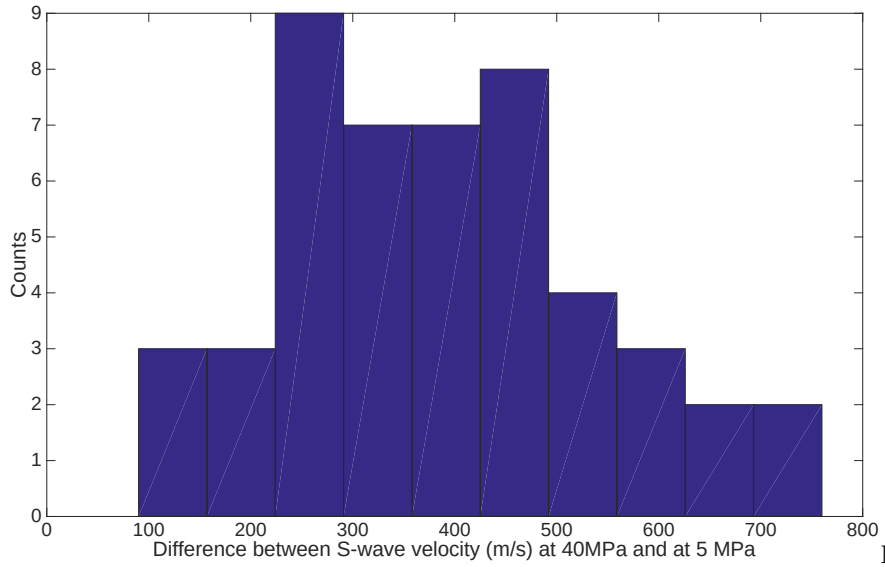

Note: Mean is 383.75 m/s with standard deviation of 158 m/s.

Figure 108. Histogram for S-wave velocity difference (m/s) between 40 MPa and 5 MPa confining pressure for dry samples.

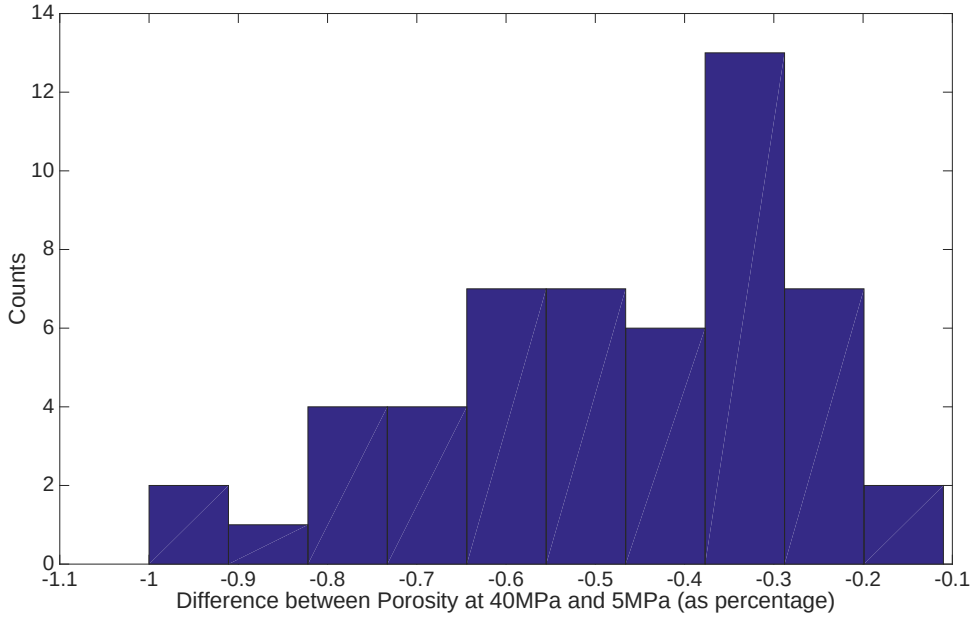

Note: Mean is 0.48% with standard deviation of 0.21%.

Figure 109. Histogram for the Porosity difference (%) between 40 MPa and 5 MPa confining pressure. **Fluid effects: Gassmann Equation**

All data presented up to this point correspond to measurements on dry samples that illustrate the behavior of the dry frame of the rocks. This condition is critical for understanding mineral frame transformation with variable pressure, uncontaminated by fluid dispersion effects that occur at ultrasonic frequencies used in the lab. However, we are also interested in the fluid effects on velocities at seismic frequencies (Mavko and Mukerji, 1995), as they would be recorded in the field at Devine Test Site. Hosston formation is brine-saturated in-situ, and its pore pressure would be increased through brine injection. Therefore we need to understand both the fluid and the pressure effects on the elastic properties.

To account for fluid effects, we use Gassmann approach (1951), which is a low frequency theory that applies to field observations. The bulk modulus of brine is assumed to be 2.5 GPa, and its density is 1010 kg/m^3. Gassmann theory allows us to calculate the elastic properties of the rock saturated with other fluids whose elastic properties are known. This theory assumes that the shear modulus of the rock does not change with fluid, but only the bulk modulus. This assumption implies that fluids do not support shear strength. Therefore, in general, it is primarily the P-wave velocity that is sensitive to fluids, while S-wave velocity varies only due to changes in fluid density. This distinct behavior of P and S-wave velocities can be exploited to separate fluid effects from pressure effects.

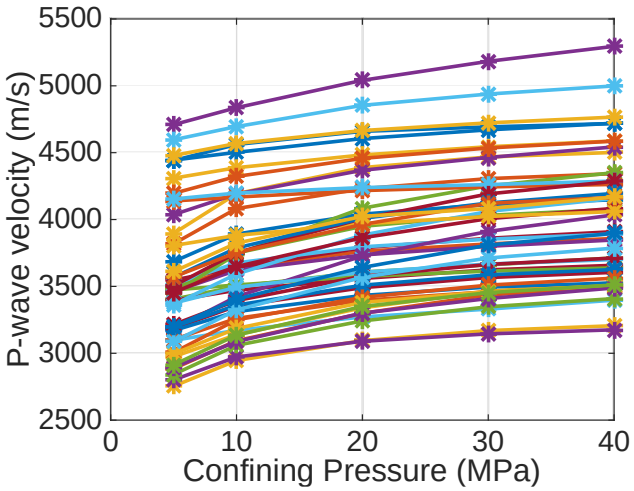

Note: dry sample data presented in Figure 105a used

Figure 110. Gassmann computed P-wave velocity from the dry samples as a function of Confining Pressure for 100% brine saturated condition.

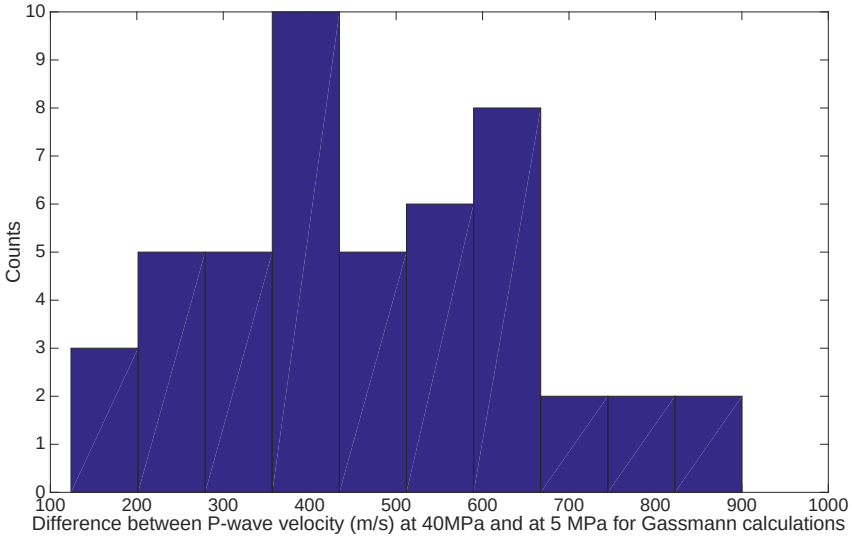

Note: Mean is 471 m/s with standard deviation of 182 m/s.

Figure 111. Histogram for P-wave velocity difference (m/s) between 40 MPa and 5 MPa confining pressure for Gassmann calculations of 100% brine saturated samples.Fluid effects on P-wave velocities are significant, as observed by comparing the corresponding histograms for dry samples (Figure 107) with Gassmann results for 100% brine saturated condition (Figure 111). The average difference between P-wave velocities at 40 MPa versus 5 MPa for saturated

condition is 471 m/s, significantly less than the same corresponding average difference for dry samples, which is 692 m/s. The average relative change for P-wave velocity for brine-saturated condition is 12%, while for the dry samples is 18%. Presence of brine stiffens the P-wave velocities of the rocks because the bulk modulus of the brine is orders of magnitude larger than that of the air.

However, S-wave velocities are not sensitive to fluids, except through density changes. Therefore, the change from dry to saturated conditions for S-wave velocities is not as large as observed by comparing histograms from Figure 108 and Figure 112. The average change in S-wave velocity from 40 MPa to 5 MPa confining pressure for saturated condition is 371 m/s (corresponding to a 16% change), while for the dry samples the same average change is 383.75m/s (corresponding to 16% change).

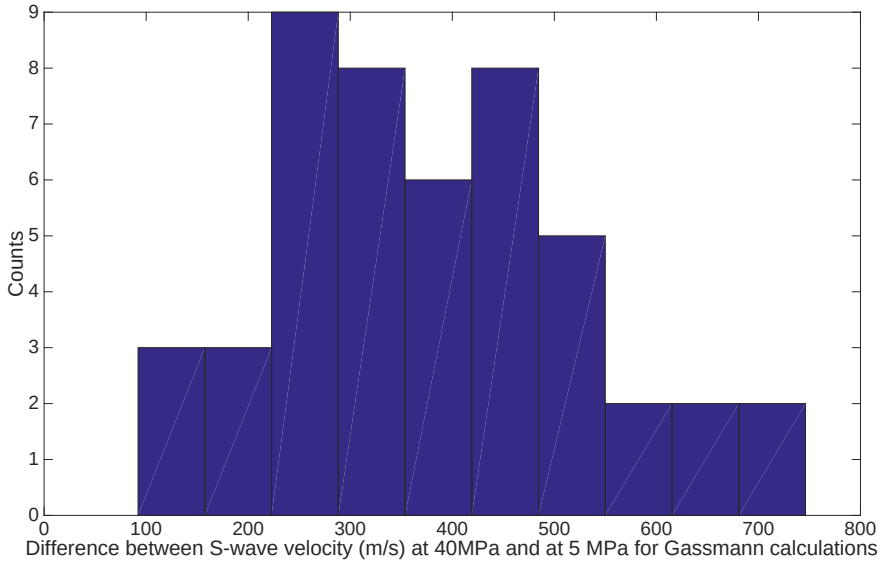

Note: Mean is 371 m/s (16% relative change) with standard deviation of 153 m/s.

Figure 112. Histogram for S-wave velocity difference (m/s) between 40 MPa and 5 MPa confining pressure for Gassmann calculations of 100% brine saturated samples.

Brine-saturated conditions diminish the pressure effects that affect the dry mineral frame of the rock, as seen with P-wave velocities. However, fluid effects are significantly smaller for the S-waves, which reflect more the changes on the mineral frame that occur with pressure changes. Therefore, multicomponent seismic data is invaluable in field studies to separated saturation and pressure effects.

XIII-2-3 Pore Pressure Effects

The computed data on Figure 110 correspond to P-wave velocity for theoretically saturated samples with 100% brine. The confining pressure values stay the same. Gassmann Equation (1951) only replaces air with brine, leaving the dry mineral frame unchanged. These data can also be displayed as a function of pore pressure, since the effective pressure for the Han data set is known to be 1MPa less than the confining pressure at each step. If we hypothetically assume the confining pressure to be fixed at 40 MPa, then the pore pressure is the difference between confining pressure and the effective pressure, which varies from 4MPa to 39MPa. Therefore, the pore pressure would vary from 1 MPa to 36 MPa. Figure 113 displays all the Gassmann results

for P-wave and S-wave velocities respectively, as a function of pore pressure. As expected, all the samples show a trend of decreasing P and S-wave velocities with increasing pore pressure, due to the opening of the crack-like pores and flaws and loosening of the grain boundaries with increasing pore pressure (i.e. decreasing effective pressure). Figure 114 shows the P to S-wave velocity ratio as a function of pore pressure that indicates a trend of increasing P-to S-wave velocity ratio (Vp/Vs) with increasing pore pressure for brine saturated samples. This indicates

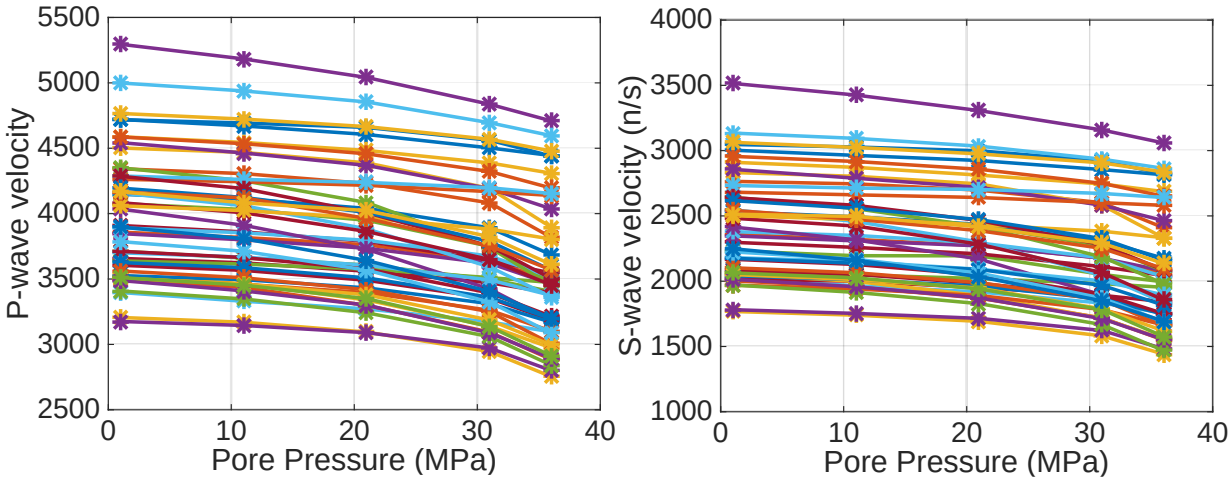

Note: dry sample data presented in Figure 105a and b used

Figure 113. Gassmann computed P-wave and S-wave velocities from the dry samples as a function of pore pressure for 100% brine saturated condition.

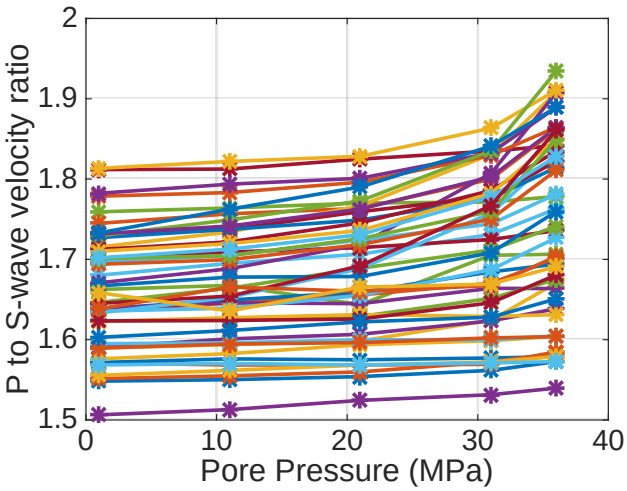

Figure 114. P to S-wave velocity ratio as a function of Pore Pressure for Gassmann calculations of 100% brine saturated samples.

that S-wave velocity decreases more with increasing pore pressure than P-wave velocity. On Figure 113 and Figure 114 it is difficult to observe the individual trends of velocities versus pressure and the large variability that exists between the samples. Therefore, Figure 115 displays the P-wave velocity, S-wave velocity and P to S-wave velocity ratio as they change with pore pressure for only two samples: one showing large variability with pore pressure, and the other low variability. On Figure 115 the blue curves correspond to a sample which changes significantly with pore pressure due to higher volume of compliant, crack-like pores, while the

black curves correspond to a sample with hardly any pressure dependence, due to a smaller fraction of the compressible pores. The porosity of the sample with large pore pressure variability (blue curves) is 11% with a clay content of 21%, while the porosity of the sample with low pore pressure variability (black curves) is 7%, with a higher clay content of 45%. Based on only these two samples we may wrongly conclude that the higher clay content may be responsible for the lower pore pressure dependence of the velocities. The clay content and porosity impact on pore pressure variability are discussed separately in a different section.

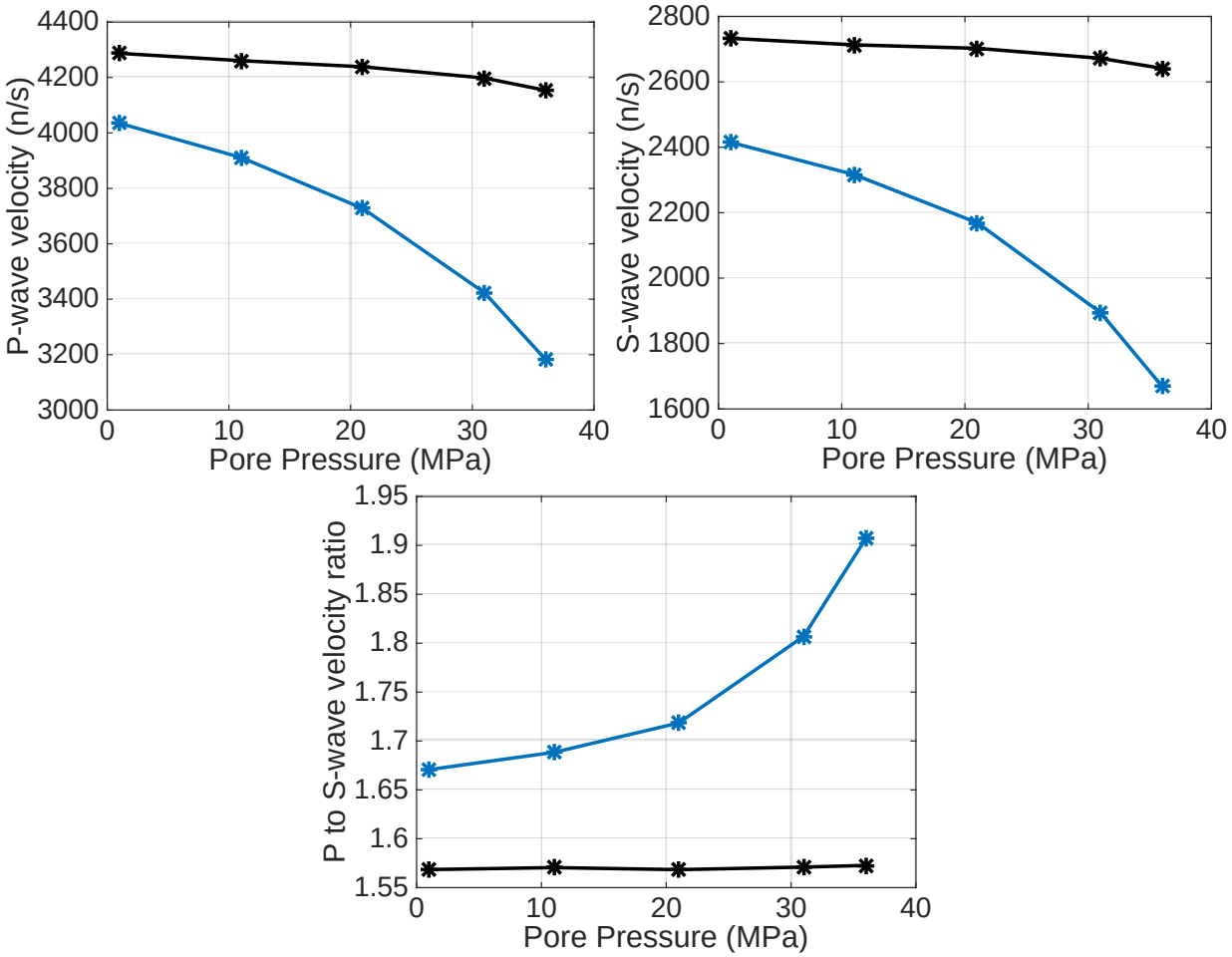

Figure 115. P-wave and S-wave velocities P to S-wave velocity ratio for 2 samples as a function of pore pressure for 100% brine saturated condition.

From Figure 115c we observe that for the sample with larger pore pressure variability of the elastic properties, the P to S-wave velocity ratio increases considerably. Therefore, multicomponent seismic data can be of crucial importance in monitoring pore pressure front movement in the subsurface.

XIII-2-4 Depth of the formation

As we can observe on Figure 115, the gradient of velocity versus pore pressure varies between samples. However, it also varies within the same sample and it tends to be larger as the pore pressure increases (or at lower effective pressure). Therefore, the initial pore pressure condition associated with the depth of the formation may influence the seismic detectability. For shallower

formations, the effective pressure is lower, and the gradient of velocity versus pressure is larger. For deeper formations, the gradient of the velocity-pressure dependence is lower. Therefore, we expect the required increase in pore pressure from hydrostatic state to be larger in deeper formation than in the shallower ones for to produce the same relative change in velocities.

We assume two different depths for the Hosston formation: 5000 ft and 6000 ft. In both cases we assume that the pore pressure conditions are hydrostatic (Bartberger et al., 2003). The initial hydrostatic pore pressure is 15 MPa at 5000 ft and 18 MPa at 6000 ft. The corresponding confining pressure values for each of the depths are 34 MPa and 41 MPa, while the effective pressure values are 19 MPa and 23 MPa, respectively. We allow the pore pressure to increase such that the effective pressure drops to a minimum of 4 MPa, which is the lowest data point in Han's data. From an engineering point of view, we should also limit the high end of pore pressure for stability conditions. This means that the maximum pore pressure is 30 MPa at 5000 ft depth, and 36 MPa at 6000 ft depth.

We compute the relative change in P and S-wave velocities with increasing pore pressure, using all the samples from Han data set. We first assume that the seismic detectability of P and S-wave velocity change is a more conservative value of 5%. However, we also consider the more optimistic scenario of excellent seismic data quality so that we can lower the limit of detectability to 3% change in velocities.

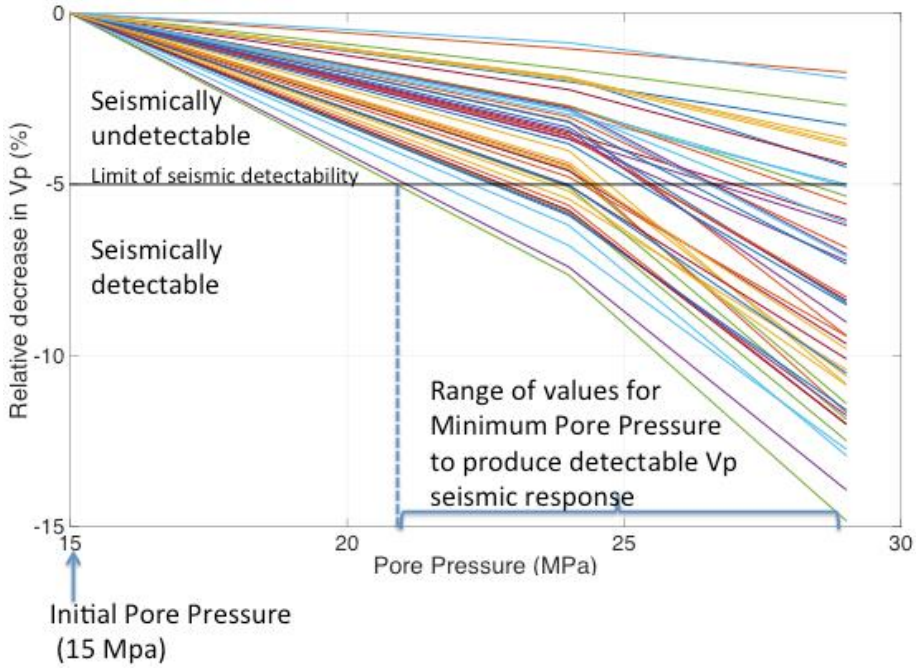

Note: Superimposed is the 5% limit of seismic detectability for the relative change in P-wave velocity and the range of minimum pore pressure values that produce a detectable seismic response.

Figure 116. Relative decrease in P-wave velocity (percentage) as a function of Pore Pressure.

Figure 116 shows the relative decrease in P-wave velocity, expressed as percentage, versus Pore Pressure. The initial hydrostatic pressure is 15 MPa, corresponding to a depth of around 5000 ft. Superimposed is the 5% limit of seismic detectability and the range of minimum pore pressure values to produce a detectable seismic response on P-wave velocity. These minimum values for pore pressure are also displayed as a histogram on Figure 117. The mean for the minimum value

of pore pressure to produce a 5% relative change in P-wave velocity is 25 MPa, and represents an increase of 10 MPa from the initial hydrostatic pore pressure of 15 MPa. Therefore, on average, we need to increase the pore pressure 10 MPa from the hydrostatic condition to produce a 5% relative change in P-wave velocity.

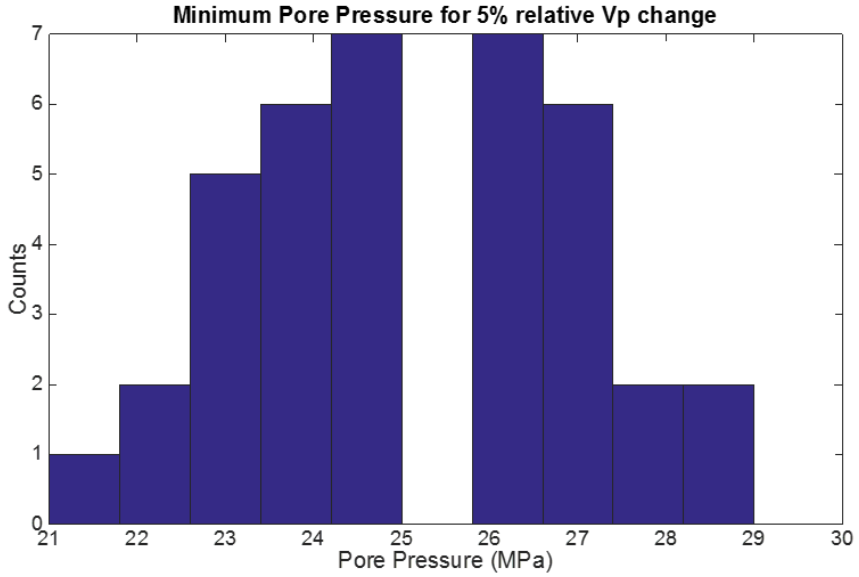

Note: Mean value is 25 MPa with a standard deviation of 2 MPa. Hydrostatic pore pressure is 15 MPa.

Figure 117. Histogram with the minimum Pore Pressure values that produce 5% change in P-wave velocity.

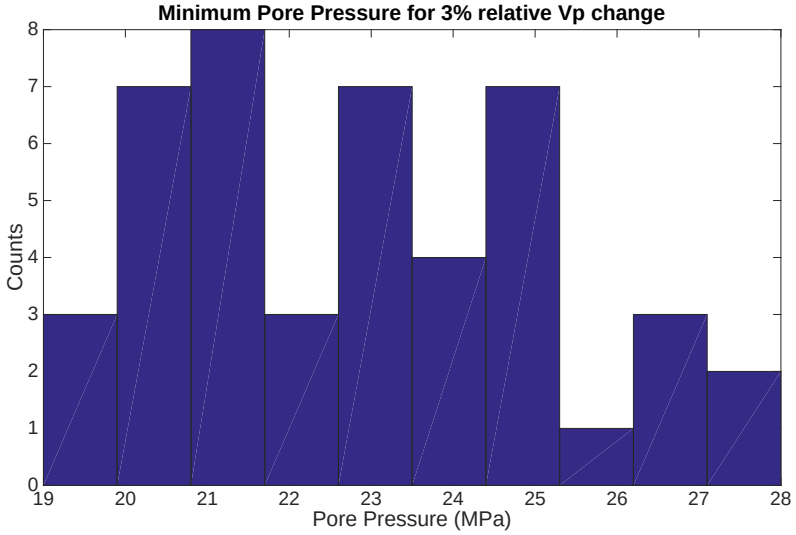

Note: Mean value is 23 MPa with a standard deviation of 2.5 MPa. Hydrostatic pore pressure is 15 MPa.

Figure 118. Histogram with the minimum Pore Pressure values that produce 3% change in P-wave velocity.

Figure 118 shows the histogram with the minimum Pore Pressure values that generate a 3% change in P-wave velocity for the brine saturated sandstone samples from Han's data. Mean value is 23 MPa with a standard deviation of 2.5MPa. The initial hydrostatic pore pressure is 15 MPa. Therefore, on average, we need to increase the pore pressure 8 MPa from 15 MPa hydrostatic pore pressure to produce a 3% relative change in P-wave velocity. If the seismic

detectability limit is lowered from 5% to 3%, then the average minimum pore pressure decreases 2 MPa, from 25 MPa to 23 MPa.

We also look at the relative decrease in S-wave velocity with increasing pore pressure for all of the Han's samples, displayed on Figure 119. Superimposed on this figure is the 5% limit of seismic detectability for the relative change in S-wave velocity together with the range of minimum pore pressure values that produce a detectable seismic response.

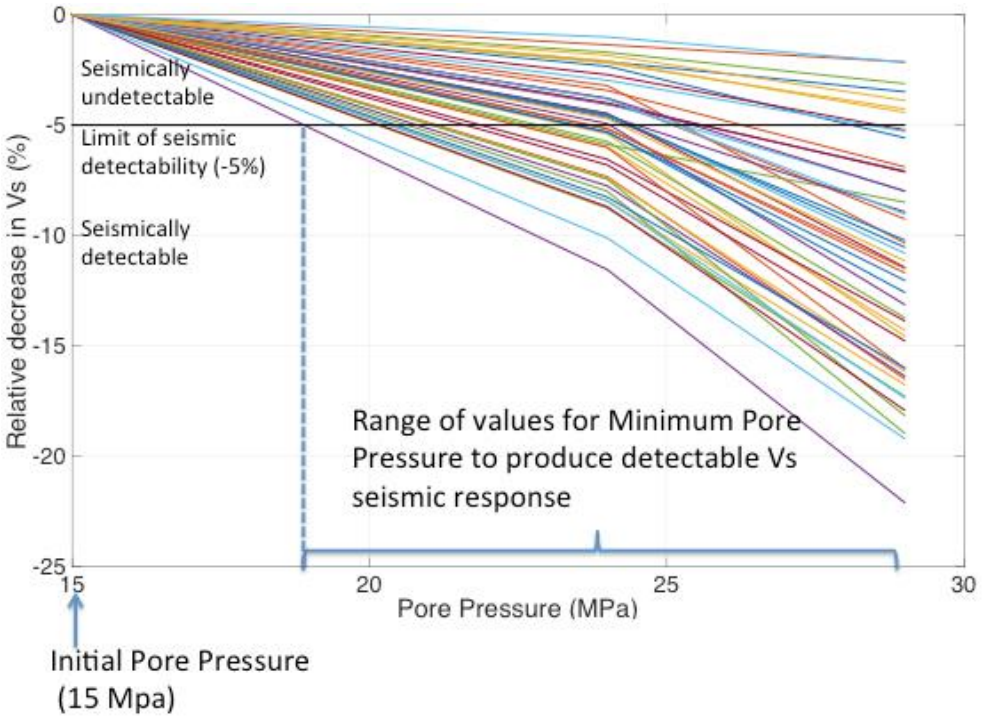

Note: Superimposed is the 5% limit of seismic detectability for the relative change in S-wave velocity and the range of minimum pore pressure values that produce a detectable seismic response.

Figure 119. Relative decrease in S-wave velocity (percentage) as a function of Pore Pressure.

The histogram for the minimum pore pressure values that produce 5% relative change in S-wave velocity are displayed on Figure 120. The mean value is 24MPa with a standard deviation of 2.5 MPa. The initial hydrostatic pore pressure is 15MPa. Therefore, on average, we need to increase the pore pressure 9 MPa from 15 MPa hydrostatic pore pressure to produce a 5% relative change in S-wave velocity, just 1 MPa lower than the average minimum pore pressure to produce a 5% change in P-wave velocity. This suggests that S-wave velocity is slightly more sensitive to pore pressure changes than P-wave velocity.

We also consider again a lower limit for seismic detectability of only 3% decrease in velocity. Figure 121 shows the histogram with the minimum pore pressure values that produce a 3% decrease in S-wave velocity. The mean value for minimum pore pressure is 21.5 MPa with a standard deviation of 2.7 MPa. This implies that we need to increase the pore pressure 6.5 MPa from 15 MPa hydrostatic state to produce a 3% change in S-wave velocity. Based on the analysis of Han's data set, lowering the seismic detectability from 5% to 3% reduces the required minimum pore pressure with 2.5 MPa.

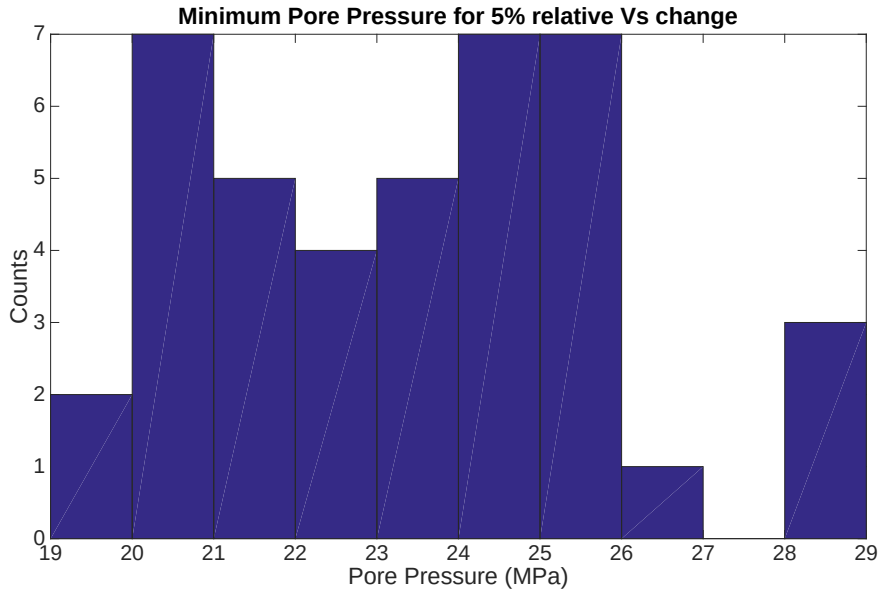

Note: Mean value is 24 MPa with a standard deviation of 2.5 MPa. Hydrostatic pore pressure is 15 MPa.

Figure 120. Histogram with the minimum pore pressure values that produce 5% change in S-wave velocity.

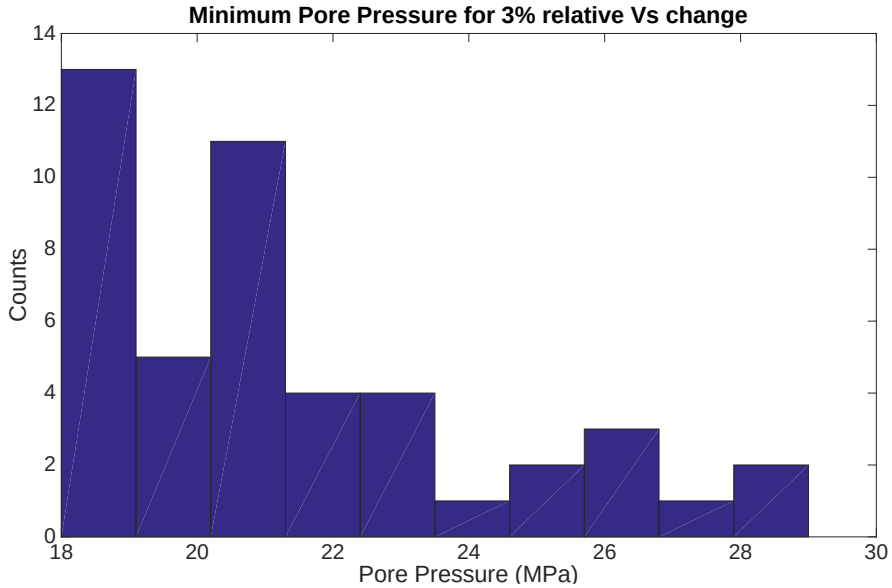

Note: Mean value is 21.5 MPa with a standard deviation of 2.7 MPa. Hydrostatic pore pressure is 15 MPa.

Figure 121. Histogram with the minimum pore pressure values that produce 3% change in S-wave velocity.

Table 15 and Table 16summarize the results of the analysis of Han's data set for an initial hydrostatic pore pressure of 15 MPa (5000 ft). Table 15 presents the expected minimum values for pore pressure and the corresponding minimum increase of pore pressure from the hydrostatic state to produce 5% change in P and S-wave velocities. Table 16 presents the same results, but assuming 3% limit of seismic detectability for P and S-wave velocity change.

Moreover, the analysis shows that there are still 3 samples from Han's data set that display no detectable change in P-wave velocity, and 2 samples that display no detectable change in S-wave

velocity out of 48 samples, even when pore pressure is increased from the assumed hydrostatic value of 15 MPa to 30 MPa. Therefore, based on this data set, we can also predict the risk of failure to seismically detect the pressure front. The probability of not detecting any changes in P-wave velocity is 6%, and in S-wave velocity 4%.

Table 15. Expected minimum pressure values and the minimum increase from hydrostatic pore pressure to produce 5% relative change in P and S-wave velocity.

Depth 5000ft (15 MPa hydrostatic Pp)	Minimum expected pore pressure (MPa)	Minimum expected increase from hydrostatic Pp (MPa)
5% change in Vp	25.0 MPa (std. 2.0 MPa)	10.0 MPa
5% change in Vs	24.0 MPa (std. 2.5 MPa)	9.0 MPa

Note: The assumed depth is 5000 ft with an initial hydrostatic pore pressure of 15 MPa.

Table 16. Expected minimum pressure values and the minimum increase from hydrostatic pore pressure to produce 3% relative change in P and S-wave velocity.

Depth 5000ft (15 MPa hydrostatic Pp)	Minimum expected pore pressure (MPa)	Minimum expected increase from hydrostatic Pp (MPa)
3% change in Vp	23.0 MPa (std. 2.5 MPa)	8.0 MPa
3% change in Vs	21.5 MPa (std. 2.7 MPa)	6.5 MPa

Note: The assumed depth is 5000 ft with an initial hydrostatic pore pressure of 15 MPa.

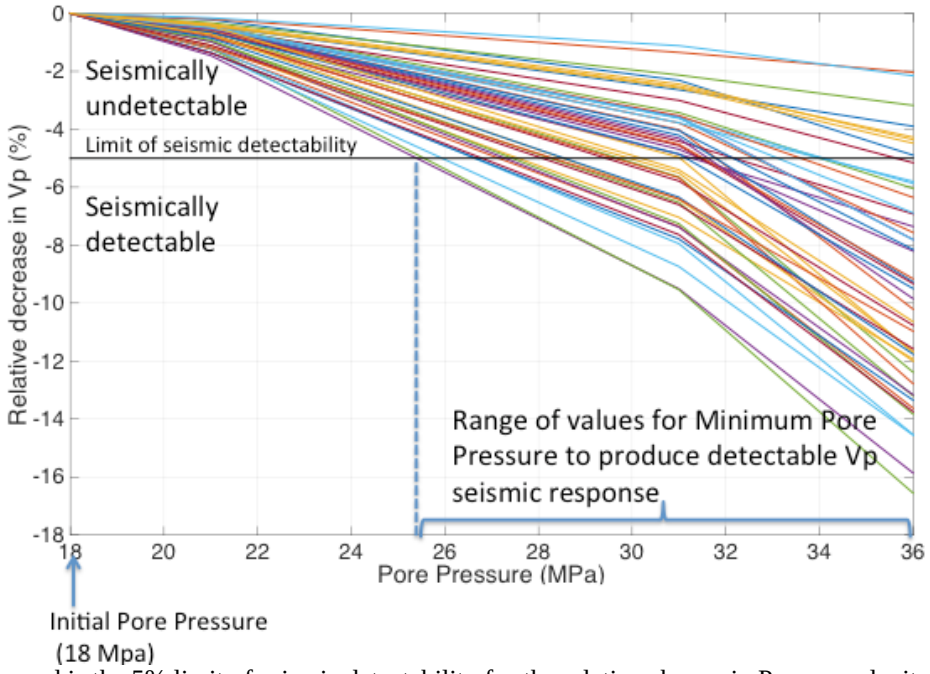

Note: Superimposed is the 5% limit of seismic detectability for the relative change in P-wave velocity and the range of minimum pore pressure values that produce a detectable seismic response.

Figure 122. Relative decrease in P-wave velocity (percentage) as a function of pore pressure

We repeat the same analysis assuming the depth of the Hosston sandstone to be 6000 ft. In this case the hydrostatic pore pressure is 18 MPa. Figure 122 is similar to Figure 116, presenting the relative decrease in P-wave velocity with increasing pore pressure, but starting at a hydrostatic pore pressure of 18 MPa (corresponding to a depth of 6000 ft). Superimposed on the figure is the 5% limit of seismic detectability for the relative change in P-wave velocity and the range of minimum pore pressure values that produce a detectable seismic response.

Figure 123 shows the histogram for the minimum Pore Pressure values to produce 5% relative change in P-wave velocity. The initial hydrostatic pore pressure is 18MPa (at 6000ft). Mean value is 31 MPa with a standard deviation of 2.7 MPa. Therefore, on average we need to increase pore pressure 13 MPa from the initial hydrostatic pore pressure of 18 MPa to produce a 5% relative change in P-wave velocity.

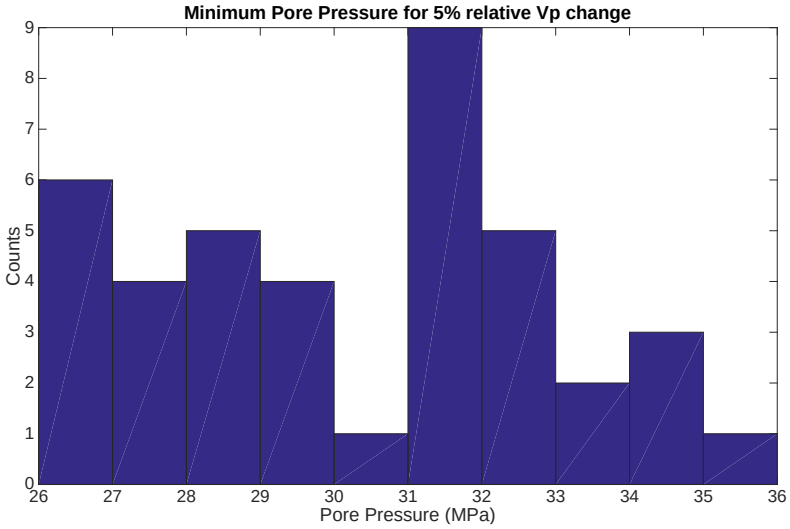

Note: Mean value is 31 MPa with a standard deviation of 2.7 MPa. Hydrostatic pore pressure is 18 MPa.

Figure 123. Histogram with the minimum Pore Pressure values to produce 5% change in S-wave velocity.

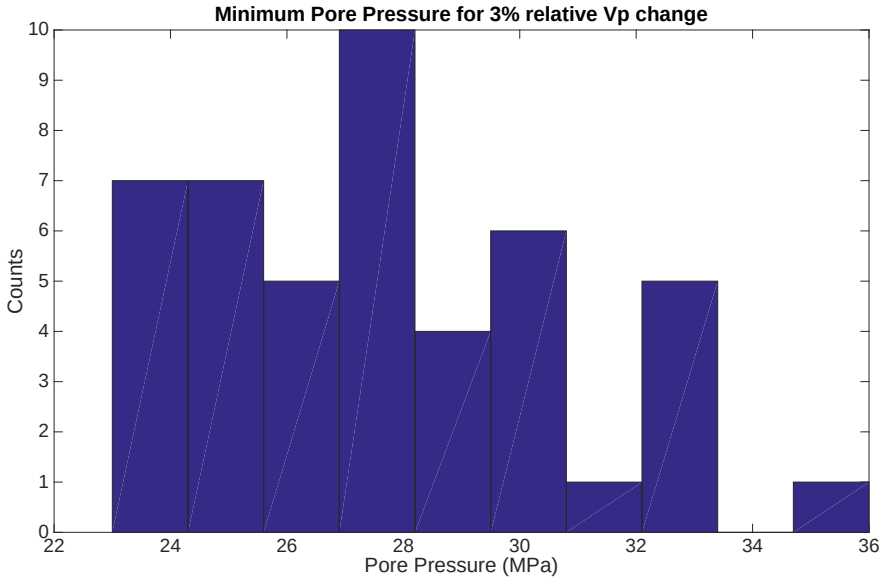

Note: Mean value is 28 MPa with a standard deviation of 3 MPa. Hydrostatic pore pressure is 18 MPa.

Figure 124. Histogram with the minimum Pore Pressure values to produce 3% change in P-wave velocity.

The histogram with the minimum pore pressure values to produce 3% change in P-wave velocity is shown on Figure 124. The mean value is 28 MPa with a standard deviation of 3 MPa. If the seismic limit of detectability is lowered to 3%, then we need to increase the pore pressure 10 MPa from the hydrostatic state to reach a value of 28 MPa.

We perform the same analysis for the relative decrease in S-wave velocity with increasing pore pressure for all of the Han's samples, displayed on Figure 125. Again we superimposed the 5% limit of seismic detectability for the relative change in S-wave velocity together with the range of minimum pore pressure values that produce this detectable seismic response.

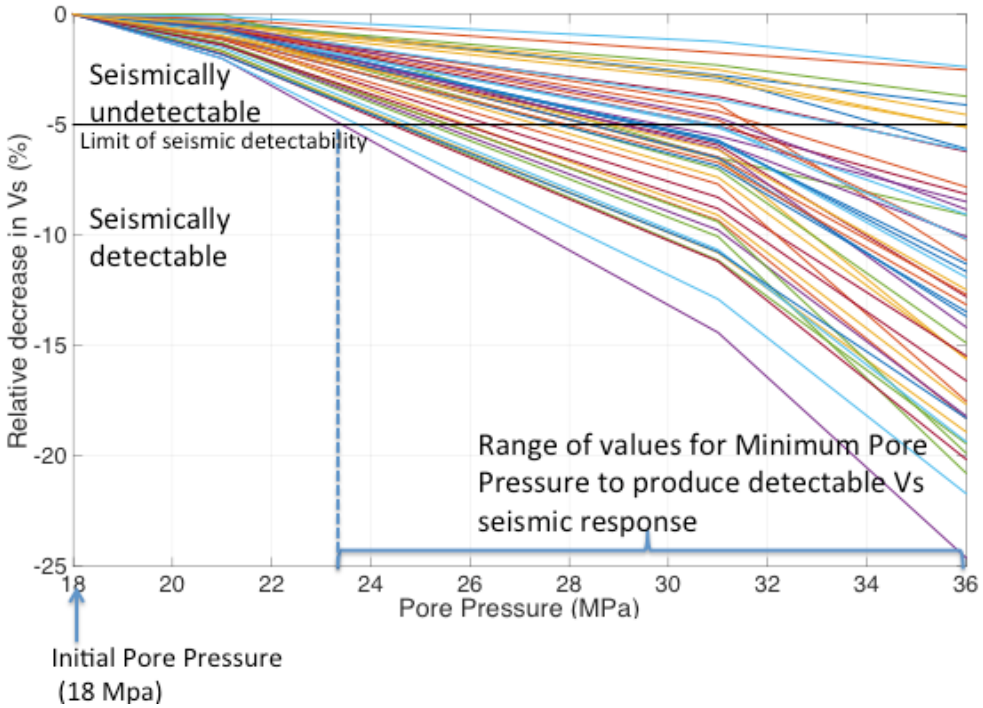

Note: Superimposed is the 5% limit of seismic detectability for relative change in S-wave velocity and the range of minimum pore pressure values that produce a detectable seismic response.

Figure 125. Relative decrease in S-wave velocity (percentage) as a function of Pore Pressure.

Figure 126 shows the histogram with the minimum pore pressure values to produce 5% change in S-wave velocity. Mean value is 29 MPa with a standard deviation of 3 MPa. From the hydrostatic pore pressure of 18 MPa we need to increase the pore pressure 11 MPa to the expected value of 29 MPa pore pressure that generates 5% change in S-wave velocity. For 3% change in S-wave velocity, the expected minimum pore pressure value is 26 MPa, the mean of the histogram displayed on Figure 127, with a standard deviation of 3 MPa. Han's data suggests that the expected value for pore pressure to produce 3% change in S-wave velocity is 26 MPa, 8 MPa more than the hydrostatic pore pressure of 18 MPa (assuming a 6000 ft depth). The same 3% change in P-wave velocity requires a slightly larger pore pressure of 28 MPa, 10 MPa more than the hydrostatic pore pressure. Consistently, the S-wave velocities appear to be slightly more sensitive to pressure changes than P-wave velocities.

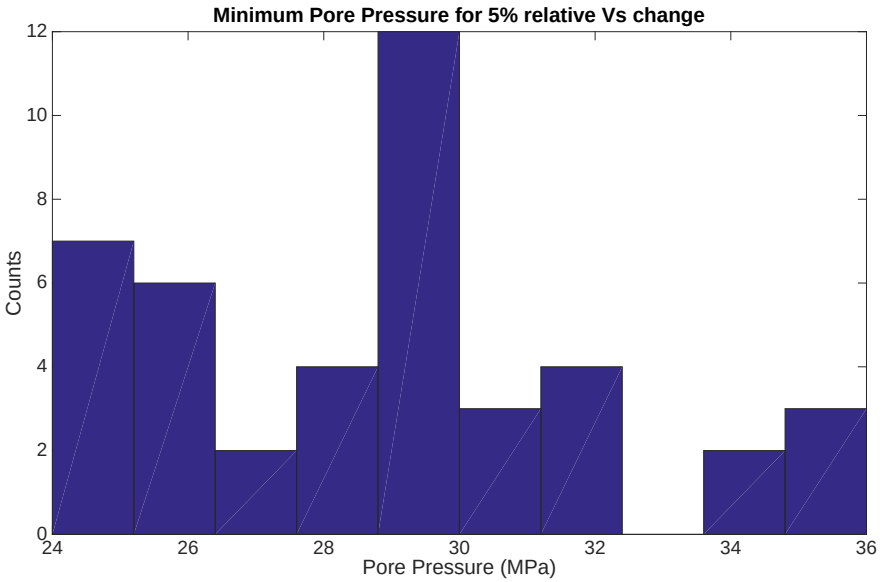

Note: Mean value is 29 MPa with a standard deviation of 3 MPa. Hydrostatic pore pressure is 18 MPa.

Figure 126. Histogram with the minimum Pore Pressure values to produce 5% change in S-wave velocity.

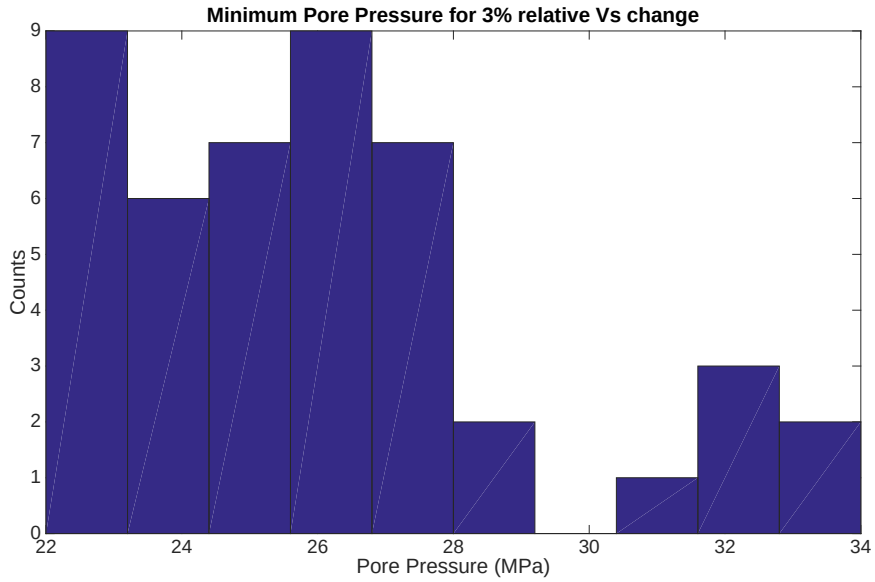

Note: Mean value is 26 MPa with a standard deviation of 3 MPa. Hydrostatic pore pressure is 18 MPa.

Figure 127. Histogram with the minimum Pore Pressure values to produce 3% change in S-wave velocity.

Table 17 and Table 18 summarize the results of the analysis of Han's data set for an initial hydrostatic pore pressure of 18 MPa (6000 ft depth). Table 17 presents the expected minimum values for pore pressure and the corresponding minimum increase of pore pressure from the hydrostatic state to produce 5% change in P and S-wave velocities, whereas Table 18 presents the same results, but for 3% change in P and S-wave velocities.

Table 17. Expected minimum pressure values and the minimum increase from hydrostatic pore pressure to produce 5% relative change in P and S-wave velocity.

Depth 6000ft (18 MPa hydrostatic Pp)	Minimum expected pore pressure (MPa)	Minimum expected increase from hydrostatic (MPa)
5% change in Vp	31.0 MPa (std. 2.7 MPa)	13.0 MPa
5% change in Vs	29.0 MPa (std. 3.0 MPa)	11.0 MPa

Note: The assumed depth is 6000 ft with an initial hydrostatic pore pressure of 18 MPa.

Table 18. Expected minimum pressure values and the minimum increase from hydrostatic pore pressure to produce 3% relative change in P and S-wave velocity.

Depth 6000ft (18 MPa hydrostatic Pp)	Minimum expected pore pressure (MPa)	Minimum expected increase from hydrostatic (MPa)
3% change in Vp	28.0 MPa (std. 3.0 MPa)	10.0 MPa
3% change in Vs	26.0 MPa (std. 2.7 MPa)	8.0 MPa

Note: The assumed depth is 6000 ft with an initial hydrostatic pore pressure of 18 MPa.

By comparing Table 15 and Table 17, as well as Table 16 and Table 18, we can observe that for the higher depth (6000 ft) we need to increase the pore pressure 2 MPa to 3 MPa more from the hydrostatic state to produce a detectable change in the seismic velocities than for the shallower depth (5000 ft). In addition, the analysis shows that the S-wave velocities are more sensitive to pressure changes. The required minimum pore pressure values to induce a visible change in seismic velocities are slightly lower than those required for the P-wave velocities, independently of depth or seismic detectability limit.

With excellent seismic data that allows imaging of 3% change in velocities at 6000 ft, the risk of not being able to monitor pore pressure front is 4%, since 2 out of the 48 sandstone samples from Han (1986) data set show undetectable change due to increasing pressure, lower than 3%. If the seismic detectability limit is 5%, then the risk of failure is 16% for P-wave data and 10% for S-wave velocity data.

XIII-2-5 The effect of porosity and clay content on velocity-pressure dependence

In this section we look for possible correlations between porosity and clay content of the Han's sandstone samples and their pressure dependence of seismic P and S-wave velocities.

Figure 128 and Figure 129 shows the relative difference for P-wave velocity and S-wave velocity respectively, measured at the lowest and the highest confining pressure values (5 MPa and 40 MPa) as a function of porosity. Superimposed on these figures are the least-square fit lines to the data. We can observe a large scatter in the data, with a very low correlation coefficient of -0.3 for both P and S-wave velocity changes with porosity. The least-square fit lines suggest that the larger the porosity, the larger the impact of pressure change on P and S-wave velocities. This implies that the higher porosity rocks may also have a larger volumetric fraction of the crack-like pores, which are pressure sensitive, but the correlation is extremely weak.

Figure 130 and Figure 131 show the minimum pore pressure values needed to produce 5% change in P and S-wave velocity respectively, as a function of porosity, when increasing pore pressure from the hydrostatic condition. The assumption in this analysis is a starting hydrostatic pore pressure value of 18 MPa, corresponding to a depth of formation of 6000 ft. Superimposed on the figures are the least-square linear fit to the data.

Figure 130 shows no correlation between porosity and the minimum values for pore pressure needed to produce a 5% change in P-wave velocity due to increasing pore pressure. Figure 131

indicates through the least-square linear fit a slight decrease of the minimum pore pressure values needed to produce 5% change in S-wave velocity with increasing porosity. This suggests that the larger the porosity of the samples, the less increase in pore pressure is needed to produce a detectable change in S-wave velocity. However, the correlation coefficient is insignificant.

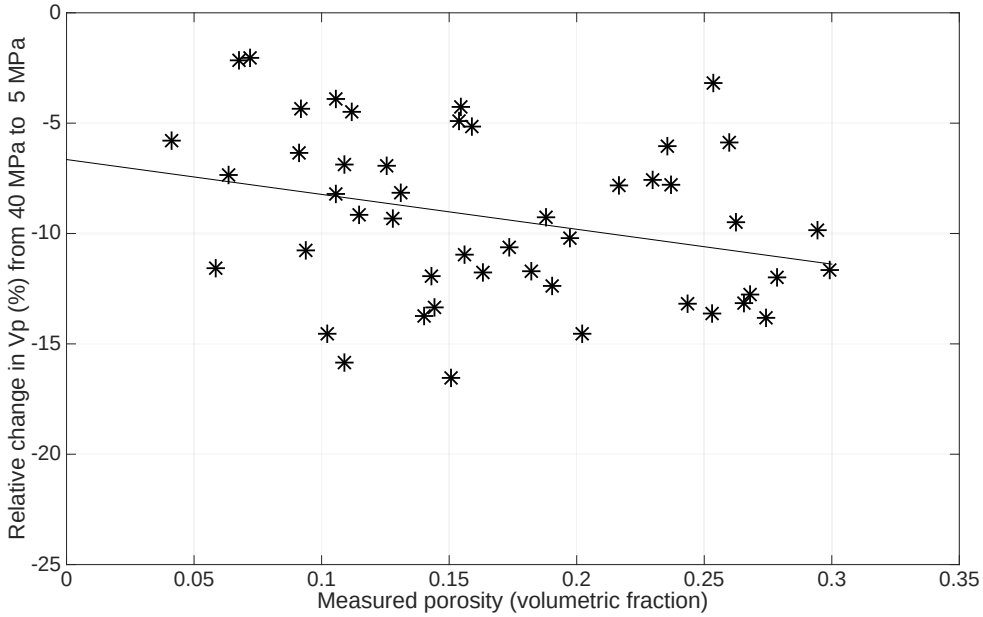

Note: Superimposed is the least-square linear fit to the data. Correlation coefficient is -0.3.

Figure 128. Relative decrease in P-wave velocity (%) from 40 MPa confining pressure to 5 MPa confining pressure as a function of porosity.

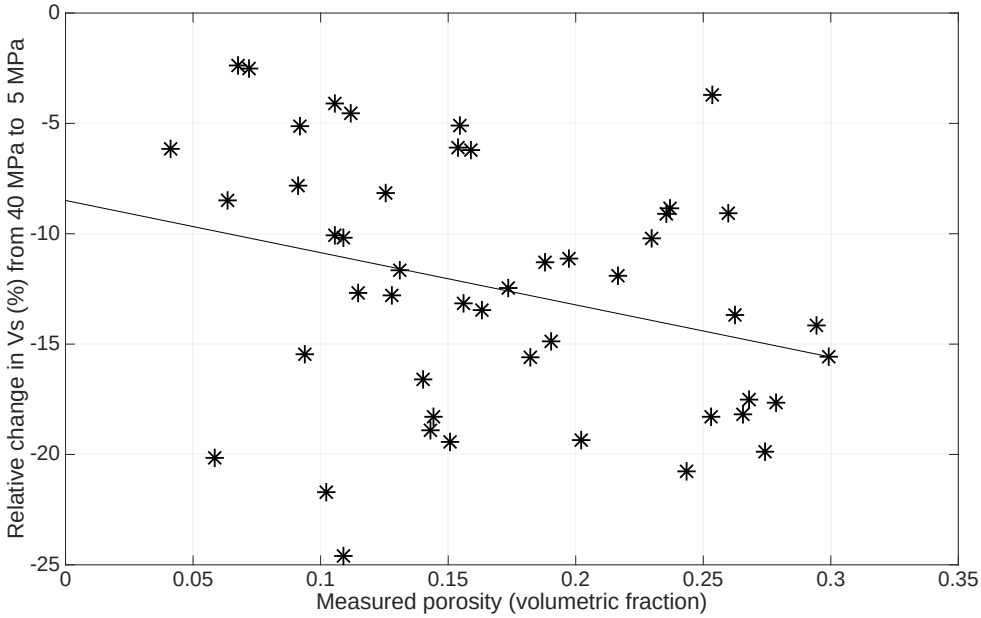

Note: Superimposed is the least-square linear fit to the data. Correlation coefficient is -0.3 (low correlation).

Figure 129. Relative decrease in S-wave velocity (%) from 40 MPa confining pressure to 5 MPa confining pressure, as a function of porosity.

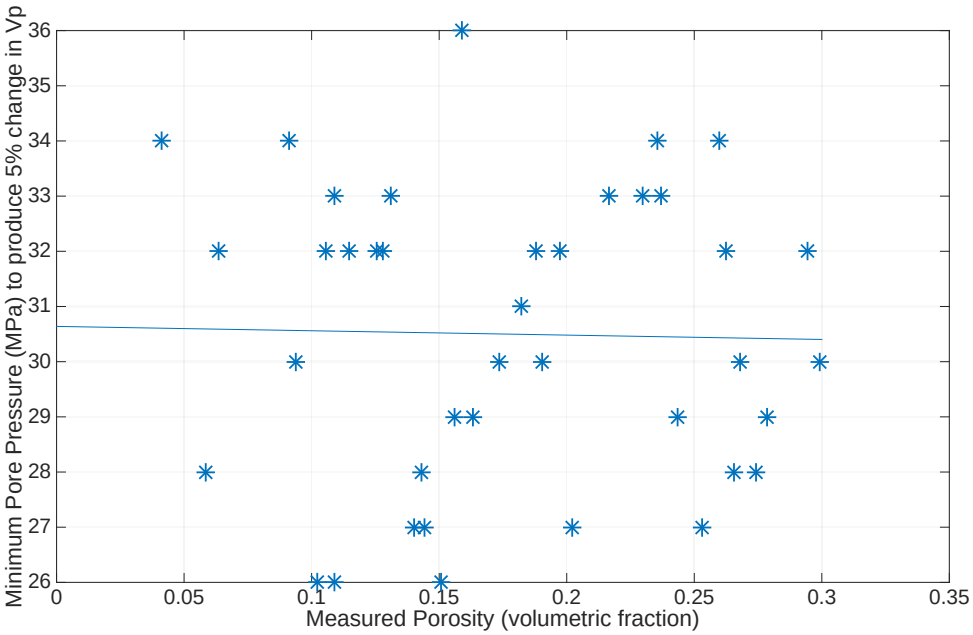

Note: The pore pressure is increased from the initial hydrostatic pore pressure of 18 MPa. Superimposed on the figure is the least-square linear fit to the data, which shows no correlation.

Figure 130. Minimum Pore Pressure values (MPa) to produce 5% change in P-wave velocity as a function of porosity.

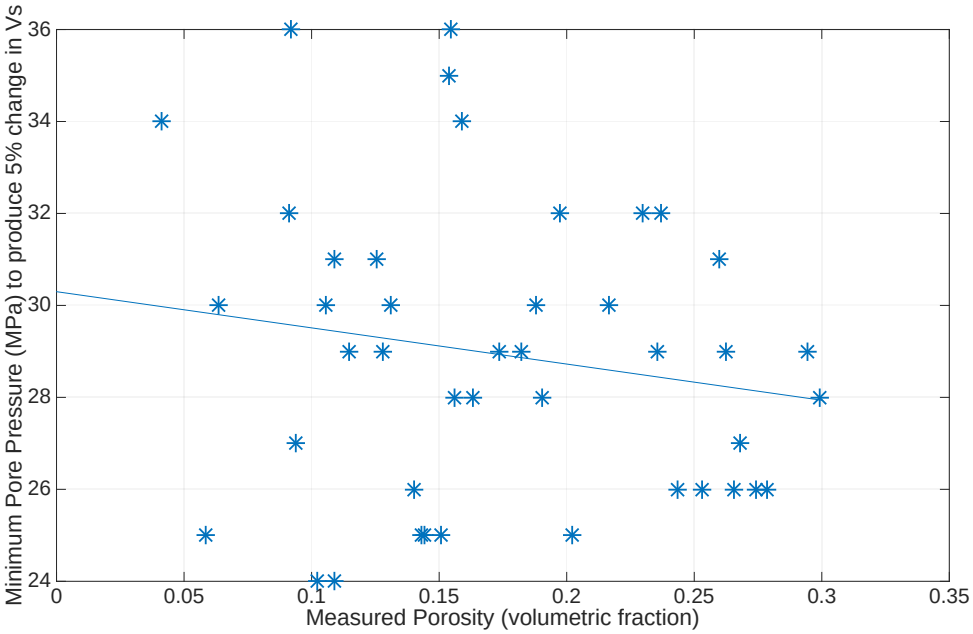

Note: The pore pressure is increased from the initial hydrostatic pore pressure of 18 MPa. Superimposed on the figure is the least-square linear fit to the data (correlation coefficient -0.17).

Figure 131. Minimum Pore Pressure values (MPa) to produce 5% change in S-wave velocity as a function of porosity.

Figure 132 shows the porosity versus the clay content for Han's data set. Superimposed on the figure is the least-square linear fit to the data, with a correlation coefficient of -0.47. This indicates that porosity of the samples decreases with increasing clay content. A plausible

explanation is that the smaller clay particles fill some of the porous space of the sandstone, reducing the porosity.

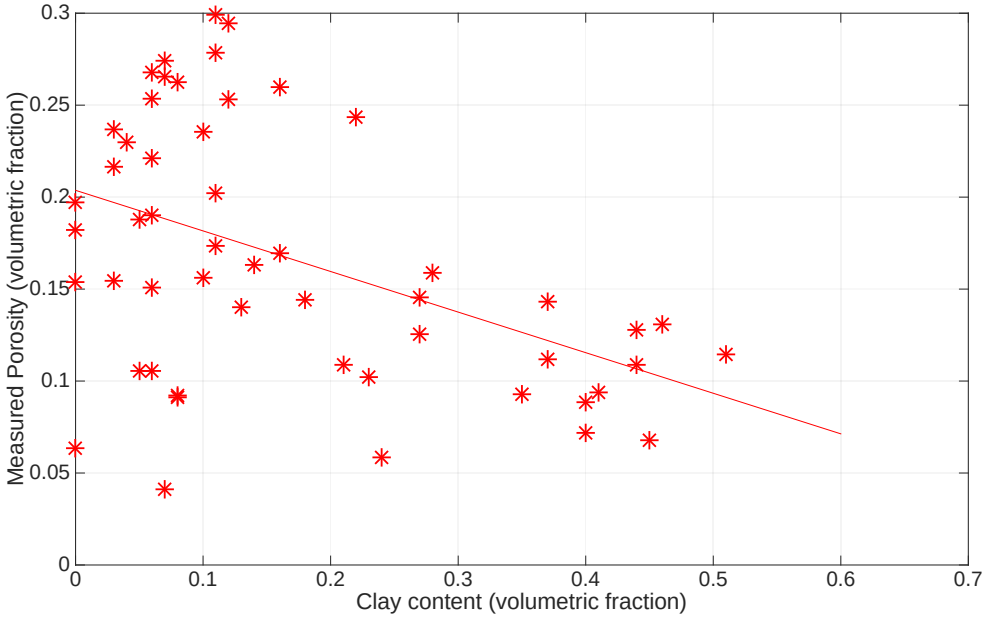

Note: Superimposed is the least-square linear fit to the data. The correlation coefficient is -0.47.

Figure 132. Measured porosity versus clay content for Han's sandstone samples.

The anti-correlation of clay content and porosity is reflected somewhat in Figure 133 and Figure 134 that show the relative difference for P-wave velocity and S-wave velocity respectively, measured at the lowest and the highest confining pressure values (5 MPa and 40 MPa) as a function of clay content. Superimposed on the figures are again the least-square fit lines to the data. Practically, there is no correlation between clay content and the relative change in P and S-wave velocities with pressure.

Based on the analysis of the porosity and clay data we can conclude that their correlation with pressure-velocity dependence is very weak.

There is an indication that the changes in velocities with pore pressure are larger (as absolute values) with increasing porosity. One explanation could be that for larger porosity there is also a larger volumetric fraction of crack-like, compressible pores that are pressure dependent. However, this correlation is very weak. This implies that not having direct observations of porosity and mineralogy for Hosston Formation at the study site is not as detrimental to the prediction of the velocity-pressure behavior, because their influence is not significant.

The main physical parameters that influence the velocity-pressure dependence are the volume and shape of the compressible pore space, which are difficult to obtain. The impact of the compressible, crack-like pores on the velocity-pressure dependence is illustrated in the following section using rock physics theoretical modeling.

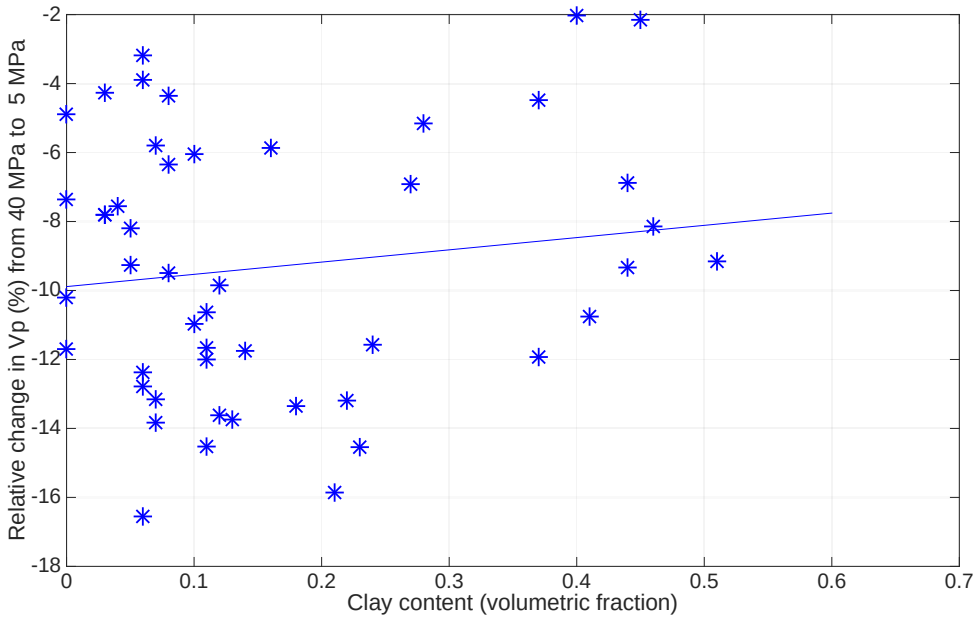

Note: Superimposed is the least-square linear fit to the data. Correlation coefficient is 0.14 (practically no correlation).

Figure 133. Relative decrease in P-wave velocity (%) from 40 MPa confining pressure to 5 MPa confining pressure, as a function of porosity.

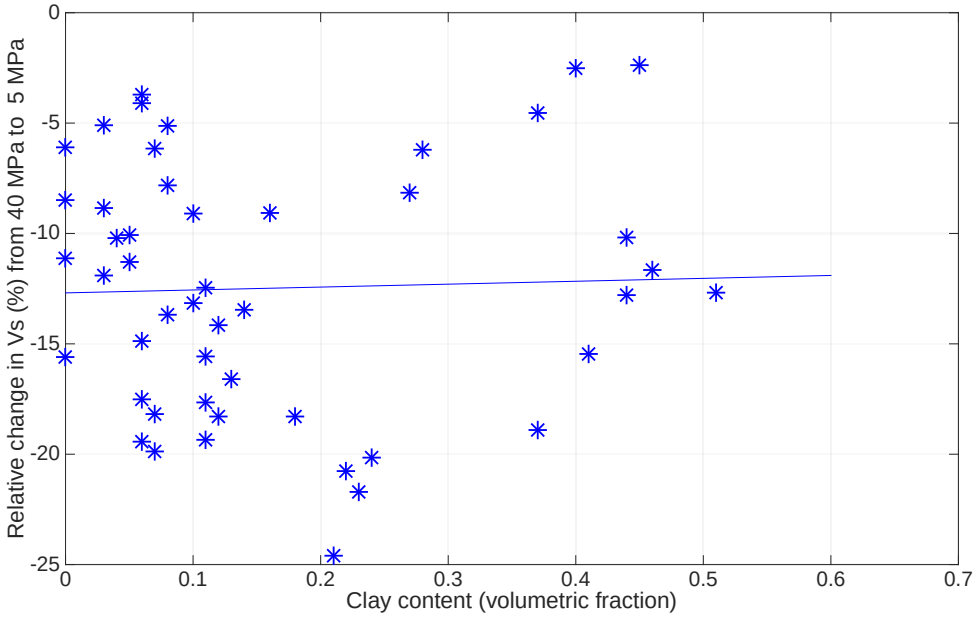

Note: Superimposed is the least-square linear fit to the data. Correlation coefficient is 0.03 (no correlation).

Figure 134. Relative decrease in S-wave velocity (%) from 40 MPa confining pressure to 5 MPa confining pressure, as a function of porosity.

XIII-3. Theoretical Rock Physics Modeling

XIII-3-1 Introduction

In this section we present a theoretical rock-physics model that allows us to define the compressible, pressure-sensitive pores in rocks using idealized shapes, such as ellipsoids. During

the fluid injection, the mineral frame weakens due to the opening of the crack-like pores and loosening of the grain boundaries.

One of the theoretical models that accounts for changes in the elastic moduli of the mineral frame is the self-consistent approximation (SCA) by Berryman (1995). This theoretical approach allows us to model the porous space of the rocks as oblate spheroids with different aspect ratios. Small aspect ratio pores are more compressible and more easily closed or opened by variations in effective pressure.

Equation 1 relates the pressure needed to close a single, isolated ellipsoidal pore to its aspect ratio and the elastic solid surrounding that pore (Mavko et al., 2009):

$$a_0 = \frac{2s_0(1-n_m^2)(3K_m+m_m)}{9K_m m_m} \quad (1)$$

In Equation 1 α_0 is the aspect ratio of the pore, σ_0 is the pressure acting on the pore and ν_m, K_m, μ_m are the Poisson's ratio, bulk modulus and shear modulus at the solid surrounding the crack. This equation shows that the stress required to open or close a crack increases with the aspect ratio of the crack.

To model a rock, we assume a uniform volumetric distribution of ellipsoidal pores with various aspect ratios. The distribution of the compressible, pressure-dependent aspect ratios of the porous space can be determined by calibrating the velocity-pressure dependence with laboratory. When such measurements are not available for the geological formation of interest, analogues can be used from published laboratory data, as presented in the previous section.

Figure 135a presents P-wave laboratory measurements as a function of effective pressure (courtesy of Chris Purcell and William Harbert of University of Pittsburg). The boxes on Figure 135a represent schematically the dry mineral frame: the black regions correspond to the mineral and the white ellipsoids correspond to the pores with various aspect ratios. The P-wave velocity increases with effective pressure due to the stiffening of the mineral frame, caused by closing of the crack-like pores (with low aspect ratios). The shape of the velocity pressure dependence is related to the shape (or aspect ratio) of the cracks that close at a given effective pressure. The fraction of porosity that is pressure dependent is very small, only a few percentages of the total porosity. However, this fraction has a strong impact on velocity-pressure dependence. Superimposed on Figure 135a are the modeling results (black curve) for P-wave velocity as a function of effective pressure. At each pressure step the distribution of aspect ratios of the crack-like pores is updated, such that the pores with certain aspect ratios are closed, as described by Equation 1. Then the bulk and shear modulus of the rock are derived using Berryman SCA, from which P and S-wave velocities are calculated.

We can observe a good agreement between the modeling results and the actual laboratory measurements of P-wave velocity. Moreover, Figure 135b shows lab measurements of the S-wave velocity (blue circles) for the same sample. The black curve represents the modeling results. Both P and S-wave velocities of the derived using rock-physics theoretical modeling are in good agreement with the laboratory data. This example suggests that, even though the model assumes idealistic pore shapes, it can capture the physical behavior of the velocities as a function of effective pressure.

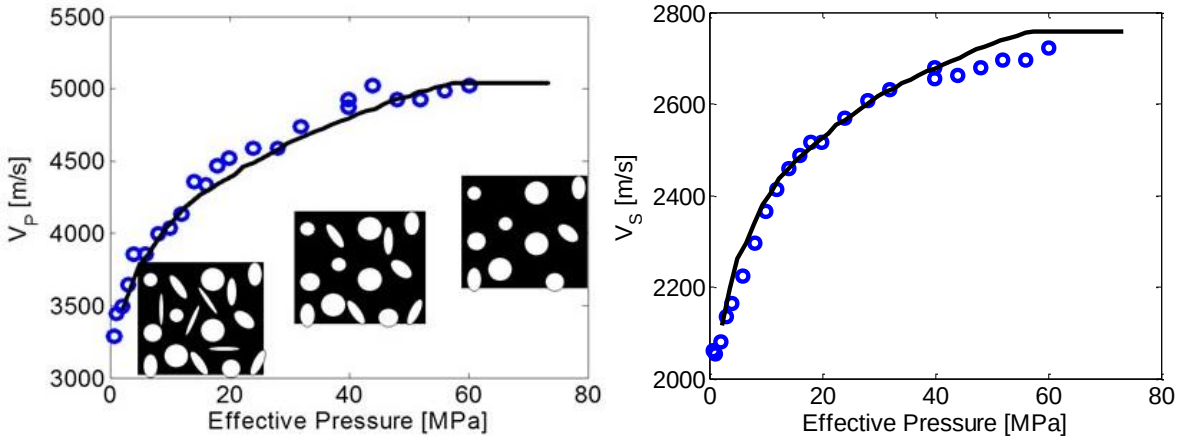

Note: Superimposed as black curves are the results for P-wave velocity and the S-wave velocity as a function of effective pressure calculated using Berryman (1995) self-consistent approach. The boxes represent schematically the dry mineral frame: the black regions are the mineral and the white ellipsoids are the pores with various aspect ratios.

Figure 135. Laboratory measurements (blue circles) of P-wave velocity (left panel) and S-wave velocity (right panel) as a function of effective pressure.

XIII-3-2 Theoretical Rock-Physics Modeling of the Hosston Formation

For Hosston Formation we consider a theoretical sandstone with a total porosity equal to 16%. The compressible, crack-like pores are modeled with a uniform distribution for the volumetric fraction of each aspect ratio considered. This distribution is chosen such that the modeled P and S-wave velocities as a function of effective pressure are within the ranges observed in the laboratory data (Han, 1986) analyzed in detail in the previous section. The total volume of the compressible pores is a key parameter on the velocity-pressure relation. The velocity variation with pressure increases with the volume of the crack-like pores. We consider two different scenarios for the Hosston Formation: Model 1 (optimistic), with a larger volumetric fraction of the compliant pores, and Model 2, (more plausible, based on the analysis of Han's data), with a lower volumetric fraction of the compressible pores. Both models have the same total porosity of 16%.

Figure 136 shows on the top-left panel the uniform distribution of volumetric fraction for the crack-like pores for the optimistic scenario. When all the compliant, pressure-dependent pores are all open, their cumulated volumetric fraction is 0.00145. These pores are very thin, so they occupy an insignificant volume. However, they have a big impact on the elastic properties of the rock, just as discussed in the previous section on lab measurements. Nonetheless, in this modeling scenario, the value of the volumetric fraction of 0.00145 is relatively large, as it will be shown. The other model considered has a smaller cumulative volumetric fraction of the compliant pores, equal to 0.00067.

As the pore pressure increases, cracks open up and weaken the mineral frame. Therefore, P and S-wave velocities decrease, as shown on the top-right panel and on the lower-left panel respectively. This observation is valid for both laboratory measurements (green curves), and the modeling results (black curves). The lower-right panel shows the P-to-S-wave velocity ratio, which increases with increasing pore pressure for both the lab measurements (green curves) and for the modeling results (black curves). The physical explanation for the increasing P-to-S-wave velocity ratio is that the S-wave velocity decreases more due to the opening of the cracks than the P-wave velocity.

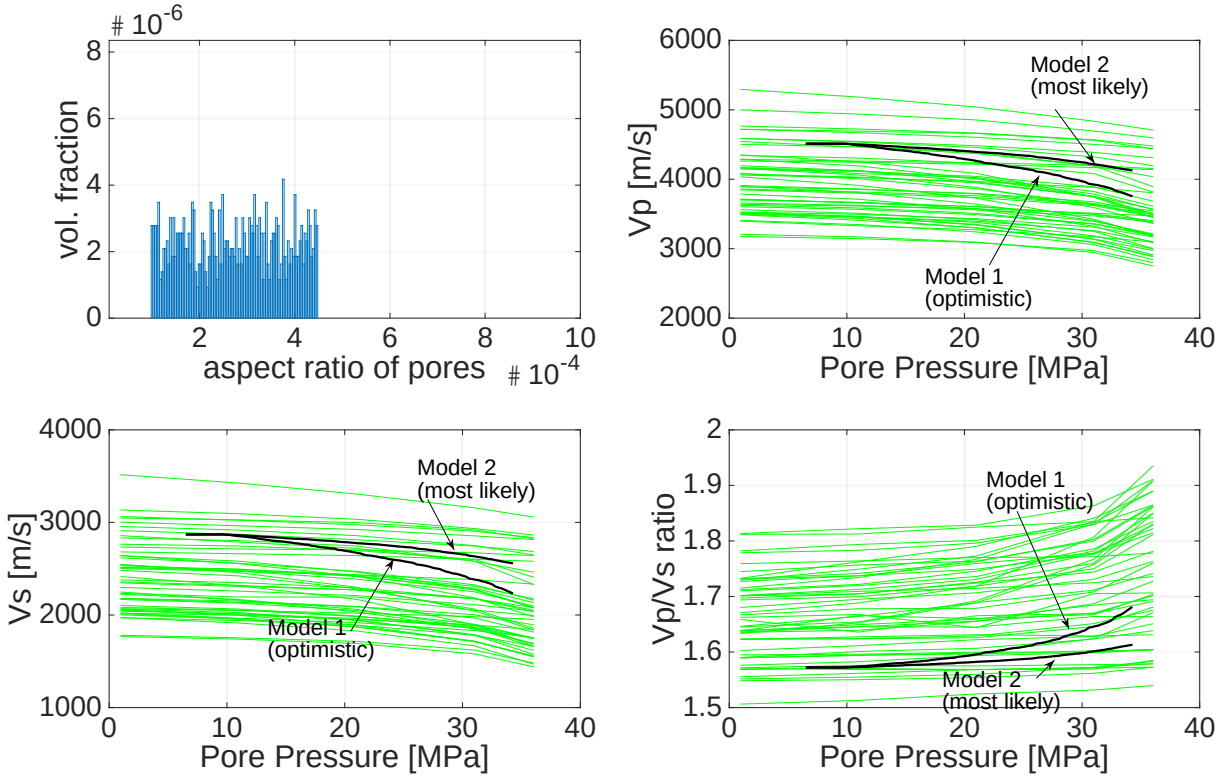

Note: Top-left: Volumetric distribution of aspect ratios for the compliant pores used in the theoretical modeling of the optimistic scenario. Top-right: P-wave velocity as a function of Pore Pressure for Han's data (green curves) and for the two theoretical models (black curves). Lower-left: S-wave velocity as a function of Pore Pressure for Han's data (green curves) and for the two theoretical models (black curves). Lower-right: P to S-wave velocity ratio as a function of Pore Pressure for Han's data (green curves) and for the two theoretical models (black curves).

Figure 136. Laboratory measurements and theoretical modeling results of velocities vs. pore pressure.

We can observe that Model 1, which has larger volumetric fraction of the crack-like pores (optimistic model), shows a larger decrease in P and S-wave velocities than Model 2, which has a lower volumetric fraction of the compressible pores. Next we analyze in more detail the two theoretical models, assuming that the depth of the Hosston Formation is 6000ft, with an initial hydrostatic state of 18 MPa.

XIII-3-2.1 Model 1: Optimistic scenario

We compute the relative decrease in P and S-wave velocities with increasing pore pressure, starting from the hydrostatic state of 18 MPa. The results for P-wave and S-wave velocities are displayed on Figure 137 and Figure 138, respectively. We consider the limit of seismic detectability to be 5% decrease in P and S-wave velocity and we represent that limit on Figure 137 and Figure 138. For P-wave velocity, the minimum required pore pressure to generate a detectable decrease for P-wave velocity is 25.15 MPa, while for the S-wave velocity is 23.75 MPa. In other words, the pore pressure should be increased 7 MPa from the hydrostatic condition to be able to detect a change in P-wave velocity and a 6 MPa to detect a change in S-wave velocity.

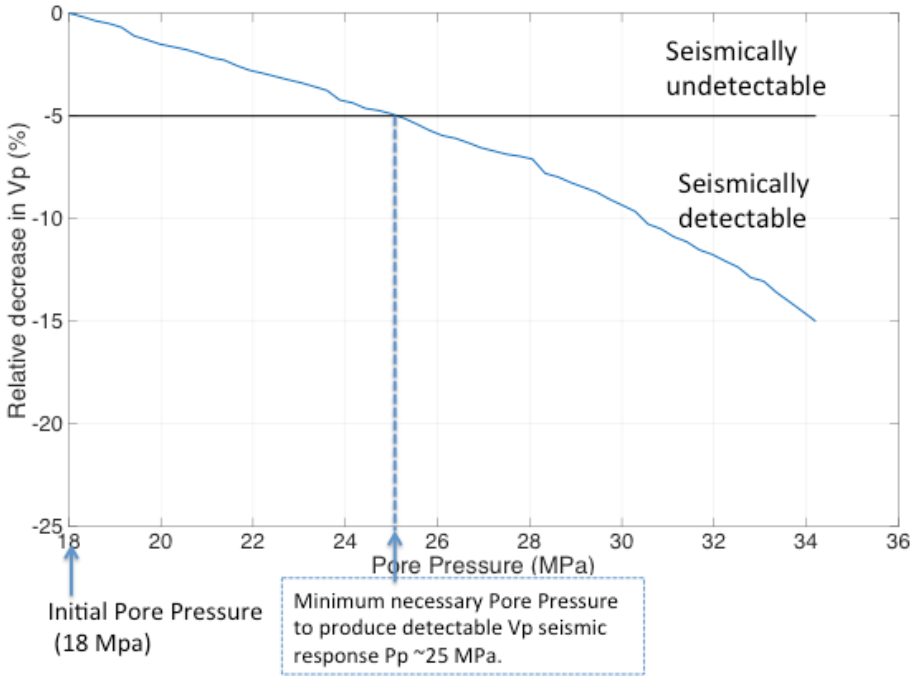

Note: Superimposed is the 5% limit of seismic detectability for relative change in P-wave velocity and the minimum required pore pressure to produce a detectable P-wave seismic response (~25 MPa). Hydrostatic pore pressure is 18 MPa.

Figure 137. Modeled relative decrease in P-wave velocity (percentage) as a function of Pore Pressure for Model 1.

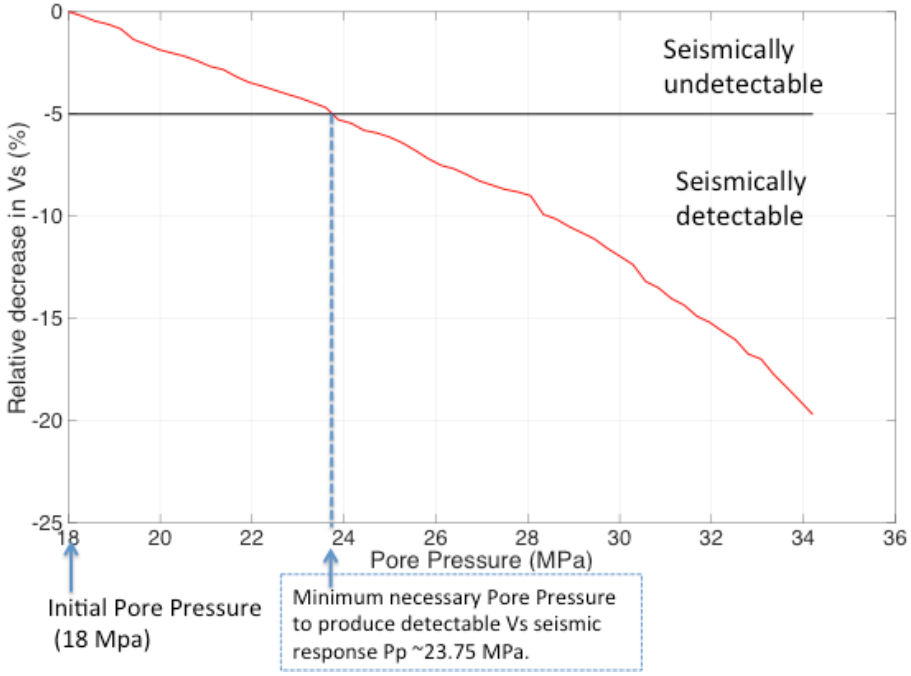

Note: Superimposed is the 5% limit of seismic detectability for relative change in S-wave velocity and the minimum required pore pressure to produce a detectable S-wave seismic response (~23.75 MPa). Hydrostatic pore pressure is 18 MPa.

Figure 138. Modeled relative decrease in S-wave velocity (percentage) as a function of Pore Pressure.

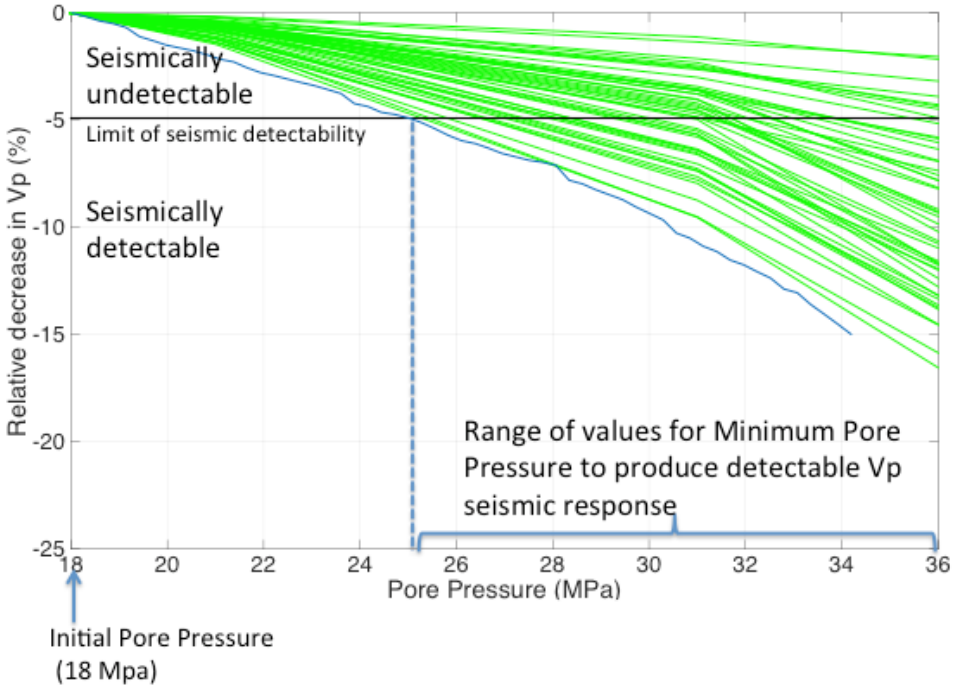

Note: Superimposed is the 5% limit of seismic detectability for relative change in P-wave velocity and the range of minimum pore pressure values that produce a detectable seismic response.

Figure 139. Relative decrease in P-wave velocity (percentage) as a function of Pore Pressure for laboratory data (green curves) and the modeling results for the optimistic scenario (blue curve).

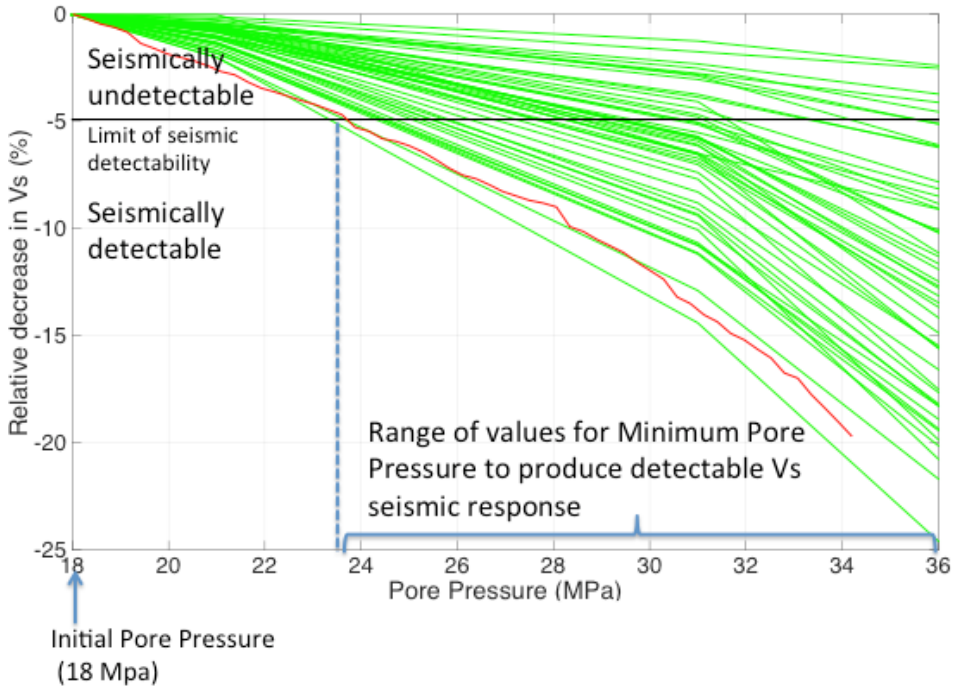

Note: Superimposed is the 5% limit of seismic detectability for relative change in S-wave velocity and the range of minimum pore pressure values that produce a detectable seismic response.

Figure 140. Relative decrease in S-wave velocity (percentage) as a function of Pore Pressure for laboratory data (green curves) and the modeling results for the optimistic scenario (red curve).

Figure 139 and Figure 140 show how the modeling results compare with Han's laboratory measurements on P and S-wave velocities. These modeling results for the relative decrease of P and S-wave velocity with increasing pore pressure indicate an optimistic scenario, for which the required pore pressure needed to produce a detectable seismic response (5% change) is at the lower range of the values derived from laboratory measurements on the 48 sandstone samples.

XIII-3-2.2 Model 2: more plausible scenario

The second model has a lower volumetric fraction of the pressure-dependent pores, equal to 0.00067. We again compute the relative decrease in P and S-wave velocities with increasing pore pressure, starting from the same hydrostatic state of 18 MPa. The results for P-wave and S-wave velocities are displayed on Figure 141 and Figure 142, respectively. The seismic detectability limit is 5% decrease in P and S-wave velocity and it is represented on Figure 141 and Figure 142 as the black line. For P-wave velocity, the minimum required pore pressure to generate a detectable decrease for P-wave velocity is 30.5 MPa, while for the S-wave velocity is 29 MPa. These values imply a 12.5 MPa increase in pore pressure from the hydrostatic condition to detect a change in P-wave velocity and a 11 MPa increase in pore pressure to detect a change in S-wave velocity.

Figure 143 and Figure 144 show how the theoretical results for both Model 1 and Model 2 compare with Han's laboratory measurements on P and S-wave velocities. As discussed, Model 1 represents an optimistic scenario, because the required pore pressure needed to produce a detectable seismic response (5% change) is 25 MPa, and is at the lower range of the values derived from laboratory measurements on the 48 sandstone samples. However, for Model 2, the required increase in pore pressure from the hydrostatic state is up to 30.5 MPa, closer to the average of 31 MPa derived from the Han data set (first row in Table 2 from previous section). Based on the comparison between modeling results and lab analysis, we conclude that Model 2 is more likely.

We can observe that both laboratory measurements and theoretical modeling indicate that S-wave velocities are more sensitive to pressure changes. The required pore pressure needed to produce 5% change in S-wave velocity is lower than that required for the P-wave velocity.

Rock-physics theoretical modeling is a powerful tool to understand the impact of various rock parameters on the velocity-pressure dependence and to link seismic observations, such as changes in P and S-wave velocities to rock properties, and in particular for this study, to pore pressure. However, laboratory measurements are crucial to calibrate the theoretical models to related variations in velocities to pore pressure changes.

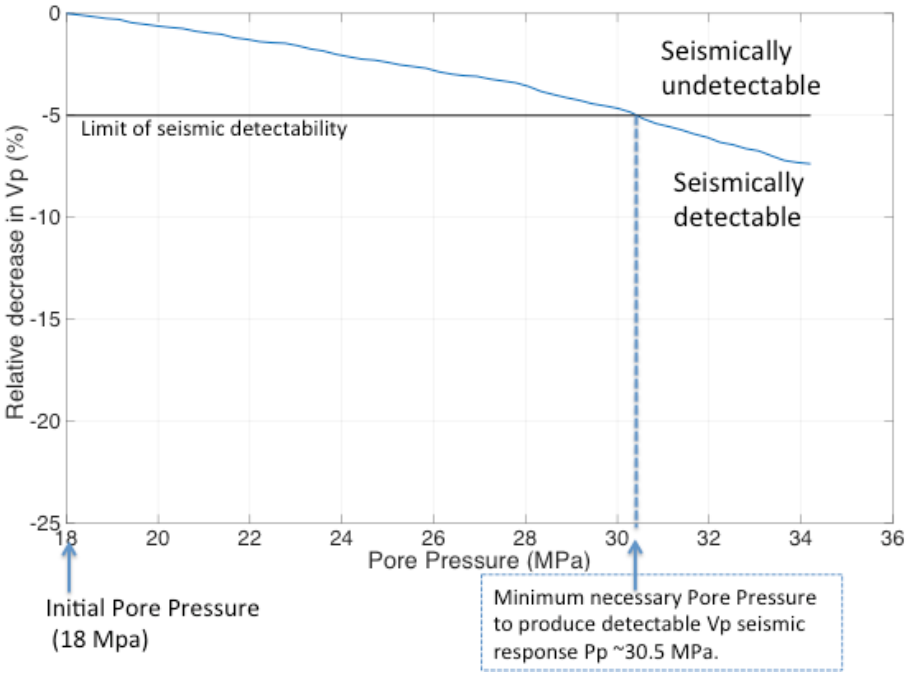

Note: Superimposed is the 5% limit of seismic detectability for relative change in P-wave velocity and the minimum required pore pressure to produce a detectable P-wave seismic response (~30.5 MPa). Hydrostatic pore pressure is 18 MPa.

Figure 141. Modeled relative decrease in P-wave velocity (percentage) as a function of Pore Pressure for Model 2.

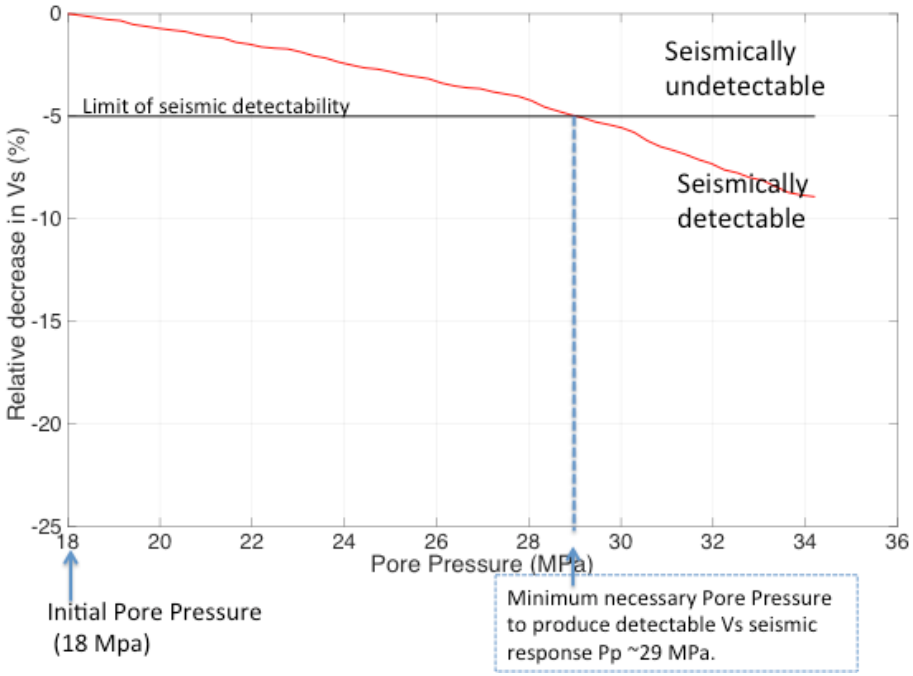

Note: Superimposed is the 5% limit of seismic detectability for relative change in S-wave velocity and the minimum required pore pressure to produce a detectable S-wave seismic response (~29 MPa). Hydrostatic pore pressure is 18 MPa.

Figure 142. Modeled relative decrease in S-wave velocity (percentage) as a function of Pore Pressure for Model 2.

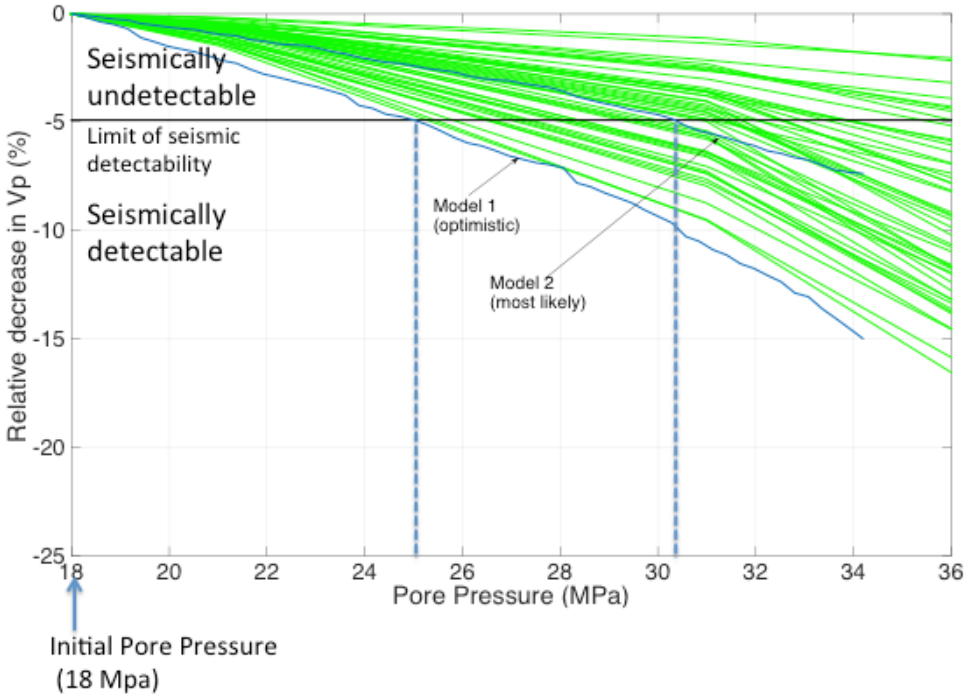

Note: Superimposed is the 5% limit of seismic detectability for relative change in P-wave velocity and the range of minimum pore pressure values that produce a detectable seismic response.

Figure 143. Relative decrease in P-wave velocity (percentage) as a function of Pore Pressure for laboratory data (green curves) and the theoretical Model 1 and Model 2 (blue curves).

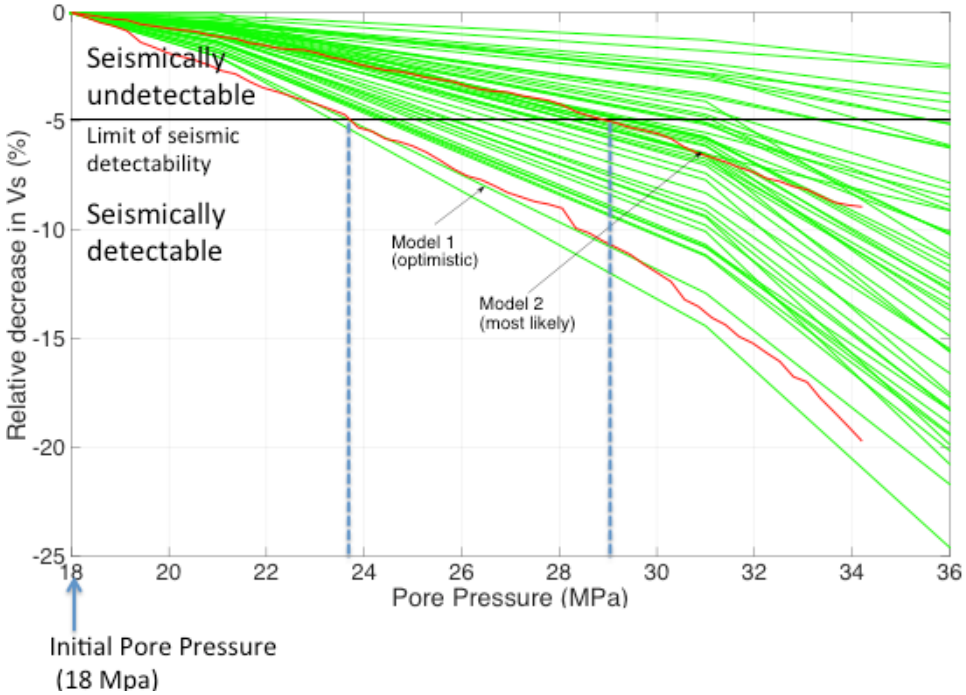

Note: Superimposed is the 5% limit of seismic detectability for relative change in S-wave velocity and the range of minimum pore pressure values that produce a detectable seismic response.

Figure 144. Relative decrease in S-wave velocity (percentage) as a function of Pore Pressure for laboratory data (green curves) and the theoretical Model 1 and Model 2 (red curves).

XIII-4. Conclusions

Increasing pore pressure softens the elastic mineral frame of the rocks, by opening crack-like pores and flaws, and by loosening grain boundaries. As a result, the P and S-wave velocities are lowered, and pore pressure changes could be monitored using seismic data. However, the pressure dependence of velocities is highly variable from sample to sample, depending on the amount and the geometric shapes of the compressible, crack-like pores. Therefore, the only way to know the pressure dependence of velocities for a particular rock is to measure it in the lab.

At this first stage of the study there are no measurements of pressure dependence of velocities from Hosston sandstone. In fact, there are no well-log data that penetrate Hosston formation at Devine Test Site. Therefore, we use a comprehensive data set by Han (1986) on 48 sandstone samples to understand and predict the velocity variations with pore pressure, as analogues to Hosston Formation. Since in nature there is a large variability in the pressure dependence of velocities even within the same geologic formation, only a statistical analysis can give guidelines of what to expect in the field in terms of monitoring pressure fronts with seismic data. Consequently, Han (1986)'s laboratory data set is crucial for calibrating rock-physics theoretical modeling and also for predicting the elastic changes that can occur within a sandstone formation with increasing pore pressure.

Since there are no direct measurements on Hosston Formation at the Devine Test Site, we use information from published research studies to infer the possible rock properties of this sandstone. The depth of the formation considered in our analysis is within 5000 ft to 6000 ft range. The average porosity of the formation is considered to be 16.6% at 6000ft, as indicated in a previous study by Bartberger et al. (2003). A happy coincidence in this research study is that the average porosity of all the samples from Han's data is in fact 16.6%. The standard deviation about this mean value from Han's data set can be viewed as the uncertainty associated with the porosity of Hosston formation. The mineralogy of the Hosston Formation is also inferred from previous studies at other sites and it is assumed to be quartz dominated, with some clay minerals (illite and chlorite) and feldspar. However, the most important parameter that affects the pressure dependence of velocities is the volume of the compressible, pressure-dependent pores, which is difficult to obtain. We have not found any published data of velocity pressure dependence for Hosston Formation. That is why Han's laboratory data set of velocities versus pressure is invaluable to this study.

Regarding the impact of the depth of formation, we conclude that for the higher depth (6000 ft) we need a higher increase in the pore pressure to produce the same relative decrease in the seismic velocities than at the shallower depth (5000 ft). The actual figures are presented in Table 15 to Table 18. For convenience, we include a table summarizing the results in this conclusion section as well (Table 19).

Based on the analysis of the porosity and clay content data we conclude that their correlation with pressure-velocity dependence is weak. There is an indication that the changes in velocities with pore pressure are larger (as absolute values) with increasing porosity. One explanation could be that at larger porosity there is also a larger volumetric fraction of the crack-like, compressible pores, and therefore a larger pressure sensitivity. However, this correlation is relatively weak, as the correlation coefficients from least-square linear fit indicate as well. Therefore, not knowing precisely the porosity and mineralogy of the Hosston Formation does not have a large detrimental effect on our predictions for its pressure-velocity dependence.

Table 19. Expected minimum pressure values and the minimum increase from hydrostatic pore pressure to produce a detectable seismic response in P and S-wave velocity (3% and 5% change).

	Minimum expected pore pressure (MPa)	Minimum expected increase from hydrostatic Pp (MPa)
Depth 5000ft (15 MPa hydrostatic pore pressure)		
5% change in Vp	25.0 MPa (std. 2.0 MPa)	10.0 MPa
3% change in Vp	23.0 MPa (std. 2.5 MPa)	8.0 MPa
5% change in Vs	24.0 MPa (std. 2.5 MPa)	9.0 MPa
3% change in Vs	21.5 MPa (std. 2.7 MPa)	6.5 MPa
Depth 6000ft (18 MPa hydrostatic pore pressure)		
5% change in Vp	31.0 MPa (std. 2.7 MPa)	13.0 MPa
3% change in Vp	28.0 MPa (std. 3.0 MPa)	10.0 MPa
5% change in Vs	29.0 MPa (std. 3.0 MPa)	11.0 MPa
3% change in Vs	26.0 MPa (std. 2.7 MPa)	8.0 MPa

Note: The assumed depths are 5000 ft with an initial hydrostatic pore pressure of 15 MPa presented at the top of the table and 6000 ft with an initial hydrostatic pore pressure of 18 MPa presented at the lower part of the table.

The main physical parameters that influence the velocity-pressure dependence are the volume and shape of the compressible pore space. We illustrate the impact of the volume and shape of the compressible pores using a theoretical rock-physics model calibrated with Han's laboratory measurements. We consider two different models: one with larger volume of the compressible pores which represents an optimistic scenario for the Hosston Formation, and a second model, with lower volume of the compressible pores, which is a more likely scenario, based on Han's comprehensive data set. The theoretical model is in fact calibrated with Han's lab data. There is a good agreement between laboratory measurements and theoretical modeling. We can observe that both lab data and theoretical results indicate that S-wave velocities are more sensitive to pressure changes than the P-wave velocities. The required pore pressure needed to produce either 3% or 5% change in S-wave velocity is lower than the corresponding pore pressure required to produce the same changes in P-wave velocity. P-to-S-wave velocity ratio is a key seismic parameter for pressure front monitoring. Lab data and theoretical modeling show that for rock samples with large pressure dependence, the Vp/Vs ratio increases significantly with increasing pore pressure.

Rock-physics theoretical modeling is a powerful tool to understand the impact of various rock parameters on the velocity-pressure dependence. The theoretical modeling also provides a link between seismic observations, such as changes in P and S-wave velocities to rock properties, and in particular for this study, to pore pressure. However, laboratory measurements are crucial to calibrate the theoretical models in order to relate variations in velocities to pore pressure changes. This laboratory data set of 48 samples is relatively large, but it is still statistically limited. Also, the resolution is not ideal, since the actual measurements are performed at only 5 pressure values. In between the measurements, the data is interpolated at a sample rate of 1 MPa. Ideal research situation would be multiple samples (more than 50) from the actual Hosston Formation, measured at smaller pressure increments. However, the acquisition of such data set requires much more resources and it is beyond the scope of this study.

Based on the analysis of the already available Han (1986)'s data set, we can also predict the risk of failure to seismically monitor the pore pressure front in a sandstone formation. With excellent seismic data that can detect changes as small as 3% in velocities, the probability of not detecting

any change with pore pressure is about 4% to 6%. Even if the seismic data allows us to monitor changes in velocities of 5% or higher, the risk of failure is about 15%. This is a relatively small risk, and with excellent seismic data acquisition and processing we can conclude that the probability to successfully monitor pore pressure changes in Hosston Formation is larger than 85%.

XIII-5. References

Bartberger, C. E., Dyman, T. S, and Condon, S. M., 2003, Potential for a Basin-Centered Gas Accumulation in Travis Peak (Hosston) Formation, Gulf Coast Basin, U.S.A., U.S. Geological Survey Bulletin 21-84-E.

Berryman, J. G., 1995, Mixture theories for rocks. In Rock Physics and Phase Relations: a Handbook of Physical Constants, ed. T. J. Ahrens. Washington, DC: American Geophysical Union.

Gassmann, F., 1951, On the elasticity of porous media, Veirteljahrsschrift der Naturforschenden Gesellschaft in Zurich, 96, 1-23.

Han, D. H., 1986, Effects of porosity and clay content on acoustic properties of sandstones and unconsolidated sediments, Ph. D. dissertation, Stanford University.

Mavko, G., Mukerji, T., and Dvorkin, J., 2009, The Rock Physics Handbook: Tools for Seismic Analysis of Porous Media. Cambridge University Press.

Mavko, G., and T. Mukerji, 1995, Seismic pore space compressibility and Gassmann's relation: Geophysics, 60, 1743-1749.

Mavko, G. and Jizba, D.,1991, Estimating grain-scale fluid effects on velocity dispersion in rocks, Geophysics, 60, 1081-1087.

Nur, A. and Simmons, G.,1969, Stress-induced velocity anisotropy in rock: An experimental study, Journal of Geophys. Research, 74, 6667.

Nur, A., 1971, Effects of stress on velocity anisotropy in rocks with cracks, Journal of Geophys. Research, 76, 2022-2034.